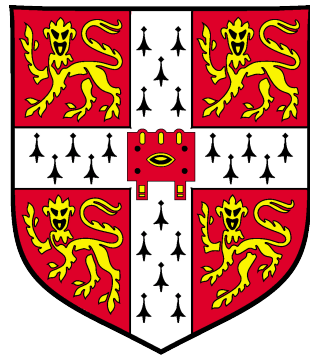


Molecular Beam Epitaxy of InGaAs and InAlAs for Low-Dimensional Electrical Transport

Paul Jonathan Simmonds



Emmanuel College
University of Cambridge

Dissertation submitted for the degree of
Doctor of Philosophy

August 2007

“ The works of the Lord are great,
sought out of all them that have pleasure therein. ”

Psalm 111:2

Declaration

This dissertation is the result of my own work carried out between October 2003 and August 2007 in the Semiconductor Physics Group at the Cavendish Laboratory and includes nothing which is the outcome of work done in collaboration, except where otherwise acknowledged. It has not been submitted in whole or part for a degree at this or any other University. It is less than sixty thousand words in length.

Paul Jonathan Simmonds, August 2007

Preface

Funding for this research came from the EPSRC, with additional financial support generously provided by the head of the group, Professor Sir Mike Pepper and the Cambridge Philosophical Society. The work presented in this dissertation would not have been possible without the assistance of many people.

I am indebted to my supervisor Professor Dave Ritchie and to Dr. Harvey Beere, who first introduced me to the technique of MBE. Their experience, guidance and encouragement are gratefully acknowledged. In addition, through many useful discussions, Dr. Ian Farrer and Dr. Paola Atkinson have enriched my understanding of III-V crystal growth.

Various aspects of this work were carried out in collaboration with Toshiba Research Europe Limited, an opportunity for which I thank Dr. Andrew Shields. I am extremely grateful to Dr. Hongwei Li who helped me with PL, AFM and electrical characterisation and who, with Dr. Beata Kardynal, made the excellent photon detection measurements presented here. My thanks too go to Dr. Stuart Holmes who gave extensive assistance with the Heliox cryostat measurements.

I owe many thanks to Dr. François Sfigakis and Dr. Abi Graham for sharing their expertise in 1D measurement. Dr. Daniele Ercolani of the Laboratorio Nazionale, Trieste, Italy was most kind in helping me to calculate band structures. The knowledge of Mary Vickers of the Department of Materials Science and Metallurgy was invaluable when interpreting my XRD measurements. Doug Heftel continues to provide an amazing level of technical support to the whole MBE team, while the experience of Melanie Tribble and Ken Cooper have helped me overcome many challenges in the cleanroom. I would also like to thank Dave Anderson for his work with the e-beam. To all those mentioned above who proof read parts of this dissertation, I am extremely grateful.

My friends in Cambridge have enriched immeasurably my time here. Max, Paul, Jo, Dhiraj, Charles, Rose, Matt, David and Becky all deserve special mention for putting up with me. Finally, I owe an unpayable debt of gratitude to my family for their constant love and encouragement.

‘ad Dei gloriam’

List of Publications

- P.J. Simmonds, H.E. Beere, H.W. Li, P. See, A.J. Shields and D.A. Ritchie, *Growth by molecular beam epitaxy of self-assembled InAs quantum dots on InAlAs and In-GaAs lattice-matched to InP*, J. Vac. Sci Tech. B, **25** 1044 (2007)
- P.J. Simmonds, H.E. Beere, S.N. Holmes and D.A. Ritchie, *Growth-temperature optimisation for low carrier-density $In_{0.75}Ga_{0.25}As$ -based HEMTs on InP*, accepted for publication in J. Appl. Phys. (September 2007)
- H.W. Li, P. Simmonds, H.E. Beere, B.E. Kardynal, P. See, D.A. Ritchie and A.J. Shields, *Optimisation of quantum dot resonant tunnelling diodes for fibre wavelength detection*, Phys. Status Solidi C, **3** 4035 (2006)
- H.W. Li, P.J. Simmonds, H.E. Beere, B.E. Kardynal, P. See, D.A. Ritchie and A.J. Shields, *Quantum dot resonant tunnelling diode for telecom wavelength single photon detection*, Appl. Phys. Lett. **91** 073516 (2007)

Contents

Preface	i
List of Publications	ii
Summary	ix
1 Properties of III-V Semiconductors	1
1.1 Introduction	1
1.2 Physical Structure	2
1.3 Density of States	3
1.4 Electrical Transport in Three-Dimensions	5
1.4.1 3D Electron Scattering Mechanisms	6
1.5 Electrical Transport in Two-Dimensions	8
1.5.1 Formation of a Two-Dimensional Electron Gas	8
1.5.2 Drude Theory	11
1.5.3 2DEG Electron Scattering Mechanisms	12
1.5.4 2D Electron Transport in a Magnetic Field	13
1.6 Electrical Transport in Low Dimensions	19
1.6.1 One-Dimensional Quantisation	19
1.6.2 Formation of 1D Electronic Systems	20
1.6.3 Quantised Electron Conductance in 1D	20
1.6.4 Electron-Electron Interaction and the 0.7 Structure	23
1.6.5 Zero-Dimensional Quantisation	25
1.7 Summary	25
2 Device Fabrication and Measurement Techniques	27
2.1 Introduction	27
2.2 Device Fabrication	27
2.2.1 Photolithography	28
2.2.2 Wet Etching	28
2.2.3 Ohmic Contact Metallisation	29
2.2.4 Insulation of Electrostatic Gates	30
2.2.5 Electrostatic Gate Metallisation	31
2.3 Device Measurement	32
2.3.1 Atomic Force Microscopy	33
2.3.2 X-Ray Diffractometry	33
2.3.3 Photoluminescence Spectroscopy	34

2.3.4	Electronic Transport	35
2.4	Summary	41
3	Molecular Beam Epitaxy	42
3.1	Introduction	42
3.2	An Overview of MBE	42
3.2.1	The MBE Growth Environment	42
3.2.2	The Mechanism of MBE Growth	46
3.2.3	Doping	49
3.2.4	Strain and Band-Gap Engineering	50
3.3	GaAs and AlAs Growth Rate Calibration	51
3.3.1	Beam Flux Measurement	51
3.3.2	X-Ray Diffractometry	51
3.3.3	Optical Pyrometry	53
3.4	InAs Growth Rate Calibration	54
3.4.1	X-Ray Diffractometry	54
3.4.2	Optical Pyrometry	55
3.4.3	Reflectance High-Energy Electron Diffractometry	56
3.5	Growth Uniformity	61
3.5.1	AlAs and GaAs Growth Rate Uniformity	61
3.5.2	AlGaAs Composition Uniformity	64
3.5.3	InAlAs Composition Uniformity	65
3.5.4	Si Incorporation Uniformity	65
3.5.5	HEMT Mobility Uniformity	66
3.5.6	Growth Defects	67
3.6	Summary	67
4	Two-Dimensional Electron Systems	69
4.1	Introduction	69
4.2	Growth of Lattice-Matched InGaAs HEMTs	70
4.2.1	Gate Response	71
4.2.2	Growth Temperature Optimisation	72
4.2.3	Electron Transport Anisotropy	74
4.3	Spin-Orbit Coupling in InGaAs HEMTs	75
4.4	Optimisation of High-Indium Content InGaAs HEMTs	83
4.4.1	Electron Mobility Enhancement	83
4.4.2	Sample Growth	84
4.4.3	Temperature Dependence of Surface Morphology	85
4.4.4	Device Illumination and Gate Response	86
4.4.5	Growth Temperature Dependence of Transport	87
4.4.6	Measurement of Electron g-Factor	91
4.4.7	Transport Dependence on InGaAs Composition	96
4.4.8	Doped InGaAs HEMTs	99
4.5	Summary	100

5 One-Dimensional Electron Systems	103
5.1 Introduction	103
5.2 Split-Gate Design	103
5.2.1 Electron-Beam Lithography	105
5.3 Split-Gate Process Development	105
5.3.1 Gate Insulation	105
5.3.2 Thin Polyimide Films I	106
5.3.3 Silicon Nitride Insulation	107
5.3.4 InGaAs Cap Removal	107
5.3.5 Thin Polyimide Films II	109
5.4 Split-Gate Fabrication	110
5.5 1D Transport Measurements	111
5.5.1 1D Transport in GaAs/AlGaAs	111
5.5.2 1D Transport in InGaAs	113
5.6 Summary	121
6 Zero-Dimensional Electron Systems: Self-Assembled Quantum Dots	122
6.1 Introduction	122
6.2 Theory of SAQD Formation	123
6.3 InAs Quantum Dots on InAlAs and InGaAs	124
6.3.1 Effect of Deposition Thickness	125
6.3.2 Uniformity of SAQD Formation	129
6.3.3 Effect of Growth Temperature	129
6.3.4 Effect of InAs Deposition Rate	131
6.3.5 Effect of Growth Interruptions	131
6.3.6 Growth of InAs SAQDs on InGaAs	133
6.4 Quantum Dot Resonant Tunnelling Diodes	135
6.5 Single Photon Detection at 1300nm	142
6.6 Summary	146
7 Conclusions and Further Work	148
7.1 Introduction	148
7.2 Molecular Beam Epitaxy and Device Fabrication	148
7.3 Two-Dimensional Electron Systems	149
7.4 One-Dimensional Electron Systems	150
7.5 Zero-Dimensional Electron Systems	151
Bibliography	162

List of Figures

1.1 Zinc-blende Unit Cell	2
1.2 Fermi-Dirac Distribution	4
1.3 Density of Electronic States	5
1.4 Hall Bar Geometry	5
1.5 Scattering Mechanisms	7
1.6 Typical GaAs/AlGaAs HEMT	8
1.7 Typical InGaAs/InAlAs QW HEMT	9
1.8 Schottky Barrier Formation	10
1.9 Electron Transport in a Magnetic Field	13
1.10 Landau Levels	15
1.11 Edge State Formation	17
1.12 Quantum Hall Effect	18
1.13 Split-Gate Design and Operation	20
1.14 1D Electron States	21
1.15 Quantisation of 1D Conductance	22
1.16 Reflection of Edge States	23
1.17 0.7 Structure	24
2.1 Schematic Diagram of Mesa Etch Photolithography	29
2.2 Schematic Diagram of Ohmic Contact Photolithography	30
2.3 Photograph of a Gated HEMT	32
2.4 Diagram of an Atomic Force Microscope	33
2.5 Photoluminescence Measurement	35
2.6 Diagram of a ^4He Bath Cryostat	36
2.7 Diagram of a ^3He Heliox Cryostat	37
2.8 Four-Terminal Resistance Circuit	38
2.9 Four-Terminal Conductance Circuit	39
2.10 Electrostatic Gate Leakage Current	40
3.1 Diagram of an MBE Growth Chamber Layout	43
3.2 AFM of Substrate Morphology	47
3.3 Modes of Crystal Growth	48
3.4 As ₄ Surface Reactions	48
3.5 Lattice Constant Dependence of Band-Gap Energy	50
3.6 XRD Spectrum of a Superlattice Structure	52
3.7 Interference Effects in Pyrometry	53
3.8 GaAs and AlAs Calibration Curves	54
3.9 InAs Calibration Curve	55

3.10	InGaAs Pyrometer Oscillations	56
3.11	RHEED Diffraction Patterns	57
3.12	RHEED Intensity Oscillations	57
3.13	InAlAs/AlAs RHEED Oscillations	58
3.14	InAs RHEED Growth Rate Calibration	60
3.15	Veeco MBE Chamber Cell Positions	62
3.16	AlAs Growth Rate Uniformity	62
3.17	GaAs Growth Rate Uniformity	63
3.18	AlGaAs Mole Fraction Uniformity	64
3.19	InAlAs Mole Fraction Uniformity	65
3.20	Si Incorporation Uniformity	66
3.21	GaAs/AlGaAs HEMT Mobility Uniformity	67
4.1	Electron Density Gate Response	71
4.2	Dependence of Magnetoresistance on Gate Voltage	72
4.3	Lattice-Matched HEMTs Electron Mobility Against Density	72
4.4	Temperature Dependence of Peak Mobility	73
4.5	Transport Anisotropy in InP-Lattice-Matched HEMTS	74
4.6	Lattice-Matched HEMT Surface Morphology	74
4.7	Gate Voltage Dependence of Rashba Spin-Splitting	76
4.8	InGaAs HEMT Gate Response at 400mK	77
4.9	Low-Field Beating in Magnetoresistance	78
4.10	Beating in Differential Transverse Resistivity	79
4.11	Evolution of Spin-Subbands with Gate Voltage	80
4.12	Orthodox Rashba Coupling Response	81
4.13	Dependence of B=0 Spin-Splitting on Electron Density 1	82
4.14	Dependence of B=0 Spin-Splitting on Electron Density 2	83
4.15	InGaAs HEMT Heterostructure	85
4.16	Surface Morphology Temperature Dependence	86
4.17	InGaAs HEMT Surface Morphology Anisotropy	86
4.18	InGaAs HEMT Magnetotransport	87
4.19	InGaAs HEMT Transport Anisotropy	88
4.20	Temperature Dependence of Electron Transport	89
4.21	Temperature Dependence of Peak Mobility	89
4.22	Simplified Model of InGaAs QW HEMT	90
4.23	Refined Model of InGaAs QW HEMT	91
4.24	Effect of Measurement Temperature on Magnetotransport	92
4.25	Arrhenius Plots for <i>g</i> -Factor Calculation	93
4.26	Landé <i>g</i> -Factors For III-V Compounds	93
4.27	Hopping Conduction Regime	94
4.28	Landau Level Profile Dependence on Magnetic Field	95
4.29	Angular Dependence of Longitudinal Resistance	96
4.30	Crossing of Spin-Split Landau Levels	97
4.31	Ungated Transport Dependence of InGaAs Composition	98
4.32	Simulations for HEMTs with Various In Composition	98
4.33	Transport Dependence of InGaAs Composition	99
4.34	Mobility Variation With InGaAs Composition	99
4.35	Transport in Doped InGaAs HEMTs	100

5.1	Split-Gate Design	104
5.2	Split-Gate Insulation	106
5.3	Polyimide Thickness Variation	107
5.4	InGaAs Cap Etch	108
5.5	Adipic Acid Etch Rate	109
5.6	Conductance of a GaAs/AlGaAs 1D Channel	112
5.7	Dark GaAs/AlGaAs 1D Conductance	112
5.8	Light GaAs/AlGaAs 1D Conductance	113
5.9	InGaAs 2DEG Split-Gate Leakage Currents	114
5.10	InGaAs 1D Conductance at 4.2K and 1.5K	114
5.11	Selected Split-Gate Sweeps	115
5.12	1D Conductance at 0.4-0.6T and Magnetoresistance	116
5.13	D.C. Bias Spectroscopy with Symmetric Gate Bias	117
5.14	D.C. Bias Spectroscopy with Lateral Bias	118
5.15	Biassing Positions for Magnet Sweeps	119
5.16	Magnetoresistance of a 1D Channel	120
6.1	AFM of InAs SAQDs on GaAs	123
6.2	InAs SAQD Calibration Heterostructure	124
6.3	Morphology Dependence on InAs Coverage	125
6.4	SAQD Size Dependence on InAs Coverage	126
6.5	Dependence of SAQD PL on InAs Coverage	127
6.6	Dependence of Peak Wavelength on InAs Coverage	128
6.7	Dependence of PL Spectrum on Measurement Temperature	128
6.8	InAs SAQD Uniformity	129
6.9	InAs SAQD Temperature Dependence	130
6.10	InAs SAQD Size Temperature Dependence	130
6.11	Dependence of SAQD PL on Growth Temperature	131
6.12	Dependence of SAQD PL on Growth Rate	132
6.13	Dependence of InAs SAQDs on Interrupt Length	132
6.14	Dependence of SAQD PL on Interrupt Length	133
6.15	Effect of Buffer Type on InAs SAQDs	134
6.16	Bulk InGaAs and InAlAs Surface Morphology	134
6.17	Effect of Device Bias on RTD Conduction Band Profile	135
6.18	RTD Peak-to-Valley Current Ratio	136
6.19	Band Diagram of RTD Containing InAs SAQDs	136
6.20	RTD Heterostructure	137
6.21	InGaAs/InAlAs RTD I-V Characteristics	138
6.22	Peak Current Density Dependence on Barrier Thickness	139
6.23	RTD I-V Characteristics at Room Temperature	140
6.24	Light Sensitivity of Large Area RTDs	140
6.25	RTD Small-Area Cross-Wire Devices	141
6.26	Deposition Thickness Dependence of InAs SAQDs on AlAs	143
6.27	Dependence on InAs Thickness for SAQDs on AlAs	143
6.28	InAs SAQD RTD Device Heterostructure	144
6.29	Photon detection and dark count rates	144
6.30	Dependence of Photon Induced Counts on Photon Flux	145

Summary

This dissertation explores the growth by molecular beam epitaxy (MBE) of high-quality InGaAs and InAlAs compounds. Studying the transport of electrons confined into two-, one- and zero-dimensional regions in these materials permits a better understanding of their sometimes unusual properties and, it is hoped, will lead to their use in the next generation of electronic and optoelectronic devices.

The properties of III-V semiconductors, with particular emphasis on InGaAs and InAlAs, are introduced in *Chapter One*. Attention is paid to the different properties that are encountered as the number of dimensions of free electron motion is reduced.

In *Chapter Two* the processes used to fabricate devices from epitaxial material are summarised. Mention is made of the need to insulate InGaAs and InAlAs to form electrostatic gates. Techniques, both for material characterisation and low-temperature electron transport measurement, are outlined.

The commissioning of a new MBE chamber is described in *Chapter Three* and the technique of epitaxy is reviewed. Growth rates are calibrated and non-uniformities of the MBE machine are quantified. A novel arrangement for a gallium cell is validated.

Chapter Four investigates two-dimensional electron transport in $\text{In}_x\text{Ga}_{1-x}\text{As}$, where $x \geq 0.53$. Following optimisation, devices are built with electron mobilities among the highest measured to-date for such structures. Low electron density two-dimensional systems, which may be of great interest to those investigating magnetotransport, are also introduced. The high electron g -factors and Rashba spin-orbit coupling effects measured are discussed with regard to potential use in ‘spintronic’ applications.

The development of a new split-gate fabrication process is described in *Chapter Five*. Subsequent measurements of one-dimensional electron transport are detailed. Non-integer conductance plateaux at $0.75(2e^2/h)$ and $0.25(2e^2/h)$ are resolved for the first time in $\text{In}_{0.75}\text{Ga}_{0.25}\text{As}$ using d.c. bias spectroscopy.

Chapter Six presents a comprehensive study of the dependence of InAs self-assembled quantum dot (SAQD) properties on MBE growth conditions. For the first time, single-photon detection at a telecom wavelength of $1.3\mu\text{m}$ is demonstrated in novel SAQD resonant tunnelling diodes.

Chapter 1

Properties of III-V Semiconductors

1.1 Introduction

This chapter serves as a general introduction to the structural and electrical properties of Group III - Group V (III-V) semiconductors. The majority of research into these materials over the last forty years has concentrated on gallium arsenide (GaAs) and aluminium arsenide (AlAs), meaning that these semiconductor systems are perhaps the best understood. The work which forms the basis of this dissertation centres on the combination of these two compounds, in some ratio, with a third binary material, indium arsenide (InAs). The result is the creation of the ternary compounds $\text{In}_x\text{Ga}_{1-x}\text{As}$ and $\text{In}_x\text{Al}_{1-x}\text{As}$, where the indium mole-fraction, $0 \leq x \leq 1$, is dictated by the combination ratio.

The GaAs/AlGaAs and InGaAs/InAlAs material systems exhibit crucial differences when indium atoms are present in relatively high-concentration. Indeed, it is these differences which make InGaAs and InAlAs attractive compounds to study. These properties of interest include lower band-gap energy, lower electron effective mass and higher Landé *g*-factor.

However, to a first approximation, these three binary materials share the same basic structure and electrical properties. Hence, this introductory chapter discusses both GaAs/AlGaAs and InGaAs/InAlAs systems interchangeably. After a brief look at the crystalline properties of these III-V materials in section 1.2, the electronic structure of these compounds is described. This dissertation describes measurements of transport characteristics where electrons are confined to regions with low dimensions. Hence, the density of electron states is derived for each confinement situation in section 1.3.

Section 1.4 looks at three-dimensional (3D) transport in bulk crystal material. The behaviour of electrons confined in two-dimensional (2D) structures and in magnetic fields is covered in some detail in section 1.5, since measurements of this kind constitute a large

part of chapter 4. Following this, transport in one-dimensional (1D) and zero-dimensional (0D) systems is discussed in section 1.6. This provides the framework for understanding the experimental results presented in chapters 5 and 6. Refs. [1–4] were indispensable in helping write the descriptions of electron transport theory presented in this chapter. In addition, Ref. [5] was used extensively for the discussion of electron transport in 1D. These sources offer the reader a far greater insight into the theory behind this subject than space in this chapter allows.

1.2 Physical Structure

The polar, binary materials GaAs, AlAs and InAs have a zinc-blende crystalline structure [Fig 1.1]. The room temperature lattice constants (a) are 5.6533 Å, 5.6605 Å and 6.0583 Å for GaAs, AlAs and InAs respectively and these three binary materials are fully miscible [6, 7]. Since the mismatch in lattice constant between GaAs and AlAs is small, thick

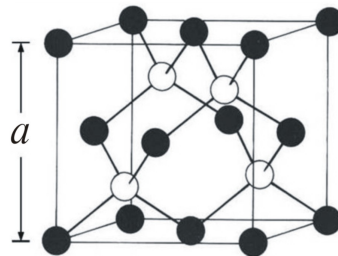


Figure 1.1: Model showing the zinc-blende crystal structure. For GaAs, the gallium atoms are represented by \circ , and the arsenic atoms by \bullet . The size of the cubic unit cell gives the lattice constant, a (after [2]).

layers of $\text{Al}_x\text{Ga}_{1-x}\text{As}$ can be grown on GaAs with little strain. The band-gap energy of $\text{Al}_x\text{Ga}_{1-x}\text{As}$ varies with x , with a transition from a direct to indirect bandgap close to $x=0.45$. As a result, this material system has long been exploited to engineer complex device heterostructures.

In the same way, the band gap energy (E_g) of $\text{In}_x\text{Ga}_{1-x}\text{As}$ can be tuned with In mole fraction by [8]

$$E_g = 1.42 - 1.615x + 0.555x^2 \quad (1.1)$$

The addition of In to GaAs reduces the band gap energy and so interband devices based around $\text{In}_x\text{Ga}_{1-x}\text{As}$ can be designed to access longer wavelength areas of the electromagnetic spectrum than devices made from GaAs/AlGaAs. The lattice constants of $\text{In}_x\text{Ga}_{1-x}\text{As}$ and $\text{In}_y\text{Al}_{1-y}\text{As}$ also vary with In mole fraction. Assuming Vegard's law holds, the relationships

$$a = 0.405x + 5.6533 \quad (1.2)$$

$$a = 0.3978y + 5.6605 \quad (1.3)$$

give the best experimental approximations for variation of the lattice constant, a , with composition for these two materials [9]. While $\text{In}_x\text{Ga}_{1-x}\text{As}$ has a direct band-gap for all values of x , the band-gap of $\text{In}_y\text{Al}_{1-y}\text{As}$ is indirect for $y < 0.3$. The large mismatch between the lattice constants of GaAs and InAs means that InGaAs and InAlAs grown on GaAs substrates will be appreciably strained for all but the lowest In concentrations. This imposes some limitations on the device structures which may be grown. However, InP has a lattice constant of 5.8687\AA and so $\text{In}_x\text{Ga}_{1-x}\text{As}$ and $\text{In}_y\text{Al}_{1-y}\text{As}$ with compositions of $x=0.532$ and $y=0.524$ can be grown lattice-matched to InP. Further discussion of strain in these compounds can be found in section 3.2.4.

1.3 Density of States

The electrons within a III-V semiconductor occupy a series of energy states. The electron density, $N(E)$, in some energy interval between E and $E+dE$ is the product of the density of these states, $D(E)$ over that interval and the probability that each is occupied, $P(E)$.

$$N(E) dE = P(E) D(E) dE \quad (1.4)$$

The Fermi energy, E_f , is defined as the energy at which the probability of occupation of an electron state is $1/2$. The Fermi-Dirac distribution

$$P(E) = \left[1 + \exp \left(\frac{E - E_f}{k_B T} \right) \right]^{-1} \quad (1.5)$$

states that at absolute zero, the occupation probability for an electron state above E_f is zero, where k_B is the Boltzmann constant. However, at non-zero temperatures, electrons within energy $k_B T$ of E_f may undergo thermal excitation to higher, empty states [Fig. 1.2]. An electron which falls within this energy bracket can be treated as a free carrier. As T is raised, more and more electrons can be thus excited, elongating the tail of the distribution.

$D(E)$ is defined as the number of states with an energy E per unit volume, per unit energy. In bulk material each electron state occupies a volume $(2\pi)^3$ and, in reciprocal space, the Fermi surface describes a sphere with radius equal to the electron wavenumber, k . The 3D density of states is thus

$$D_{3D}(E) = \frac{\partial}{\partial E} \left(\frac{\frac{4}{3}\pi k^3}{(2\pi)^3} \right) \quad (1.6)$$

E and k are related by

$$E = \frac{\hbar^2 k^2}{2m^*} \quad (1.7)$$

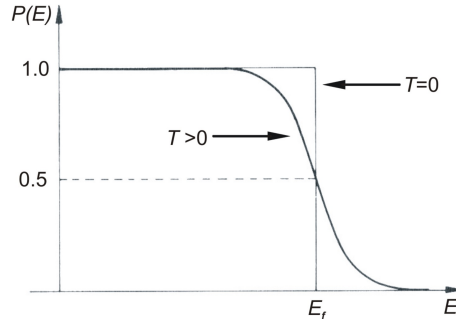


Figure 1.2: Fermi-Dirac distribution at zero and finite temperature, showing the energy dependence of the occupation probability, $P(E)$, of an electron state, and the position of E_f (after [2]).

where \hbar is the Planck constant (h) divided by 2π and m^* is the effective electron mass (see section 1.5.2). Combining Eqn. (1.6) with Eqn. (1.7) and adding a factor of 2 for spin-degeneracy within the system, it transpires that the 3D density of states is given by

$$D_{3D}(E) = \frac{1}{2\pi^2} \left(\frac{2m^*}{\hbar^2} \right)^{\frac{3}{2}} E^{\frac{1}{2}} \quad (1.8)$$

In sufficiently high magnetic fields, the spin degeneracy in III-V materials can be lifted, as will be seen in section 1.5.4 and again in chapter 4. The density of states in these systems will therefore be half that shown in Eqn. (1.8).

For electrons confined in two-dimensions (2D), the Fermi surface now describes a circle of radius k in reciprocal space with each electron state occupying an area $(2\pi)^2$. $D(E)$ for a 2DEG is shown to be a constant given by

$$D_{2D}(E) = \frac{m^*}{\pi\hbar^2} \quad (1.9)$$

Similar analysis yields the following spin-degenerate expression for the density of states of electrons confined in a 1D ‘quantum wire’

$$D_{1D}(E) = \frac{1}{\pi} \left(\frac{2m^*}{\hbar^2} \right)^{\frac{1}{2}} E^{-\frac{1}{2}} \quad (1.10)$$

Finally, for 0D systems, the electrons are confined in all three dimensions. These systems, called quantum dots, behave as pseudo-atoms whose states exist only at discrete energies. The ideal density of states can therefore be described by a series of delta functions

$$D_{0D}(E) = 2\delta(E) \quad (1.11)$$

although in practice these have a finite width due to thermal and disorder broadening. The shape of the density of states for each of the four confinement situations is shown in Fig. 1.3.

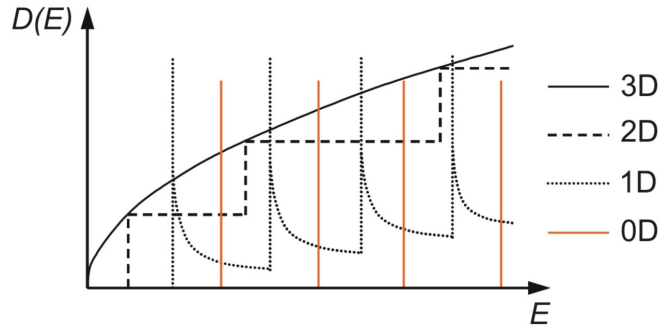


Figure 1.3: Density of electronic state functions for the four confinement situations discussed (not to scale).

1.4 Electrical Transport in Three-Dimensions

The electrical characteristics of bulk semiconductor layers provide useful information about material quality. The properties most commonly quoted are the longitudinal resistivity, ρ_0 , the electron mobility, μ , and the free-electron density, n . These can be calculated from measurements of the transverse, or Hall resistance coefficient, R_H and the longitudinal resistance, R_{xx} . In order to make such measurements, epitaxial material is processed into a Hall bar [Fig 1.4], using the fabrication methods discussed in chapter 2. A constant

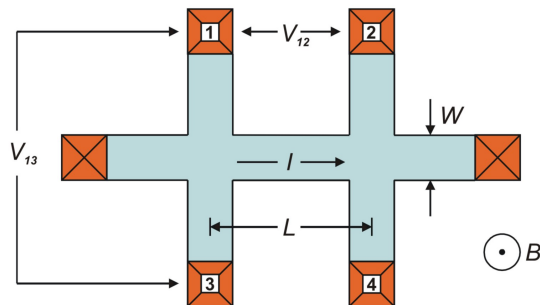


Figure 1.4: Schematic diagram of the Hall bar geometry used for four-terminal voltage measurements. The orange squares represent Ohmic contacts and the magnetic field, B , is shown coming out of the page.

current, I , is made to flow between the source and drain of the device and the longitudinal voltage V_{12} (or V_{34}) is measured. In the presence of a perpendicular magnetic field, B , a Hall voltage is developed and is measured as V_{13} (or V_{24}). R_H and R_{xx} are then calculated as follows

$$R_H = \frac{V_{13}}{IB} \quad (1.12)$$

$$R_{xx} = \frac{V_{12}}{I} \quad (1.13)$$

The four-terminal nature of these measurements allows resistances due to the leads and contacts to be removed from the calculations. From these two quantities ρ_0 , μ and n can be determined [10]

$$\rho_0 = \frac{R_{xx}WT}{L} \quad (1.14)$$

$$\mu = \frac{R_H}{\rho_0} \quad (1.15)$$

$$n = \frac{1}{TR_{He}} \quad (1.16)$$

where W and L are the Hall bar dimensions shown in Fig. 1.4 and T is the electrical thickness of the channel. T is found by subtracting the depletion region thicknesses from the total thickness of the doped layer [11]. These measurements are performed in magnetic fields up to 1T, both at room temperature, and at 77K via immersion in liquid nitrogen. Further details about constant-current electrical measurement techniques can be found in section 2.3.4.

1.4.1 3D Electron Scattering Mechanisms

As electrons move through a bulk crystal, they are subject to random collisions which can result in large angle scattering. These impacts limit the overall electron mobility. The major scattering mechanisms affecting bulk electron transport can be grouped under two sub-headings: phonon scattering and impurity scattering. If treated independently, the contribution from each of these can be combined [12]. Matthiessen's rule states that the overall mobility can be determined from a reciprocal sum of the mobility (μ_i) limited by each scattering process [13]

$$\frac{1}{\mu} = \sum_i \frac{1}{r_{Hi}\mu_i} \quad (1.17)$$

where r_{Hi} are the Hall factors contributing to each scattering mechanism. Since these typically take values in the range $1.0 \leq r_{Hi} \leq 1.3$ they are often approximated by unity [11]. Fig. 1.5 shows the scattering processes which dictate electron mobility above 4.2K. It is clear that peak theoretical electron mobilities for high purity GaAs, of perhaps $3 \times 10^5 \text{ cm}^2/\text{Vs}$, are realised close to 77K. Above this temperature, phonon scattering is the dominant mechanism, whilst below this value the mobility is lowered due to the increasing impact of ionised impurity scattering. These two mechanisms are summarised briefly below.

Phonon Scattering

Phonons are quantised lattice vibrations and as such are highly temperature dependent. At room temperature, polar optical phonons dominate. Electrons are scattered from dipole moments formed by optical-mode phonons interacting with atomic charges [14].

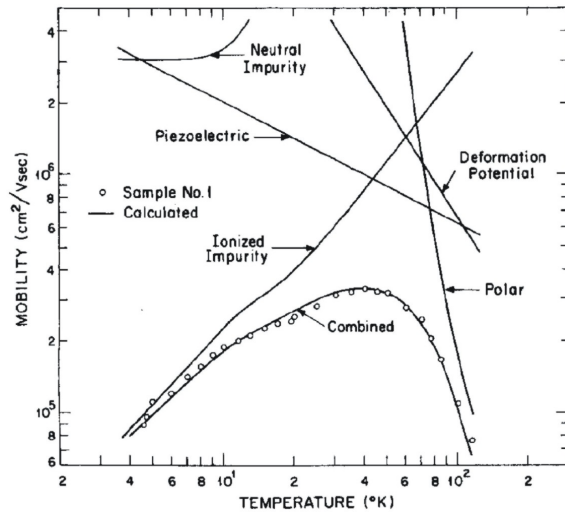


Figure 1.5: The calculated temperature dependence of the overall mobility in a sample of bulk, high-purity, unintentionally-doped GaAs. The mobility curves for each of the various contributing scattering mechanisms are shown, along with experimental data demonstrating good agreement with theory (reproduced from [12]).

As sample temperature is reduced below $\sim 60\text{K}$, optical phonon scattering is superseded by scattering from acoustic-mode phonons. Lattice vibrations cause changes in atomic spacing. This deformation locally changes the band gap and these potential variations act as scattering centres [15]. However, since III-V semiconductors are polar crystals with inversion asymmetry, these atomic displacements also cause piezoelectric effects, which also vary the potential and act as additional scattering centres [16].

Impurity Scattering

Impurity scattering is caused by both extrinsic and intrinsic species: the relative importance of each is dependent on electron density [17]. Dopant impurities constitute these extrinsic scattering centres. When dopant atoms are intentionally added to a heterostructure to provide carriers, the Coulomb potential of each resulting ion acts as a scattering centre.

However, the intrinsic incorporation of unwanted background impurities during epitaxy also results in scattering centres. Background impurities originate from partial pressures of contaminant species within the MBE chamber and, for a constant growth rate, will incorporate homogeneously throughout the heterostructure. Background impurity scattering explains the requirement for ultra-high chamber purity since bulk incorporation of unwanted species can be reduced to $\sim 1 \times 10^{13}\text{cm}^{-3}$ by rigorous baking and clean-up procedures. The issue of chamber cleanliness is addressed in chapter 3.

1.5 Electrical Transport in Two-Dimensions

1.5.1 Formation of a Two-Dimensional Electron Gas

In order to increase electron mobility from bulk values, a common approach involves the confinement of free electrons into a two-dimensional sheet. One heterostructure used for this purpose is a GaAs/AlGaAs high electron mobility transistor (HEMT), routinely grown in this group as a convenient measure of material and chamber quality [Fig. 1.6]. Onto a

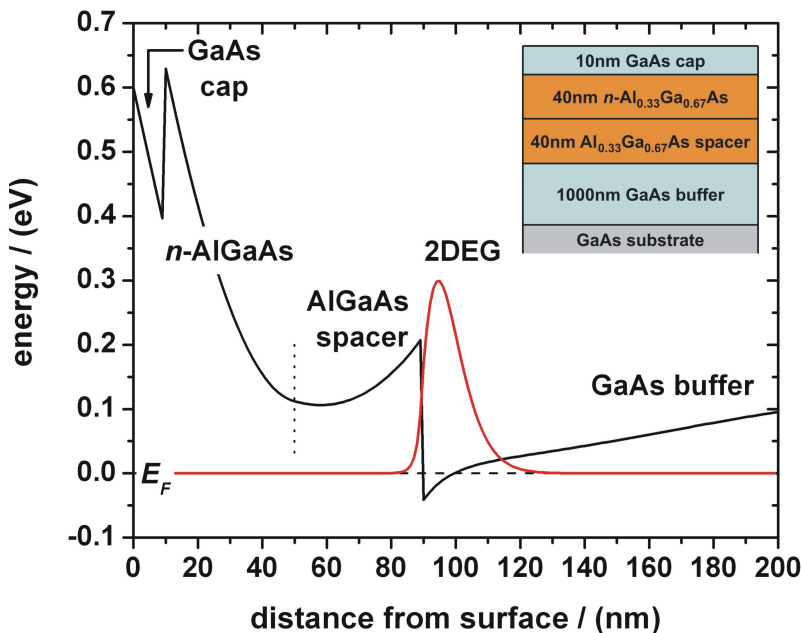


Figure 1.6: The inset shows a schematic diagram of the heterostructure of a typical GaAs/AlGaAs HEMT sample. The main picture shows the conduction band profile (black) and electron wavefunction (red) of this HEMT [18].

(0 0 1) GaAs substrate, a 1000nm GaAs buffer is grown to trap defects and impurities and provide a smooth surface for subsequent epitaxy. This is followed by a 40nm $\text{Al}_{0.33}\text{Ga}_{0.67}\text{As}$ undoped spacer layer, 40nm $\text{Al}_{0.33}\text{Ga}_{0.67}\text{As}$ n -doped to $1.5 \times 10^{18} \text{ cm}^{-3}$ and finally a 10nm GaAs cap.

Transfer of electrons from the doped layer results in bending of the conduction band. A quasi-triangular potential well is formed below the Fermi energy (E_F) at the heterojunction between the GaAs buffer and the undoped AlGaAs spacer. Since the width of this well is of the same order of magnitude as the electron wavelength, the energy of the confined electrons is quantised perpendicular to the GaAs/AlGaAs interface. This ‘sheet-like’ body of electrons moves freely in the other two directions and its behaviour can be described by that of a two-dimensional electron gas (2DEG), with a *sheet* electron density, n_s . In Fig. 1.6 and in all similar figures in this dissertation, the conduction band profile and electron

wavefunction were calculated using the ‘1D Poisson/Schrödinger’ program, written by Dr. G. Snider at the University of Notre Dame, to obtain self-consistent solutions to the Schrödinger and Poisson equations [18].

An alternative 2DEG heterostructure which appears more frequently in this dissertation is an InGaAs/InAlAs HEMT based around a quantum well (QW) [Fig. 1.7]. Firstly,

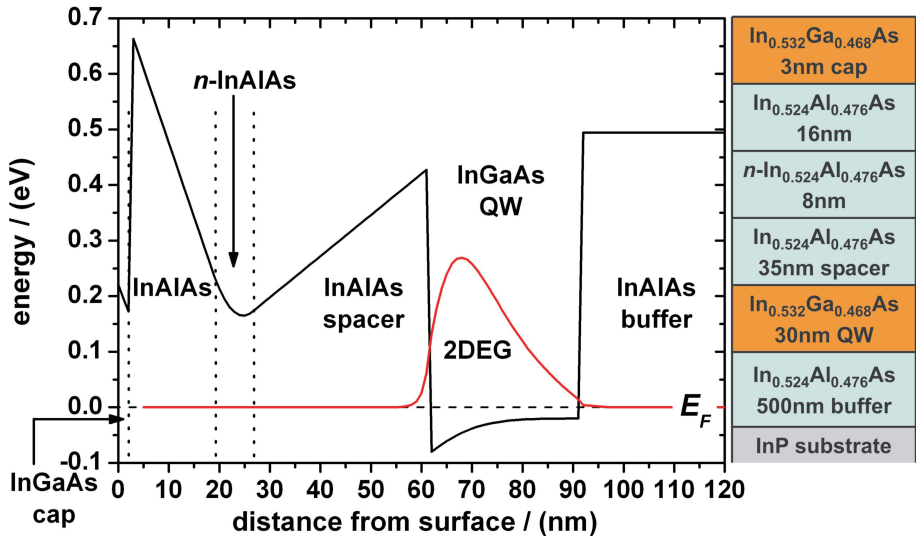


Figure 1.7: The schematic diagram to the right shows the heterostructure of a typical InGaAs/InAlAs HEMT which is lattice-matched to an InP substrate. The main picture shows the conduction band profile (black) and electron wavefunction (red) of this HEMT [18].

a smoothing In_{0.52}Al_{0.48}As buffer is grown onto a (0 0 1) InP substrate. A thin undoped spacer layer of In_{0.52}Al_{0.48}As is used to separate the *n*-doped In_{0.52}Al_{0.48}As from the In_{0.53}Ga_{0.47}As QW. The thin In_{0.53}Ga_{0.47}As cap is required to prevent oxidation of the Al-containing layers.

The InGaAs QW is surrounded by the higher bandgap of the InAlAs. In this case, the conduction band offset between the barriers and well has been determined to be 0.51eV, which is equivalent to $\sim 70\%$ of the total band gap discontinuity of 0.73eV at the In_{0.53}Ga_{0.47}As/In_{0.52}Al_{0.48}As heterojunction [19]. Electrons originating in the *n*-doped InAlAs layer tunnel through the undoped spacer into the conduction band minimum of the QW. The InGaAs QW width is such that electron confinement once again occurs perpendicular to the InAlAs/InGaAs interface and a 2DEG is formed. One advantage of this structure is that the QW width and hence the quantisation energies can be easily tuned.

At low temperature, phonon scattering becomes almost negligible and ionised impurity scattering dominates. The inclusion of the undoped spacer layer is a technique known as modulation-doping which was developed in order to reduce this scattering mechanism.

This spacer layer, introduced between the ionised dopant impurities and the 2DEG, spatially separates electrons from the charge centres. This scattering mechanism is distance dependent and is reduced exponentially by thickening the spacer. However, this also reduces electron density in the 2DEG. This, in turn, lowers electron-electron screening which can itself reduce mobility. Electron density can be increased by increasing the doped layer thickness or concentration but there is clearly some trade-off between electron mobility and density. Use of an optimised spacer layer in GaAs/AlGaAs-based 2DEGs was shown to increase electron mobility by an order of magnitude over the peak bulk mobility shown in Fig. 1.5 [20]. Even with modulation doping however, 2DEG transport will still be affected by background impurity scattering.

Finally, it is important to note that the Fermi-level is pinned at the surface through contact with a metal. The conduction and valence bands of the semiconductor bend to align the Fermi-energies and a Schottky potential barrier, of height Φ_B , is formed at the surface [Fig. 1.8a)]. The value of Φ_B , at the metal-In_xGa_{1-x}As junction has been shown

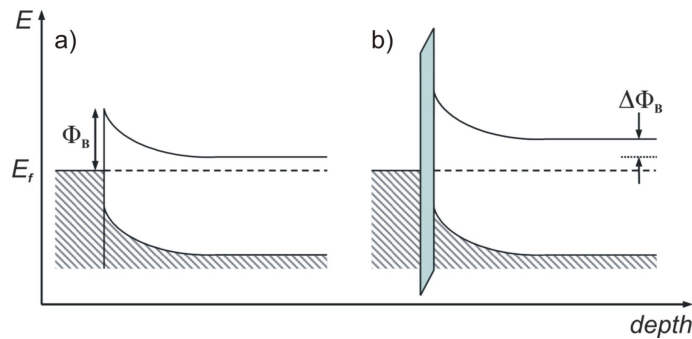


Figure 1.8: a) shows schematically the formation of a Schottky barrier at a metal-semiconductor interface through band bending. In b), the introduction of an insulating layer at the interface results in an increase in the Schottky barrier height, $\Delta\Phi_B$.

to vary with In mole-fraction x , as [21]

$$\Phi_B(eV) = 0.95 - 1.90x + 0.90x^2 \quad (1.18)$$

Therefore, Φ_B lies between 0.196eV and 0.031eV for the mole fraction range $0.53 \leq x \leq 0.75$. These values are extremely small in comparison with the corresponding 0.9eV Schottky barrier formed at a GaAs-metal interface. As discussed in section 2.3.4, the application of a d.c. bias to metal surface gates is often used to vary 2DEG carrier density. The large Schottky barrier formed at the GaAs surface means that the required electrostatic behaviour of such gates is readily observed for GaAs/AlGaAs devices. However, the low values of Φ_B for InGaAs means that rather than behaving electrostatically, leakage currents form between gate and QW, compromising performance.

This low- Φ_B characteristic therefore has some ramifications in terms of device design.

The use of an electrically insulating layer at the interface between the semiconductor and metal artificially increases the Schottky barrier height and prevents leakage currents [Fig. 1.8b)]. In addition, the presence of the insulating layer will result in a small change to the actual barrier height, $\Delta\Phi_B$. This increase arises from the presence of additional dipoles formed due to sheet-charges in the insulator close to the semiconductor interface [22]. Gate insulation is discussed further in chapter 2.

1.5.2 Drude Theory

Drude theory provides a useful, classical model for the transport of electrons in a 2DEG. Electrons are assumed to be free and to move within the flat-bottomed potential well of the sample. As explained in section 1.3, electrons within $k_B T$ of E_f can be treated as free carriers. However, the assumption of a uniform potential background within the crystal is not generally valid: the nature of the lattice is such that electrons in fact encounter periodic variations in potential [23].

This issue can be circumvented by adopting the convention of an effective electron mass, m^* . This modification means that the effect of the lattice potential on the electron is taken into account and so facilitates calculation of electron response to outside forces alone. GaAs has a low-temperature effective mass ratio $m^*/m_0 = 0.067$, where m_0 is the free electron mass. For InAs this ratio is considerably smaller, taking a value of 0.026 at low-temperature [24].

If a group of free electrons are acted upon by an external electric field, \vec{E} , there will occur a net motion of these electrons in the direction of the field, with a certain drift velocity $\vec{\nu}$. As discussed in section 1.4.1, random collisions occur during motion, each of which may scatter the electron through some large angle and momentarily set the drift velocity to zero. Taking these scattering events into account, the general form for the equation of motion of the electrons is

$$m^* \frac{d\vec{\nu}}{dt} = -\frac{m^* \vec{\nu}}{\tau} + e(\vec{E} + \vec{\nu} \times \vec{B}) \quad (1.19)$$

where τ is the relaxation time between collisions and \vec{B} is an external magnetic field. The current density, \vec{J} , is

$$\vec{J} = n_s e \vec{\nu} = \sigma \vec{E} \quad (1.20)$$

where n is the electron density, and σ is defined as the conductivity. Combining the steady state solution of Eqn. (1.19) in the absence of a magnetic field, with Eqn. (1.20) gives

$$\sigma = \frac{n_s e^2 \tau}{m^*} \quad (1.21)$$

Electron mobility, μ , is defined by the ratio between drift velocity and the electric field and so from Eqn. (1.20),

$$\mu = \frac{e\tau}{m^*} \quad (1.22)$$

Clearly, for a constant electron density, both σ and μ are limited only by the average time between collisions, τ . The average electron velocity at E_f is the Fermi velocity, ν_f . Using Eqn. (1.7) this can be written

$$\nu_f = \frac{\hbar k_f}{m^*} \quad (1.23)$$

and hence the mean free path, l is simply

$$l = \nu_f \tau \quad (1.24)$$

1.5.3 2DEG Electron Scattering Mechanisms

In addition to the bulk scattering processes discussed in section 1.4.1, three other mechanisms are encountered for 2DEGs. Their effects become increasingly pronounced in high-quality material at very low temperature, as the contribution from other scattering mechanisms is reduced. Where only one electron subband is occupied, interface-roughness scattering and alloy-disorder scattering will be experienced [25]. For higher electron densities, intersubband scattering also becomes significant.

Interface-Roughness Scattering

Roughness at the interfaces confining the 2DEG can scatter electrons. Devices are often designed so that the 2DEG is formed at a single heterojunction, such as in Fig. 1.6. The single interface means that electrons undergo half the scattering compared to a QW. Alternatively, ultra-high mobilities $> 30 \times 10^6 \text{ cm}^2/\text{Vs}$ have been achieved using a relatively wide QW so that the electrons don't 'feel' the interfaces as much [26]. Interface roughness is highly dependent on the materials comprising the heterojunction, the substrate crystal orientation [27], and the growth conditions used, including arsenic overpressure and substrate temperature. In addition, cleaved-edge growth and the use of growth interrupts to anneal a surface, have both been shown to result in interface smoothing [28, 29].

The Fermi wavelength, λ_f is the electron wavelength of an electron at E_f . λ_f is dependent on n_s as

$$\lambda_f = \sqrt{\frac{2\pi}{n_s}} \quad (1.25)$$

Flatter surfaces reduce the effect of interface-roughness scattering. However, as n_s increases, λ_f contracts. Even if the surface roughness is very low, limited only by monolayer-high steps at terrace edges on the crystal surface, a sufficiently large n_s will mean that λ_f is of the same order of magnitude as these features and so scattering will still occur.

Alloy-Disorder Scattering

For ternary or higher-order alloys, inhomogeneity in the distribution of the material components causes small variations in the lattice potential which act as scattering centres.

The composition of a ternary III-V material, $A_xB_{1-x}C$ is critical in dictating the degree of disorder in the lattice and hence the amount of scattering that occurs. The stoichiometric end-point binary materials AC and BC do not demonstrate alloy-disorder scattering, and so there will be a maximum for this scattering process where $x=0.5$. This is a particular issue for the InP lattice-matched materials, $In_{0.53}Ga_{0.47}As$ and $In_{0.52}Al_{0.48}As$, introduced in section 1.2. Maximum electron mobility in $In_xGa_{1-x}As$ has been demonstrated at $x=0.75$ [30, 31].

Intersubband Scattering

At high n_s , the first electron subband fills and the population of the second subband begins to increase. Electrons scattering between these two subbands can reduce mobility [32]. For the $In_{0.75}Ga_{0.25}As$ channels discussed in chapter 4, significant population of the second subband starts to occur for carrier densities above $3 \times 10^{-11} \text{ cm}^{-2}$ [33].

1.5.4 2D Electron Transport in a Magnetic Field

Reconsider Eqn. (1.19); this time for a portion of the 2DEG extending in the x direction. The electrons, confined to the xy plane, occupy only the lowest subband. A current density J_x flows in the presence of a finite, magnetic field, \vec{B}_z normal to the plane of quantisation [Fig. 1.9]. The Lorentz force $-e\vec{v} \times \vec{B}$ deflects electrons downwards. An electric field; the

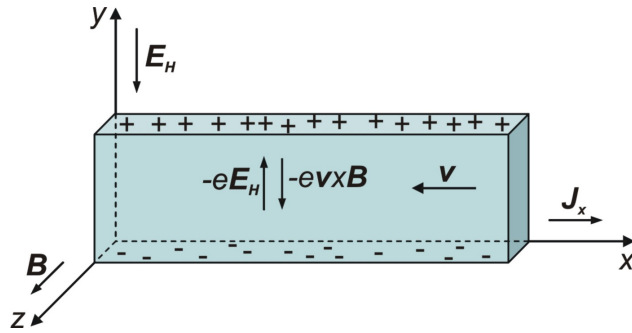


Figure 1.9: A schematic picture of a section of a 2DEG extending along the x -axis in the presence of a perpendicular magnetic field. The origins of the Lorentz and Hall forces are shown (after [2]).

Hall field, E_H ; is therefore set up between the top and bottom surfaces of the Hall bar. The resultant force on the electron $-eE_H$ balances the Lorentz force and hence overall drift velocity in the y direction (\vec{v}_y) is zero. The x and y components of the steady state solution to Eqn. (1.19) are then

$$E_x = \frac{m^* \nu_x}{e\tau} \quad (1.26)$$

$$E_y = -\nu_x B \quad (1.27)$$

Dividing these two results through by J_x , we obtain the longitudinal and transverse resistivities

$$\rho_{xx} = \frac{1}{n_s e \mu} \quad (1.28)$$

$$\rho_{xy} = \frac{-B}{n_s e} \quad (1.29)$$

Since $\rho = 1/\sigma$, a comparison of Eqn. (1.28) with Eqns. (1.21) and (1.22) shows that the presence of a magnetic field does not affect electrical conductivity. The magnitude of ρ_{xy} is proportional to the Hall voltage created between the top and bottom surfaces of the channel (c.f. Eqns. (1.12) and (1.16)). Eqn. (1.29) can therefore be used to determine n_s from a measurement of this voltage.

Landau Levels

In the presence of a magnetic field, B_z , electron motion in the plane of a two-dimensional gas of free electrons is converted into cyclotron motion by the Lorentz force. The confined electrons move in orbits of quantised radius, r_L , where

$$r_L = \sqrt{\frac{(2n_L + 1)\hbar}{eB_z}} \quad (n_L = 0, 1, 2, \dots) \quad (1.30)$$

where n_L is known as the Landau level index. Parallel to B_z however, electron motion is unaffected. Landau showed that the Hamiltonian operator of the Schrödinger equation describing this behaviour contains two additional terms [4]. Assuming spin degeneracy, the eigenenergies for the modified Schrödinger equation take the form

$$E = \frac{\hbar^2 k_z^2}{2m^*} + \left(n_L + \frac{1}{2}\right) \hbar\omega_c \pm \frac{1}{2}g\mu_B B \quad (1.31)$$

where g is the Landé g -factor and μ_B is the Bohr magneton. The first term in Eqn. (1.31) is the free electron eigenenergy in the direction of the applied field, where k_z is the wavevector normal to the 2DEG. Where only the lowest subband is occupied, this first term is fixed due to constant k_z . Except for certain materials in high magnetic fields, the energy of the spin-dependent third term is typically significantly smaller than the cyclotron energy and so can often be neglected. The second term gives the energy of the cyclotron motion, where ω_c is the cyclotron resonance frequency, defined as

$$\omega_c = \frac{eB_z}{m^*} \quad (1.32)$$

What Eqn. (1.31) shows therefore, is that the density of states function in the xy plane is quantised into discrete Landau levels separated by the cyclotron energy. Although these should exhibit the form of a delta-function, in reality, sample disorder and thermal excitation broadens each Landau level. If the broadening is large compared with the

Landau level separation, the long tails of adjacent levels will overlap. However, where $k_B T \ll \hbar\omega_c$, the energy interval between adjacent levels means that extended states are realised, separated by tails of localised states [Fig. 1.10]. It is these extended states which are responsible for electron transport.

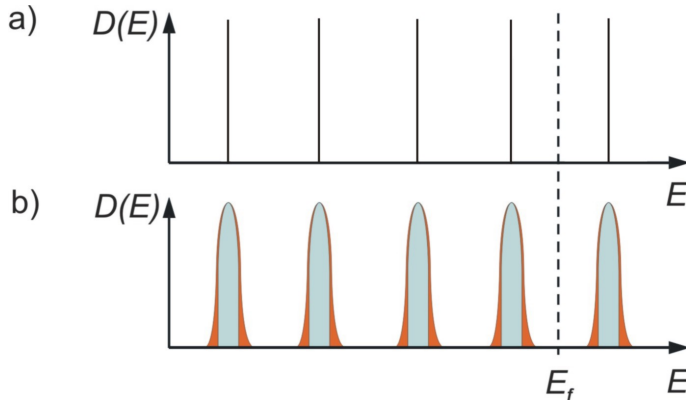


Figure 1.10: Landau levels formed in a perpendicular magnetic field. **a)** The levels are ideal-case non-broadened delta-functions. **b)** The presence of disorder has broadened each level. The central, blue regions represent the extended states in each level while the peripheral, orange tails are the localised states arising from the system disorder.

Shubnikov-de Haas Oscillations

The Fermi level is highly dependent on the magnetic field. Consider the situation where E_f lies within some Landau level and where the electron density is constant. As the magnetic field is increased, the degeneracy of each Landau level also rises and so electrons transfer to lower levels. At some critical field, the Landau level within which the Fermi energy lies will become empty and so E_f immediately moves to the level below. The density of states at the Fermi level is high when E_f coincides with the extended states of a Landau level and so longitudinal resistivity is low. However, when E_f lies in the localised states between Landau levels, such as in Fig. 1.10, the density of states at this energy is very low and near-insulating behaviour is observed. The Einstein conductivity equation confirms that this variation in $D(E_f)$ is associated with an oscillation in the 2DEG conductivity.

$$\sigma = \frac{1}{2} l e^2 \nu_f D(E_f) \quad (1.33)$$

These are known as Shubnikov-de Haas (SdH) oscillations. Since subsequent maxima in the oscillations occur when E_f coincides with the centre of a Landau level, Eqn. (1.31) gives these peak values at

$$E_f = \left(n_L + \frac{1}{2} \right) \frac{\hbar e B_z}{m^*} \quad (1.34)$$

Successive minima occur halfway between each maximum value. From Eqn. (1.34), a plot of n_L against $1/B_z$ will give a straight line with gradient γ such that

$$\gamma = \frac{E_f m^*}{\hbar e} \quad (1.35)$$

The electron density, n_{2D} , within the 2DEG is found by integrating the spin-degenerate density of states function (Eqn. (1.9)) up to E_f . Combining this with Eqn. (1.35) gives the relationship

$$\Delta \left(\frac{1}{B} \right) = \frac{e}{n_{2D} \pi \hbar} \quad (1.36)$$

This approach provides an alternative to Hall voltage measurements (see section 1.4 and Eqn. (1.29)) for determining n_{2D} . Fast Fourier transforms (FFT) are commonly used to extract the SdH oscillation frequency for use in the above calculation. Again, a factor of $1/2$ should be added to the right-hand side of Eqn. (1.36) were spin-degeneracy lifted.

Longitudinal and transverse resistivities rather than conductivities are the generally measured quantities and these are related by

$$\rho_{xx} = \frac{\sigma_{xx}}{\sigma_{xx}^2 + \sigma_{xy}^2} \quad (1.37)$$

$$\rho_{xy} = \frac{\sigma_{xy}}{\sigma_{xx}^2 + \sigma_{xy}^2} \quad (1.38)$$

Provided that the transverse conductivity takes a non-zero value, ρ_{xx} will go to zero when E_f is between Landau levels, and oscillate with σ_{xx} .

The Quantum Hall Effect

Eqns. (1.12) to (1.16) and (1.29) show that classically, the gradient of the transverse Hall resistance is constant with increasing magnetic field intensity. However, quantised plateaux in the Hall resistance slope of a 2DEG were first reported in 1980: the quantum Hall effect (QHE) [34]. Each plateau coincided with a minimum in the longitudinal resistivity and took values

$$\rho_{xy} = \frac{h}{\nu e^2} \quad (\nu = 1, 2, 3, \dots) \quad (1.39)$$

Assuming spin-degeneracy, ν is the ‘filling factor’, equal to twice the number of occupied Landau levels. As discussed, minima in ρ_{xx} occur when E_f lies between two Landau levels, that is, where $\rho_{xx} = \sigma_{xx} = 0$. From Eqn. (1.38), the transverse conductivity is simply given by the reciprocal of the RHS of Eqn. (1.39).

It should be noted that odd-numbered Quantum Hall plateaux arise as the result of the lifting of spin-degeneracy within a Landau level by the magnetic field. Where B or g are large, the spin-dependent term in Eqn. (1.31) starts to become significant and peaks in the SdH oscillations will begin to split. The nature of some of the high-indium content materials discussed in this dissertation are such that the Landé g -factors are large and so

spin-splitting is observed, even at low magnetic fields. These effects are discussed further in chapter 4.

In a classical picture of the QHE, electrons describe cyclotron orbits in the presence of a magnetic field. Close to the edges of the channel, electron transport occurs via ‘skipping’ since complete orbits are not possible [Fig. 1.11a)]. The quantum mechanical

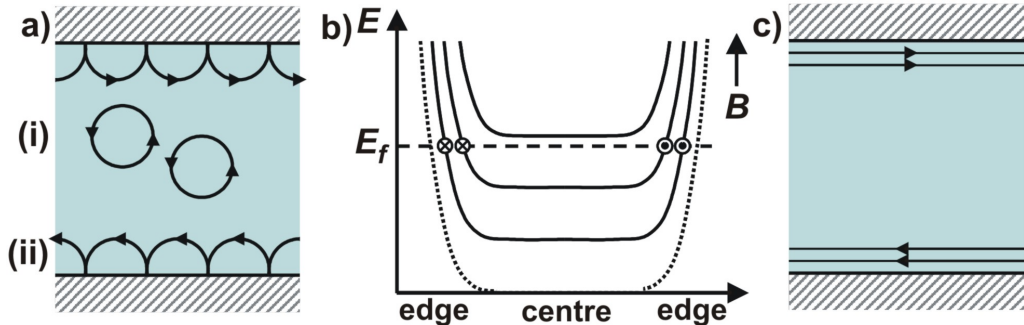


Figure 1.11: a) shows schematically a classical picture of electron transport via (i) cyclotron orbits and (ii) skipping orbits. b) demonstrates how Landau levels are bent upwards at the edges of a channel, with the dotted line showing the 2DEG potential. The edge states formed at the intersection of the Landau levels with E_f (dashed line) are represented by \otimes , where the direction of electron transport is into the page, and \odot , out of the page. c) schematically presents a plan view of the same channel showing the two edge states.

explanation of the QHE instead uses the idea of edge states. The sides of the channel act as potential barriers which increase the energy of the edges of the Landau levels [Fig. 1.11b)]. Completely filled Landau levels in the centre of the channel therefore cross E_f at the edges of the mesa, forming what are called ‘edge states’. In the centre of the channel, electrons are restricted to lateral motion. Forward motion occurs only where there is a potential gradient which is perpendicular to the device bias; that is, at the channel edges. Hence, electron transport along the channel takes place via these edge states alone. The direction of electron transport in the edge states at either side of the channel is chiral, the ‘handedness’ of which is determined only by the magnetic field vector.

The number of edge states is given by the number of Landau levels below E_f , or the spin-resolved filling factor in the 2DEG, ν_{2D} . The channel shown in Fig. 1.11b) therefore has two edge states. Fig. 1.11c) schematically represents a plan view of this same channel. These edge states can be approximated as one-dimensional (1D) channels and, since these edge states are typically far apart, back-scattering is negligible [35].

Building on earlier work by Landauer [36], Büttiker developed the idea of current flow as electron transport between reservoirs, connected by one-dimensional (1D) channels [37]. Consider an arbitrarily-shaped sample of some conducting material which connects N electron reservoirs, the i th of which is at an electrochemical potential, μ_i . μ combines

the electrostatic and kinetic contributions to electron energy, to determine the highest occupied electron state of a reservoir. Connections between each reservoir and the central conductor are through lossless leads consisting of N_i 1D channels. At the interface between each lead and the central region, a certain amount of current from the j th lead enters the i th lead, with a transmission coefficient (T_{ij}). In addition, the reflection coefficient (R_i) dictates what proportion of the current flowing from the i th lead into the central region is returned to that same lead. By summing the contributions from all leads, the total current in the i th lead is given by

$$I_i = \frac{e}{h} \left[(N_i - R_i)\mu_i - \sum_{i \neq j} T_{ij}\mu_j \right] \quad (i, j = 1, 2, 3, \dots, N) \quad (1.40)$$

Since, as discussed, the edge states in a 2DEG are 1D and scattering from one edge state to another across the channel is highly suppressed, this Landauer-Büttiker formalism can be used to explain the origin of the QHE. Fig. 1.12a) shows schematically a Hall bar in a magnetic field, for which E_f lies between two Landau levels and there are ν_{2D} edge states. A current I flows into Ohmic contact 1 and out of Ohmic contact 4. The remaining four

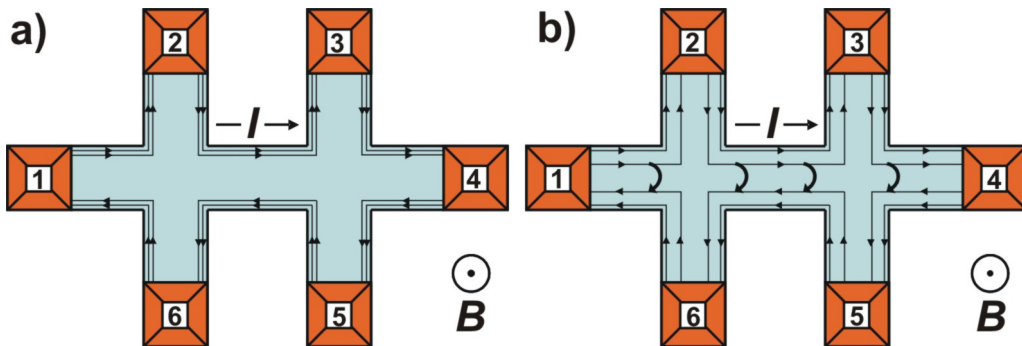


Figure 1.12: Schematic representations of a Hall bar in a magnetic field pointing out of the page. In a) E_f is midway between two Landau levels such that the edge states are tightly bound to the sides of the channel and back scattering is suppressed. In b) a Landau level is now coincident with E_f . The edge states of the level move towards the channel centre. Unfilled Landau states then provide a route for electrons to scatter between edge states on opposite sides of the channel.

contacts are voltage probes from which no current flows. Assuming each contact is of good quality, R_i is zero. The chiral, lossless edge states mean that T_{ij} is one between an Ohmic contact and its clockwise neighbour, and zero to its neighbour in the anticlockwise direction. A voltage, V , between two reservoirs creates a difference in their electrochemical potentials, such that $\mu_i - \mu_j = eV$. Hence, the Hall resistance measured between contacts 2 and 6 is given by

$$R_H = \frac{\mu_2 - \mu_6}{eI} \quad (1.41)$$

Using Eqn. (1.40), the current at each Ohmic contact can be determined. For contacts 1, 2 and 3 the current is

$$I_1 = \frac{e}{h} (\nu_{2D}\mu_1 - \nu_{2D}\mu_6) = I \quad (1.42)$$

$$I_2 = \frac{e}{h} (\nu_{2D}\mu_2 - \nu_{2D}\mu_1) = 0 \quad (1.43)$$

$$I_3 = \frac{e}{h} (\nu_{2D}\mu_3 - \nu_{2D}\mu_2) = 0 \quad (1.44)$$

Adding the first two expressions together and combining with Eqn. (1.41) gives

$$R_H = \frac{1}{\nu_{2D}} \frac{h}{e^2} \quad (1.45)$$

In addition, Eqn. (1.44) shows that $\mu_3 = \mu_2$. Hence, when E_f is in the localised states between two Landau levels, a plateau is formed in the Hall resistance at the value given by Eqn. (1.45) and the longitudinal resistance goes to zero, as seen in the SdH oscillations.

Now, if the magnetic field is increased, E_f is moved downwards. The edge states in the highest Landau level move towards the centre of the channel [Fig. 1.12b)]. When E_f coincides with this next Landau level, some extended states will become empty. In combination with the relative proximity of the antithetic edge states, the presence of these unfilled Landau states mean that electrons can scatter from one side of the channel to lower potential edge states on the other. This depopulation is associated with a change in voltage. The longitudinal resistance thus becomes non-zero and R_H begins to rise.

1.6 Electrical Transport in Low Dimensions

This section discusses electron confinement in 1D and 0D systems.

1.6.1 One-Dimensional Quantisation

If the width of a 2DEG can be reduced until it is of the same order of magnitude as the Fermi wavelength, the electrons become laterally confined into a 1D quantum ‘wire’, of some finite length. This confinement splits each subband energy level of the 2DEG into a ‘ladder’ of quantised 1D states. If the 1D channel is shorter than the mean free path of an electron (see Eqn. (1.24)) then electronic motion inside the wire is independent of scattering and is determined solely by the electrostatic potential of the channel. This is described as the quantum ballistic transport regime. For a channel extending along the x -axis with a parabolic confining potential, the dispersion relation for the 1D electron states is given by

$$E_n(k_x) = eV_0 + \frac{\hbar^2 k_x^2}{2m^*} + (n - \frac{1}{2})\hbar\omega_0 \quad (n = 1, 2, 3, \dots) \quad (1.46)$$

The first two terms on the right of Eqn. (1.46) describe the electrostatic and kinetic components of the energy of an electron moving along the channel. The final term describes

the energy of the quantised motion due to the constriction, where n is the integer 1D subband index and ω_0 is a measure of the confinement strength.

1.6.2 Formation of 1D Electronic Systems

A 1D constriction can be achieved in a 2DEG through the use of metallic split-gates positioned on the semiconductor surface [38–40]. Chapter 5 describes the processing techniques used to fabricate these split-gates on $\text{In}_x\text{Ga}_{1-x}\text{As}/\text{In}_y\text{Al}_{1-y}\text{As}$ devices. When a negative bias is applied to the split-gates, the height of the surface Schottky barrier is increased in the region below the gates. This bias serves to locally raise the conduction band energy inside the 2DEG, thus reducing the electron density. Given sufficient negative gate bias, the lowest energy state is raised above E_f and the 2DEG becomes locally depleted of carriers. As the magnitude of the negative gate bias is further increased, the size of this depleted region grows, extending around and below each gate. This is shown schematically in Fig. 1.13. The width of the 2DEG can thus be effectively controlled by the amount of bias applied to the gates.

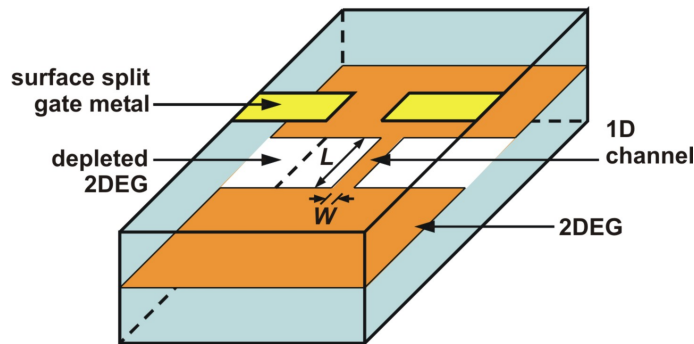


Figure 1.13: A schematic view of some split-gates (yellow) on a semiconductor surface. The 2DEG is represented by the orange sheet and the regions which have been depleted of electrons are shown in white.

At some critical bias, this width is decreased sufficiently that the lateral quantisation of electron energies described above will occur. Symmetrical bias can be applied to both gates to create a 1D region midway between the split-gates. Alternatively, differential biasing can be used to alter laterally the position of the quantum wire.

1.6.3 Quantised Electron Conductance in 1D

Quantisation of electrical conductance in a 1D channel was first observed by two groups in 1988 [41, 42]. In the ballistic transport regime, if electrons moving in some direction have a different electrochemical potential, μ , to those moving in the opposite direction, a net current flows. As described on page 18, the Landauer-Büttiker formalism allows

a description of resistance in terms of the relative probabilities of electron transmission and reflection between electron reservoirs. In the ballistic transport regime, conductance quantisation is robust against a small amount of scattering, which can be ignored to a first approximation [43, 44].

Below the critical gate-bias at which electron energy becomes quantised, further reductions in gate voltage serve both to increase the electrostatic potential (V_0) and to increase the confinement strength of the 1D channel, ω_0 . As a result, energy separation between the

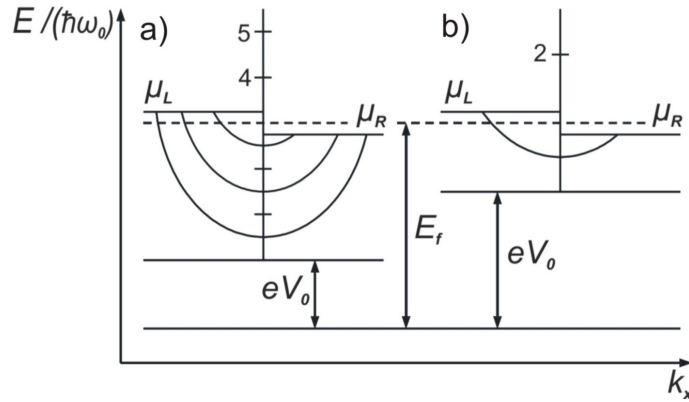


Figure 1.14: The occupation of electron states within a 1D channel in which there is net current flow caused by a potential difference between two electron reservoirs. a) and b) show the situation for two different gate biases, where $|V_a| < |V_b|$ (after [5]).

electron subbands is increased and the number of occupied electron states in the channel, N_{1D} , is reduced [Fig. 1.14]. The assumption is made that once an electron has entered the channel, it cannot be reflected at the other end. Hence all electron states carrying current with a positive velocity, ν_x , are filled to an energy μ_L , and all those travelling with $-\nu_x$ have an electrochemical potential of μ_R , where

$$\nu_x = \frac{1}{\hbar} \left(\frac{dE_n(k_x)}{dk_x} \right) \quad (1.47)$$

The conductance through the channel (G_{1D}) is given by the reciprocal of the channel resistance (I/V) and so

$$G_{1D} = \frac{1}{V} \sum_{n=1}^{N_{1D}} \int_{\mu_R}^{\mu_L} \frac{e}{2} \nu_n(E) D_{1D,n}(E) dE \quad (1.48)$$

where $D_{1D,n}(E)$ is the density of states in 1D. Using Eqn. (1.46) to evaluate Eqn. (1.47) and then multiplying by Eqn. (1.10), the product of $\nu_n(E)$ and $D_{1D,n}(E)$ gives the constant $4/h$, assuming spin-degeneracy. Since for a source-drain bias, V , $\mu_L - \mu_R = eV$, Eqn. (1.48) becomes

$$G_{1D} = \frac{2e^2}{h} N_{1D} \quad (1.49)$$

and after looking at Fig. 1.14 it follows that N_{1D} is given by the relationship

$$N_{1D} = \left(\frac{E_f - eV_0}{\hbar\omega} + \frac{1}{2} \right) \quad (1.50)$$

truncated to an integer. So, from Eqns. (1.49) and (1.50), 1D electron conductance is quantised into levels separated by $2e^2/h$. This is manifested as a series of plateaux in the channel conductance at integer values of this conductance quantum [Fig. 1.15]. For

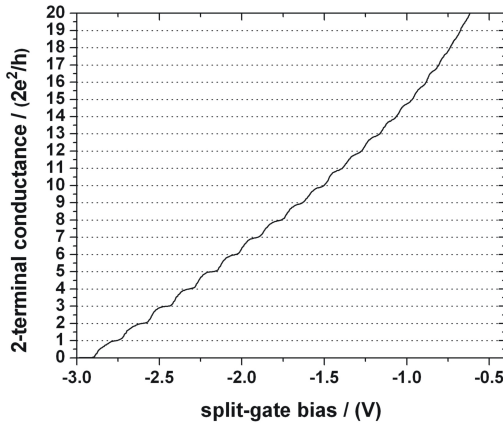


Figure 1.15: Quantised conductance plateaux measured using a split-gate to create a 1D channel in a GaAs/AlGaAs 2DEG. This plot can be seen in context on page 113.

systems in which spin-degeneracy is lifted, additional plateaux are observed at odd-integer values of e^2/h .

Reflection of Edge States

The idea of edge states introduced in section 1.5.4, is useful for showing that electrons can be reflected at a 1D constriction if the number of edge states in the 1D channel, ν_{1D} is less than the number in the 2DEG, ν_{2D} [Fig. 1.16]. The four-terminal longitudinal resistance, R_{4t} , through the 1D channel is given by

$$R_{4t} = \frac{\mu_6 - \mu_5}{eI} \quad (1.51)$$

For the situation when E_f is in the localised states between Landau levels and the edge states are tightly bound, this can be evaluated by using Eqn. (1.40) to find the current in contacts 1, 2 and 6.

$$I_1 = \frac{e}{h} (\nu_{2D}\mu_1 - \nu_{2D}\mu_6) = I \quad (1.52)$$

$$I_2 = \frac{e}{h} (\nu_{2D}\mu_2 - \nu_{2D}\mu_1) = 0 \quad (1.53)$$

$$I_6 = \frac{e}{h} [\nu_{2D}\mu_6 - \nu_{1D}\mu_5 - (\nu_{2D} - \nu_{1D})\mu_2] = 0 \quad (1.54)$$

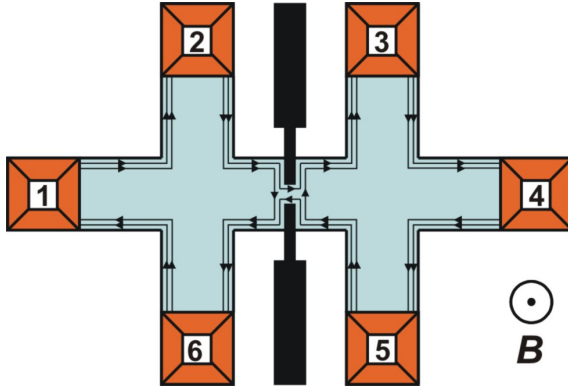


Figure 1.16: A negative bias applied to a split gate (black) results in the formation of a 1D channel. If the number of edges states in the quantum wire is less than in the 2DEG (as here where $\nu_{1D} = 1$ and $\nu_{2D} = 2$), reflection of an edge state back into the 2DEG will occur.

From the second expression it is clear that $\mu_1 = \mu_2$. Hence, combining the first and third expressions and substituting into Eqn. (1.51) gives

$$R_{4t} = \frac{h}{e^2} \left[\frac{1}{\nu_{1D}} - \frac{1}{\nu_{2D}} \right] \quad (1.55)$$

If the number of edge states within the channel is equal to the number in the 2DEG, R_{4t} goes to zero, as for the 2D case. In the same way, the two-terminal resistance, R_{2t} , is given by

$$R_{2t} = \frac{\mu_1 - \mu_4}{eI} = \frac{1}{\nu_{1D}} \frac{h}{e^2} \quad (1.56)$$

which is equivalent to adding R_H (see Eqn. (1.45)) to Eqn. (1.55). The diagonal resistance, R_d , defined as

$$R_d = \frac{\mu_2 - \mu_5}{eI} = \frac{1}{\nu_{1D}} \frac{h}{e^2} \quad (1.57)$$

is equal to R_{2t} and is dependent only on the filling factor in the 1D channel. However, this measurement has the advantage over R_{2t} that, as a four-terminal measurement, the series resistances of the Ohmic contacts and measurement circuitry are removed. See section 2.3.4 for more detail on four-terminal measurements.

1.6.4 Electron-Electron Interaction and the 0.7 Structure

An additional feature to the integer plateaux is often observed in the conductance measurements of high-quality, spin-degenerate 1D channels [Fig. 1.17]. The first conductance plateau in these data appears at $2e^2/h$ as expected. However, for the trace measured in the absence of a magnetic field, a small shoulder is apparent close to $0.7(2e^2/h)$. This feature, often referred to as the ‘0.7 structure’, has been shown to be an intrinsic feature of 1D channels which is the result of spin-related electron-electron interactions [45].

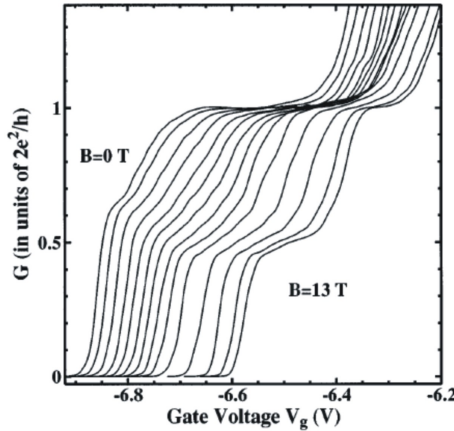


Figure 1.17: Electrical conductance measured in a GaAs quantum wire at 60mK showing the first conductance plateau at $2e^2/h$. The evolution of the structure resolved at $0.7(2e^2/h)$ is shown with increasing parallel magnetic field, $0 \leq B_{\parallel} \leq 13\text{ T}$, in 1T steps. The traces have been offset by 0.015V for clarity (reproduced from [45]).

However, a complete explanation of the 0.7 structure has not been provided to date and continues to be the subject of much research [46–48]. Fig. 1.17 shows the evolution of the 0.7 structure with increasing in-plane magnetic field. This feature moves continuously until its position coincides with the first spin-split plateau at $0.5(2e^2/h)$, indicating partial spin-polarisation.

If the magnetic field strength is increased further, there will be a point at which the energy of the first spin-up subband and the second spin-down subband intersect. Where this occurs, a feature, equivalent to the 0.7 structure, appears in the conductance data. This behaviour is repeated at other spin-subband crossings and such features are usually referred to as the ‘0.7 analogues’. These have themselves been the topic of detailed study [49].

The technique of d.c. bias spectroscopy can be used to probe these various structures. By applying an increasingly large bias between the source and drain of a device, such that a voltage is dropped across the 1D channel, the position of the 0.7 structure can be moved until it lies at $0.85(2e^2/h)$ [50]. Increasing this bias yet further results in the appearance of an additional conductance feature close to $0.25(2e^2/h)$. This has been previously confirmed for the GaAs/AlGaAs material system to originate from spin polarisation of the non-degenerate momentum subband at $0.5(2e^2/h)$ at high d.c. bias [51]. Interestingly, this feature is not affected by the application of a magnetic field and appears even in the absence of an applied field. This seems to indicate that this is a fully spin-polarised subband which can be induced purely by sufficiently large d.c. bias.

The 0.7 structure and its analogues exhibit an unusual temperature dependence [49]. For a quantum wire formed in a 2DEG with high n_s , these features disappear at suffi-

ciently low temperatures. However, they also exhibit the ability to survive sample heating, remaining even after the quantised conductance plateaux have been smeared out due to thermal broadening [52, 53]. The origin of these effects is related to the confinement potential but again is not understood clearly. However, the high and low temperature behaviours are thought to be caused by different mechanisms.

1.6.5 Zero-Dimensional Quantisation

The logical conclusion to the progression from 3D to 1D electron systems discussed so far in this chapter is the confinement of electrons in all three-dimensions. These 0D regions are usually referred to as quantum dots (QDs) and the discrete electron states within these systems mean that they behave rather like pseudo-atoms. Within a QD no free-electron motion is possible. Transport into and out of the dot is via tunnelling and within the dot, only excitation and relaxation processes occur. The size of the QD dictates the intersubband spacing.

QDs have been realised in III-V semiconductors via an extension of the electrostatic techniques described previously in this section. By applying a bias to a series of gates in some circular or rectangular geometry, electrons in a 2DEG can be confined into a small central region. However, the approach discussed in this work uses the nature of certain III-V materials to directly grow physical QDs during the epitaxial process. As discussed in section 1.2 the strain between two crystalline materials is dependent on their relative lattice constants. For some systems with high strain, certain growth conditions result in growth via the Stranski-Krastanov mechanism (see page 47) and the spontaneous formation of small, defect-free, 3D islands of material through strain relaxation. Since these islands are typically of the order of a few tens of nanometres in size they are small enough for 3D electron confinement to occur. By altering the growth conditions it is often possible to vary the size and density of the islands in these arrays of so-called ‘self-assembled’ QDs (SAQDs). It is this self-assembled approach to achieving QD structures on InGaAs and InAlAs which is investigated in chapter 6 of this dissertation.

1.7 Summary

The theoretical background to the work comprising the subsequent chapters of this dissertation has been presented. The III-V materials GaAs, AlAs and InAs were introduced. The combination of these binary compounds into the ternary materials $\text{In}_x\text{Ga}_{1-x}\text{As}$ and $\text{In}_y\text{Al}_{1-y}\text{As}$ was discussed. The density of states functions for electrons confined within 3D, 2D, 1D and 0D regions of such materials were derived. An experimental method for the determination of electron mobility and density within bulk material was presented and discussed in terms of scattering process limitations.

2D electron transport in InGaAs/InAlAs was then covered in some detail: heterostructure design was used to form high-mobility 2DEGs, the behaviour of which were modelled using an effective-mass approach to the Drude theory. Transport in magnetic fields was then addressed. The concept of Landau levels was introduced, together with explanations for the origin of the Shubnikov-de Haas oscillations and Quantum Hall Effect; both of which are measured extensively in chapter 4.

The chapter concluded with a brief look at low-dimensional, 1D and 0D electron systems in InGaAs/InAlAs. Firstly the mechanism for using split-gates to confine 2DEG electrons into a 1D quantum wire and the theory behind the quantisation of electrical conductance in such a channel was discussed. The Landauer-Büttiker formalism was used to demonstrate that edge states can be reflected at a 1D constriction, leading to a finite longitudinal resistance, even when the highest Landau level is completely filled. The 0.7 structure and its analogues were introduced. These are commonly observed anomalies in the conductance data which are not fully accounted for by current theory. Measurements of 1D transport in InGaAs/InAlAs materials can be found in chapter 5. Finally, the confinement of electrons into 0D quantum dots was outlined, with particular reference to SAQDs, which are covered in detail in chapter 6.

Chapter 2

Device Fabrication and Measurement Techniques

2.1 Introduction

All III-V material used for this dissertation was grown ‘*in-house*’, using molecular beam epitaxy (MBE) which is described in chapter 3. Transformation of this raw epitaxial material into useable devices is covered in section 2.2, which comprises the first half of this chapter. All fabrication work was carried out in a class 10,000 cleanroom. Most of this III-V material was $\text{In}_x\text{Ga}_{1-x}\text{As}$ and $\text{In}_x\text{Al}_{1-x}\text{As}$ ($x \geq 0.53$), grown on InP substrates. Nevertheless, it was possible to adopt most of the standard GaAs/AlGaAs processing steps.

A common device is the HEMT (see section 1.5.1). A structure containing a two-dimensional electron gas is processed into a Hall bar with probes for measuring longitudinal and transverse (Hall) voltages. Standard gated-HEMT processing is described since these steps constitute the basic building blocks needed to fabricate most other devices. A gate is used to vary electron density. As discussed on page 10, Φ_B at a metal- $\text{In}_x\text{Ga}_{1-x}\text{As}$ junction is very low. This means that here the electrostatic gates must be insulated from the semiconductor. Where additional processing stages were required in particular cases, the details are discussed in later chapters.

Section 2.3, which constitutes the second part of this chapter, discusses the techniques used to assess the structural, electrical and optical properties of both raw epitaxial material and completed devices.

2.2 Device Fabrication

MBE wafers were cleaved into chips, typically 10mm × 10mm. This was achieved by scoring the wafer surface with a diamond-tipped scribe. Applying pressure to either side

of this scratch creates a crack which then propagates along a crystal plane. The cleaved chip was immersed in acetone and briefly placed in an ultrasonic bath to remove any dirt or dust. The chip was then rinsed in propanol and blown dry using N₂ gas. One such chip provides sufficient space for six to nine standard HEMT devices.

2.2.1 Photolithography

Photolithography is essentially a pattern-transfer technique. A ‘resist’ chemical on the chip surface which is sensitive to UV light is illuminated through some template. For the positive resist used in this work, the developer preferentially etches away all regions exposed to the UV light. However, negative resists are also available, for which all unexposed areas are removed during developing. The first photolithography step is to wet-etch a mesa onto the chip. As with all other photolithographic work, this was carried out in a yellow-area inside the clean-room, in which the resist chemicals are protected from accidental exposure to UV light.

Spin-Coating

The chip is coated with Shipley Microposit S1813 resist. After heating to 125 °C for one minute to ensure a dry surface, it was placed on a spinner and held in place with a vacuum chuck. The resist was passed through a 0.2μm particle filter and applied to the chip using a syringe. The spinner rotates at 5500rpm for 30s to form a thin, even layer of resist. The chip was then baked for two minutes at 90 °C to remove some solvent and slightly harden the resist.

Exposure, Developing and Ashing

The pattern to be transferred to the chip is stored on a mask. This is a glass slide, on one side of which the required photolithography patterns have been written into a layer of chrome. Standard GaAs/AlGaAs J-Mask 10A and 10B masks were used for this work. A Karl Suss aligner was used to adjust the chip position relative to the mask pattern using x, y and θ micrometers. The chip was then brought into contact with the mask and exposed for 6.5s using a 350W UV lamp, with a wavelength of ~310nm. Areas of exposed resist were then removed by immersing the chip in Shipley MF319 developer for 30s and then rinsing in deionised water. Any residual resist was removed from the edges of the developed profile by ‘ashing’ the chip in an O₂ plasma for 60s.

2.2.2 Wet Etching

An H₂SO₄:H₂O₂:H₂O (1:8:80) etchant was mixed and allowed to stabilise. This solution etches InGaAs and InAlAs at ~10nm/s but does not react with resist. The mesa stripe

was hence created by gently agitating the chip in the etch solution. Areas still covered with resist are not etched, although some undercutting may occur. By etching down to the undoped buffer layer the 2DEG is electrically isolated. The chip was then rinsed in deionised water. A schematic diagram of the photolithography process is shown in Fig. 2.1.

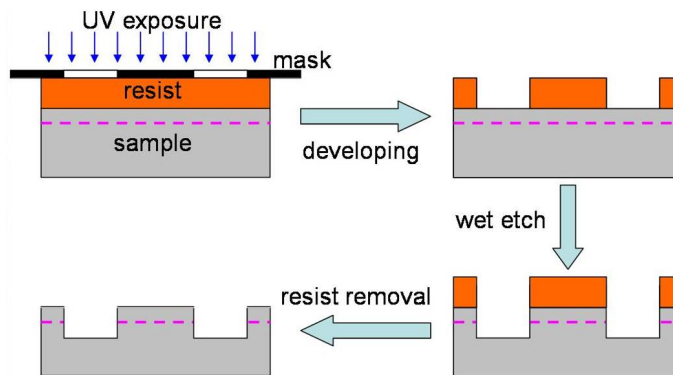


Figure 2.1: Schematic diagram showing the steps required to etch a mesa stripe. The purple dashed line represents the position of the 2DEG.

The remainder of the resist was then removed by immersing the chip in acetone, followed by a propanol rinse and drying with N₂ gas. The etch depth was measured on a Dektak instrument, which uses a stylus to profile the mesa stripe. A standard mesa is 80μm wide with an electrical length-to-width ratio of 9:1.

2.2.3 Ohmic Contact Metallisation

In order to electrically contact the device, Ohmic contacts were created on the mesa via the evaporation and subsequent annealing of slugs of a gold-germanium-nickel (AuGeNi) mixture.

Undercut Photolithography

Another stage of photolithography was used to open up windows in a layer of resist through which metal could be deposited. The process is very similar to that described in section 2.2.1, except that prior to development the chip was immersed in chlorobenzene for three minutes. This hardens the resist surface and hence during developing the softer underlying layers were more readily removed creating an undercut profile. Two minutes were required to fully develop the exposed resist and an O₂ plasma ash was performed as required.

AuGeNi Evaporation and Lift-off

The chip was agitated for 15s in a 10% solution of HCl:H₂O to remove the ubiquitous oxide layer from the semiconductor surface. It was then placed into an evaporator which was evacuated to a base pressure of $\sim 5 \times 10^{-7}$ mbar. A slug of AuGeNi was heated in a tungsten boat until it evaporated, coating the chip surface. In this mixture, the Ni acts to wet the semiconductor surface and promote adhesion of the AuGe eutectic mixture, Ge is an *n*-dopant, while Au is the main component of the low-resistance electrical contact. 80-100nm was typically deposited. The ‘lift-off’ process was achieved by immersing the chip in acetone. The undercut created by the chlorobenzene soak allowed acetone to remove all remaining resist along with any overlying metal.

Annealing of Ohmic Contacts

To electrically contact the metals on the surface and the 2DEG, the chip was annealed under forming-gas (4% H₂ in N₂). Heavily *n*-doped columns of Au are formed extending down into the device. The temperature was ramped to 430 °C, held for 80s and then cooled. The actual chemistry of the anneal process is fairly complex but is described in literature [54, 55]. A diagram summarising the Ohmic contact metallisation process is shown in Fig. 2.2

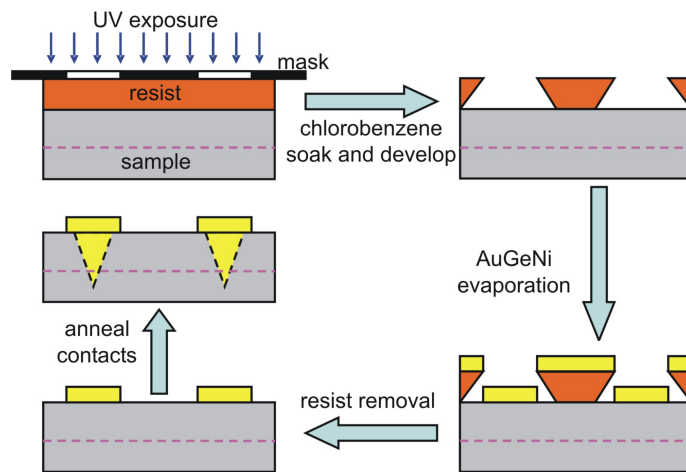


Figure 2.2: Schematic diagram showing the steps required to create Ohmic contacts on a device. The yellow regions represent AuGeNi metal while the purple dashed line indicates the 2DEG position.

2.2.4 Insulation of Electrostatic Gates

As discussed in section 2.1, metal gates must be insulated from In_xGa_{1-x}As to enable electrostatic operation. HD Microsystems polyimide was used as the insulator in this

work. Transparent at optical wavelengths, it is a polymer which can be spun-on, exposed and developed, similarly to the standard photolithography resist. The only real difference is that polyimide acts as a negative resist: exposed areas of polyimide become cross-linked during illumination and remain on the device after developing. This means that the same mask used to form the top-gate with positive resist can be used to place a layer of polyimide above the mesa, onto which the gate can later be placed. Polyimide has a limited shelf-life and so it is stored in the dark at -20°C . In addition, polyimide is extremely hydrophilic, readily absorbing water. The dielectric properties of the resulting film are severely compromised if wet polyimide is used.

Polyimide Spinning

The polyimide solution was allowed to warm to ambient temperature before it was opened, thus limiting condensation of water vapour. The relative humidity, RH, of the processing environment was critical. In general, polyimide processing is only carried out where $\text{RH} \leq 60\%$. The chip was pre-baked at 125°C for five minutes to dry the surface. After applying the polyimide solution, the hot chip was spun at 8000rpm for 60s. The chip was then baked for three minutes at 65°C , followed by another three minutes at 90°C .

Polyimide Exposure

An identical alignment process was used to that described previously for photolithography. Since the same mask was to be used for both this step and the top-gate metallisation, four 80s exposures with a 350W UV lamp were made on each device, with the chip moved between each one. This created a large exposed area of polyimide, which greatly simplified subsequent gate alignment.

Polyimide Developing and Curing

The chip was then immersed for 30s in HD Microsystems Polyimide developer, rinsed in n-butyl acetate, and dried with N_2 gas. The developed polyimide was finally cured in a furnace under N_2 . The temperature was ramped at $\sim 2^{\circ}\text{C}/\text{minute}$ from room temperature to 250°C , whereupon it was baked for one hour and then allowed to cool back to ambient temperature.

2.2.5 Electrostatic Gate Metallisation

To form a metal gate, the same steps were used as described in section 2.2.3. In this case, the mask opened a stripe in the resist above the large area of cured polyimide. Through this, NiCr was evaporated, the thickness of which was limited to 7nm. This meant that it was relatively transparent to light from a red LED to allow device illumination (see

section 2.3.4). A second metallisation step was then required to form bond-pads, with arms running up the sides of the mesa to electrically contact the NiCr. 20nm of Ti was evaporated, followed by 80nm of Au. The Ti promotes adhesion to the semiconductor, while the Au creates the low-resistance contact. Since gate metal is only required at the surface of the semiconductor, neither the NiCr or the Ti/Au gates are annealed.

The various elements described in this section can be identified on a photograph of a completed HEMT device [Fig. 2.3]. The central mesa channel, running left to right,

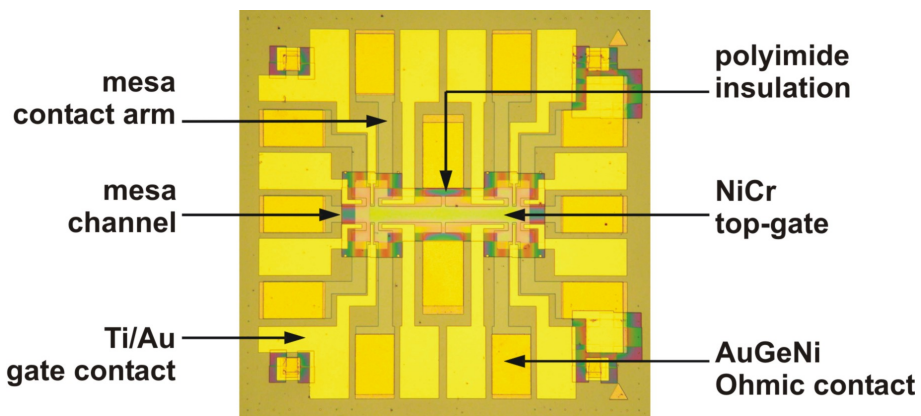


Figure 2.3: Optical microscope photograph of a completed $2\text{mm} \times 2\text{mm}$ HEMT device with an insulated optical gate.

is connected with the AuGeNi Ohmics contacts. The central iridescent polyimide region above this is particularly easy to identify, on top of which is light-grey stripe of the transparent NiCr top-gate.

Packaging and Bonding

Individual devices were cleaved off the chip and glued into a 20-pin leadless chip carrier (LCC) package using a non-conductive GE varnish. These packages are accepted by the probes used for device measurement. Using a Kulicke and Soffa Industries ball-bonder, the Ohmic and gate bond-pads were connected to the LCC with Au wires.

2.3 Device Measurement

Various techniques are used to characterise the structural and optical properties of the raw epitaxial material and these are discussed in sections 2.3.1 to 2.3.3. In addition, electrical transport in devices is assessed, often at low-temperature. Such measurements are described in the remainder of this chapter.

2.3.1 Atomic Force Microscopy

Atomic force microscopy (AFM) uses the deflection of a scanning tip to image the three-dimensional (3D) surface morphology of a sample. A Digital Instruments Nanoscope running eponymous software, was used for all such measurements. The AFM tip consists of a cantilevered stylus made of silicon/silicon nitride. Once in close contact with the semiconductor, piezoelectrics scan the tip across the surface. Moving in the xy plane, it is deflected due to Van de Waals' forces acting between atoms at the end of the tip and on the surface. Cantilever deflection is monitored by the reflection of a laser beam [Fig. 2.4]. In

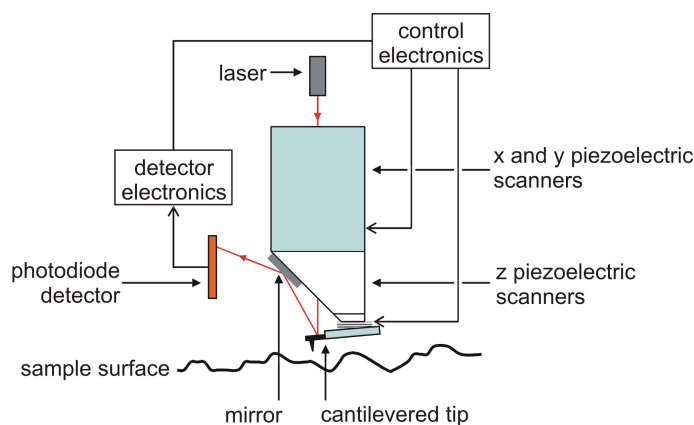


Figure 2.4: Schematic diagram showing the main components of an AFM head (not to scale).

tapping mode, a piezoelectric driver oscillates the cantilever close to its resonant frequency. As the tip ‘taps’ against the surface, the high resolution measurements are made. Between these measurements, the tip and sample are not in contact and the cantilever can be moved across the surface without damaging the tip. As the tip approaches the sample, the oscillation amplitude is reduced as a result of the atomic force it experiences due to the surface. A piezoelectric feedback circuit maintains constant amplitude by adjusting the tip-to-sample distance. The vertical offset of the AFM head is then a direct function of the surface morphology. Heights can be resolved to within 1 Å which permits the imaging of most surface features, from monolayer-high terraces to self-assembled quantum dots.

2.3.2 X-Ray Diffractometry

X-ray diffractometry (XRD) is a powerful crystallographic tool used to probe the structure of III-V material. For this work, a Philips GEN 6 X’Pert high-resolution XRD instrument was used, located in the Department of Materials Science and Metallurgy, University of Cambridge. Maximum angular resolution of this machine is 0.0001° (0.36 arcsec). The x-ray source has a Cu target and a symmetric 4 x Ge 220 monochromator is used to select the

$K_{\alpha-1}$ line from the emitted radiation, which has a wavelength (λ) of 1.541\AA . A collimated x-ray beam is incident on the semiconductor surface and diffracted by the atomic planes. Measurement of the angular dependence of this diffraction facilitates calculation of the interatomic spacing, or crystalline lattice constant, from Bragg's law [56]

$$n\lambda = 2d \sin \theta \quad (2.1)$$

where n is the integer diffraction order, d is the lattice spacing and θ is the angle between the incident beam and the crystal planes. Consider a simple III-V heterostructure comprised of a strained epilayer of ternary material grown on a substrate: for example, $\text{Al}_x\text{Ga}_{1-x}\text{As}$ on GaAs. The XRD spectrum of this sample will consist of two well-resolved diffraction peaks; one from the substrate and one from the epilayer. From the size of the Bragg angle splitting between these peaks, the lattice constant of the $\text{Al}_x\text{Ga}_{1-x}\text{As}$ can be determined.

The lattice constant of the $\text{Al}_x\text{Ga}_{1-x}\text{As}$ is dependent on its composition. Vegard's law states that the lattice constant of a ternary material can be linearly interpolated between its two binary boundary conditions [57]. However, some deviation from linearity has been demonstrated for the $\text{Al}_x\text{Ga}_{1-x}\text{As}$ lattice constant. Gehrsitz *et al.* determined a quadratic bowing parameter which modifies the Vegard relation [58]. From this correction, x can be extracted from the substrate-AlGaAs peak-splitting in arc seconds, $|\delta\theta|$, where

$$|\delta\theta| = -47x^2 + 425.9x \quad (2.2)$$

A full discussion of these calculations, along with a general review of XRD can be found in numerous sources; for example Refs. [59, 60]. The use of XRD for measurement of material composition is described in section 3.4.1.

2.3.3 Photoluminescence Spectroscopy

Photoluminescence (PL) is another useful tool for investigating the structure and crystal-quality of III-V semiconductor material and heterostructures. A 488nm Ar+ pump laser is used to excite valence electrons high into the conduction band. These decay non-radiatively into excitons and the light emitted by subsequent exciton relaxation is measured using a Bruker Fourier Transform Infra-Red (FTIR) spectrometer. One of two In-GaAs detectors is used. The first, operating at room temperature, measures wavelengths between 800nm and 1700nm. The second is Peltier cooled and measures a wider wavelength range from 800nm to 2500nm, albeit with an order of magnitude less sensitivity.

Peaks on the PL spectrum provide valuable information about the band-structure of a sample. The composition of ternary material can be calculated and cross-referenced with XRD analysis. Peaks with high spectral intensity and low full-width at half-maximum

(FWHM) indicate crystal material of good quality. In addition, PL is used extensively to probe the optical properties of SAQDs, as discussed in chapter 6.

PL measurements were carried out at 4.2K to limit lattice vibration which would otherwise broaden the PL peaks. A small sample chip, was mounted on a ‘cold-finger’ which permitted x, y, z and θ micrometer movement. This was cooled, using a continuous-flow of liquid ^4He , in a cryostat with an optical window. Various components were then assembled on an optical bench [Fig. 2.5]. The laser power incident on the sample could

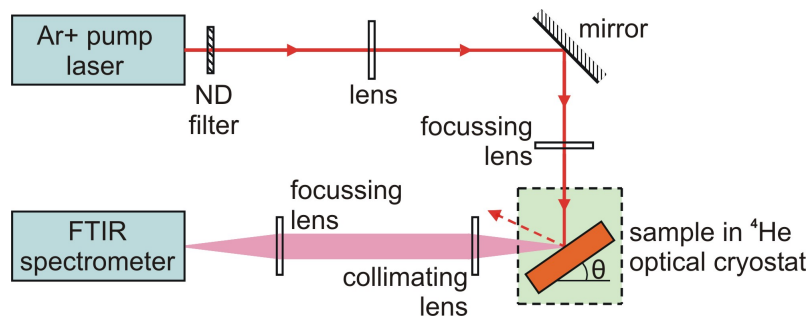


Figure 2.5: Schematic diagram showing the apparatus used for measuring PL. The dashed red line represents the specular reflection of the laser from the sample.

be controlled by inserting various neutral density (ND) filters into the beam path. The laser beam was focussed onto the chip through the cryostat window. The beam diameter at the sample was $\sim 60\mu\text{m}$, meaning that chip sizes could be kept small. Ten to fifteen could be simultaneously cooled. The emitted photoluminescent radiation was collimated and focussed into the FTIR spectrometer. However it was important to ensure that the sample angle, θ , was adjusted such that the specular reflection did not also enter the collection optics. The FTIR spectrometer was connected to a computer on which spectral analysis was performed with Bruker *Opus* software. All PL analysis was carried out at the Cambridge Research Laboratory of Toshiba Research Europe Limited, with the assistance of Dr. H.W. Li.

2.3.4 Electronic Transport

Cryostat Design

The electron transport measurements in this work were typically performed at low temperature, since several scattering processes are heavily suppressed in a sufficiently cold sample (see section 1.4.1). For samples of bulk material, assessment is routinely carried out at 77K by immersing the chip of interest in liquid N_2 . Similarly, a check on the transport properties and device characteristics of a device such as a HEMT can be quickly carried out at 4.2K by dipping a chip into liquid ^4He . However, both magnetotransport assessment and measurement at lower temperatures require the use of a cryostat.

^4He Bath Cryostat

An Oxford Instruments Variable Temperature ^4He cryostat containing an 8T superconducting magnet was used for most assessment at 1.5K in this work [Fig. 2.6]. The chip

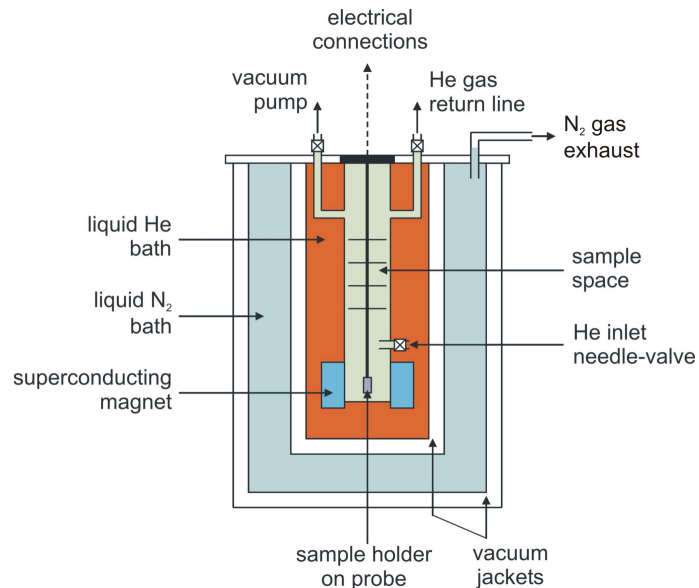


Figure 2.6: Schematic diagram showing the internal layout of a pumped ^4He cryostat. Valve locations are represented by \otimes .

package is connected electrically to the bottom of the probe. This is lowered into the cryostat and the surrounding sample space is evacuated to $\sim 6\text{mbar}$. The introduction of ^4He to the sample space through a needle-valve initially cools the sample to 4.2K. However, continued pumping of the sample space reduces the ^4He boiling point to 1.5K, further cooling the sample. Balancing the ^4He flow via the position of the needle valve provides a stable base temperature. Sample temperature is measured by a thermometer on the probe. A heater in the bottom of the sample space allows the measurement temperature to be altered. The outer N_2 bath and vacuum jackets reduce the thermal load on the ^4He bath and reduce wastage. ^4He boil-off gas is collected to be recondensed. The superconducting magnet can supply perpendicular fields between 0 and 8T.

One other such cryostat was used in the course of this research. This also had a base temperature of $\sim 1.5\text{K}$, but a slightly larger magnet with a maximum field of 10T. This second system was housed inside a metal screened-room which reduced measurement noise and was protected against voltage ‘spikes’. This made it ideal for measuring less robust devices.

^3He Cryostat

To achieve measurement temperatures below 1K, an Oxford Instruments ‘Heliox’ system at the Cambridge Research Laboratory of Toshiba Research Europe Limited was used, with the assistance of Dr. S.N. Holmes. This uses ^3He to achieve a base temperature of $\sim 400\text{mK}$ and can deliver magnetic fields up to 10T. This lower measurement temperature removes more thermal noise and so improves resolution. ^3He is tremendously expensive and so is circulated around a closed loop within the cryostat [Fig. 2.7]. The chip, attached to the probe, is inserted into the cryostat and the sample space is evacuated and cooled to $\sim 4.2\text{K}$ with liquid ^4He . The pressure above the ^3He is reduced using a sorption pump (‘sorb’) at 4.2K which cools the sample space to base temperature. The sample will then remain at base until the sorb becomes saturated with ^3He , after which time it quickly warms. In order to re-cool the sample, the sorb is heated to 45K to drive off the ^3He . During heating, the sorb is thermally decoupled from the ^4He pot to prevent this from also being warmed. The ^3He vapour emitted by the hot sorb is recondensed by the cold liquid ^4He pot. Once the ^3He pot has been refilled with the now-liquid ^3He , the sorb is recooled by the ^4He pot to $\sim 4.2\text{K}$. As the sorb cools it reabsorbs ^3He and the sample temperature is once again reduced to base. Intermediate temperatures between base and $\sim 1\text{K}$ can be achieved by operating the cryostat in the usual way but simultaneously applying a small amount of heating to the sorb. This reduces the pumping power of the sorb and so the base temperature increases accordingly.

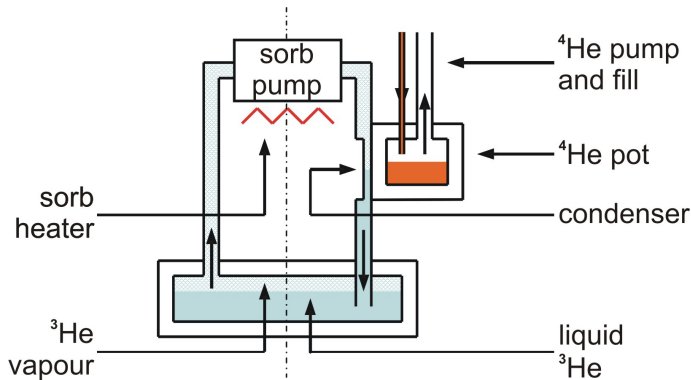


Figure 2.7: Schematic diagram showing the internal layout of a ^3He Heliox cryostat. Normal sample-cooling with the cold sorb pump is represented by the half of the diagram to the left of the dotted line. The section on the right of this line represents operation during the sorb regeneration cycle when the heater is on. Depending on the system used, the sample either sits directly in the pumped ^3He -cooled sample space, or is cooled via conduction through a cold finger.

Phase-Sensitive Techniques: Constant-Current

Both bulk material and heterostructures are typically fabricated into Hall bars to allow four-terminal measurement of longitudinal (R_{xx}) and Hall (R_{xy}) resistances. Four-terminal measurements use two pairs of Ohmic contacts: one to supply the current and one to measure voltages. These chips are connected to a measurement probe and cooled in either a dewar or cryostat. The techniques used for electrical measurement will typically be the same for both bulk material and device heterostructures.

Once the chip temperature has stabilised, the probe is connected to the assessment circuitry [Fig. 2.8]. A current, which is kept small ($\sim 100\text{nA}$) to avoid electron heating,

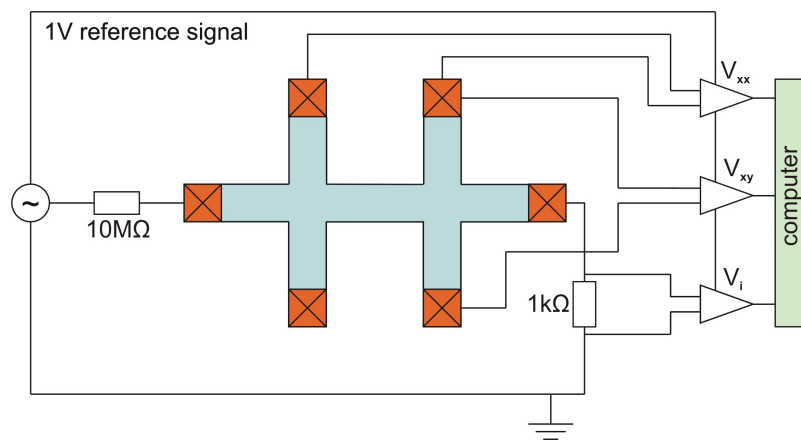


Figure 2.8: Circuit diagram for constant current four-terminal resistance measurements. Standard conventions are used, with the three lock-amplifiers shown at right.

is applied between the source and drain of the channel. Given the low current, a d.c. measurement would not be appropriate, due both to very low signal-to-noise ratios and large d.c. offsets. Instead, an a.c. phase-sensitive method is used. At 1.5K, a 1V a.c. reference signal, with frequency, ν_{ref} (typically 85.3Hz) is dropped across a $10\text{M}\Omega$ resistor to generate a 100nA current. The current used inside the colder Heliox cryostat may be even smaller. The voltages across the device are then measured, with respect to ν_{ref} , using two Stanford Research Systems SR830 lock-in amplifiers. These only amplify signals at ν_{ref} and hence noise sources at other frequencies are suppressed. Assuming that the resistance of the device is much smaller than the $10\text{M}\Omega$ resistor, the current remains constant. To confirm this, the voltage dropped across a $1\text{k}\Omega$ resistor in series with the device, is monitored with a third lock-in amplifier. The longitudinal and Hall voltages are simultaneously measured by two independent pairs of voltage probes. These are converted to resistance values, allowing the carrier density and mobility to be calculated (see page 6). An Acorn Archimedes computer running *Cryomeas* and *LabAssistant* software written by Dr. C.J.B. Ford at the University of Cambridge, is used both for control of the cryostat

and for data analysis.

Phase-Sensitive Techniques: Constant-Voltage

Alternatively samples can be measured using a constant voltage [Fig. 2.9]. Particularly suitable for devices with one-dimensional (1D) channels where resistance is typically several $k\Omega$ (see chapter 5), electrical conductance is measured. A 1V a.c. reference signal

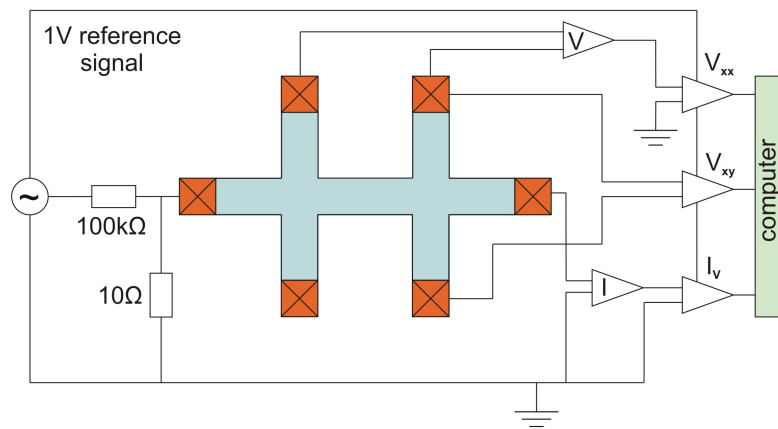


Figure 2.9: Circuit diagram for the constant voltage four-terminal conductance measurements. Standard conventions are used. The current and voltage pre-amplifiers are labelled I and V accordingly.

goes through a potential divider, typically reducing the voltage to $100\mu\text{V}$. As before, this must be kept small to prevent electron heating. This voltage is dropped between the device source and drain and then passed through a current pre-amplifier before going to the I_v lock-in. A blocking capacitor (not shown) is interposed between the amplifier and the sample to prevent any d.c. signals passing back to the device. In addition, a voltage pre-amplifier is used to increase the V_{xx} signal before it goes to the relevant lock-in. Conductance is then calculated from the current and voltage measurements.

Gated and Illuminated Measurements

Application of a d.c. bias to an electrostatic gate overlying the channel can be used to vary the 2DEG carrier density, n_s . The metal gate creates a Schottky barrier at the semiconductor surface and defines the position of the Fermi level. The low height of the Schottky barrier at the metal-In_xGa_{1-x}As interface has been discussed but the use of polyimide insulation means that leakage currents can be prevented.

The application of a positive bias reduces the surface barrier height which pushes the band edge down inside the QW, further below E_f , thus increasing n_s . Conversely, a negative gate bias will serve to lift the conduction band relative to E_f and deplete the

number of carriers. Given a sufficiently large negative bias, the channel can be made to ‘pinch-off’, at which point so few carriers remain that current cannot pass. A Keithley 236 source measure unit (SMU) is used to apply this bias, whilst at the same time, measuring any leakage current between the gate and channel.

At sufficiently high bias, the polyimide will eventually breakdown and leakage will occur. The voltage required to induce a leakage current is essentially a function of polyimide thickness. A 300nm thick film of polyimide will typically exhibit leakage currents of less than 1nA, for biases up to $\sim 15\text{V}$ [Fig. 2.10].

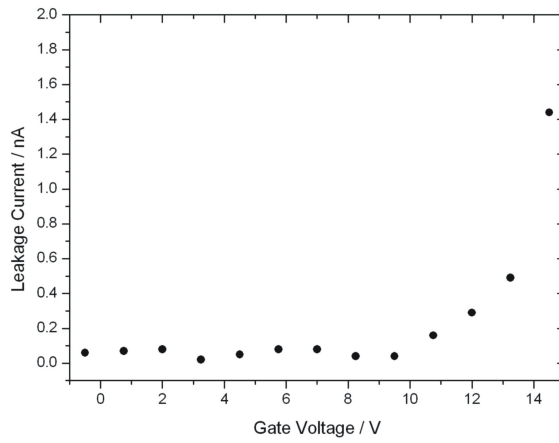


Figure 2.10: The variation of leakage current with applied d.c. bias for a typical electrostatic gate, insulated with 300nm polyimide, above an InGaAs QW HEMT.

In addition, a sample can be illuminated inside a cryostat or dewar by use of a red LED mounted on the sample probe. Si doping can give rise to D-X centres which trap and weakly bind electrons. These binding energies are greater than $k_B T$ at cryogenic temperatures [61]. However, the electrons can be freed using LED illumination, thus increasing n_s and reducing the 2DEG resistance [62, 63]. Electron mobility is also increased due to an enhancement in electron-electron charge screening. This technique is known as persistent photoconductivity (PPC) since the decay time-constant for these electrons is of the order of 10^5s . For a detailed review of these effects, see Ref. [64].

Through a combination of device illumination and gate biasing, curves of electron mobility against carrier density can be plotted for each sample. For GaAs/AlGaAs heterostructures, there exists a power law dependence of μ on n_s , where

$$\mu \sim n_s^\alpha \quad (2.3)$$

Determination of the value of α in this relationship gives some indication as to the transport-limiting scattering mechanism. For low- n_s , where $\alpha \geq 1.5$, Coulomb scattering from ionised dopant impurities dominates, while at higher- n_s , where $\alpha \leq 0.9$, background

impurity scattering limits transport. Between these limits, α varies mainly as a function of device design [65].

Current-Voltage Measurements

A Hewlett-Packard semiconductor parameter analyser is used to measure the current-voltage (I-V) characteristics of a device, also typically at low temperature. This contains four SMUs, each of which either applies a voltage and measures a current, or vice versa to perform a four-terminal measurement. I-V measurements are useful to check for the linear Ohmic response of electrical contacts. In addition, they also permit the assessment of particular device characteristics, such as peak-valley current ratio in a resonant tunnelling diode (see section 6.4). Applied voltages are usually d.c. although a.c. signals may be used to limit electron heating, particularly for large current densities. The applied voltage is limited to prevent the measured current exceeding a compliance value of perhaps 50-100nA.

2.4 Summary

In this chapter, the fabrication process for a standard gated-HEMT is described, the individual steps of which can also be applied to the fabrication of a wide variety of other devices. A series of photolithography steps allow the etching and metallisation of selected areas of a chip. In this way, a current channel can be created which is electrically isolated except where Ohmic contacts have been placed. An overlying, insulated gate can then be added as required. Finally the completed chip is packaged ready for measurement. Various techniques for assessing the structural, optical and electrical properties of III-V semiconductor material and devices have been covered in the latter sections of the chapter. Surface morphology can be explored using AFM. Material composition and crystal quality can be assessed through XRD and PL. The ability to cool devices to low-temperature, either by immersion in a liquid cryogen, or via use of a cryostat, has been outlined. The operation of ^3He and ^4He cryostats used in this research was described. Finally, the a.c. lock-in and d.c. SMU techniques used for four-terminal, low-temperature electrical measurements have been discussed and the context within which each might be used was explained.

Chapter 3

Molecular Beam Epitaxy

3.1 Introduction

During the 1960s, the first semiconductor films were grown by a variety of methods; from liquid- and vapour-phase epitaxy, to sputtering techniques. However, towards the end of the decade, work by Arthur and Cho, amongst others, led to what is now called molecular beam epitaxy (MBE) [66–68]. For the first time, MBE enabled reproducible growth of high-quality semiconductor crystals, with accurate control of layer thickness, material composition and dopant incorporation. The first part of this chapter provides an overview of the growth of III-V semiconductors by MBE; in particular those based on the gallium arsenide (GaAs) and indium phosphide (InP) material systems. A Veeco MOD Gen. II MBE chamber was used for all growth in this dissertation. When this work was started, this machine had been only recently installed and hence an extensive commissioning process was required prior to any research being carried out. The growth rates of the Al and Ga cells needed calibration and this work is covered in section 3.3. Calibration of the In cell was also essential for the work presented in this dissertation. Due to strain considerations, alternative methods had to be used to measure InAs growth rate and these are covered in section 3.4. In section 3.5, the uniformity of growth in the new MBE chamber is assessed. Optimal growth temperature is material dependent and hence this topic is covered with respect to some real devices chapter 4.

3.2 An Overview of MBE

3.2.1 The MBE Growth Environment

MBE Chamber Layout

The MBE chamber is an ultra-clean environment, within which the user can vary conditions such as pressure and temperature, to achieve those most propitious for epitaxial

growth. Growth of III-V material for this work used the Group III elements Ga, Al and In; the Group V element As; and an *n*-type dopant, Si. The molecular beams from which MBE gets its name, are created by heating these elements in effusion cells. These beams react with one another on the surface of a heated substrate crystal to form a thin crystal film, or epilayer.

A schematic diagram of an MBE chamber shows the major components of the machine discussed in this section [Fig. 3.1]. It should be noted that this diagram shows a VG-V80H chamber and not the Veeco system. However, the basic components labelled here are common to both machines.

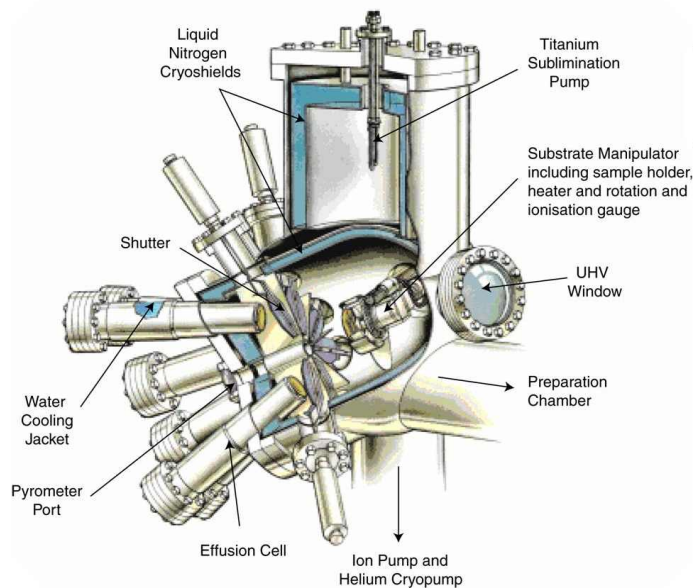


Figure 3.1: Schematic diagram showing the main components of a V80 MBE chamber. Reproduced from a VG Semicon Ltd. brochure.

MBE takes place under ultra-high vacuum (UHV), with a base pressure of the order of 5×10^{-11} Torr (see below). In order to optimise material quality, chamber cleanliness is of paramount importance. The machine is therefore opened only for essential maintenance or to replenish exhausted effusion cell material. The length of time between such events is maximised at all costs and may be as long as two years.

The system consists of three sections separated by UHV valves; the growth chamber, the preparation chamber and the load lock. This arrangement ensures that samples can be loaded and unloaded without impacting the UHV conditions in the growth chamber. The vacuum in each section is maintained by a combination of cryo- and ion-pumping. Both the growth and preparation chambers are fitted with an SRS 200 residual gas analyser (RGA) to monitor partial pressures of background gases. These ensure that unwanted species are not transferred between chambers. Whenever the load lock is brought up to

atmospheric pressure for sample transfer, an overpressure of dry N₂ suppresses ingress of contaminants while the chamber is open. The base pressures of the load lock and the preparation chamber, of $\sim 10^{-9}$ Torr and $\sim 10^{-10}$ Torr respectively, reflect the cleanliness hierarchy of the chambers. Movement of the substrates between the three chambers is achieved using a combination of magnetically-coupled trolleys and transfer arms. Heater stages in the preparation chamber permit thermal degassing of substrates prior to growth.

Two common contaminant species detrimental to the quality of the growing epilayer are carbon and oxygen, from O₂, CO₂ and H₂O. To achieve the required levels of cleanliness within the MBE machine as a whole, but in particular inside the growth chamber, the following conditions and procedures are rigorously adhered to.

Ultra-High Vacuum

UHV conditions are achieved through a combination of ion, sublimation and cryopumps, which together remove most species from the chamber. The growth chamber also has two cryopanels: double-walled units through which liquid nitrogen (LN₂) flows. These too act as pumps, with gaseous species condensing on the cold surfaces. The cryoshield, in the main part of the chamber, pumps the area around the substrate. The cryoshroud, located between the effusion cells, helps reduce cross-talk between adjacent sources. As a consequence of the UHV conditions, the concentration of unwanted species incorporated into the epitaxy is low enough that material quality is not compromised, despite relatively low growth rates close to one monolayer per second ($\sim 1\mu\text{m}/\text{hr}$). With the growth chamber at base, all partial pressures, with the exception of H₂, are below 10⁻¹³ Torr.

Substrate Preparation

Substrates are high-purity single crystals, often produced via a vertical-gradient freeze process. Those used in this work were single crystals of (0 0 1) GaAs and InP, 500 μm thick. However, some variants were used in these experiments, including *n*-type or semi-insulating (SI) and single- or double-side polished.

Epi-ready substrates negate the need for wafer cleaning prior to loading. The Veeco chamber uses both 2" and 3" substrates, which are mounted on molybdenum (Mo) blocks. They are clipped in place with a sapphire heat-diffusing disc positioned behind the wafer. Substrates are loaded and unloaded from the machine, using dedicated, ultra-clean tools. At all times that the blocks and virgin substrates are outside of the load-lock, great care is taken to avoid contamination.

After an initial outgas at 150 °C in the load lock to remove water vapour, the blocks are transferred to the preparation chamber where they undergo at least two degas cycles to ~ 250 °C. Since InP dissociates at lower temperatures than GaAs, care is taken when heating InP substrates *in vacuo*, to prevent the formation of a pitted, In-rich surface [69].

Once the outgas pressure is $\leq 10^{-9}$ Torr, a substrate is ready for growth. As the substrate is heated under arsenic, the amorphous native oxide is desorbed from the surface of GaAs at $\sim 580^\circ\text{C}$, and from InP at $\sim 470^\circ\text{C}$ [70, 71]. Heating of an InP substrate results in not only As \rightarrow P substitution but also diffusion of As atoms into the subsurface regions of the InP. An $\text{InAs}_x\text{P}_{1-x}$ sublayer is thus formed at the InAs/InP system interface [72]. After a final 20 minute degas $\sim 50^\circ\text{C}$ hotter than the growth temperature, a substrate is ready for epitaxy.

Material Purity

The purity of epitaxial source material is critical. Manufacturers typically specify the elements for III-V MBE as being 99.99999% pure. However, this so-called ‘7N’ purity still corresponds to a background impurity level of 10^{15}cm^{-3} . It is important therefore that all impurity species have either a much higher or lower vapour pressure than the charge material. They will then be either rapidly outgassed or experience negligible evaporation at growth temperatures.

The effusion cells consist essentially of a crucible containing the source material, which is surrounded by heating elements. Crucibles are composed of a refractory material, such as the ceramic pyrolytic boron nitride (PBN). Cell temperatures are typically $700 - 1100^\circ\text{C}$. Rather than being water-cooled, the LN_2 cryoshroud is used to minimise outgassing of the stainless steel at these temperatures. Before filling, new crucibles and cells undergo a rigorous outgassing procedure in a separate UHV chamber to protect the MBE machine from contamination.

Chamber Maintenance and Cleaning

On the infrequent occasions that the MBE system is opened, it is brought up to atmospheric pressure using dry N_2 . Similarly to the situation during substrate loading (see page 44), a positive pressure of N_2 is maintained inside the chamber to limit contamination. Maintenance is carried out using dedicated, ultra-clean tools and care is taken to ensure that at no point do any contaminated objects touch the inside of the chamber. The arsenic cell is filled last due to the propensity of arsenic to oxidise to AsO . After roughing with a turbo pump, ion and cryopumps are used to reduce the pressure to high vacuum, whereupon a thorough leak check is performed. Seals are exposed to a local helium environment and the RGA monitors for any increase in the He peak.

Despite the above precautions, various contaminants will have entered the chamber and these must be removed. Two major species present will be water and native oxides, the main concern being the reaction of O_2 with As deposits on the chamber walls. Since AsO dissociates above $\simeq 180^\circ\text{C}$ the temperature of the chamber is raised to 200°C by surrounding the entire machine with heated metal covers and baking it. After several days

of baking, the H₂O and AsO will have been pumped from the chamber and the ambient pressure of the chamber will be $\leq 10^{-10}$ Torr.

The cryopanels are cooled to -150°C and the effusion cells heated to idling temperatures. The substrate manipulator and effusion cells to be used are outgassed at temperatures in excess of their normal operating temperatures for a short time. The As cell is not however outgassed in this way, since this would result in extremely rapid depletion of the cell contents. The As cell is unique in that it has a needle-valve on the output. When closed, this seals the cell off from the chamber. In lieu of a sustained high temperature degas, rapid opening and closing of the As needle-valve, in combination with heating cycles, is used to drive off any volatile contaminants. Following outgassing, each cell is maintained at some idling temperature. This material-dependent temperature is chosen to be low enough for minimal flux generation, but sufficiently high to prevent recontamination.

The first samples grown will be layers of bulk *n*-doped GaAs on SI (001) GaAs substrates. In addition to calibrating the Si cell, the thick layers of material deposited on the cold cryopanels and walls of the chamber help bury impurities. Once the Ga, As and Si cells are clean, the Al is melted. Growth with Al assists with the chamber clean-up process since it acts as a useful ‘getter’, reacting with other species and eliminating them as potential contamination sources. A series of high-energy electron transistors (HEMTs) will be grown. These devices are discussed in detail in chapter 4. HEMT electron mobility increases with time as free impurity species are removed from the chamber. Finally, the indium is outgassed in preparation for growth of the InGaAs/InAlAs-based structures covered in the subsequent chapters of this dissertation.

3.2.2 The Mechanism of MBE Growth

Inside the growth chamber the substrate is mounted onto the manipulator which is used to position the block in front of the effusion cells. During growth, heaters on the manipulator control the substrate temperature via radiative coupling. The block is otherwise thermally isolated. The sapphire disc behind the substrate increases heating efficiency by aiding the coupling of heater radiation into the substrate, particularly at low temperatures. In addition, the diffusive nature of the disc improves heating uniformity.

Substrate temperature is measured both by a thermocouple on the manipulator and with an Ircon Modline V optical pyrometer, mounted at normal incidence to the substrate. The hot substrate emits thermal radiation, the spectrum of which is temperature dependent. This radiation enters the pyrometer through a UHV viewport which is heated to prevent As coating. The pyrometer is tuned to measure the spectral intensity of the wavelength region from $0.91 - 0.97\mu\text{m}$, since for temperatures $> 400^{\circ}\text{C}$, the substrate is opaque at these wavelengths. Assuming that the emissivity of the system is known, the temperature of the substrate surface can be calculated from these intensities. A detailed

description of optical pyrometry can be found elsewhere [73]. A third technique for temperature measurement was also used during some sample growths. The BandiT system, manufactured by KSA, uses a white light source and spectrometer to probe the substrate band-edge. Comparison with the calibration curve for a standard substrate of identical type, enables calculation of the absolute temperature [74].

As molecular beams from the cells impinge on the heated substrate, they react with the heated surface. Atoms may become adsorbed, at which point they are free to migrate across the surface until a suitable bonding site in the growing lattice is found. (001) substrates and epilayers typically exhibit a terraced morphology [Fig. 3.2]. Monolayer-thick planes are preferentially elongated in the $[\bar{1}10]$ crystal axis direction, with steps formed between neighbouring terraces. These step-edges have a locally high density of dangling bonds and hence growth nucleation at these sites is highly favourable. Various compet-

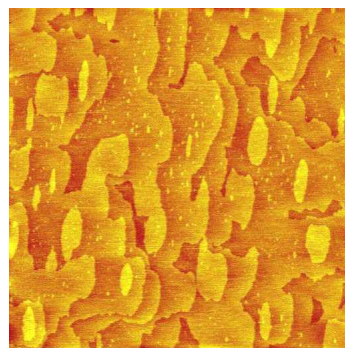


Figure 3.2: Atomic Force Microscopy (AFM) $2.5 \times 2.5 \mu\text{m}^2$ image of terraces on an InGaAs epilayer, showing anisotropic extension in the $[\bar{1}10]$ direction (vertical on image).

ing kinetic and thermodynamic processes dictate rates of adsorption, desorption, surface migration and reaction rate. However, given suitable growth conditions, the result is the formation of a crystalline lattice. There are three main modes of growth which have been formalised [Fig. 3.3] [75]. Energy for adatom surface migration is mainly length-determined by the substrate temperature [76]. Given sufficient thermal energy, and assuming the surface is suitably flat so as not to reduce its mean free path, the adatom will migrate to the highly reactive step-edges and become incorporated into the growing lattice. In this way, growth proceeds in a two-dimensional (2D) fashion, by the extension and coalescence of terraces and this is hence known as the step-flow, or Frank-van der Merwe (FM) mode [77]. The second growth process is the Stranski-Krastanov (SK), or step-flow and islanding mode [78]. Initially growth proceeds as for the step-flow mode, with the formation of a 2D epilayer. However, strain builds up due to a mismatch between the epilayer and substrate lattice constants. Following the deposition of a critical thickness of material, a 2D to 3D transition occurs, and growth subsequently proceeds via the formation of 3D islands. The third growth mode is the islanding, or Volmer-Weber (VM) growth mode

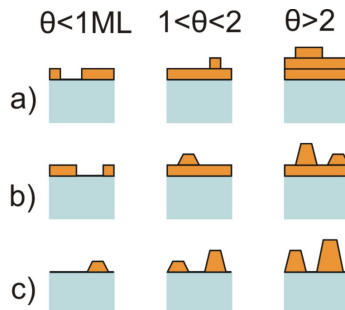


Figure 3.3: Schematic diagram of the modes of crystal growth (where θ indicates deposition thickness in monolayers (ML)): a) Step-flow, or FM mode; b) Step-flow and islanding, or SK mode; c) Islanding, or VM mode.

[79]. A colder substrate suppresses adatom migration. Where material of sufficiently high lattice mismatch is deposited, 3D islands are formed wherever the atoms are incident on the substrate surface.

Unless otherwise stated, in this work all growth took place under an overpressure of As_4 . Arsenic atoms join the lattice through surface reactions between two chemisorbed As_4 molecules [80]. Four As atoms join the crystal lattice and an As_4 molecule is lost from the surface [Fig. 3.4]. As described on page 46, the arsenic effusion cell has a needle-valve which, for a constant cell temperature, can be used to change the beam flux and hence overpressure. Calculated from beam equivalent pressures (BEPs), a V/III ratio of ~ 30 was required for stable growth of the InAlAs and InGaAs in this dissertation. At typical substrate temperatures of $500 - 600^\circ\text{C}$ for growth, the sticking coefficient of Group III atoms on GaAs is close to unity. Excess Group III species on a GaAs surface will increase the sticking coefficient of As to a maximum of 0.5 [82]. Under these standard conditions, no

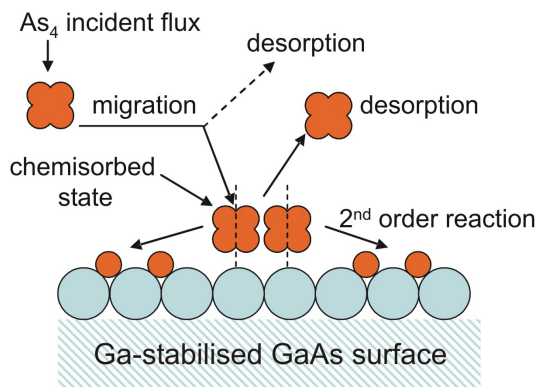


Figure 3.4: Schematic diagram showing surface reactions of As_4 during the growth of GaAs. The As atoms are represented in orange and the Ga atoms in blue (after [81]).

more As will be incorporated into the growing lattice than is required for stoichiometric epitaxy to occur. The growth rate will therefore be dictated by the arrival rate of the Group III species at the surface.

Molecular beam flux and hence growth rate is a function of effusion cell temperature. Material composition in ternary compounds is dictated by the relative growth rates, in ML/s, of the two Group III binaries. For example, consider the deposition of Ga under an arsenic overpressure, with a flux corresponding to a GaAs growth rate of 1ML/s. Indium is deposited simultaneously with a flux equivalent to a growth rate for InAs of 0.5ML/s. The combination of the two beams results in the growth of $\text{In}_{0.33}\text{Ga}_{0.67}\text{As}$ at 1.5ML/s. The geometry of the chamber means that at the substrate plane, beam fluxes are often non-uniform. Homogeneity can be increased via substrate rotation at typically 10-30 rpm during growth. However, a gradient in material composition may still exist between the centre and edge of the wafer. This issue of uniformity is addressed in section 3.5.

Shutters, variously made of Ta and PBN, can be interposed between the cells and the substrate. The beams incident on the substrate can thus be selected. The shutters operate on a time scale of < 0.1s. Since typical growth rates are of the order of 1ML/s, accuracy of deposition thickness can be controlled to within one monolayer and atomically flat heterojunctions can be theoretically achieved [83].

However, there are also kinetic considerations. Sticking coefficients and respective volatilities of the various growth species are highly temperature dependent [84, 85]. There exists therefore a range of growth temperatures within which conditions are favourable for stoichiometric growth. Outside of these limits, conditions become rapidly divergent from equilibrium: the preferential desorption of one component with respect to another may occur, resulting in non-stoichiometric material composition. This is usually, although not always, unwanted.

3.2.3 Doping

The III-V semiconductors discussed here are typically semi-insulating, with high bulk-resistivities. Additional free-carriers can be introduced through the inclusion of dopant atoms in the crystal lattice. The Group IV element Si used in this work has the potential to act as an amphoteric dopant, occupying either lattice site. However, in the InGaAs and InAlAs materials investigated here, Si incorporation at Group III sites is highly favourable. Each Si atom donates an electron and so it acts as a negative ‘*n*-type’ dopant, with very little self-compensation [8].

Amphoteric behaviour becomes more pronounced at high Si doping densities, with Si incorporating increasingly at Group V sites, although at low growth temperatures, doping concentrations $\sim 6 \times 10^{19} \text{ cm}^{-3}$ have been reported [86]. Above this level Si tends to incorporate increasingly on the As sites or to form precipitates which, along with increased

Ga-atom vacancy generation, lead to a decrease in material quality [87]. Typical dopant concentrations are in the range $1 \times 10^{15} - 5 \times 10^{18} \text{ cm}^{-3}$, which require beam fluxes several orders of magnitude lower than for other species. The benefits of Si as a dopant are its generally low diffusivity and surface segregation. This makes it relatively straightforward to selectively dope discrete regions of a device heterostructure. Indeed, Si δ -doping, the doping of a single crystal monolayer, is used routinely which is possible due only to these characteristics.

3.2.4 Strain and Band-Gap Engineering

As mentioned on page 47, differences in lattice constant between a substrate and deposited material will result in strained epitaxial growth. Depending on the relative lattice constants, the epilayer is either stretched or compressed in the plane of the heterojunction and this energy is stored by a distortion of the lattice in the direction of growth. However, once a certain critical thickness is reached, the epilayer will relax in some way and release this energy. This can take the form of a SK (2D to 3D) transition, as discussed, or via the creation of dislocations [88].

Where ternary, or higher-order materials are grown, the lattice parameter, and hence layer strain, is determined by material composition. However, what is of interest in terms of heterostructure design is that the band-gap energy also varies with lattice parameter, and so can be tuned by composition variation [Fig. 3.5].

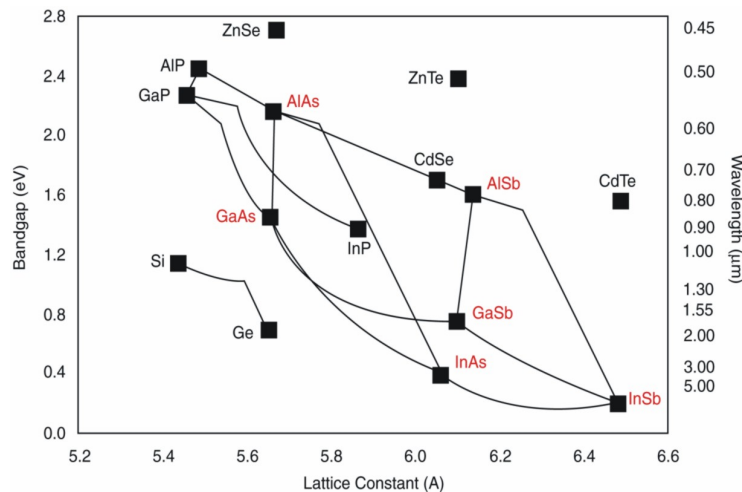


Figure 3.5: Lattice parameter dependence of band-gap energy and emission wavelength for various semiconductor materials. Growth of ternary materials allows the inter-binary regions to be exploited, as suggested by the black lines. The kink in the InAlAs composition curve indicates the transition from a direct to an indirect band-gap. With the exception of the antimonides, all materials in orange can be grown on the Veeco system (reproduced from [89]).

3.3 GaAs and AlAs Growth Rate Calibration

When this research was started, sample growth had just commenced on the newly installed Veeco MBE machine. Chamber cleaning was progressing as a consequence of the deposition of clean epitaxial material onto the chamber walls. The ability to grow epilayers with abrupt heterojunctions, well-defined thicknesses and good material uniformity, is one of the strengths of MBE as a growth technique. To be able to exploit these capabilities, accurate calibration of material growth rate and assessment of epitaxial uniformity for this new system, was essential. The remainder of this chapter discusses these issues, with particular regard to the Al, Ga and In sources.

3.3.1 Beam Flux Measurement

As discussed on page 49, assuming an excess of the Group V component, III-V material growth rate is governed by the arrival rate of the Group III atoms at the substrate surface. Growth rates can hence be assessed simply via measurement of Group III cell beam fluxes. This is achieved with a nude-ionisation flux gauge. Beam species incident on the gauge are ionised and collected. The magnitude of the resulting current gives a measurement of the beam flux, but it should be noted that this value does not take into account the relative gauge sensitivity to different ions [90]. In addition, such measurements cannot be used for the Si cell, since typical beam fluxes are too low. The ionisation gauge is mounted on the opposite side of the manipulator to the substrate, and can be rotated into place to measure beam flux at the substrate growth position.

For a fixed cell temperature, the As₄ BEP is measured for various needle-valve positions, while Group III BEPs are measured as a function of cell temperature. Samples are then grown with various fluxes and assuming the GaAs, AlAs and InAs growth rates are known, a calibration curve can be plotted for each cell. A plethora of methods exist which can be used to ascertain GaAs and AlAs growth rates, including RHEED (see section 3.4.3), ellipsometry and atomic flux absorption measurements [84]. However, the techniques used here were x-ray diffractometry (XRD) and optical pyrometry.

3.3.2 X-Ray Diffractometry

As described in section 2.3.2, XRD can be used to calculate material lattice constants. However, XRD also offers an approach to determine AlAs and GaAs growth rates and this can be achieved via the growth of a single composite heterostructure. Fig. 3.6 shows the 004 reflection XRD spectrum of such a sample and the details of its structure (inset). It contains both an Al_{0.33}Ga_{0.67}As bulk layer and a GaAs/Al_{0.33}Ga_{0.67}As superlattice (SL) with 20 bi-layer repeats. Given the similarity of the GaAs and AlAs lattice parameters (see Fig. 3.5) the structure is fully strained. The well-resolved substrate and bulk AlGaAs

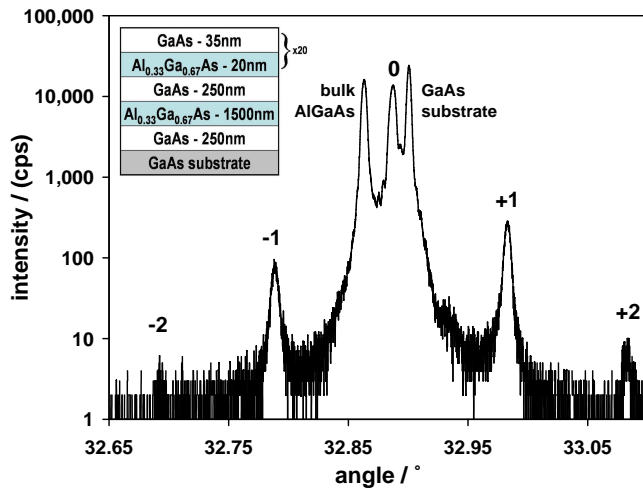


Figure 3.6: XRD spectrum of a sample used for growth rate calibration, containing both a bulk AlGaAs layer and a GaAs/AlGaAs SL. **Inset:** A schematic diagram of the heterostructure.

diffraction peaks are labelled on the spectrum. The splitting angle between these peaks enables the lattice constant and hence the actual Al mole fraction, x , of the $\text{Al}_x\text{Ga}_{1-x}\text{As}$ to be calculated. In Fig. 3.6, this peak-splitting was measured at 136.08 arc seconds, which corresponds to a mole fraction of $x = 0.3316$ from the Gehrsitz relationship, Eqn. (2.2). The zero-order peak, labelled ‘0’ in Fig. 3.6, arises from the superposition of reflections from the AlGaAs and GaAs layers of the SL. The splitting between this and the substrate peak corresponds to the average composition of the two SL layers. In addition, a series of lower-intensity satellite peaks are resolved, labelled ‘±1’ and ‘±2’, which are equally spaced on either side of the zero-order peak. These originate from successive bi-layer periods of the SL acting as macroscopic diffraction planes. The splitting between neighbouring satellite peaks is inversely proportional to the bi-layer period and can be used to calculate this thickness, Λ [91]. For two satellite peaks, with orders i and j , and scattering angles ω_i and ω_j ,

$$\Lambda = \frac{(i - j)\lambda}{2(\sin \omega_i - \sin \omega_j)} \quad (3.1)$$

where λ is the x-ray wavelength. For the data shown in Fig. 3.6, the thickness of a GaAs/AlGaAs period was calculated to be 53.97 nm. The total growth rate can be deduced. Furthermore, since the time taken to grow each layer is known, the following equations can be solved simultaneously.

$$x = \frac{R_{\text{AlAs}}}{R_{\text{GaAs}} + R_{\text{AlAs}}} \quad (3.2)$$

$$\Lambda = \left(R_{\text{GaAs}} t_{\text{GaAs}} + (R_{\text{GaAs}} + R_{\text{AlAs}}) t_{\text{AlGaAs}} \right) \quad (3.3)$$

where R_{III-V} are the growth rates and t_{III-V} are the growth times for each SL layer. The resulting growth rates of AlAs and GaAs for the above sample were calculated to be $0.487 \pm 0.006 \mu\text{m}/\text{hr}$ and $0.982 \pm 0.012 \mu\text{m}/\text{hr}$ respectively.

3.3.3 Optical Pyrometry

One drawback to XRD as a technique for calculating growth rates lies in its *ex-situ* nature. Feedback of any change to the calibration curves is very slow. As described on page 46, optical pyrometry is used to measure substrate temperature. However, it can also be used as an *in-situ* measurement of growth rates. When a heterostructure consisting of materials with different refractive indices is grown, a Fabry-Perot (FP) optical cavity is created between the heterojunction and the surface of the growing epilayer [Fig. 3.7 (left)]. Multiple internal reflections at the pyrometer wavelength, λ_p , are set up and these interfere. Consequently, apparent temperature oscillations will be measured by the pyrometer as the epilayer thickness, or cavity length, increases during growth [Fig. 3.7 (right)]. Maximum intensity occurs for every increase in optical path length of $\lambda/2\eta$,

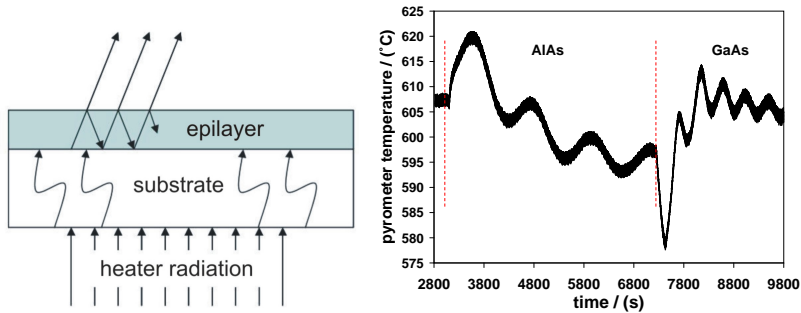


Figure 3.7: **Left:** Schematic diagram showing the origin of interference in optical pyrometry. The FP cavity is formed in the epilayer between the heterojunction and the growth surface. **Right:** Oscillations in the apparent pyrometer temperature during the growth of AlAs and GaAs, with nominal growth rates of $0.50 \mu\text{m}/\text{hr}$ and $1.00 \mu\text{m}/\text{hr}$ respectively.

where η is the refractive index of the cavity material [73]. Assuming η is known at some temperature for a particular epilayer material, the growth rate can be calculated from the oscillation period. The oscillation periods corresponding to $1 \mu\text{m}/\text{hr}$ growth rates were derived experimentally as $452.5 \pm 2.5 \text{ s}$ for GaAs and $564 \pm 11 \text{ s}$ for AlAs in Ref. [92], values which have since been verified in this group. For Fig. 3.7 (right), AlAs and GaAs growth rates of $0.495 \pm 0.005 \mu\text{m}/\text{hr}$ and $1.013 \pm 0.009 \mu\text{m}/\text{hr}$ were calculated respectively.

At the start of a growth run, growth rate calibration curves for the Ga and Al cells are compiled by growing a series of samples at various growth rates and measuring the pyrometer oscillations [Fig. 3.8]. Oscillations are then measured daily for GaAs and AlAs grown on a calibration wafer, to enable immediate feedback. Comparison of these with

the calibration curves means small adjustments to cell temperature can be made prior to sample growth.

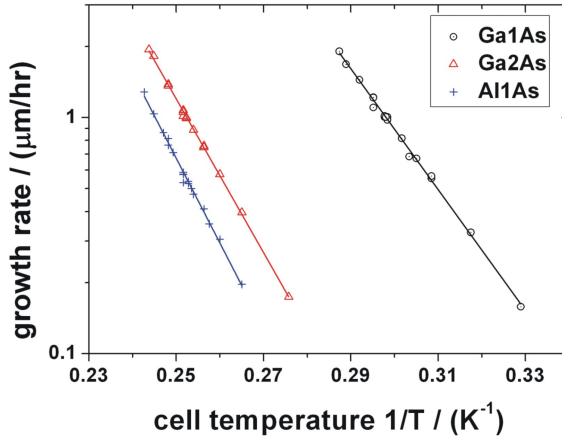


Figure 3.8: Typical growth rate calibration curves for the Ga1, Ga2 and Al1 cells, determined from measurement of pyrometer oscillations.

3.4 InAs Growth Rate Calibration

The growth of high-quality In-containing materials is central to this dissertation. Epitaxy of bulk InGaAs and InAlAs required growth rates close to $0.5\mu m/hr$, whereas the growth of InAs quantum dots, covered in chapter 6, mandated growth rates an order of magnitude lower. As a result, calibration of the InAs growth rates over this wide range was critical. This calibration was complicated by the large strain between InAs and both GaAs and InP substrates. This section discusses the approaches used to circumvent these difficulties and accurately determine the InAs growth rate.

3.4.1 X-Ray Diffractometry

A strain of 7% exists for InAs grown on GaAs [93], with the critical thickness for the 2D to 3D transition shown to be 1.6ML [94]. Provided the In mole fraction (x) is small, thin strained layers of $In_xGa_{1-x}As$ and $In_xAl_{1-x}As$ can be grown on GaAs. However, the materials investigated in this dissertation have compositions where $x \geq 0.52$, with relaxation thicknesses on GaAs of less than 10nm [8]. As discussed on page 3, $In_xGa_{1-x}As$ and $In_xAl_{1-x}As$ with $x \approx 50\%$ can be grown lattice-matched to InP. However, In compositions higher or lower than this will also be highly mismatched to the substrate. An alternative to the growth of superlattices described in section 3.3.2 and Ref. [95] is therefore required.

Relaxed bulk InGaAs and InAlAs samples of various indium composition were grown on GaAs. To confirm complete film relaxation, asymmetric double-axis XRD spectra were

measured, enabling calculation of the in-plane lattice constant components. Assuming that the GaAs and AlAs growth rates are known, a calibration curve for InAs growth rate can be compiled from peak splitting in the single-axis XRD spectra [Fig. 3.9]. Although

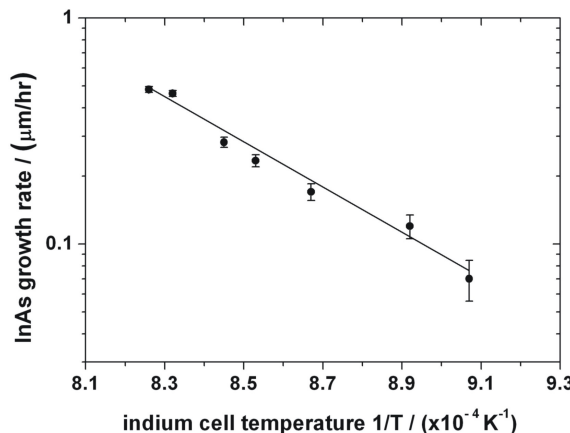


Figure 3.9: Growth rate calibration curve for the In1 cell, determined from XRD measurements of relaxed bulk samples.

suitable for growth rates $\geq 0.1 \mu\text{m}/\text{hr}$, for the very low growth rates used in the growth of InAs quantum dots, the epitaxy of fully relaxed calibration samples becomes unfeasibly long. Moreover, as discussed in section 3.3.3, the *in-situ* measurement of growth rates is usually preferred.

3.4.2 Optical Pyrometry

In-situ growth rate determination by pyrometer oscillations has been demonstrated for $\text{In}_x\text{Ga}_{1-x}\text{As}$ grown on GaAs and for lattice-matched InGaAs and InAlAs on InP [89, 96]. However, this technique is complicated by the nearly identical refractive indices of InAs and GaAs, meaning that the interferometric response is heavily suppressed. In addition, the $\text{In}_x\text{Ga}_{1-x}\text{As}$ band-gap is such that radiation is readily absorbed by the epilayer. This leads to actual sample heating, which is then superimposed on any oscillations, swamping the already small time-dependent response [Fig. 3.10]. Because the band-gap energy is reduced with increasing In content, sample heating was particularly pronounced during growth of the samples for this dissertation, where $x \geq 0.5$. It was almost impossible to measure any useful oscillation period from the pyrometer response. In addition, if the growth conditions were not carefully chosen, a continued temperature rise during prolonged bulk growths led to deterioration in surface morphology. This was manifested as an increasingly noisy signal.

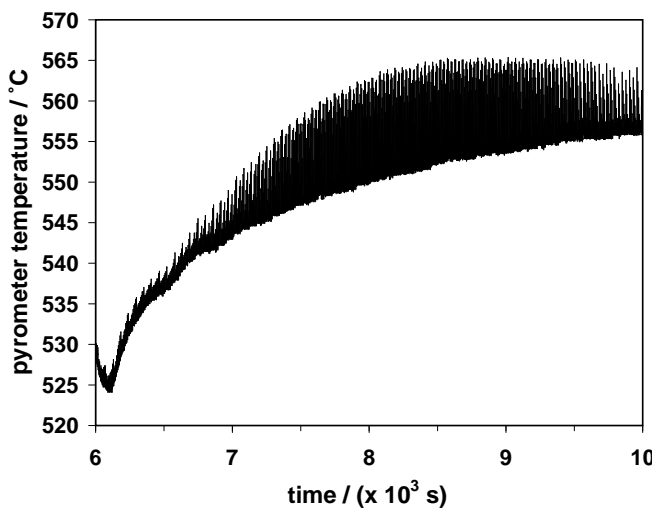


Figure 3.10: Pyrometer response during the growth of $2\mu\text{m}$ $\text{In}_{0.18}\text{Ga}_{0.82}\text{As}$.

3.4.3 Reflectance High-Energy Electron Diffractometry

An alternative *in-situ* method for InAs growth rate measurement was therefore required. Reflectance High-Energy Electron Diffractometry (RHEED) uses a Staib Instrumente electron gun to make real-time measurements of epitaxial growth rate [97]. A filament current of 1.5A, with a beam voltage of 14kV, was used to create a beam of fast electrons. This was made incident on the substrate surface, at some shallow angle, in order to probe the very top layers of the growing crystal. A diffraction pattern was created in the reflected beam which is displayed on a phosphor screen. A diffuse image indicates a non-crystalline structure, such as the amorphous native oxide on a virgin substrate [Fig. 3.11 (left)]. RHEED can be used to monitor the transition from a diffuse to a well-resolved diffraction pattern, which corresponds to the thermal removal of this oxide. Since this desorption occurs at a known temperature, this is a useful calibration of substrate temperature. It has been noted that for an ideal 2D surface, with no divergence in the incident RHEED beam, the Ewald sphere would cut the rods of the reciprocal lattice into infinitely short points [90]. However the series of rods actually observed in the diffraction image for ‘flat’ sample surfaces indicates a deviation from a true-2D morphology, mainly due to terracing [Fig. 3.11 (centre)]. The arrangement of these streaks for various crystal orientations has allowed various surface reconstructions to be deduced [98, 99]. Here, a 2×4 reconstruction can be seen, which is typical for an As-terminated GaAs (0 0 1) surface. Spots in the k -space image in Fig. 3.11 (right) correspond to a three-dimensional (3D) surface morphology in real space.

For the step-flow growth mode, described on page 47, the surface reflectivity varies with step edge density. Reflectivity is maximal for a completed atomic layer, falling to

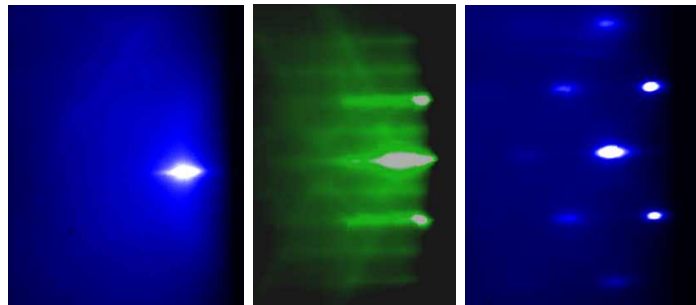


Figure 3.11: **Left:** Diffuse RHEED image from amorphous native oxide on GaAs. **Centre:** RHEED pattern of a GaAs substrate with diffraction rods indicative of a near-2D surface. **Right:** Diffraction spots on a RHEED pattern during the growth of InAs on GaAs.

a minimum when half of the subsequent monolayer has been grown which is when step edge density is highest. As a result, oscillations in the intensity of the RHEED pattern are observed during epitaxy, the period of which corresponds directly to the monolayer growth time Fig. 3.12 [100]. The bright, specular spot of the reflected RHEED beam is clear on all three images in Fig. 3.11. It was the intensity of this spot that was monitored during growth since it was shown to give the largest amplitudes and most reproducible results. A KSA system, consisting of a CCD camera and software, was used to record and analyse the intensity oscillations. Fast Fourier transforms (FFTs) were used to extract the oscillation frequency; a particularly useful tool where the data was noisy or highly damped [101]. Knowledge of the lattice constant for the material then enabled calculation of the growth rate from this frequency.

It was found that the calculated growth rate was highly sensitive to the location of the RHEED beam with a difference in apparent growth rate of $\sim 20\%$ over the field of view

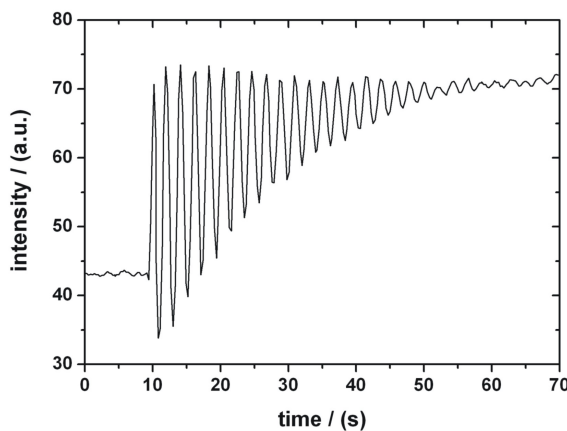


Figure 3.12: Intensity oscillations of the RHEED specular spot recorded during the growth of an AlAs layer at $\sim 0.5\mu\text{m}/\text{hr}$.

of the camera. A central RHEED beam position was therefore defined to ensure accurate and reproducible measurements. In agreement with published results, it was shown that these positional errors were further minimised by using pieces of substrate smaller than 1cm^2 [102].

Two approaches were used to measure InAs growth rate with RHEED. The first, for lower growth rates, involved the epitaxy of $\text{In}_x\text{Al}_{1-x}\text{As}$ and AlAs layers on GaAs substrates. For the second an InAs substrate was used, onto which strain-free InAs could be grown directly.

AlAs/InAlAs RHEED Oscillations

It has been shown that comparison of GaAs and InGaAs RHEED oscillations provides a means of calculating the InAs growth rate [103]. This approach was extended here to determine the InAs growth rate from AlAs and InAlAs RHEED oscillations. The growth rates of AlAs and InAlAs were measured by RHEED. Assuming a constant AlAs growth rate throughout, the InAs growth rate was then given by the difference in oscillation period between the two.

On top of a GaAs buffer, InAlAs growth was initiated and RHEED intensity oscillations measured. Once these had damped away, the In and Al shutters were closed and a growth interrupt under As_4 was started in order to smooth the surface. Next, the Al shutter was opened to start AlAs growth. Resulting RHEED oscillations for InAlAs and AlAs grown at 480°C on GaAs are shown in Fig. 3.13. The In flux in this case was $\sim 5\text{nA}$, with an AlAs growth rate of $0.5\mu\text{m}/\text{hr}$. FFT analysis gave InAlAs and AlAs growth rates of 0.902ML/s

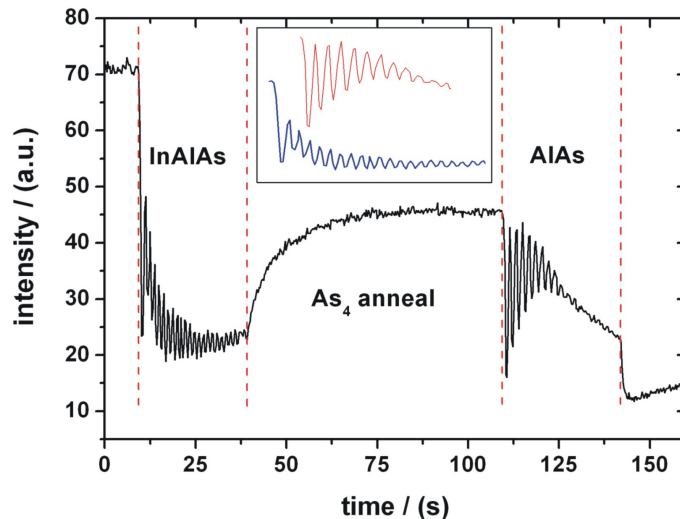


Figure 3.13: RHEED intensity response during the growth of InAlAs and AlAs layers separated by a short anneal under As_4 . The inset shows the magnified InAlAs (blue) and AlAs (red) oscillations.

and 0.566ML/s respectively, which corresponds to an InAs growth rate of 0.336ML/s. Repeating this experiment for different InAs growth rates allows a calibration curve to be built. There are drawbacks to using RHEED; not least is the time taken to initially set up the experiment and obtain a diffraction pattern of suitable quality. However, once in position, Fig. 3.13 shows that these measurements can be carried out in a matter of minutes. This is true even at extremely low InAs growth rates; a clear advantage of using RHEED over the *ex-situ* XRD method of growth rate measurement. The time taken to collect an entire calibration dataset is limited only by the time taken for the In flux to stabilise between changes in cell temperature.

RHEED oscillations are best observed where a surface exhibits good 2D morphology. This meant that, given the inherent strain in this system, only layers with relatively low In-concentration; that is low InAs growth rate; could be examined. For In fluxes higher than 6nA, the InAlAs layer critical thickness was reached after less than 30s with the ensuing 3D growth mode confirmed by the evolution of a spotty diffraction pattern. However, techniques can be used which extend the range of available growth rates while maintaining a flat surface. AlAs buffers can be grown between subsequent InAlAs layers to smooth the morphology. In addition, annealing the surface under As₄ has been shown, both theoretically and experimentally, to help flatten the surface [104, 105]. Evidence of this can be seen in Fig. 3.13: the recovery of the beam intensity during the growth interrupt shows a reduction in step edge density due to surface migration.

InAs/InAs RHEED Oscillations

InAs at any growth rate can clearly be deposited strain-free on InAs substrates, although these are significantly more expensive than GaAs. A 1cm² piece of InAs substrate was indium-mounted on a Mo block, located so as to coincide with the measurement position used in the earlier RHEED work. The RHEED intensity was then measured during InAs growth and oscillations with 20 periods or more were obtained.

RHEED oscillation amplitudes typically damp away with time as local step densities begin to vary randomly [106]. The decay constant of this damping can be minimised through substrate temperature and V/III ratio optimisation [107]. In addition, In desorption is known to increase with substrate temperature so a reduction in the observed InAs growth rate was expected at elevated temperature [108]. A temperature optimisation experiment was performed using RHEED, which showed negligible change in oscillation quality for substrate temperatures between 460 °C and 520 °C. However, it did establish that InAs growth rate was constant to within ±0.025ML/s over this temperature range, indicating negligible In desorption below 520 °C. Above this temperature it was found to be extremely difficult to measure RHEED oscillations. For beam fluxes in the range 240-320nA, both RHEED oscillation quality and calculated growth rate were shown to be

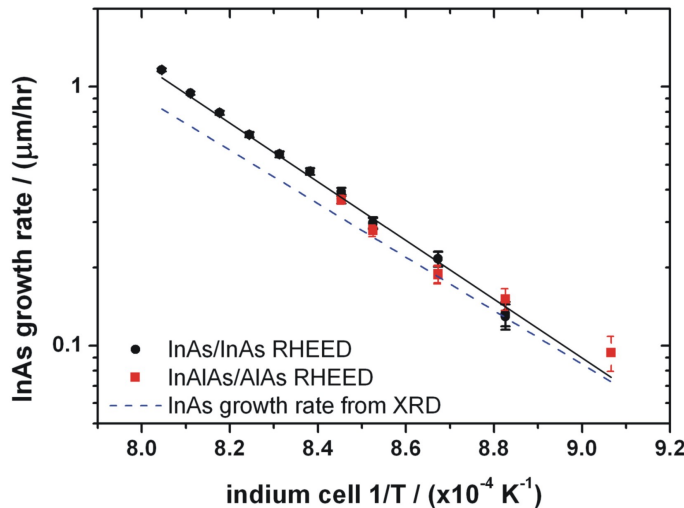


Figure 3.14: InAs growth rate calibration curve from RHEED oscillation data compiled in sections 3.4.3 and 3.4.3. The dashed blue line shows the best-fit to the data in Fig. 3.9.

independent of As_4 overpressure.

A second calibration curve of InAs growth rates was then compiled and combined with the data from section 3.4.3 [Fig. 3.14]. The two methods of determining InAs growth rate from RHEED oscillations agree to within the measurement error. This close correlation validates the approach used in section 3.4.3, at least over the range of cell temperatures investigated. For comparison, the line of best-fit from Fig. 3.9 is included; the InAs growth rate calibration determined using XRD. Although both lines agree to within error at low In cell temperatures, they diverge at elevated growth rate. For a typical InAs growth rate of $0.5 \mu\text{m}/\text{hr}$, the error between the two lines is $\pm 2\%$.

The substrate was rotated during XRD sample growth and not during RHEED. However, rotation was only found to affect growth rate by $\pm 1.4\%$ and so this cannot be solely responsible for the observed discrepancy. An alternative explanation for the divergence is given by so-called ‘shutter-transients’. A closed shutter in front of a cell acts as a heat baffle, establishing a temperature/phase equilibrium. When the shutter is opened suddenly at the start of growth, this equilibrium is disrupted and an artificially high beam flux will be incident on the substrate. A finite time is required for the beam flux to return to its steady state. Depending on the size and type of cell, these temporal flux variations, or shutter-transients, may take several minutes to fully decay.

The time taken to grow bulk samples for XRD analysis means that the contribution from shutter transients to the overall error in calculated growth rate will be negligible. However, since RHEED oscillations are measured directly after a cell shutter is opened, transients will have a significantly more pronounced effect. Overestimates in the calculated growth rate of $\pm 3\%$ have been previously demonstrated [102], confirming that

shutter transients are likely to be a major factor in the divergence between the curves in Fig. 3.14. Where extremely accurate control of growth rate is required, it may be necessary to characterise these transients. To this end, the use of Group V-initiated RHEED oscillations has shown to enable growth rate correction [109]. Alternatively, the use of PBN shutters directly reduces the magnitude of the transients, since PBN is transparent at the wavelengths of the heat radiation from the cells.

It is worthwhile making the observation here that, during the course of this work, indium-based growth was shown to have negligible effect on the quality of GaAs/AlGaAs material grown in the same chamber. Separated by two months of purely In-based work, identical GaAs/AlGaAs HEMTs were grown with mobilities of $1.7 \times 10^6 \text{ cm}^2/\text{Vs}$ and $3.2 \times 10^6 \text{ cm}^2/\text{Vs}$. This lack of an indium memory-effect meant that the chamber could be switched rapidly between growth of different material systems.

3.5 Growth Uniformity

The previous sections describe how reliable GaAs, AlAs and InAs growth rate calibration curves can be constructed. However, as mentioned on page 49, beam fluxes at the substrate plane are not always uniform. There may also be variations in temperature across a substrate due to differential radiative coupling from the Ohmic heaters, or locally cool spots close to the block support pins. These combined effects result in growth rate and dopant incorporation gradients across a sample. This means that devices made from different areas of wafer may behave differently. The assessment and quantification of such non-uniformities for the new Veeco MBE chamber is discussed in this section.

3.5.1 AlAs and GaAs Growth Rate Uniformity

One Al cell and two Ga cells, were used for the majority of GaAs and AlAs growth covered in this dissertation. The Al1 and Ga1 cells are situated in $+30^\circ$ upward-looking ports on the growth chamber. Ga2 is in a shallow downward-looking port at -12° [Fig. 3.15]. All three are specially-designed Veeco SUMO cells. The upward-looking Al and Ga1 cells can be filled to $\sim 270\text{g}$, while the downward-looking geometry of the Ga2 cell limits the capacity to $\sim 50\text{g}$. During commissioning of the MBE chamber, these SUMO cells were relatively new products with very little performance data available. In particular, nothing had been reported concerning the operation of a SUMO cell in a downward-looking port; that is, with the configuration used here for the Ga2 cell. Although a second Al source was fitted, with a capacity of $\sim 8\text{g}$ it is used only as a contingency option.

AlAs and GaAs growth rate uniformities were investigated across 3" (76mm) diameter substrates. Two GaAs/AlGaAs XRD calibration structures were grown as shown in

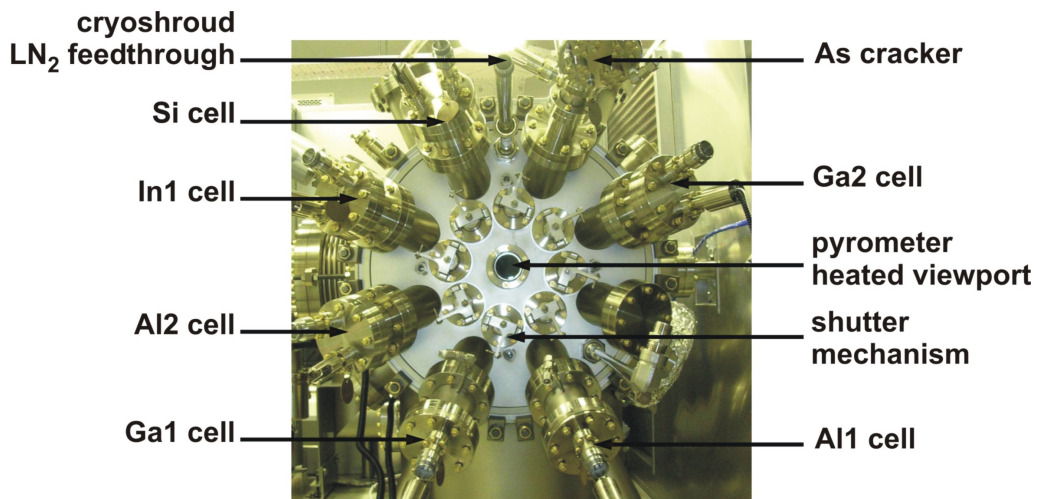


Figure 3.15: View of the Veeco showing the effusion cell locations (photograph taken by Dr. H.E. Beere).

Fig. 3.6 (inset), utilising (Al1, Ga1) and (Al1, Ga2) respectively. Substrate rotation meant that composition varied only radially. XRD spectra were taken at 5mm intervals across the diameter of each sample. Using Eqns. (3.1) to (3.3), the AlAs and GaAs growth rates were calculated and plotted against position [Figs. 3.16 and 3.17]. The growth rate variation of AlAs for the two samples agrees to within a measurement error of $\pm 0.003\mu\text{m}/\text{hr}$. The samples can hence be evaluated with confidence against one another. For all three cells, growth rate is relatively stable in central areas of the substrate. Over the middle

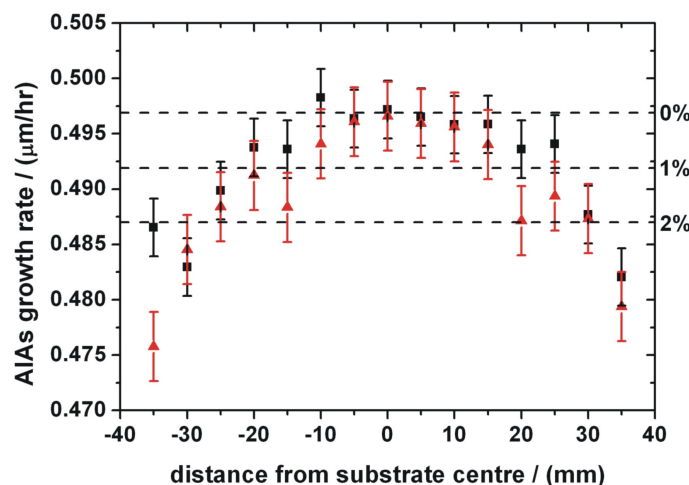


Figure 3.16: Variation in AlAs growth rate with position across a 3" substrate for the (Al1, Ga1 - ■) and (Al1, Ga2 - ▲) SL XRD calibration samples. The dashed lines are provided as a guide to the eye and indicate percentage change in growth rate with respect to the wafer centre.

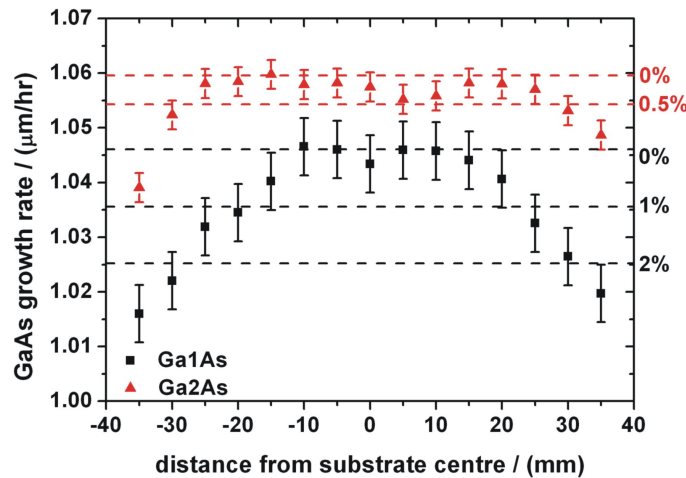


Figure 3.17: Variation in GaAs growth rate with position across a 3" substrate, for both Ga sources. The dashed lines indicate percentage change in growth rate with respect to the wafer centre and are coloured such that they correspond to the data points.

30mm radii of these samples, uniformity to within 2% is exhibited for both the Al1 and Ga1 cells. The Ga2 cell is shown to more uniform still, with a growth rate variation of < 0.5% over this same region. Growth rates fall in the outer 7mm of the wafers, an effect which is particularly pronounced for the two upwardly-mounted sources; Ga1 and Al1.

Temperature variation is expected to be less than $\pm 2\%$ across a 3" substrate, with the hottest regions at the centre of the substrate. Depending on overall temperature and As₄ overpressure a small *increase* in growth rate may result at the cooler wafer edges, where Group III sticking coefficients might be marginally higher. However, cell geometries have been designed in order to limit divergence of the molecular beam, while a second heater zone on the tip of each SUMO also allows beam uniformity to be fine tuned. Effused material is thus concentrated onto the centre of the substrate. Lower fluxes towards the periphery of the beams would therefore appear to be an intuitive conjecture. Although it is impossible to fully deconvolve the contributions to growth rate variation from these two effects, the conclusion is that the dominant factor in the observed rate response is beam flux non-uniformity.

The growth rate spread for each the three cells across the full 3" wafer diameter is summarised in the table below. The variation over the central region corresponding to a 2" substrate is also shown.

Material	Variation over 3"	Variation over 2"
Ga1As	$\pm 1.45\%$	$\pm 0.65\%$
Ga2As	$\pm 0.80\%$	$\pm 0.10\%$
Al1As	$\pm 1.40\%$	$\pm 0.40\%$

These values constitute an upper limit on growth rate spread since material from the very

edge of a wafer is rarely used for device fabrication. Growth rate variation of less than $\pm 1.5\%$ across a 3" wafer indicates good material uniformity from these cells. It is also clear that devices can be fabricated from almost anywhere on a 2" wafer. Interestingly it is the unknown quantity of the downward-looking Ga2 SUMO cell which exhibits the flattest rate response of the three cells. This may be the first published data validating the effectiveness and uniformity of a SUMO cell in a downward-looking port.

3.5.2 $\text{Al}_x\text{Ga}_{1-x}\text{As}$ Composition Uniformity

The variation of $\text{Al}_x\text{Ga}_{1-x}\text{As}$ composition across the two calibration samples was calculated from these growth rates, using Eqn. (3.2) [Fig. 3.18]. This demonstrates that highly

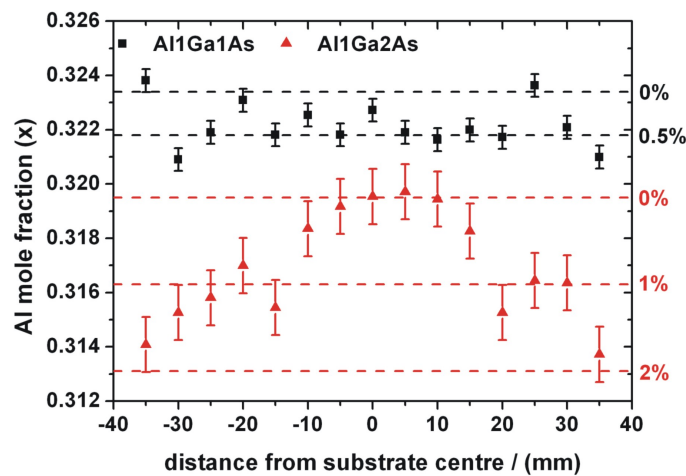


Figure 3.18: Variation in the Al mole fraction, x , in the $\text{Al}_x\text{Ga}_{1-x}\text{As}$ layers of the (Al1, Ga1) and (Al1, Ga2) SL XRD calibration samples. The dashed lines indicate percentage change in x with respect to the wafer centre and are coloured such that they correspond to the data points.

uniform AlGaAs can be grown. Excluding the unused outermost 7mm, the maximum spread in the Al mole fraction for the samples grown with Ga2 is $\pm 1\%$, while for Ga1 the variation is less than half this value. That growth with Ga1 results in a more uniform epilayer seems somewhat counterintuitive, given the larger variation in growth rate seen for this cell in Fig. 3.17 above. However, as Fig. 3.16 shows, the AlAs growth rate is consistent in both samples. The low GaAs growth rate seen at the wafer edges for Ga1 would hence result in a higher Al mole fraction in the AlGaAs. This however is balanced by the corresponding reduction in AlAs growth rate at the edges. The overall result is a reasonably constant value of x across the wafer. Conversely, the Ga2As growth rate is fairly constant and as a result, the AlAs growth rate reduction at the wafer edges dominates the Al composition and is responsible for the larger variation observed. Despite these small variations, it is possible to conclude that overall compositional uniformity on

the new Veeco machine is of sufficient quality to satisfy the vast majority of epitaxial applications.

3.5.3 $\text{In}_x\text{Al}_{1-x}\text{As}$ Composition Uniformity

The In mole fraction uniformity was measured across two, 2" $\text{In}_x\text{Al}_{1-x}\text{As}$ calibration samples using XRD [Fig. 3.19]. These were two nominally identical bulk samples grown to be lattice matched to InP. Although they have slightly different overall composition, both samples show an identical compositional trend between centre and edge. In concentration is higher by $\sim 1.5\%$ at the edges of both samples. AlAs growth rate was previously shown to vary by $\pm 0.4\%$ across a 2" wafer, with growth rate lowest at the edges. From the InGaAs composition, the AlAs and InAs growth rates must be approximately the same, leading to the deduction that the InAs growth rate is uniform to within $\pm 1.0\%$.

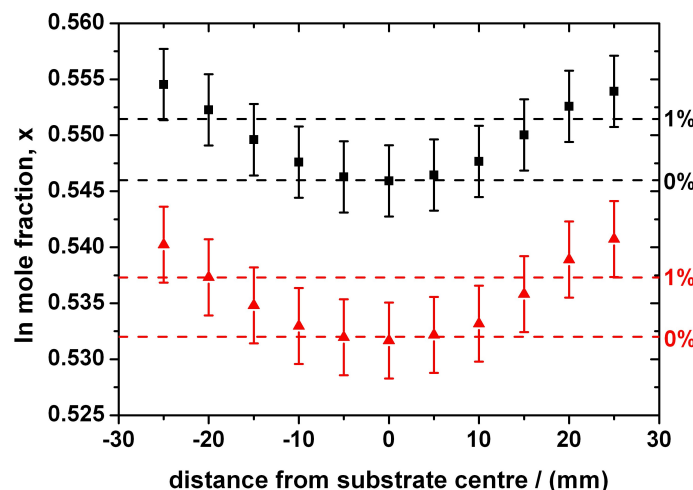


Figure 3.19: Variation in the In mole fraction, x , in two bulk $\text{In}_x\text{Al}_{1-x}\text{As}$ calibration samples.

3.5.4 Si Incorporation Uniformity

The free-electron density in a sample of bulk n -GaAs, nominally Si doped to $2 \times 10^{18} \text{ cm}^{-3}$, has been mapped across a 2" wafer [Fig. 3.20]. Hall bars were fabricated at $\sim 2\text{mm}$ intervals across the sample diameter. Hall transport measurements at room temperature and 77K (see chapter 2) gave the electron density for each device. There is no discernable trend across the wafer, with electron density constant to within $\sim 2\%$, a value close to the measurement error.

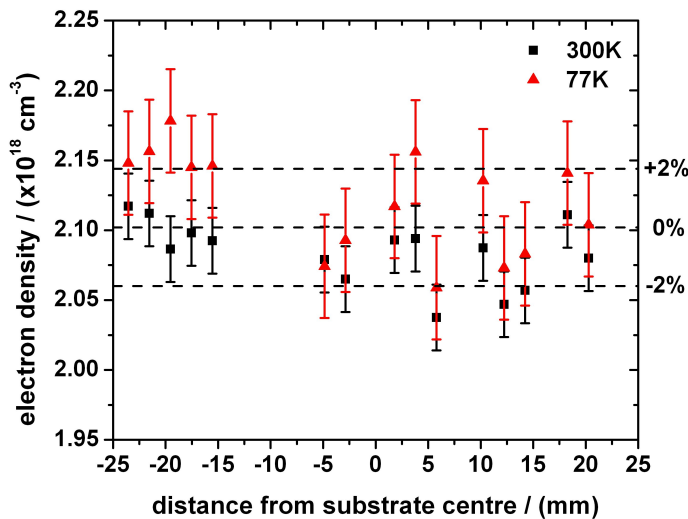


Figure 3.20: Variation of the electron density in n -doped GaAs nominally doped to $2 \times 10^{18} \text{ cm}^{-3}$. Dashed line represents mean overall electron density for both distributions.

3.5.5 HEMT Mobility Uniformity

GaAs/AlGaAs HEMTs (see section 1.5.1) are used as a benchmark device for assessing material quality. Measurements of electron mobility and density in such structures allow the current state of the growth chamber to be quickly checked. Since the uniformity of growth with the Ga, Al and Si cells has formed the major portion of the preceding sections, growth of these HEMT devices was the logical conclusion to this work.

A standard 40nm GaAs/AlGaAs HEMT, with the structure summarised in Fig. 1.6, was grown on a 3" (001) GaAs substrate. Devices were fabricated at intervals along a radius of the wafer, thus allowing the 2DEG electron mobility to be plotted as a function of distance from the substrate centre [Fig. 3.21]. From the measurements made in the dark, mobility appears to be fairly constant across a central region of radius $\sim 30\text{mm}$ but then decreases rapidly towards the edge of the wafer. This trend is exaggerated in the measurements made after device illumination and 25mm from the centre the mobility is reduced by $> 10\%$. This variation arises due to some combination of the non-uniformities in growth rate, temperature, composition and dopant incorporation observed above. The fact that electron mobility is extremely sensitive to slight changes in these parameters explains the relatively large trends observed here. Nevertheless, material with a mobility of $> 2 \times 10^6 \text{ cm}^2/\text{Vs}$ is more than adequate for the majority of uses.

HEMTs grown with the unproven downward-looking Ga2 SUMO cell had mobilities which were generally even higher than those grown with Ga1, with maximum figures of $\mu \sim 5 \times 10^6 \text{ cm}^2/\text{Vs}$ measured at 1.5K. This confirms that, in combination with uniform growth rates and material composition, high-quality epitaxy can be readily achieved on

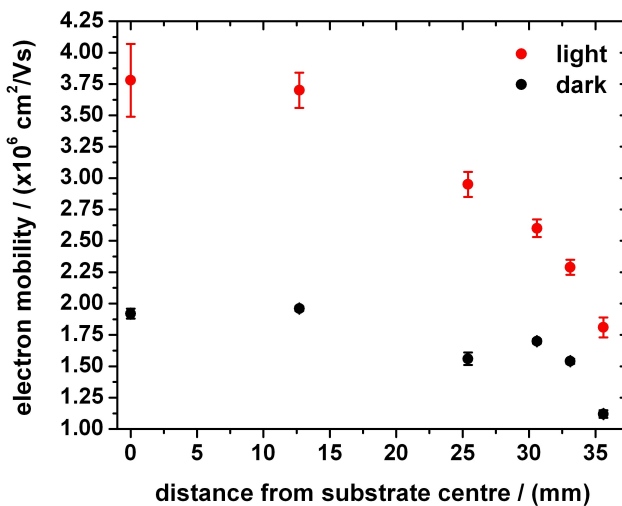


Figure 3.21: Variation of the electron mobility with radius on a 3" 40nm GaAs/AlGaAs HEMT, measured in both dark and light at 1.5K.

the Veeco MBE chamber.

3.5.6 Growth Defects

Although high-quality material can be grown with the downward-looking Ga SUMO, Ga cells are often a source of growth defects. Small gallium droplets formed on the cell lip become dislodged and impact on the wafer surface. This can be minimised by heating the crucible tip which reduces droplet condensation. Nevertheless, a typical defect density for Ga1As was $\sim 500\text{cm}^{-2}\mu\text{m}^{-1}$, whereas for the downward-looking Ga2As this value was $\sim 2000\text{cm}^{-2}\mu\text{m}^{-1}$. The manufacturer quotes defect densities for these cells of $< 500\text{cm}^{-2}\mu\text{m}^{-1}$ and so this topic is still under investigation. However, while the presence of defects is clearly undesirable, devices are usually small enough that, for these quoted densities, the majority of chips are unaffected.

3.6 Summary

This chapter introduced the technique of MBE, describing its suitability for growth of high quality III-V semiconductor material. Some aspects of the commissioning process for a new MBE machine were then described, with particular attention given to the creation of workable growth rate calibration curves and measurement of growth uniformity.

The use of XRD to build these calibration curves was discussed, together with the drawbacks to this *ex-situ* approach. The benefit of measuring GaAs and AlAs growth rates *in-situ* using optical pyrometry was presented. The immediate feedback offered by this technique meant that it was used for daily calibration. Next, calibration of InAs growth

rates by XRD and optical pyrometry were discussed and the advantages using RHEED were presented. Two different approaches to measuring growth rate with RHEED were shown to agree to within measurement error. However, shutter transients were shown to be an important consideration where highly accurate RHEED calibrations were required.

Growth rate uniformity across a 3" wafer was shown to be better than 1.5% for the Al and Ga cells, while variation across a 2" wafer was less than 0.65%. The Al mole fraction in $\text{Al}_x\text{Ga}_{1-x}\text{As}$ varies by a maximum of 0.6% across a 3" substrate. This work reports, perhaps for the first time, good quality growth from a Ga SUMO cell in a downward-looking port; both in terms of material uniformity and HEMT mobility. Performance is shown to be at least as good as for a similar cell in a conventional upward-looking port. InAs growth rate varies by $\sim 1.5\%$ across a 2" wafer, while incorporation of Si was shown to be essentially uniform over this same area. GaAs/AlGaAs HEMT mobility reduces quickly towards the wafer edges. However, assuming a minimum acceptable mobility of $2 \times 10^6 \text{ cm}^2/\text{Vs}$, the entire wafer is essentially of useable quality.

Chapter 4

Two-Dimensional Electron Systems

4.1 Introduction

High electron mobility transistors (HEMTs) were introduced in section 1.5. Through a reduction in scattering, the confinement of electrons within a two dimensional region greatly improves transport properties compared with bulk material. Ever since the earliest GaAs/AlGaAs modulation-doped, two-dimensional, electron gases (2DEGs) were grown towards the end of the 1970s, there has been a relentless drive towards ever higher electron mobility. An increase of approximately three orders of magnitude has taken place over the last thirty years as various improvements have occurred in the design of both MBE chambers and device heterostructures [110]. These advances in material quality have led directly to the discovery of new physics; for example, the fractional quantum Hall effect [26, 111].

As introduced in section 1.1, the ternary compounds $\text{In}_x\text{Ga}_{1-x}\text{As}$ and $\text{In}_x\text{Al}_{1-x}\text{As}$ exhibit various properties of interest such as low band-gap energies [8], high effective g -factors [112], a large spin-orbit coupling constant [113] and a very small Schottky barrier at the metal-semiconductor interface. The magnitude of the effective g -factor in these materials, compared with that of GaAs for example, means that transport is highly asymmetric for electrons with different spin quantum numbers. This is seen directly in the splitting of resistance peaks at low fields in magnetotransport experiments (see section 1.5.4) and in various spin-orbit interactions, such as Rashba coupling [114].

These materials are expected to play an important role in the emerging field of ‘spintronics’, wherein information is carried by electron spin-states. Electrons with different spin states are manipulated by such devices as the spin-filter [115, 116]. Tunability of electron g -factor in a device is an extremely desirable property. One technique which has been demonstrated uses both front and back gates to control the position of the electron

wavefunction in a heterostructure composed from layers of materials with different Landé g -factors [117–120].

The growth of high-quality InGaAs material from which similar devices could be potentially made was the motivation behind the work presented in this chapter. The electron transport properties of various compositions of $\text{In}_x\text{Ga}_{1-x}\text{As}$ (where $x \geq 0.53$) were investigated by incorporating them into HEMT structures. The optimisation of $\text{In}_{0.53}\text{Ga}_{0.47}\text{As}$ quantum well (QW) heterostructures is discussed in section 4.2 and material with very high electron mobility is demonstrated. In section 4.3 a study is made of spin-orbit interaction effects observed in these devices and a novel dependence of Rashba coupling on the carrier density is presented.

The optimisation of undoped $\text{In}_{0.75}\text{Ga}_{0.25}\text{As}$ QW HEMTs is described in section 4.4. Peak mobilities equal to the highest published to-date for these structures were achieved but with a significant reduction in the sheet electron density, n_s . There are significant overlaps between this section and a paper summarising this work which has been submitted for publication [121]. Measurement of the effective g -factor of this material and the dependence of electron transport on InGaAs composition are covered subsequently. Finally, the growth of doped $\text{In}_{0.75}\text{Ga}_{0.25}\text{As}$ QW HEMTS is presented.

4.2 Growth of $\text{In}_{0.53}\text{Ga}_{0.47}\text{As}$ HEMTs

$\text{In}_{0.53}\text{Ga}_{0.47}\text{As}$ and $\text{In}_{0.52}\text{Al}_{0.48}\text{As}$ are lattice matched to InP. During the remainder of section 4.2, these materials are referred to respectively as InGaAs and InAlAs. The value of the bare g -factor of bulk InGaAs has been variously measured to be between -3 and -5, although the effective g -factor obtained inside InGaAs QWs can be significantly higher than this [122–125].

A series of InGaAs/InAlAs HEMTs with the heterostructure shown in Fig. 1.7 were grown on semi-insulating (0 0 1) InP substrates. In order to optimise growth temperature, samples were grown at 410 °C, 440 °C, 460 °C, 470 °C and 480 °C, as measured by optical pyrometry. The V/III beam-equivalent pressure (BEP) was maintained at ~ 30 , with growth rates for both InGaAs and InAlAs of $\sim 1\mu\text{m}/\text{hr}$. No intentional change to growth temperature made during epitaxy.

XRD analysis revealed compositional uniformity to be better than $\pm 0.5\%$ and all layers were thus fully strained. Hall bar devices were fabricated from these samples using the techniques described in section 2.2. Chips were processed in two orthogonal directions for each sample, parallel to both the [1 1 0] and [$\bar{1}$ 1 0] crystal axes. This was in order to quantify any anisotropy in the electronic transport.

4.2.1 Gate Response

Transparent NiCr gates were positioned above the channel so that the sheet electron density (n_s) could be varied both by illumination and gate bias. As described previously, the metal-InGaAs Schottky barrier is very low, at 0.196eV. Initial experiments showed that this was insufficiently high to prevent leakage currents and consequently 200-300nm of polyimide was used to insulate the gate from the channel.

Cooled to 1.5K in a ^4He cryostat, the constant-current, phase-sensitive technique described in section 2.3.4 was used to measure the electron transport properties of these 2DEGs. Firstly, the dependence of n_s on the gate bias (V_g) was assessed [Fig. 4.1]. V_g was varied from channel pinch-off up to the onset of gate leakage. The response shown

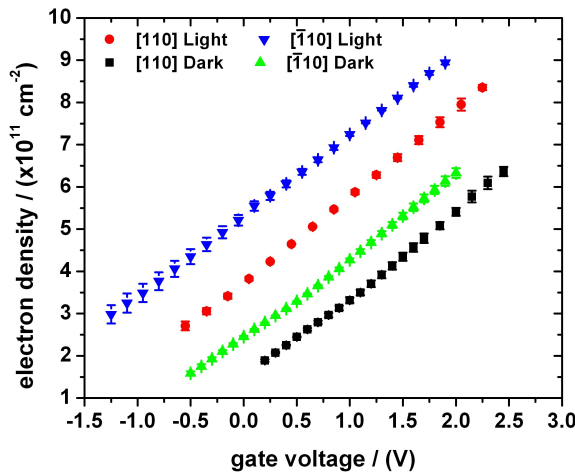


Figure 4.1: Response of the electron density in an InGaAs HEMT, grown at 410 °C, to changing gate bias. Two orthogonal chips from the same sample were measured both in the dark and following illumination.

here was typical of all the devices. A linear dependence with a gradient of ~ 1.9 for all dark and light measurements is found. There is a small vertical offset between the two orthogonal chips which is likely to be due to differences in insulator thickness.

The effects of gate voltage and illumination on the Shubnikov-de Haas (SdH) and Hall resistance measurements (see section 1.5.4) were then determined [Fig. 4.2]. The resistance of the 2DEG at zero field is reduced both by illumination, through persistent photoconductivity (see page 40) and under increasing forward gate bias. The number of filled Landau levels increases, multiplying the number of SdH oscillations measured in the longitudinal resistance. In addition, there is a second frequency component present in the SdH data from the illuminated device at $+3V_g$, which was confirmed by the appearance of a second peak in the fast Fourier transform (FFT) spectrum. There is no evidence of parallel conduction in these devices since the R_{xx} minima go to ~ 0 . As a result, this superimposed second frequency is indicative of the onset of second subband population at $n_s = 3 \times 10^{11}$.

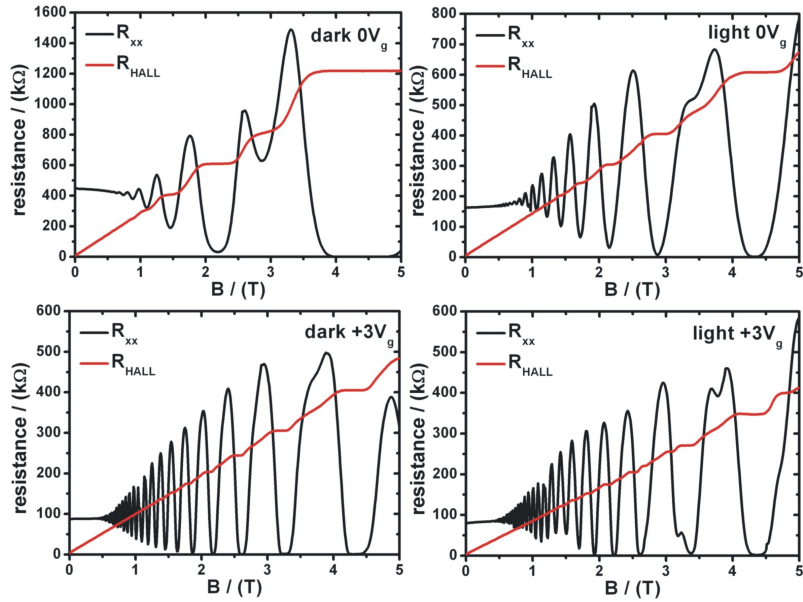


Figure 4.2: Typical response of the SdH and Hall resistances with gate voltage and device illumination in a perpendicular magnetic field. The data shown was measured for an InGaAs HEMT chip grown at 460 °C and fabricated parallel to the [1 1 0] axis.

4.2.2 Growth Temperature Optimisation

Curves of μ against n_s were compiled for each HEMT sample in both dark and light [Fig. 4.3]. Since these curves are plotted on a log.-log. scale, the gradient of the lin-

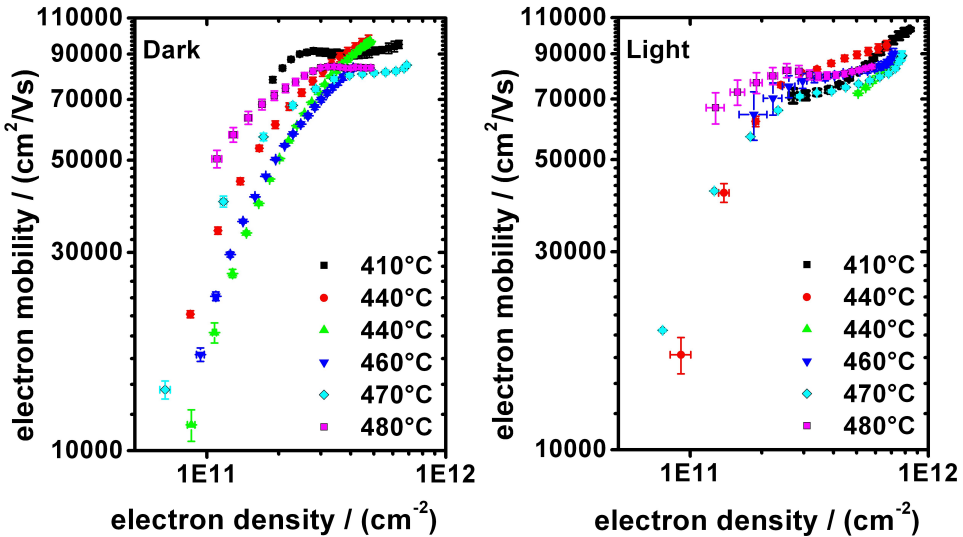


Figure 4.3: Growth temperature dependence of curves of μ against n_s for InGaAs HEMTs, measured in the dark (Left) and light (Right).

ear fit to each gives the exponent of the power-law dependence (see page 40). Samples grown at the two extreme temperatures of 410 °C and 480 °C share relatively low values of $0.55 \leq \alpha \leq 0.58$, which indicates that transport is limited by background impurity scattering [Eqn. (2.3)]. The other samples have values in the range $1.32 \leq \alpha \leq 1.94$, indicating that transport is limited by remote ionised-impurity scattering. After illumination, the curves flatten, with a mean value of $\alpha = 0.37 \pm 0.01$; a situation much like that for the 410 °C and 480 °C samples in the dark.

The relationships between α and scattering mechanism were originally derived for the GaAs/AlGaAs system [65]. They assume single subband occupation and do not take into account alloy-disorder or interface-roughness scattering. As discussed on page 12, alloy-disorder within the $\text{In}_x\text{Ga}_{1-x}\text{As}$ system is expected to be close to maximal where $x \sim 0.50$. Since such large values of α are obtained at low electron density, this is proposed as the limiting scattering mechanism. As n_s is increased, interface-roughness scattering becomes dominant, until ISS emerges as the limiting factor at high- n_s .

To gain a clearer understanding of the effect of growth temperature on transport properties, the peak electron mobilities were plotted against growth temperature [Fig. 4.4]. Although a certain degree of scatter is noted for the dark measurements, after illumination

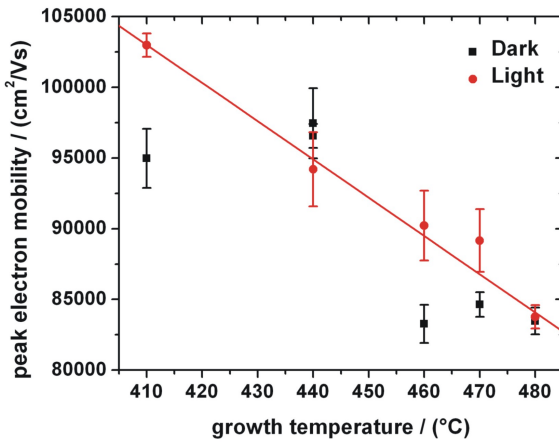


Figure 4.4: Dependence of InGaAs HEMT peak mobility on growth temperature, over the range 410 °C – 480 °C. The line shown is a best fit to the data measured after device illumination.

there is a trend towards higher μ with lower growth temperature. Size of this increase in μ was relatively small however, at $\sim 20\%$ over this 70 °C range. This indicates that growth of good quality material is possible over a wide temperature interval. Peak electron mobility and density values of $1.1 \times 10^5 \text{ cm}^2/\text{Vs}$ at $8.9 \times 10^{11} \text{ cm}^{-2}$ were measured at 1.5K for the sample grown at 410 °C. Given the large contribution from alloy-disorder scattering in these materials, a value of $\mu > 1 \times 10^5 \text{ cm}^2/\text{Vs}$ is extremely respectable, placing it amongst the highest mobilities ever recorded for such InGaAs/InAlAs structures [126].

4.2.3 Electron Transport Anisotropy

Curves of μ against n_s were plotted for each sample, using the orthogonal Hall bars described above [Fig. 4.5]. For all values of n_s investigated, μ is higher parallel to $[1\bar{1}0]$

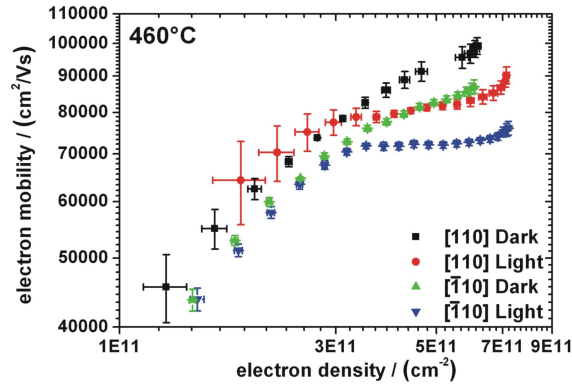


Figure 4.5: μ against n_s curves for two InGaAs HEMT devices fabricated orthogonally to one another from the same sample. Measurements were made both in the dark and following illumination. The sample studied here was grown at 460 °C.

(black and red data) than along $[\bar{1}10]$ (green and blue data). This is representative of all the samples measured. Hence, in common with GaAs/AlGaAs devices, $[110]$ is considered to be the high-mobility axis for InGaAs [64]. All subsequent work was carried out on Hall bars with this orientation.

AFM images reveal a quasi-2D morphology on each sample [Fig. 4.6]. As growth temperature is increased from 410 °C to 480 °C, the surfaces become more ordered, with

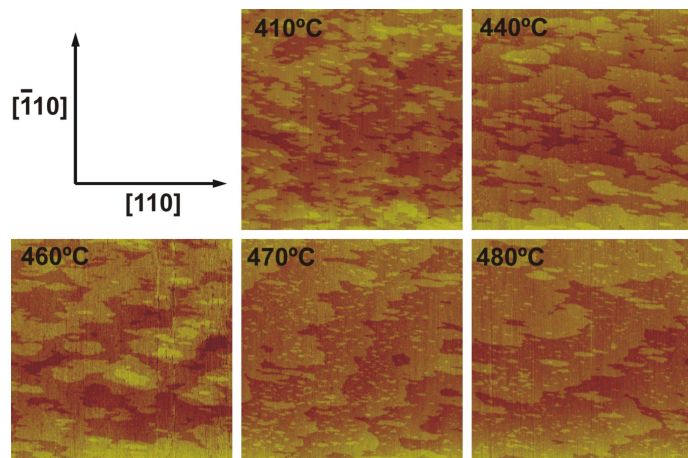


Figure 4.6: $2.5 \times 2.5 \mu\text{m}^2$ AFM images showing the effect of growth temperature on the surface morphology of InGaAs HEMTs. For ease of comparison, the z -axis scale is 3nm on each.

increasingly large terraces. Adatoms now have higher energy to diffuse across the growth surface to find a suitable bonding site. The step-flow growth mode therefore proceeds more uniformly for the hotter samples. In each case, these terraces extend preferentially along the [1 1 0] axis. An electron travelling parallel to [1 1 0] will therefore encounter a higher number of step-edges, each of which is a potential source of interface-roughness scattering. This explains the higher mobility parallel to [1 1 0].

Another noteworthy feature of Fig. 4.5 is the response of the devices to illumination. Although both data sets show good correlation between the dark and light plots at low carrier density, above $\sim 3 \times 10^{11} \text{ cm}^{-2}$ they diverge. Mobility is lowered in the illuminated devices compared with that in the dark. As already confirmed by the data in Figs. 4.1 and 4.2, the number of electrons is increased by LED illumination. In GaAs/AlGaAs devices, such an increase in carrier density typically leads to *higher* electron mobility due to an increase in electron-electron charge screening effects (see page 40).

As mentioned previously, the shape of the illuminated curves above $n_s = 3 \times 10^{11} \text{ cm}^{-2}$ can be explained by an increase in intersubband scattering (ISS). As the second subband population increases, the probability of electron scattering between the two subbands also rises and mobility begins to deteriorate. Eventually, if carrier density continues to increase, electron-electron screening will reduce the effect of ISS and μ once again rises. After illumination, the second subband begins to populate at a lower electron density compared with the dark device. This behaviour has been observed previously for GaAs/AlGaAs HEMTs [64]. Device illumination reduces the depletion field gradient, changing the potential gradient of the band structure. In turn, subband spacing is reduced, which leads to this early population of the second QW energy level.

4.3 Spin-Orbit Coupling in $\text{In}_{0.53}\text{Ga}_{0.47}\text{As}$ HEMTs

Consider a charged particle moving in the presence of a perpendicular electric field (E_\perp). In that particle's rest frame, E_\perp appears like a magnetic field. The spin magnetic moment of the particle then couples to that magnetic field to give a spin-dependent energy. This spin-orbit coupling (SOC) lifts the degeneracy between electron and hole spin states even at zero applied magnetic field. This can occur for sheet electrons in a 2DEG which is in some E_\perp . For the InGaAs 2DEGs discussed here, there are two origins of E_\perp [127].

The first arises from the fact that III-V semiconductors with a zinc-blende structure lack an inversion centre. The resulting field inside the crystal results in spin-splitting. Although the magnitude of this bulk inversion asymmetry (BIA), or *Dresselhaus* term [128], is fixed by the nature of the crystal, it is highly anisotropic. For 2DEGs formed in the plane of (0 0 1) such as those here, the Dresselhaus term is relatively small. Although it has been resolved experimentally [129], the effects of BIA can usually be neglected.

The second origin of E_{\perp} is structural inversion asymmetry (SIA), for example due to an asymmetric device heterostructure [130, 131]. The strength of this SIA, or *Rashba* term [114], is proportional to the electric field gradient at the conduction band. As a result, the magnitude of the resulting Rashba spin-splitting can be altered by tuning the SIA of a quantum well via application of a gate voltage. As a potential route to the realisation of the spin transistor [115], this area has recently been of great interest. The second spin-split subband which is created by the Rashba interaction has been observed as a second frequency in the SdH oscillations [132]. This gives rise to a beating effect at low magnetic field, the strength of which can be altered by gate voltage [Fig. 4.7]. Note that in the

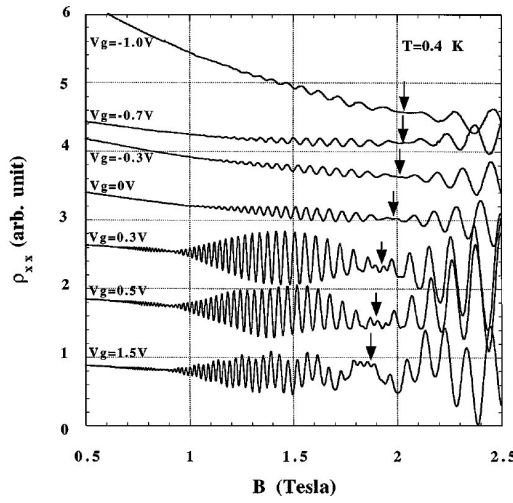


Figure 4.7: Gate voltage dependence of the population of a second spin-split subband, seen as low-field beating in the SdH oscillations for a 2DEG formed in an inverted $\text{In}_{0.53}\text{Ga}_{0.47}\text{As}$ channel (reproduced from [132]).

bottom trace for which $V_g = 1.5V$, a third frequency is apparent on the oscillations. This is characteristic of population of the second spin-degenerate channel subband.

The influence of the electron density on the SOC contribution to electron transport properties was investigated for the $\text{In}_{0.53}\text{Ga}_{0.47}\text{As}$ QW HEMTs described in section 4.2. After cooling the samples to 400mK in a ^3He cryostat, magnetotransport measurements were repeated for two devices; one grown at 410°C and the other at 460°C , as measured by optical pyrometry. The peak μ and n_s of the HEMT grown at 410°C were measured at 400mK to be $1.0 \times 10^5 \text{cm}^2/\text{Vs}$ and $5.6 \times 10^{11} \text{cm}^{-2}$. Similar measurements on the sample grown at 460°C yielded values of $\mu = 9.4 \times 10^4 \text{cm}^2/\text{Vs}$ at $6.6 \times 10^{11} \text{cm}^{-2}$. Broadly speaking, these two devices displayed the same response to the following experiments and so are discussed interchangeably.

Using both infra-red illumination and gate voltage (V_g), n_s could be varied between single and double electron subband occupancy. The overall response was consistent with

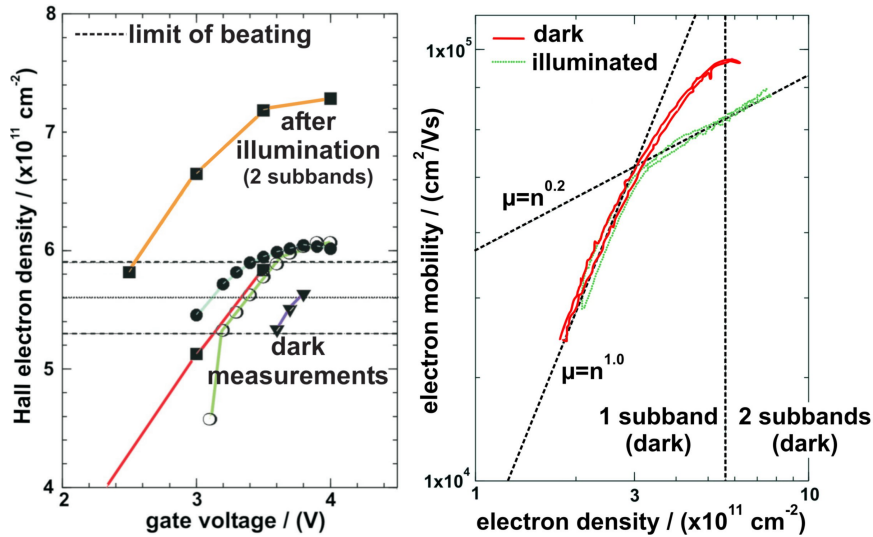


Figure 4.8: **Left:** Dependence of the electron density on gate voltage for the sample grown at 460 °C. **Right:** Curves of μ against n_s measured in both the dark and after illumination. All measurements were made at 400mK.

that in Figs. 4.1 and 4.5. Fig. 4.8 (left) displays results from several electrical measurements made on the same chip. The orange-coloured curve shows a measurement made after device illumination where the second QW subband had become populated. The other four plots were measured after cooling down the sample in the dark. The scatter seen here arises due to a combination of thermal cycling of the device between successive measurements and from hysteresis of the gate, particularly after high biases have been applied.

Fig. 4.8 (right) shows how μ as a function of n_s is affected by device illumination. The onset of second subband population in the dark (red curve) can be seen just below $6 \times 10^{11} \text{ cm}^{-2}$, accompanied by a reduction in mobility due to intersubband scattering. Population of the second subband occurs at $n_s = 3 \times 10^{11} \text{ cm}^{-2}$ after illumination (green curve) due to a reduction of the depletion field gradient, as discussed on page 75. The gradient of the plots, $d\mu/dV$ are indicative of alloy-disorder scattering at low n_s and interface-roughness scattering at high n_s .

SOC effects were observed in the SdH oscillations. Fig. 4.9 is representative of the response measured for these samples. With a clear node close to 0.9T, there is also evidence of a second node at $\sim 0.45\text{T}$. It should be noted that these effects were observed when the device was measured after cooling in the dark, but not seen once the device had been illuminated. This was almost certainly because illumination drastically reduces the size of the built-in electric field [64]. The beating effect indicates two closely spaced oscillation frequencies of similar amplitude. This is confirmed by the FFT of these data which reveals two peaks due to the two electron spin populations. These SdH frequencies

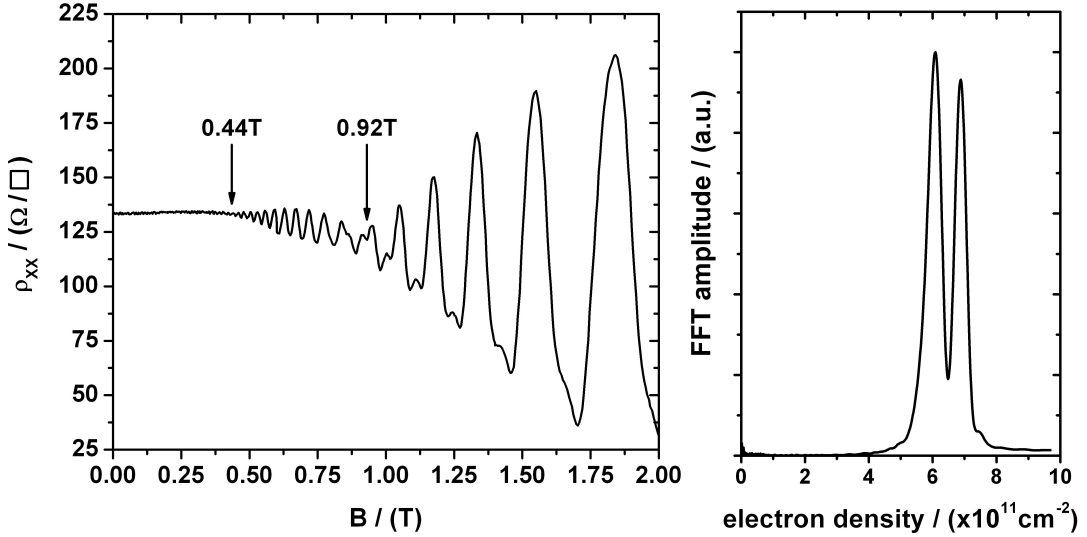


Figure 4.9: **Left:** Typical low-field beating observed in the SdH oscillations of an $\text{In}_{0.53}\text{Ga}_{0.47}\text{As}$ HEMT grown at $460\text{ }^\circ\text{C}$. The arrows mark the position of the first two nodes. **Right:** FFT of longitudinal resistivity data. These measurements were made at 400mK .

(f_{\pm}^{SdH}) are related to the two $B = 0$ spin-subband densities (n_{\pm}) by [133]

$$n_{\pm} = \frac{e}{h} f_{\pm}^{SdH} \quad (4.1)$$

The origin of this beating could not be some parallel conduction effect since $\rho_{xx} \rightarrow 0$ at the Hall plateaux. It was also shown not to be due to magneto-intersubband scattering (MIS). Whereas the magnitude of MIS is known to increase with measurement temperature [134], this beating was seen to disappear above 1.5K . This was not an intersubband scattering effect as the SdH beating was observed in electron density regimes where both one and two subbands were occupied. Finally, it was shown not to arise from sample inhomogeneity. The observed results were reproducible after thermal cycling. In addition, corresponding beating effects were evident in the first differential of the transverse resistivity [Fig. 4.10]. This phenomenon has been shown to be indicative of good sample uniformity [135].

The conclusion was therefore that this was indeed $B = 0$ spin-splitting as a result of Rashba SOC. In both samples it was possible to identify three distinct regions of transport behaviour. For the sample grown at $460\text{ }^\circ\text{C}$ these are indicated by the horizontal dashed lines in Fig. 4.8 (left). Just above device pinch-off ($V_g \sim -1.5\text{V}$), no beating was observed in the SdH oscillations and only one electron population was shown to be present in the FFT data [Fig. 4.11]. This would seem to indicate that the QW structure is inversion symmetric at this perpendicular electric field since the Rashba term appears to be zero. Then, above some threshold value of n_s , $B = 0$ spin-splitting was observed. Beating begins to develop in the SdH oscillations, accompanied by the appearance of a second peak in the

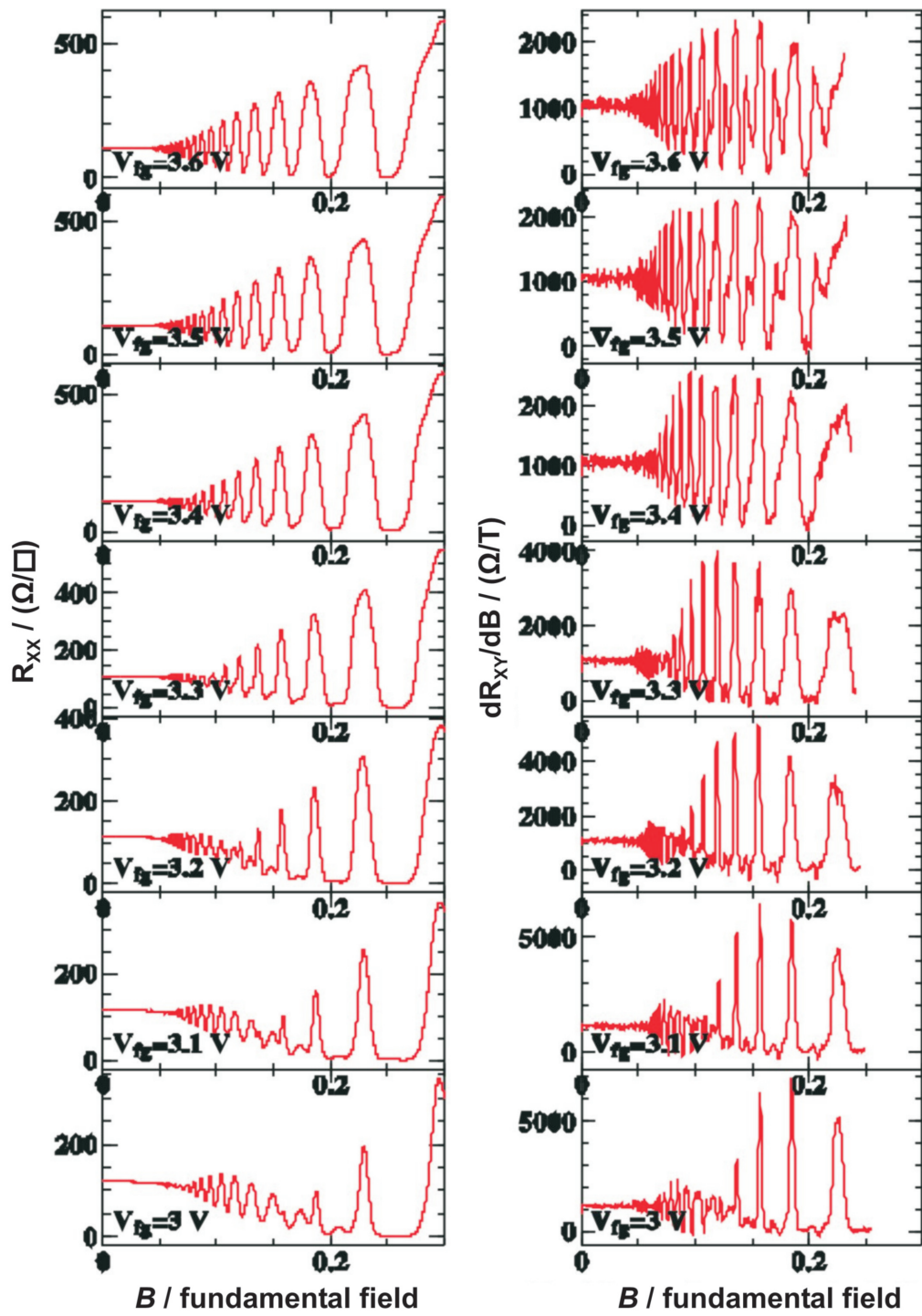


Figure 4.10: Low-field beating observed in both the R_{XX} and dR_{XY}/dB data at 400mK.

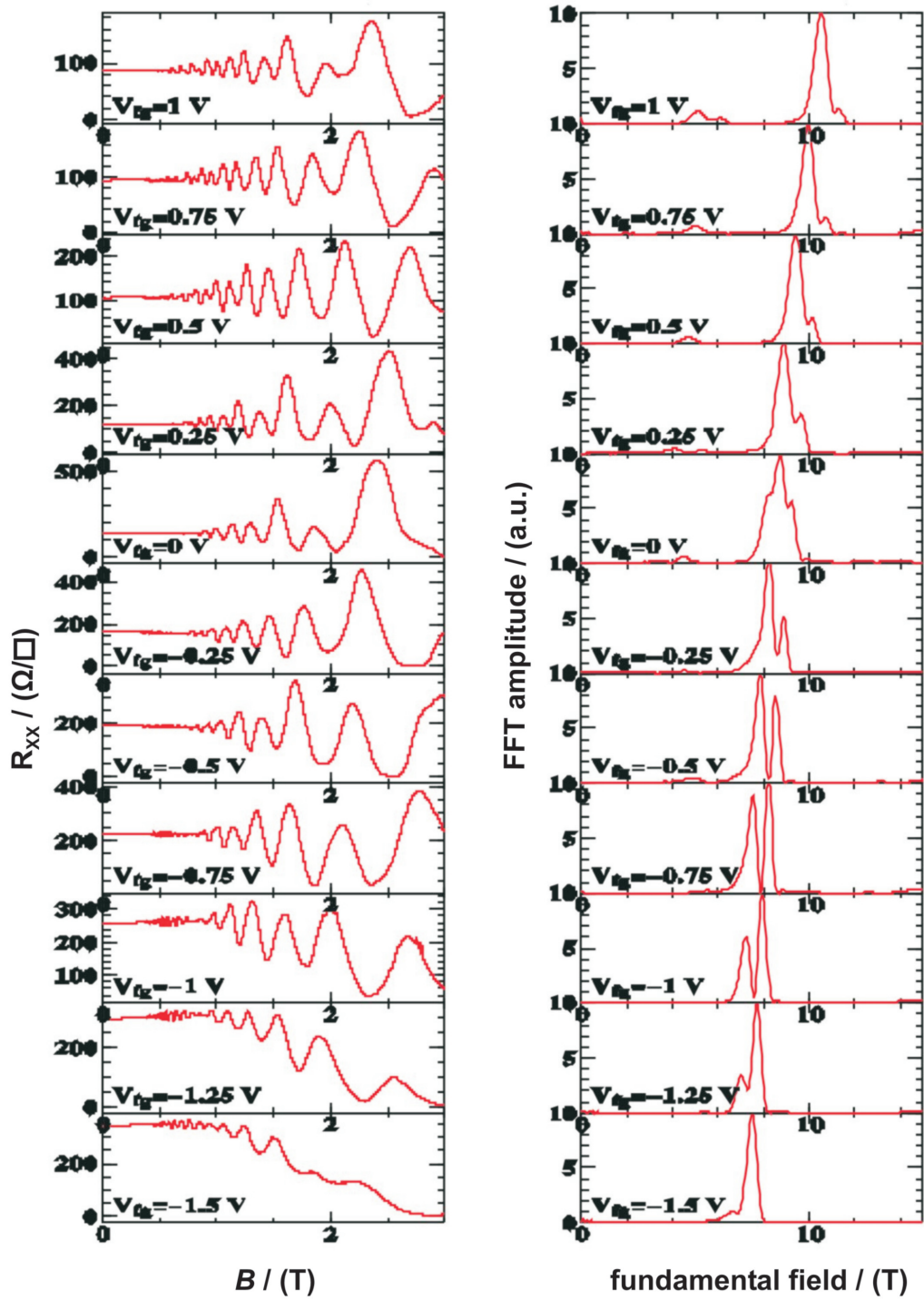


Figure 4.11: The evolution of the $B = 0$ spin-split subbands as a function of increasing gate voltage, shown both as changes to the SdH beating effect and the FFT spectrum. These were measured at 400mK for the HEMT grown at 410 °C.

FFT spectrum at slightly lower electron density. The two spin populations have similar magnitude in the FFT at $\sim -0.75V_g$. After this point the spin population with slightly higher density decreases in magnitude until beating is suppressed and finally just one peak remains. This indicates that inversion symmetry has once again been achieved within the QW and spin-degeneracy restored. The range of electron densities for which beating in the SdH oscillations was observed was sample dependent. For the HEMT grown at 460 °C, Rashba SOC was observed for densities $5.3 \times 10^{11}\text{cm}^{-2} < n < 5.9 \times 10^{11}\text{cm}^{-2}$. A much wider range of $4.8 \times 10^{11}\text{cm}^{-2} < n < 1.0 \times 10^{12}\text{cm}^{-2}$ was displayed by the sample grown at 410 °C.

What is interesting is that this appears to be the opposite of the Rashba SOC response that has been observed before [Fig. 4.12]. Published data show that such systems typically display spin-splitting even at very low applied fields. The two peaks in the FFT spectrum then begin to converge as the perpendicular field is increased. At a single point corresponding to one particular gate bias, the system becomes inversion symmetric. A single peak is seen in the FFT and spins are degenerate. Further increases in field result in loss of symmetry and a return to spin-split subbands. The unusual SOC response presented

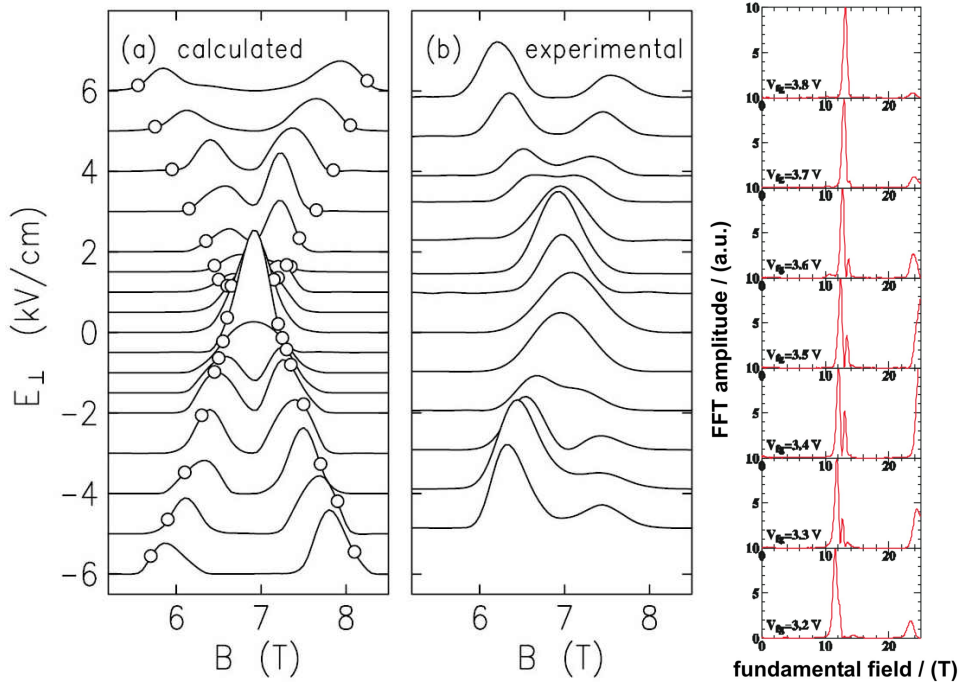


Figure 4.12: The development of $B = 0$ spin-split subbands as a function of increasing perpendicular field, observed in a previous study of a 2D hole system with density $3.3 \times 10^{11}\text{cm}^{-2}$ (reproduced from [136]). The white circles in (a) signify their experimental peak positions (b). For comparison, a set of 400mK measurements from the HEMT grown at 460 °C is shown to the right.

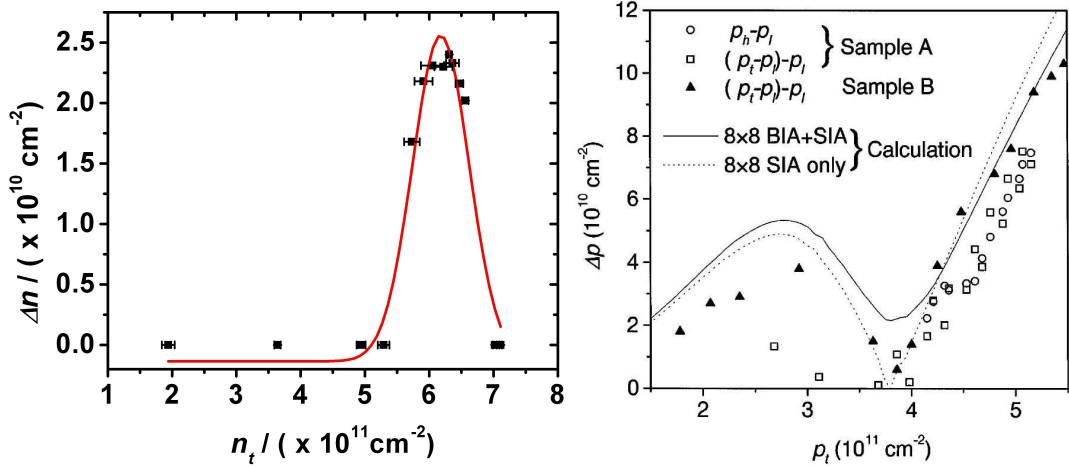


Figure 4.13: **Left:** Variation in the magnitude of $B = 0$ spin-splitting with total electron density for the HEMT grown at 460 °C. The red line shows a Gaussian distribution fitted to the data as a guide to the eye. **Right:** A similar plot from a previous study of a 2D hole system, comparing experimentally observed spin-splitting with that predicted by theory (reproduced from [129]).

here can perhaps be seen more clearly by looking at the magnitude of the spin splitting (Δn) where

$$\Delta n = n_+ - n_- \quad (4.2)$$

Plotting total electron density (n_t) against Δn allows a further comparison with published data [Fig. 4.13]. The response from the 2DEG is again the inverse of that observed previously. Instead of a single point of inversion symmetry surrounded by regions of finite spin-splitting, side-bands where $\Delta n = 0$ surround a central peak where the magnitude of spin-splitting rises to a maximum of $\sim 2.5 \times 10^{10} \text{ cm}^{-2}$. Indeed, according to the theoretical results shown here, Δn should always be greater than zero due to the contribution from the Dresselhaus term.

In addition, returning to Fig. 4.11, it is possible to discern analogous spin-splitting of the second QW electron subband for the HEMT grown at 410 °C. These are manifested as the small double peaks in the FFT spectrum with fundamental fields close to 5T. Repeating the analysis in Fig. 4.13 (left) Δn can be plotted against n_t for both QW subbands [Fig. 4.14]. Although significantly noisier than the data in Fig. 4.13, the overall response in this sample is the same, with $\Delta n = 0$ at high and low n_s . What this also demonstrates however is that the SOC effects observed in the first subband are mirrored by the response of the electrons in the second QW subband. It is possible that the noise on these data is due to some artefact of the spin-split Fermi contours shown in Ref. [133].

The magnitude of the spin-splitting in this system is zero in the absence of applied V_g and finite under some forward bias, instead of vice versa. Unlike the SOC systems

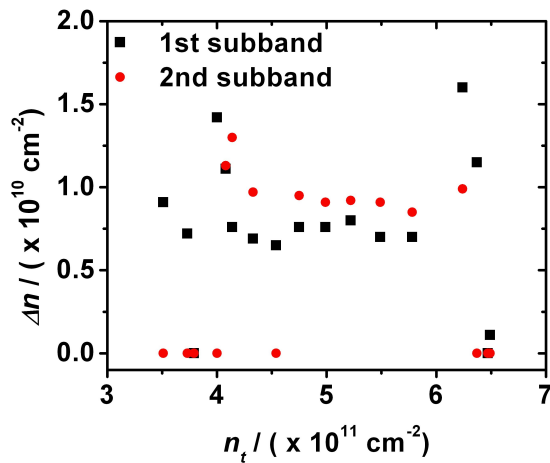


Figure 4.14: Variation in the magnitude of $B = 0$ spin-splitting with total electron density for the HEMT grown at 410°C . Data is shown for the first two QW electron subbands.

studied previously, a precise gate bias is not required to create a symmetric system. This means that a device could potentially be built to exploit this system where spin-degenerate transport occurs unless a gate bias is applied. This increases both the potential stability and speed with which such a device could operate. Although the precise origin of the unusual SOC response presented here is not yet clearly understood, it is hoped that future work will help clarify this point. Detailed theoretical modelling of these $\text{In}_{0.53}\text{Ga}_{0.47}\text{As}$ QW HEMTs will enable the evolution of the perpendicular field with gate voltage to be studied. This may suggest an explanation for the appearance of two regimes where inversion symmetry can be found.

4.4 Optimisation of $\text{In}_{0.75}\text{Ga}_{0.25}\text{As}$ HEMTs

In section 1.5.3 it was discussed that low-temperature electron mobility in a 2DEG with single subband occupation is limited by scattering from alloy-disorder, interface-roughness, remote ionised-dopants and background impurities. By careful heterostructure design, some scattering contributions can be reduced, or even removed entirely, leading to an increase in μ .

4.4.1 Electron Mobility Enhancement

As shown in section 4.2.2, at low n_s , mobility in $\text{In}_{0.53}\text{Ga}_{0.47}\text{As}$ HEMTs is limited by alloy disorder scattering. This mechanism is reduced as indium composition is increased from $x=0.53$. Hence, μ also increases, reaching a maximum where $x=0.75$ [30].

The lattice mismatch that exists between InAs and InP means that $\text{In}_{0.75}\text{Ga}_{0.25}\text{As}$ is highly strained with respect to InP substrates. This limits the thickness of InGaAs that can

be deposited before strain relaxation. Typically this process takes place via the formation of dislocations which act as additional scattering centres and reduce μ . An $\text{In}_y\text{Al}_{1-y}\text{As}$ buffer with graded composition is therefore used to control the strain relaxation. Starting with InAlAs which is lattice-matched to the substrate, the composition is ramped linearly over several hundreds of nanometres until the desired lattice constant is reached. Material grown on top of such a buffer will ideally be almost completely relaxed and have a low dislocation density. Surfaces will be flatter and interface-roughness scattering reduced.

Values of $\mu = 400,000 \text{ cm}^2/\text{Vs}$ at $n_s=6.3\times10^{11}\text{cm}^{-2}$ have been demonstrated for a 2DEG in an $\text{In}_{0.75}\text{Ga}_{0.25}\text{As}$ QW, with the addition of a thin InAs layer to further reduce alloy scattering [137]. A high carrier density enhances electron-electron charge screening, thus reducing remote-ionised-dopant scattering. However, in a completely undoped structure, impurity scattering is limited solely by the concentration of background impurities. Although n_s will be significantly lower, fewer filled Landau levels may permit observation of certain effects at lower magnetic field, provided that μ is unaffected by this change [138, 139]. For the purpose of this work, a figure of merit of $\mu \geq 100,000 \text{ cm}^2/\text{Vs}$ will be used.

A 2DEG in such an undoped structure with $\mu = 215,000\text{cm}^2/\text{Vs}$ at $n_s=2.84\times10^{11}\text{cm}^{-2}$ has been demonstrated [140]. An InAlAs step-graded buffer was used to change the lattice constant from that of a GaAs substrate up to that of $\text{In}_{0.85}\text{Al}_{0.15}\text{As}$. On top of this, an $\text{In}_{0.75}\text{Ga}_{0.25}\text{As}$ QW was grown, surrounded by $\text{In}_{0.75}\text{Al}_{0.25}\text{As}$ barriers. The ‘over-grading’ of the buffer was a deliberate attempt to maximise strain relaxation in the subsequent layers. It was shown that the 2DEG electrons probably originate from a donor state 0.12-0.15eV below the InAlAs barrier conduction-band minimum. An earlier study found similar electron traps $\sim 0.15\text{eV}$ below the band-edge of $\text{In}_{0.52}\text{Ga}_{0.48}\text{As}$, which were attributed, through growth temperature dependence, to defects caused by arsenic interstitials [141]. Such an origin would mean that this trap should appear in InAlAs of all compositions and so these traps would be distributed throughout the whole graded InAlAs buffer. The aim of the work in this section was to reduce still further the electron density limit for which a 2DEG with $\mu \geq 100,000\text{cm}^2/\text{Vs}$ could be formed. A thinner InAlAs buffer might therefore result in a reduction in n_s . InP substrates were used since lattice mismatch to $\text{In}_{0.75}\text{Ga}_{0.25}\text{As}$ is much smaller than for the $\text{In}_{0.75}\text{Ga}_{0.25}\text{As}/\text{GaAs}$ system. This means that for the same composition gradient, a significantly thinner InAlAs buffer on InP would achieve equivalent lattice relaxation.

4.4.2 Sample Growth

A series of samples was grown on semi-insulating (0 0 1) InP substrates with the aim of optimising growth temperature. The V/III BEP ratio was maintained at ~ 30 , with a maximum growth rate of $1.3\mu\text{m}/\text{hr}$ during the active layers. The growth tempera-

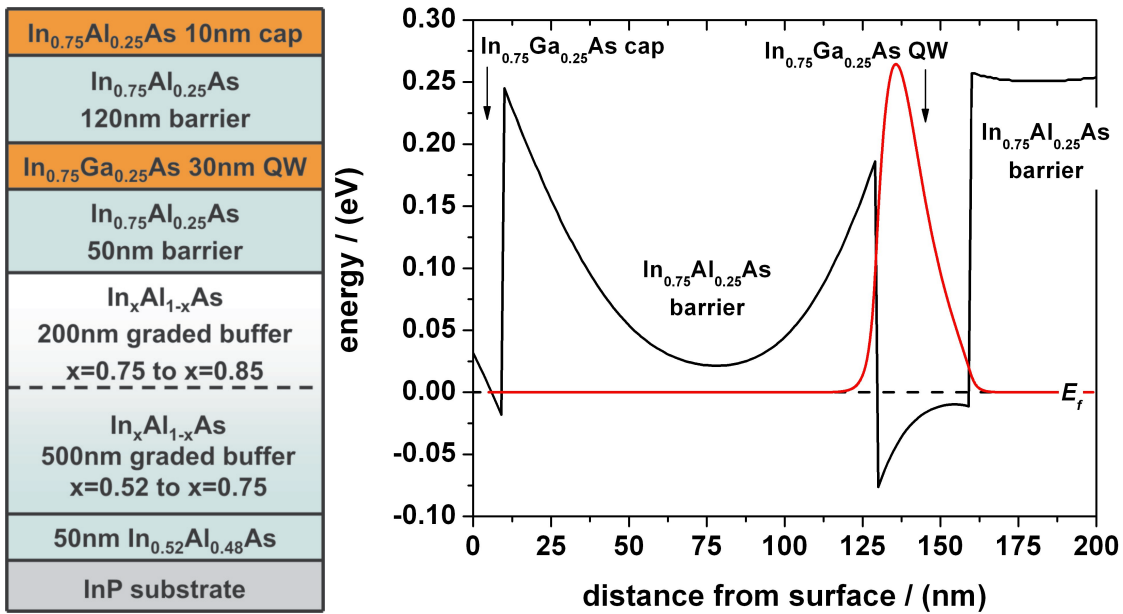


Figure 4.15: **Left:** Schematic diagram showing the heterostructure used for the $\text{In}_{0.75}\text{Ga}_{0.25}\text{As}$ QW HEMTs. **Right:** The conduction band profile calculated for this HEMT. E_f is marked by the dashed black line, while the solid red line indicates the electron wavefunction solution [18].

tures were 470 °C, 440 °C, 410 °C, 380 °C and 350 °C, as measured by optical pyrometry. Again growth temperature was not changed intentionally during epitaxy. The HEMT heterostructure is shown in Fig. 4.15 (Left). 50nm of lattice-matched InAlAs was grown, followed by a two-stage, graded $\text{In}_x\text{Al}_{1-x}\text{As}$ buffer, after Ref. [140]. During the first 500nm, the indium content was ramped from $x=0.52$ to $x=0.75$. Over the next 200nm the composition was graded yet further, up to $x=0.85$. Growth was then interrupted for five minutes under an As_4 overpressure to allow the In cell temperature to stabilise. This had the added effect of allowing surface smoothing to occur, minimising interface-roughness scattering. 50nm of $\text{In}_{0.75}\text{Al}_{0.25}\text{As}$ was then grown, followed by a 30nm $\text{In}_{0.75}\text{Ga}_{0.25}\text{As}$ QW, a 120nm $\text{In}_{0.75}\text{Al}_{0.25}\text{As}$ top barrier and finally a 10nm $\text{In}_{0.75}\text{Ga}_{0.25}\text{As}$ cap. No layers were doped intentionally. The conduction band structure and electron density for these HEMTs was calculated from a self-consistent solution of the Schrödinger and Poisson equations [18] [Fig. 4.15 (Right)]. Devices were built using the standard fabrication techniques described in chapter 2, with an insulated, transparent NiCr gate.

4.4.3 Temperature Dependence of Surface Morphology

The composition of the $\text{In}_x\text{Ga}_{1-x}\text{As}$ QW material was measured as $x = 0.73 \pm 0.01$ using XRD. Active layer relaxation was found to be $\sim 95\%$ from a comparison of symmetric and

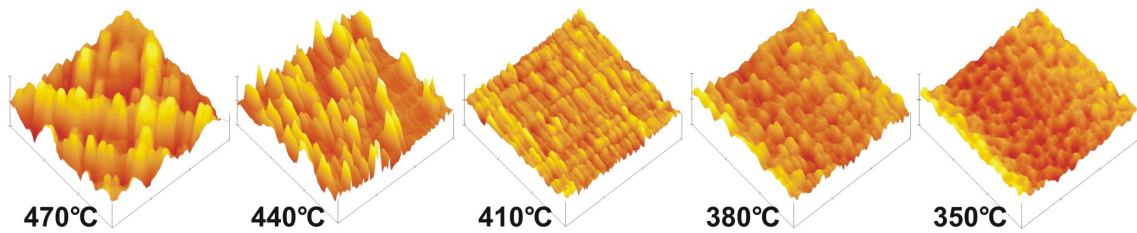


Figure 4.16: $15 \times 15\mu\text{m}^2$ AFM images showing the growth temperature dependence of the surface morphology of In_{0.75}Ga_{0.25}As QW HEMT samples. For ease of comparison, the z -axis scale is 30nm in each case.

asymmetric double-axis XRD spectra. AFM images of the sample surfaces are shown in Fig. 4.16. For growth temperatures $\geq 440^\circ\text{C}$, sample surfaces appear ‘cross-hatched’ to the naked eye. As temperature is reduced, the surface becomes flatter, which is in good agreement with previous work [142]. The root-mean-square (RMS) roughness is reduced from 7.23nm to 3.49nm as the growth temperature is lowered from 470°C to 350°C . A corrugated surface is apparent on the sample grown at 410°C , with striations running parallel to $[\bar{1}10]$. Sections were taken through the AFM data for this sample, parallel to both the $[110]$ and $[\bar{1}10]$ axes and an average feature height of $2.59 \pm 1.60\text{nm}$ was measured [Fig. 4.17]. The periodicity of the features was found to be $0.34 \pm 0.11\mu\text{m}$ in the $[110]$ direction and $1.60 \pm 0.42\mu\text{m}$ parallel to $[\bar{1}10]$. This gives a length-to-width ratio for these corrugations of approximately five.

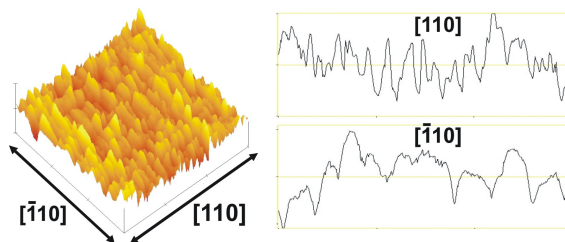


Figure 4.17: Enlarged view of the $15 \times 15\mu\text{m}^2$ AFM image shown in Fig. 4.16 for the In_{0.75}Ga_{0.25}As QW HEMT grown at 410°C . The z -axis scale is 20nm and representative line sections through the image, parallel to the two crystal axes, are shown.

4.4.4 Device Illumination and Gate Response

Brief ($\leq 1\text{s}$) illumination with a red LED was required to achieve stable operation in some devices, particularly those where $n_s \leq 5 \times 10^{10}\text{cm}^{-2}$. However, it was noteworthy that subsequent illumination had negligible effect on n_s . Gate response was modelled by

treating the metal/polyimide/semiconductor as a simple parallel-plate capacitor, with the capacitance C given by

$$C = \frac{dQ}{dV} = \frac{\epsilon_0 \epsilon_r A}{t} \quad (4.3)$$

where A is plate area, t is plate separation and ϵ is dielectric constant. Charge is related to the carrier density by $Q = eAn$ and so

$$\frac{dn}{dV} = \frac{\epsilon_0 \epsilon_r}{et} \quad (4.4)$$

For the *HD Microsystems* polyimide used, $\epsilon_r = 2.9$ at room temperature. So, for a polyimide thickness of $t = 450\text{nm}$, gate response is calculated as $dn/dV = 0.356 \times 10^{11}\text{cm}^{-2}/\text{V}$. This is in good agreement with the experimental value of $dn/dV = 0.385 \times 10^{11}\text{cm}^{-2}/\text{V}$. The small error may be due to a change in ϵ_r at low temperature. *HD Microsystems* were unable to provide this data for their polyimide.

4.4.5 Growth Temperature Dependence of Transport

Longitudinal and transverse resistance measurements were carried out in perpendicular magnetic fields of up to 5T. Mobility was $\mu = 194,000 \text{ cm}^2/\text{Vs}$ for the sample trace in Fig. 4.18, while the electron density was calculated to be $n_s = 1.58 \times 10^{11}\text{cm}^{-2}$ from the gradient of the Hall slope. A single peak in the FFT spectrum corresponds to

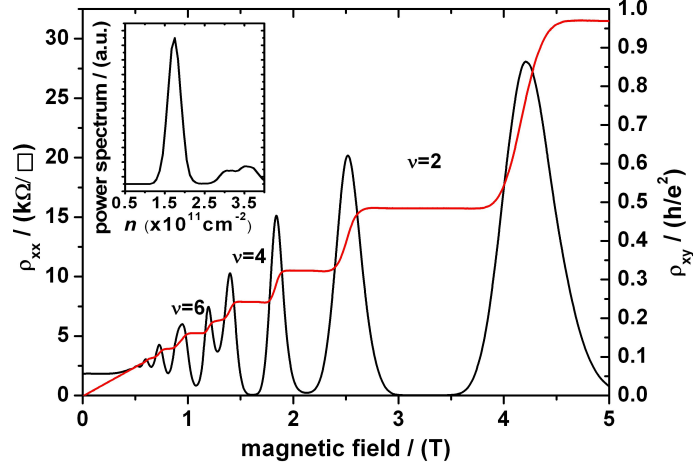


Figure 4.18: Typical Shubnikov de Haas oscillations and quantised Hall plateaux at 1.5K for an $\text{In}_{0.75}\text{Ga}_{0.25}\text{As}$ QW HEMT grown at 410°C in a perpendicular magnetic field. The inset shows the FFT of the ρ_{xx} data.

$n_s = 1.63 \times 10^{11}\text{cm}^{-2}$ which correlates well with the above value. The broadened resistance peak close to 1T suggests the onset of Zeeman spin-splitting, while for the subsequent peak at $\sim 1.25\text{T}$, spin degeneracy has clearly been lifted. Electron transport anisotropy was again investigated and curves of μ against n_s were plotted for orthogonal

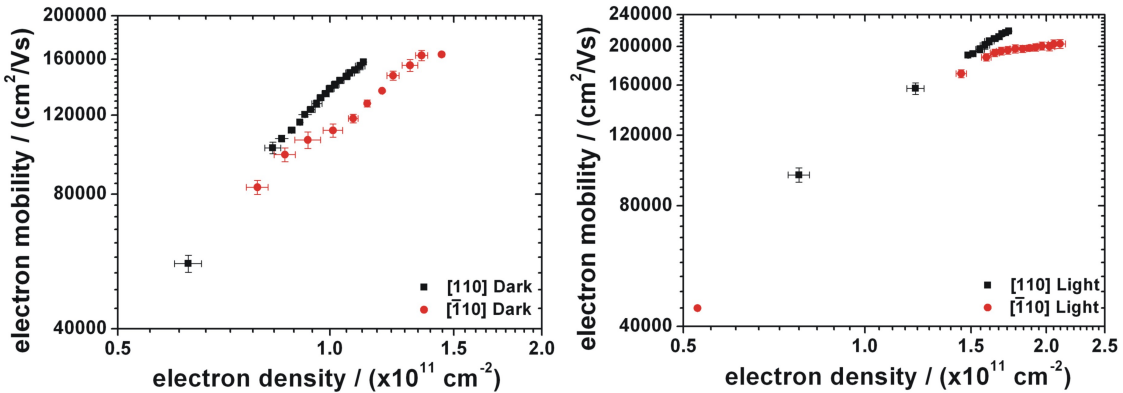


Figure 4.19: Dark (Left) and light (Right) measurements at 1.5K showing the dependence of μ on n_s , in both $[1\bar{1}0]$ and $[\bar{1}10]$ directions, for an $\text{In}_{0.75}\text{Ga}_{0.25}\text{As}$ QW HEMT sample grown at 410°C .

channels [Fig. 4.19]. Electron density is increased following illumination. In both the dark and after illumination, the curves are collinear at low n_s . However, μ saturates more quickly at high- n_s for devices fabricated parallel to $[\bar{1}10]$. Parallel to $[110]$, for similar values of n , μ is $\sim 10\%$ larger. This is in agreement with the findings on page 74 for the $\text{In}_{0.53}\text{Ga}_{0.47}\text{As}$ HEMTs that the high-mobility direction for this material is parallel to $[110]$. This anisotropic behaviour was representative of all samples measured. Again, the reason for this difference appears to be the surface morphology. In Fig. 4.17, the surface features were shown to be five times longer in the $[\bar{1}10]$ direction than parallel to $[110]$. At the highest values of n_s achieved here, the Fermi wavelength (λ_F , see Eqn. (1.25)), is reduced to 60nm. It is proposed that at high- n_s , λ_F is of the same order of magnitude as the larger features along $[\bar{1}10]$. As a result, interface-roughness scattering is greater in this direction compared with the $[110]$ axis. All subsequent work was therefore carried out with electron transport parallel to $[110]$.

Comparison of μ against n_s curves for each sample enabled an investigation of electron transport dependence on growth temperature [Fig. 4.20]. Mobility is observed to saturate at high- n_s in all cases. FFT analysis of the SdH oscillations reveals single subband population in all samples, even at maximum carrier density. Unlike the situation for the $\text{In}_{0.53}\text{Ga}_{0.47}\text{As}$ HEMTs, ISS cannot therefore be responsible for the observed saturation in μ . The gradient of the curves from the two median samples grown at 410°C give $\alpha = 0.48$. This indicates that transport is limited by background impurity (BI) scattering. This is in good agreement with previous work into scattering in these undoped structures [33], which showed that for $n < 2 \times 10^{11}\text{cm}^{-2}$, μ is limited by BI scattering. At higher n_s , the contribution due to alloy-disorder scattering becomes significant and it is this that is therefore responsible for limiting peak mobility. The high mobilities measured here therefore

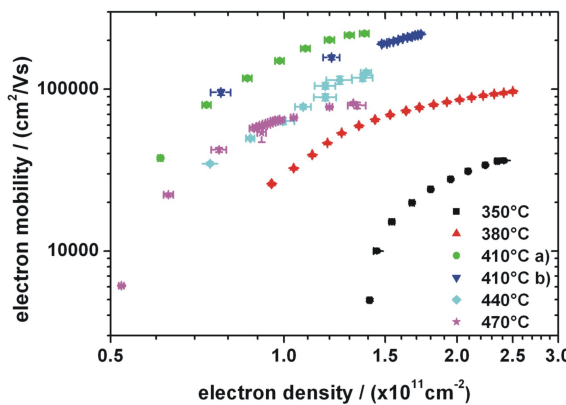


Figure 4.20: μ as a function of n_s after illumination at 1.5K, for $\text{In}_{0.75}\text{Ga}_{0.25}\text{As}$ QW HEMT samples grown between 350 °C and 470 °C.

indicate low levels of background impurity species within the MBE chamber. The benefits gained by reducing interface roughness scattering through surface smoothing, outweigh any deleterious effects deriving from the inclusion of impurity species during these growth interruptions. However, a full study of this was beyond the time limits of this dissertation.

Decreasing growth temperature from 410 °C to 350 °C reduces peak mobility from $221,000 \pm 6,000 \text{ cm}^2/\text{Vs}$ to $47,000 \pm 900 \text{ cm}^2/\text{Vs}$. At these low temperatures growth becomes increasingly non-stoichiometric. The ratio of total-Group III to Group V is no longer unity and arsenic is incorporated in ever higher concentrations. This reduces mobility through a special case of alloy-disorder scattering. However, peak mobility is also reduced above 410 °C, with $65,000 \pm 1,300 \text{ cm}^2/\text{Vs}$ measured at 470 °C. This is due to lower n_s and reduced electron-electron charge screening. In addition, Fig. 4.17 shows a reduction in surface flatness as the temperature is raised, increasing interface-roughness scattering. The peak mobilities show a good fit to a Gaussian distribution, indicating that

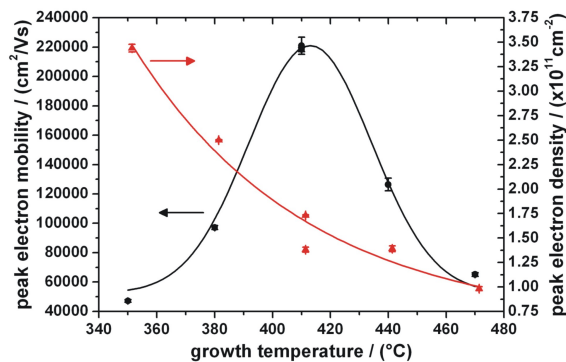


Figure 4.21: Variation in peak- μ and $-n_s$ at 1.5K for $\text{In}_{0.75}\text{Ga}_{0.25}\text{As}$ QW HEMT samples grown between 350 °C and 470 °C.

a growth temperature of 410 °C is close to optimal [Fig. 4.21]. An exponential decrease in peak electron density, from $n_s = 3.44 \pm 0.04 \times 10^{11} \text{ cm}^{-2}$ to $n_s = 0.98 \pm 0.02 \times 10^{11} \text{ cm}^{-2}$, is observed over this same temperature interval. This too could be explained by an increase in arsenic defects with reduced growth temperature. Further work on such structures will involve an investigation into the effect of As₄ and As₂ overpressure on the optimal growth temperature.

The HEMTs grown at 410 °C agree exactly with the highest peak- μ at 1.5K published to-date for these undoped structures [140]. The importance of the result presented here however, is that this high mobility value has been achieved with an electron density as low as $n_s = 1.36 \times 10^{11} \text{ cm}^{-2}$; that is, with a two-fold reduction in n_s compared with that earlier work. Indeed these samples display electron mobilities of $\mu \geq 100,000 \text{ cm}^2/\text{Vs}$ where n_s is as low as $n_s = 0.8 \times 10^{11} \text{ cm}^{-2}$. Just above 2DEG pinch-off, n_s was typically $\sim 0.5 \times 10^{11} \text{ cm}^{-2}$.

Reducing the InAlAs buffer thickness does indeed appear to have resulted in a reduction in n_s , whilst not affecting μ . This supports the conclusion that the 2DEG electrons originate from a trap in the InAlAs bandgap. To provide additional insight, the band structure and electron density in these devices were modelled through self-consistent solutions to the Poisson and Schrödinger equations. Simulations in that previous work assumed that the electron trap existed only below the band edge of the In_{0.75}Al_{0.25}As barriers [140]. Modelling a donor state with an activation energy of 0.125eV and a bulk electron density of $2.3 \times 10^{16} \text{ cm}^{-3}$ gave the closest fit to experimental data.

To assess the effect of similar traps throughout the entire graded InAlAs buffer, a simple initial model assumed that each region of the buffer contributed an identical number of carriers per unit thickness [Fig. 4.22]. Total electron densities were hence calculated both

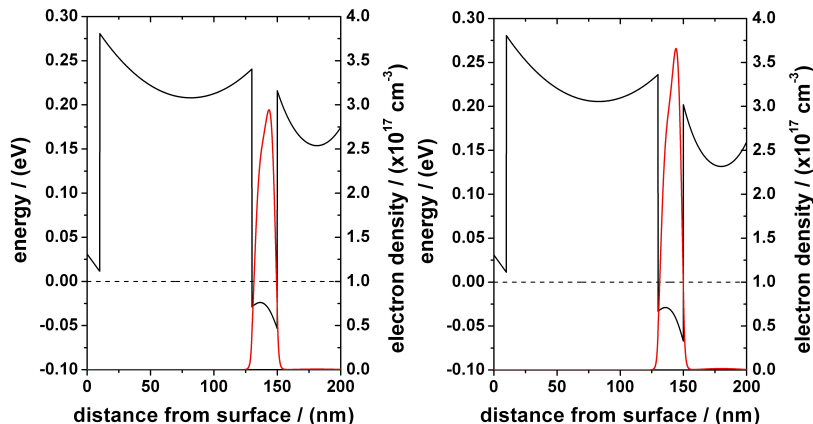


Figure 4.22: Simplified simulations of band structure and electron density for In_{0.75}Al_{0.25}As QW HEMT devices with a 750nm InP-lattice-matched buffer (**Left**) and a 1300nm GaAs-lattice-matched graded-InAlAs buffer (**Right**).

for the 750nm InP-lattice-matched buffer and bottom barrier used in this work and a 1300nm GaAs-lattice-matched buffer/barrier used in that earlier study [140]. These total ‘dopant’ densities of $1.44 \times 10^{17} \text{ cm}^{-3}$ and $2.49 \times 10^{17} \text{ cm}^{-3}$ respectively, were assigned in both cases to the bottom $\text{In}_{0.75}\text{Al}_{0.25}\text{As}$ barrier. This simple model shows that reducing the InAlAs buffer thickness from 1300nm to 750nm decreases electron density by $\sim 75\%$, a value with similar order of magnitude to the experimental findings here.

In a bid to improve the model slightly, the $\text{In}_x\text{Al}_{1-x}\text{As}$ material parameters were altered to include a donor state 0.125eV below the conduction band edge for all compositions. A bulk electron density of $2.3 \times 10^{16} \text{ cm}^{-3}$ was once again assumed [Fig. 4.23]. This attempt

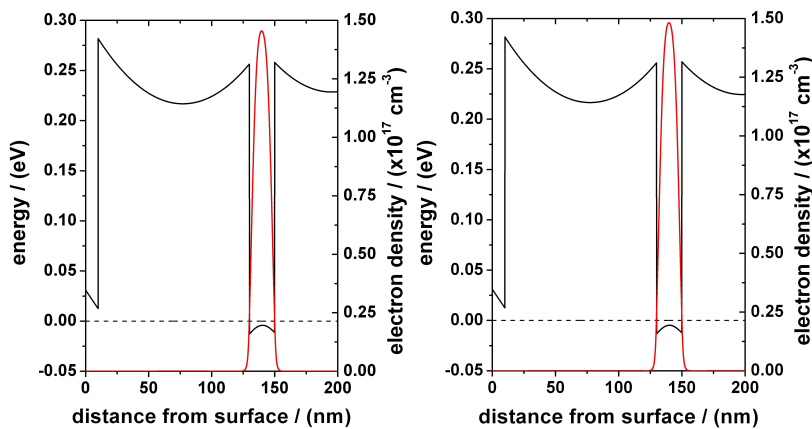


Figure 4.23: Refined band structure and electron density simulations for $\text{In}_{0.75}\text{Al}_{0.25}\text{As}$ QW HEMT devices with (**Left**) a 750nm InP-lattice-matched and (**Right**) a 1300nm GaAs-lattice-matched graded-InAlAs buffer [18]. This and the preceding figure were modelled with the assistance of Dr. D. Ercolani of the Laboratorio Nazionale in Trieste.

at a somewhat more sophisticated model also demonstrates that a thicker InAlAs buffer results in an increase in the electron density. However, the enhancement calculated here is $< 5\%$: significantly lower than the two-fold increase observed experimentally. Further work will therefore necessarily involve improvements to this model to further understand this system.

4.4.6 Measurement of Electron *g*-Factor

As explained in section 4.1, one of the more interesting aspects of high-indium content InGaAs structures is the large electron *g*-factor. A measurement of the magnitude of the *g*-factor in $\text{In}_{0.75}\text{Ga}_{0.25}\text{As}$ was therefore desirable. It has been shown that the bare *g*-factor of a material can be altered inside semiconductor heterostructures, resulting in the measurement of an exchange enhanced *g*-factor, g^* . The Zeeman interaction creates spin-up and spin-down electron populations of unequal size. This means that each spin-type will have a different exchange energy, thus increasing spin-splitting [143, 144].

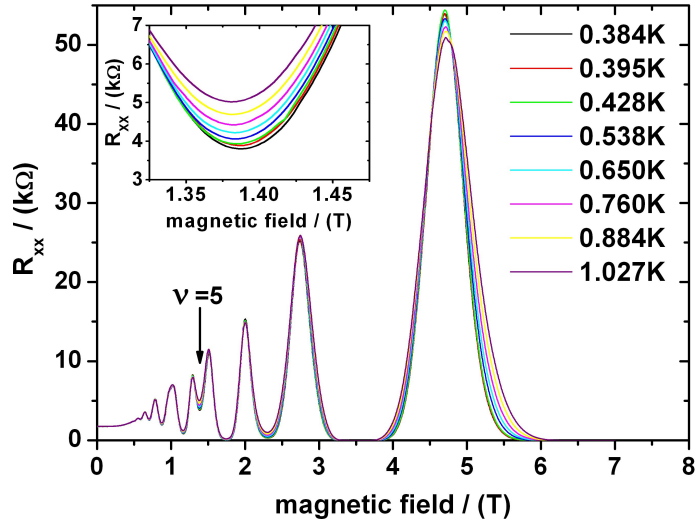


Figure 4.24: The effect of measurement temperature on the magnetotransport properties of an $\text{In}_{0.75}\text{Ga}_{0.25}\text{As}$ QW HEMT sample grown at $410\text{ }^\circ\text{C}$. **Inset:** Detail of the spin-split minimum at filling factor $\nu = 5$.

A method has been demonstrated for measuring g^* via thermal activation [145]. As a result, dependence of magnetotransport on the measurement temperature was investigated for a sample grown at $410\text{ }^\circ\text{C}$ [Fig. 4.24]. An $\text{In}_{0.75}\text{Ga}_{0.25}\text{As}$ HEMT, grown at $410\text{ }^\circ\text{C}$, was cooled in a ${}^3\text{He}$ Heliox cryostat (see section 2.3.4). A peak electron mobility of $227,000 \pm 5,000\text{ cm}^2/\text{Vs}$ was measured. Ref. [146] describes this thermal activation method for calculating g^* in detail. Assuming discrete Landau levels, the temperature dependence of the longitudinal conductance (σ_{xx}) of the spin-split minima at odd-filling factors is proportional to the Landau level energy gap (ΔE), such that

$$\sigma_{xx} \propto \exp\left(\frac{-\Delta E}{2k_B T}\right) \quad (4.5)$$

The resistance of the spin-split minimum at $\nu = 5$ increases by less than 0.3% as the temperature is raised from 0.38K to 1.03K . An Arrhenius plot of $\ln[\sigma_{xx}]$ against $1/T$ for each filling factor enables the determination of ΔE [Fig. 4.25]. g^* can then be found from the gradient of a plot of ΔE against B , since

$$\Delta E = g^* \mu_B B \quad (4.6)$$

However, the two distinct gradients on each of these plots lead to different values for ΔE . Given that spin-split minima were resolved only at $\nu = 3$ and $\nu = 5$, just two points were available for this graph. Depending which value of ΔE from Fig. 4.25 was used, values for g^* of -1.383 and -0.800 were calculated. Comparison of these values with the data presented in Fig. 4.26 immediately suggests a problem. Given that the Landé g -factors for $\text{In}_{0.53}\text{Ga}_{0.47}\text{As}$ and InAs are close to -5 and -15 respectively, an expected value for

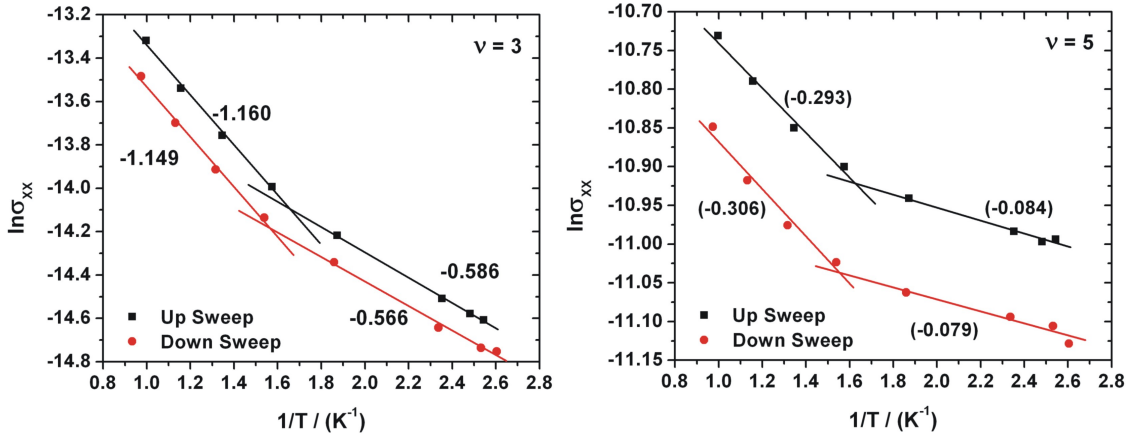


Figure 4.25: Arrhenius plots for $\nu = 3$ (**Left**) and $\nu = 5$ (**Right**) from the data presented in Fig. 4.24. Two magnetic field sweep directions are shown for each.

$\text{In}_{0.75}\text{Ga}_{0.25}\text{As}$ might be -10. It would appear therefore that rather than an enhancement of the bare g -factor by the exchange interaction, a reduction has been measured here.

This anomalous result can be explained if electron transport is in the ‘hopping’ conduction regime. Impurities or disorder in the channel create small random fluctuations superimposed on the conduction band potential. When n_s and hence E_f is high, conduction electrons will not interact appreciably with these potential variations. However, if the position of E_f is low, which is the case for these $\text{In}_{0.75}\text{Ga}_{0.25}\text{As}$ HEMTs, this disorder appears as islands in the electron sea. Electrons become localised to these impurities and

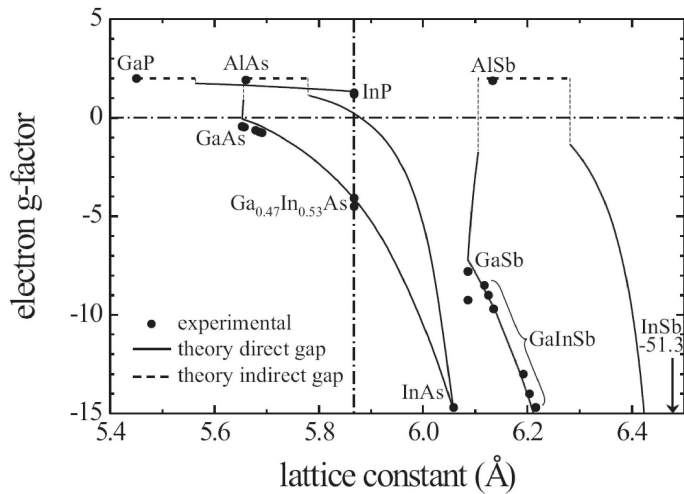


Figure 4.26: Variation in bare g -factor with lattice constant for various III-V compounds (reproduced from Ref. [125])

conduction is achieved only by hopping between states [Fig. 4.27]. Assuming $k_B T > \Delta E$

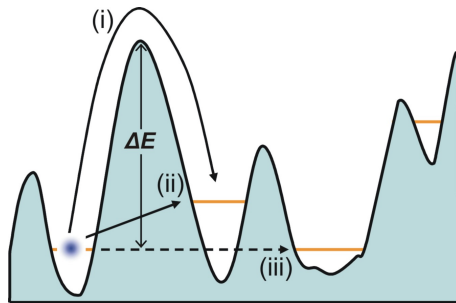


Figure 4.27: Schematic diagram showing (i) thermal activation, (ii) nearest-neighbour hopping and (iii) variable-range hopping conduction between impurity states in a channel where E_f is low.

where ΔE is the depth of some disorder potential well, electrons can be thermally activated into neighbouring states. If $k_B T < \Delta E$ then conduction proceeds instead by nearest-neighbour hopping where electrons tunnel between adjacent states via phonon emission or absorption. Finally, where $k_B T \ll \Delta E$, there is insufficient energy to excite electrons into nearby states. However, hopping may still occur between distant impurity states, provided they are close enough in energy. This is known as variable-range hopping. Ref. [147] discusses this topic in greater detail.

The values of ΔE calculated for $\nu = 5$ are smaller than $k_B T$. The two gradients in the plots in Fig. 4.25 suggest a transition from one hopping mode to another close to 600mK. Such behaviour has been observed in other materials [148, 149]. At low temperature, conduction changes from nearest-neighbour hopping to variable-range hopping between localised states in the tails of the Landau levels. ΔE for these transitions will be very small, leading to the large underestimate in the calculated value of g^* . However, transport cannot be explained solely by hopping since strong localisation would have led to a ‘smearing’ of the Shubnikov-de Haas oscillations in Fig. 4.24. An alternative explanation might be provided by invoking the concept of ‘skyrmions’. Instead of the formation of a pair of spin-split Landau levels, electrons coexist in one level, adopting a lower-energy, spin-wave configuration such that no electron is neighboured by another with identical spin. Skyrmions have been observed previously in similar systems[150], typically when the exchange-enhanced g -factor is small. This could explain the low values of g^* measured here.

The coincidence method was therefore used as an alternative technique to measure the g -factor [143]. Non-perpendicular magnetic fields are used to vary the ratio between the Zeeman and cyclotron energies; that is the second two terms in Eqn. (1.31). This is possible because the Zeeman term is dependent on total magnetic field, whereas the cyclotron energy is a function of perpendicular field only. Where the ratio is an integer,

there is a coincidence between the spin-down energy state of one Landau level with the spin-up energy state of a lower level [Fig. 4.28]. From a knowledge of the angle (θ_c) between

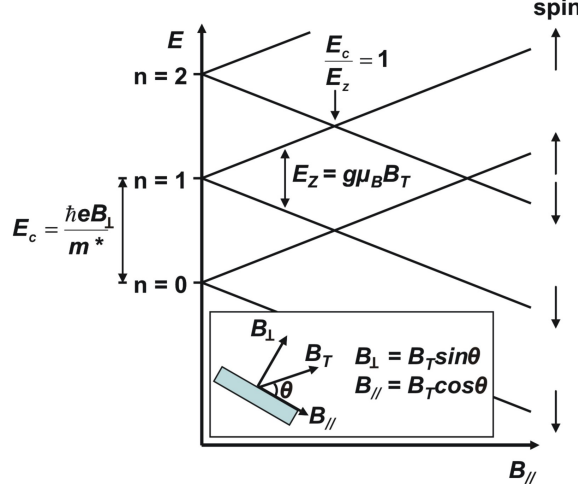


Figure 4.28: Schematic diagram showing how the application of a magnetic field parallel to the spin-up condition can be used to vary the Landau level profile in a material with negative g -factor. The inset shows the measurement geometry used, where B_T , B_{\parallel} and B_{\perp} are the total, parallel and perpendicular magnetic field components respectively (after [151]).

the 2DEG and the total field at these coincident points, g^* can be calculated from

$$g^* = n \left[2 \left(\frac{m_0}{m^*} \right) \sin(\theta_c) \right] \quad (4.7)$$

where n is the integer ratio of E_c/E_z . Previous work has established $m^* = 0.04m_0$ in $\text{In}_{0.75}\text{Ga}_{0.25}\text{As}$ [152, 153].

A HEMT from the same $\text{In}_{0.75}\text{Ga}_{0.25}\text{As}$ sample as used for the previous measurement of g^* was cooled to $\sim 1.5\text{K}$ in a ${}^3\text{He}$ cryostat. It was mounted on a probe with the facility to rotate the angle of the sample relative to the magnetic field. After illumination and with the sample completely perpendicular to the magnetic field ($\theta = 90^\circ$), longitudinal and transverse resistance measurements were made as a function of magnetic field. The electron density and mobility were calculated to be $1.44 \times 10^{11}\text{cm}^{-2}$ and $180,000\text{ cm}^2/\text{Vs}$ respectively. The sample was then rotated such that some proportion of the total applied field was now parallel to the 2DEG and these measurements were repeated. To establish θ accurately, the angle of the Hall slope at low field was compared with the R_H measured in fully perpendicular field using Eqn. (4.8)

$$\theta = \sin^{-1} \left(\frac{1}{R_H} \frac{d\rho_{xy}}{dB_T} \right) \quad (4.8)$$

As $\theta \rightarrow 0$, the ratio B_{\perp}/B_T becomes infinitely small. The maximum total field available was 12T, which therefore placed a limit on the minimum angle that could be used. Longitudinal magnetoresistance was plotted as a function of measurement angle [Fig. 4.29].

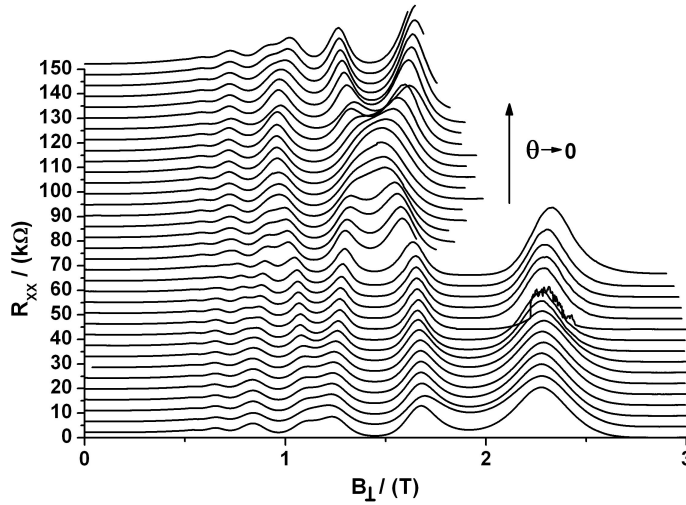


Figure 4.29: Angular dependence of the longitudinal magnetoresistance of a 2DEG formed in a 30nm-wide $\text{In}_{0.75}\text{Ga}_{0.25}\text{As}$ QW. The arrow indicates the direction of decreasing angle, where $\theta = 90^\circ$ in the lowest trace and 7.71° in the top trace. Each measurement was normalised to B_\perp and, for clarity, a constant vertical offset has been used.

Crossings of spin-split maxima in R_{xx} are resolved at filling factors $\nu = 4$ ($B_\perp \sim 1.5\text{T}$) and $\nu = 6$ ($B_\perp \sim 1\text{T}$). These indicate points of coincidence between E_c and E_z for which $n = 1$. It should be noted that anticrossings of the spin-split Landau levels which have been seen for 2DEGs in InAs are not observed [154]. This is because spin-orbit coupling is lower in $\text{In}_{0.75}\text{Ga}_{0.25}\text{As}$. By plotting the perpendicular magnetic field position of the peaks in Fig. 4.29 against $1/\sin(\theta)$, values of θ_c for these crossings can be accurately obtained [Fig. 4.30]. From Eqn. (4.7), the well-defined coincidence at $\nu = 4$ gives a value of $|g^*| = 9.15 \pm 0.14$. This corresponds closely with the value predicted for the bare g -factor in Fig. 4.26. The crossing at $\nu = 6$ is resolved less accurately. However, taking a value close to centre of the coincident region (as indicated by the red arrow in Fig. 4.30) a value of $|g^*| = 8.12 \pm 0.31$ is obtained. These two values of $|g^*|$ are almost identical to those measured previously for $\text{In}_{0.75}\text{Ga}_{0.25}\text{As}$ [153]. That $|g^*|$ is increased at higher filling factor is believed to derive from a reduction in electron-electron exchange interactions [144].

4.4.7 Transport Dependence on InGaAs Composition

To investigate the InGaAs composition interval between $x=0.53$ and $x=0.75$, a series of HEMT samples were grown at 410°C . The basic undoped structure was as shown in Fig. 4.15, except that the indium mole fraction in the $\text{In}_x\text{Ga}_{1-x}\text{As}$ and $\text{In}_x\text{Al}_{1-x}\text{As}$ active layers was either $x=0.65$, $x=0.70$ or $x=0.75$. The total two-stage graded-buffer thickness was maintained at 700nm. To achieve equivalent relaxation for the various compositions, the second stage ‘over-graded’ the composition by 10%. For example, for an

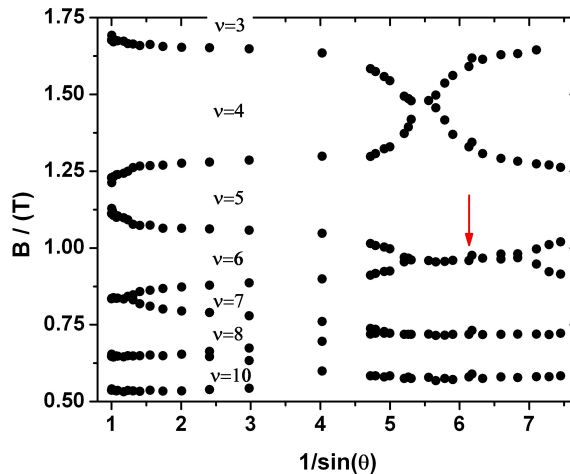


Figure 4.30: Position of the SdH maxima from Fig. 4.29 as a function of measurement angle, showing crossings of spin-split Landau levels. Values of the filling factor have been included for clarity. The presence of the red arrow is explained in the text.

In_{0.65}Ga_{0.35}As channel, the InAlAs buffer had a surface composition of $x=0.75$. All other growth conditions were unchanged.

XRD analysis confirmed the indium mole fraction of these active layers to be $x=0.66$, $x=0.69$ and $x=0.74$, while epilayer relaxation above the graded buffer was $> 90\%$. Hall bars were fabricated parallel to [1 1 0] with insulated, optically-transparent top-gates. Cooled to 1.5K in a ⁴He bath cryostat, magnetotransport measurements were performed for each sample. After illumination, μ and n_s were measured for each with the gate at ground [Fig. 4.31]. As the In mole fraction is raised from $x=0.65$ to $x=0.75$, μ is increased from $95,000 \text{ cm}^2/\text{Vs}$ to $124,000 \text{ cm}^2/\text{Vs}$ while interestingly, n_s is decreased from $1.76 \times 10^{11} \text{ cm}^{-2}$ to $0.94 \times 10^{11} \text{ cm}^{-2}$. The reduction in alloy-disorder scattering more than compensates for any loss in electron-electron charge screening.

Fig. 4.32 displays the results of modelling the band structure and electron density in these devices. In keeping with the experimental results, n_s undergoes a two-fold reduction as the In mole fraction is increased. It can be seen in Fig. 4.32 that the band-edge of the bottom (right-hand) InAlAs barrier becomes increasingly skewed as x is reduced from 0.75 to 0.65. This reduces the effective barrier thickness. The probability of electrons originating in the graded InAlAs buffer tunnelling into the QW is therefore enhanced as the In mole fraction is reduced.

Curves of μ against n_s were constructed for each sample [Fig. 4.33]. There is a definite improvement in the transport properties as x is increased from 0.65 to 0.70 due to a reduction in alloy-disorder scattering. However, the $x=0.70$ and $x=0.75$ samples appear to be essentially collinear. Given that these growths took place almost at the end of a growth campaign, the As₄ pressure was falling throughout the growth day. This is

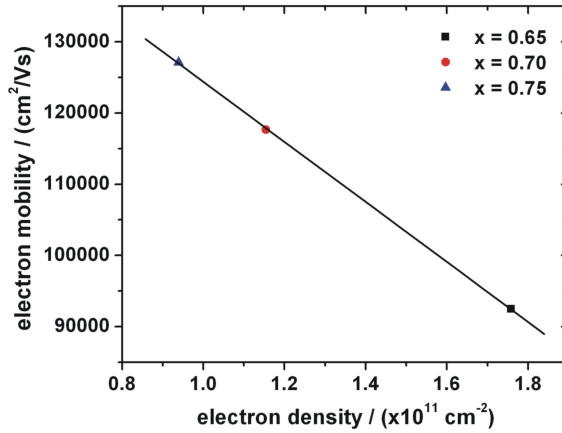


Figure 4.31: Ungated μ and n_s data for $\text{In}_x\text{Ga}_{1-x}\text{As}$ HEMTs with $x=0.65$, $x=0.70$ and $x=0.75$, measured after illumination. A linear fit to these points is included.

perhaps reflected in the fact that none of these samples conducted in the dark. The last sample grown, for which $x=0.75$, may therefore have been affected by this low V/III ratio. Comparison of the $x=0.65$ and $x=0.70$ samples with the nominally identical $x=0.75$ HEMTs grown at 410°C previously (see Fig. 4.21) confirms that increasing x further does indeed improve transport characteristics [Fig. 4.34]. This is in agreement with previous work [29]. Returning to the figure of merit of $\mu \sim 100,000 \text{ cm}^2/\text{Vs}$ used previously, this work demonstrates that $\text{In}_x\text{Ga}_{1-x}\text{As}$ material of excellent quality can be grown over the full composition range $0.53 \leq x \leq 0.75$. This is an encouraging first step towards the realisation of tuneable g -factor devices built around this material system.

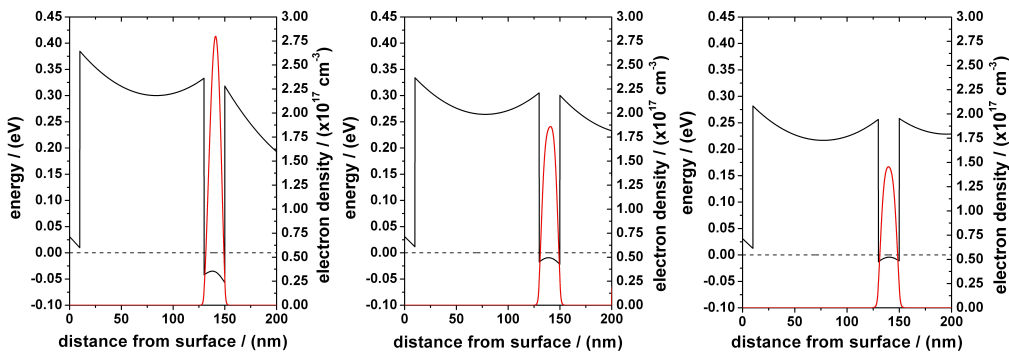


Figure 4.32: Simulated band structures and electron densities for $\text{In}_x\text{Ga}_{1-x}\text{As}$ HEMTs with $x=0.65$ (Left), $x=0.70$ (Centre) and $x=0.75$ (Right) [18].

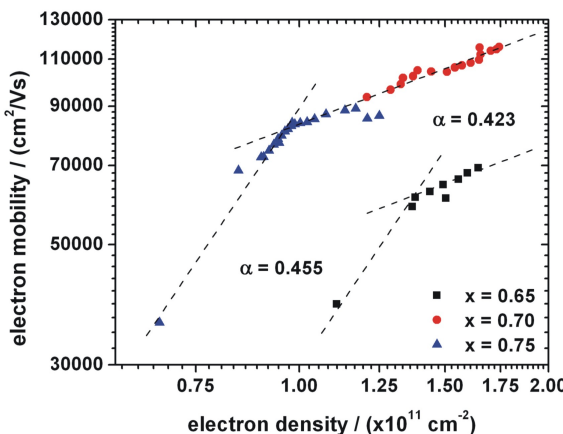


Figure 4.33: Curves of μ against n_s after illumination, showing the effect of InGaAs composition on electron transport in $\text{In}_x\text{Ga}_{1-x}\text{As}$ HEMTs. The dashed lines indicate linear fits to these data, with the power dependences shown.

4.4.8 Doped InGaAs HEMTs

No analogue of the SOC effects seen in section 4.3 for the $\text{In}_{0.53}\text{Ga}_{0.47}\text{As}$ HEMTs was observed for the undoped $\text{In}_{0.75}\text{Ga}_{0.25}\text{As}$ HEMTs. It was proposed that since those SOC effects were shown to be highly dependent on n_s , the carrier density was too low in these samples to enter the regime where beating effects are noted on the SdH oscillations. As a result, the final three HEMT samples of the growth campaign were grown at 410°C as shown in Fig. 4.15 but including a n -doped layer. The total thickness of the top InAlAs barrier was maintained at 120nm. However, a 15nm layer was Si-doped and this was

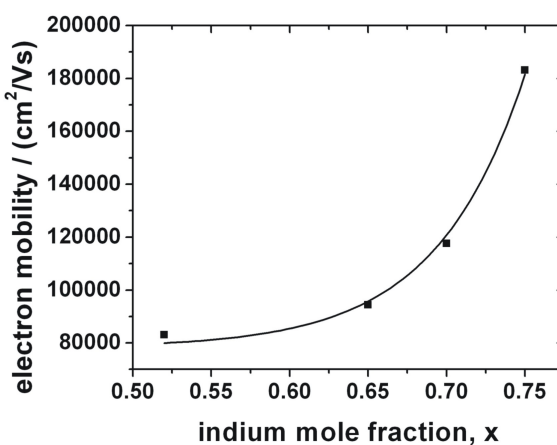


Figure 4.34: Variation in peak mobility for the $\text{In}_x\text{Ga}_{1-x}\text{As}$ HEMTs grown with $x=0.65$ and $x=0.70$. Data from an earlier HEMT grown in section 4.4.5 at 410°C with $x=0.75$ and a Si-doped $\text{In}_{0.53}\text{Ga}_{0.47}\text{As}$ HEMT from section 4.2 are provided for comparison. The line shows an exponential fit.

separated from the channel by a 60nm undoped InAlAs spacer. The nominal doping densities were $1 \times 10^{18}\text{cm}^{-3}$, $1 \times 10^{17}\text{cm}^{-3}$ and an undoped control device.

Again these devices did not conduct in the dark. After illumination, the SdH oscillations definitively show parallel conduction for both of the n -doped samples. This indicates that band bending due to the additional charge has pulled the conduction band edge below E_f in the vicinity of the doped layer. In future samples therefore, doping densities of $< 1 \times 10^{17}\text{cm}^{-3}$ or δ -doping should be used. The μ against n_s curves show that compared with the undoped control, electron density is increased in both n -doped samples as expected [Fig. 4.35]. The sample doped at $1 \times 10^{18}\text{cm}^{-3}$ shows an approximate three-fold

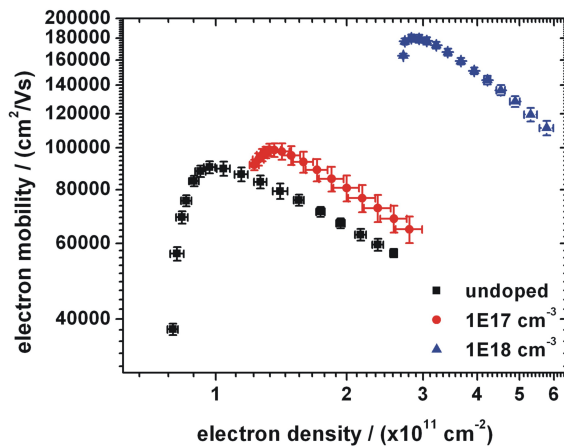


Figure 4.35: Curves of μ against n_s showing the effect of n -doping density on transport properties for a series of $\text{In}_{0.75}\text{Ga}_{0.25}\text{As}$ HEMTs.

increase in peak electron density to $\sim 3 \times 10^{11}\text{cm}^{-2}$. This is accompanied by a doubling of the peak electron mobility to $\sim 180,000\text{cm}^2/\text{Vs}$. What is slightly unusual is the shape of these curves. After rising to some peak- μ , further increases in n_s result in a lowering of the mobility. However, the fact that this response is seen identically in the undoped sample leads to the conclusion that this behaviour is not caused by sample doping. As mentioned on page 97, As_4 pressure during these final growths was quickly approaching the point where growth of these samples could not be supported. This is the likely cause of the unexpected response. Growth of doped samples at various InGaAs compositions will be repeated in future to investigate SOC effects in these materials.

4.5 Summary

A series of $\text{In}_{0.53}\text{Ga}_{0.47}\text{As}$ QW HEMTs were grown lattice-matched to (001) InP substrates. Electron density in these 2DEGs could be varied, both through device illumination and the application of gate bias. In this way, the magnetotransport properties of these

HEMTs were assessed. Electron mobility was shown to be higher for transport parallel to [1 1 0] compared with that along [̄1 1 0]. This was shown to be a direct result of anisotropic sample morphology. Alloy-disorder scattering was shown to be the limiting mechanism at low n_s , superseded by interface-roughness scattering as n_s is increased. Mobility is reduced at the very highest values of n_s as intersubband scattering begins.

Plotting peak electron mobility against sample growth temperature, it was possible to show that, at least for measurements made following illumination, 2DEG transport properties improved as growth temperature was decreased over the range from 480 °C to 410 °C. However, the size of the increase in mobility was only $\sim 20\%$ over this 70 °C range, showing that these heterostructures appear to be fairly insensitive to growth temperature. Peak electron mobility and density values of $1.1 \times 10^5 \text{ cm}^2/\text{Vs}$ at $8.9 \times 10^{11} \text{ cm}^{-2}$ were measured at 1.5K for the sample grown at 410 °C. This means that these devices have transport properties amongst the highest ever recorded for such structures.

Spin-orbit coupling effects were observed in these $\text{In}_{0.53}\text{Ga}_{0.47}\text{As}$ QW HEMTs. Beating in the SdH oscillations, accompanied by double peaks in the FFT spectra were shown to be a result of Rashba coupling which gives rise to spin-splitting in the absence of an applied magnetic field. However, the response of the magnitude of this splitting (Δn) to changing gate-bias and hence electron density, was unusual. Δn could be tuned from zero at low electron density, to some peak value as n_s was increased. Further increases in n_s led to suppression of the spin-splitting and an apparent return to inversion symmetry within the QW. Electrons in both the first and second QW energy levels were shown to exhibit this response. This is the opposite of what has been observed previously in such systems, where a single point for which $\Delta n = 0$ can be found. The origin of this behaviour is however still unclear and will be the focus of future work. Nevertheless, such a system could be exploited in a future device where fast, stable switching between spin-degenerate and spin-split transport would be possible.

A series of undoped $\text{In}_{0.75}\text{Ga}_{0.25}\text{As}$ QW HEMTs were then grown. In the same way, the transport properties of these 2DEGs were measured and shown to have improved characteristics compared with the $\text{In}_{0.53}\text{Ga}_{0.47}\text{As}$ QW HEMTs, due to a reduction in both alloy-disorder and remote-ionised-dopant-impurity scattering. Identical transport anisotropy was found with mobility higher parallel to [1 1 0]. The growth temperature was studied for these heterostructures and found to be optimal at 410 °C. A peak electron mobility of $2.2 \times 10^5 \text{ cm}^2/\text{Vs}$ was measured for this material at 1.5K. This value equals the highest mobility measured to date for these undoped devices but, crucially, the electron density required to achieve this has been approximately halved to a value of $1.4 \times 10^{11} \text{ cm}^{-2}$. It is expected that high- μ , low- n_s material such as this will enable the study of interesting physics at lower magnetic fields.

The effective *g*-factor in these $\text{In}_{0.75}\text{Ga}_{0.25}\text{As}$ QWs was measured by a coincidence

technique to be $|g^*| = 9.2$, a value close to the theoretical bare g -factor for this material. A thermal activation method for the same measurement showed that due to the low n_s , electron transport was in the hopping regime for this 2DEG.

$\text{In}_x\text{Ga}_{1-x}\text{As}$ QW HEMTs were grown with compositions between $x=0.53$ and $x=0.75$. Although growth conditions were non-ideal due to a highly depleted arsenic cell, growth of high quality material was nevertheless demonstrated. This work demonstrates that $\text{In}_x\text{Ga}_{1-x}\text{As}$ can be grown with $\mu \geq 1 \times 10^5 \text{ cm}^2/\text{Vs}$ over the entire range $0.53 \leq x \leq 0.75$. This range of InGaAs compositions opens up access to bare g -factors between -5 and -10. The combination of high $|g^*|$ with high electron mobility make these materials ideal candidates for use in tuneable g -factor devices and for other spintronic applications.

Chapter 5

One-Dimensional Electron Systems

5.1 Introduction

Section 1.6 introduced the concept of using electrostatic split-gates (SGs) to confine 2DEG electrons into 1D channels. SG operation was described, together with explanations of some of the features commonly observed in 1D transport measurements.

This chapter is concerned with SG fabrication on the $\text{In}_{0.75}\text{Ga}_{0.25}\text{As}$ -based 2DEGs described in chapter 4 and subsequent use of these for 1D transport measurements. As with the 2D case, a large body of knowledge exists for 1D transport in GaAs/AlGaAs but rather less for the InGaAs/InAlAs system. The high Landé g -factor of these materials could permit the 0.7 structure [45] and its analogues [49] to be studied at significantly lower magnetic fields than in GaAs. It is hoped that this work will contribute to the effort to fully explain these phenomena.

A suitable fabrication process had to be created since SGs of this kind had not been previously made in this group. Section 5.2 begins with a discussion of the importance of careful SG design. The problems associated with fabricating working SG devices from InGaAs/InAlAs materials are then addressed, together with a description of the development of an optimised process, in sections 5.3 and 5.4. Electrical 1D transport measurements with operational SG devices are covered in section 5.5.

5.2 Split-Gate Design

The dimensions of a SG are critical to its performance [Fig. 5.1]. The yellow area in the AFM image in Fig. 5.1a) is a Ti/Au split-gate, positioned on the surface of the brown-coloured semiconductor. The small gap in the gate is where the quantum wire will be formed: here the split-gate separation is 500nm. When a negative bias, V_g , is applied to

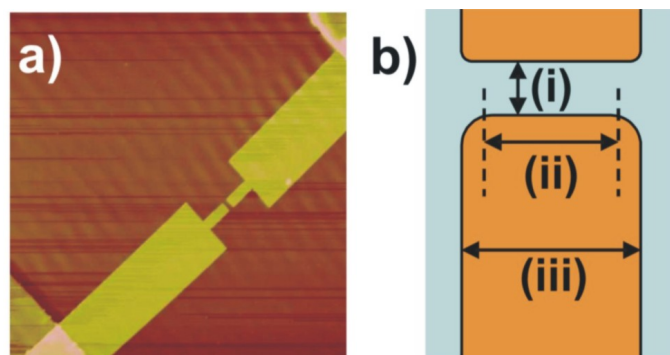


Figure 5.1: a) A $25\mu\text{m} \times 25\mu\text{m}$ AFM image of a pair of SG. b) Schematic diagram showing (i) SG separation and (ii), (iii) SG length.

the gates, to a first approximation the shape of the metal defines the profile of the depleted region below it (see Fig. 1.13). In Fig. 5.1b), if (i) is too large then it may be impossible to create a 1D channel for the range of gate voltages available. If (i) is too small, control over the width of the 1D region will be compromised. The magnitude of (ii) defines the length of the 1D channel. If longer than the electron mean free path, quantum ballistic-transport will not be achieved. However, if (ii) is too short then unwanted evanescent modes will contribute to the channel conductance [5].

If an electron encounters a feature with dimensions of the order of its Fermi wavelength, λ_f , resonant effects may be observed in the transport behaviour. To avoid this, the corners of the gates can be rounded, such that the radius of curvature is greater than λ_f [155]. In Fig. 5.1b), this radius of curvature is given by [(iii)-(ii)]/2. However, overly rounded corners reduce definition in the length of the confinement region.

The lowest values of electron density, n_s , measured in the HEMT devices discussed in chapter 4 were of the order of $5 \times 10^{10} \text{ cm}^{-2}$ for the undoped $\text{In}_{0.75}\text{Ga}_{0.25}\text{As}$ -based structures (see page 90). Using Eqn. (1.25), $\lambda_f \leq \sim 120\text{nm}$. Radii of curvature of 200nm, 100nm and 0nm (i.e. square) were therefore investigated as suitable corners for the gates.

The optimal design to achieve good electron confinement was unknown. Therefore, using the dimensions of the standard $80\mu\text{m}$ -wide Hall-bar photolithography mask as a starting point, designs were created which allowed four differently-sized SGs to be positioned onto a single Hall-bar. Two different four-gate designs were used giving a total of eight different SG types, the dimensions of which are summarised in the following table. The lengths (i), (ii) and (iii) are as defined in Fig. 5.1.

split-gate	(i)/nm	(ii)/nm	(iii)/nm	split-gate	(i)/nm	(ii)/nm	(iii)/nm
1	500	100	500	5	500	400	600
2	500	300	700	6	500	600	800
3	600	200	600	7	500	200	400
4	500	200	600	8	500	400	400

5.2.1 Electron-Beam Lithography

The SGs are substantially smaller than the other features on a standard gated HEMT. This fact complicates the photolithography and metal lift-off stages. To achieve the required level of control over these dimensions during processing, an alternative to standard optical photolithography was required.

Electron-beam (e-beam) lithography was therefore used to define the SGs. As the name suggests, a high-energy electron gun creates a thin electron-beam, the direction of which is accurately controlled using electrostatic deflection plates. The chip surface is covered in a chemical resist, the properties of which are altered via exposure to the e-beam. A computer program is used to control the e-beam tool and ‘write’ the SG design into the resist. Resolution of the pattern is limited not just by the beam size but also by electron scattering processes within the resist [156]. Exposed areas of resist are then developed away and metal is evaporated into the resulting windows to form the SGs. E-beam lithography is done *in-house* using a Leica VB6 tool. The 100kV beam has a minimum diameter of 3nm and alignment accuracy to within 15nm. This is more than adequate for the SG dimensions used in this work.

AutoCAD software was used to design the SG pattern since the resulting drawings could be read directly by the e-beam tool. Marks were added to this pattern to allow the e-beam to accurately align the SGs with the underlying Hall-bar. A grid spacing of 5nm was used to define the design in *AutoCAD* to minimise any digitisation effects on the rounded-corners.

5.3 Split-Gate Process Development

5.3.1 Gate Insulation

Chapter 2 describes the processing steps required to build the standard gated HEMT devices discussed in chapter 4. However, creating a 1D channel in these devices is non-trivial. As discussed previously, the SGs need to be insulated, both from the underlying channel and from the overlying transparent metal top-gate. The initial approach was again to use polyimide. Isolating the SGs from the top-gate was relatively straightforward. The entire central region of the device was covered in 200-300nm polyimide. The top-gate was then deposited on top of this. The polyimide would not only give good electrical insulation between the two metal gates, it would also offer protection to the fragile SGs underneath.

The top-gate underwent a small redesign and, whilst essentially remaining a rectangular stripe running the length of the mesa, side arms were added to facilitate connection with the contact arms away from the insulated area. It is possible for microscopic spikes of metal to form at the sides of the mesa during the SG metallisation steps. These can then pierce through the overlying polyimide and cause leakage. The central gate metal

was therefore designed to be $20\mu\text{m}$ wide, positioned in the centre of the $80\mu\text{m}$ wide mesa. By ensuring that the top-gate was spatially separated from the channel edges, the risk of contact with any metal spikes was removed. However, the entire SG was still covered by the top-gate and so the overall electron density could still be varied in the region of the quantum wire [Fig. 5.2].

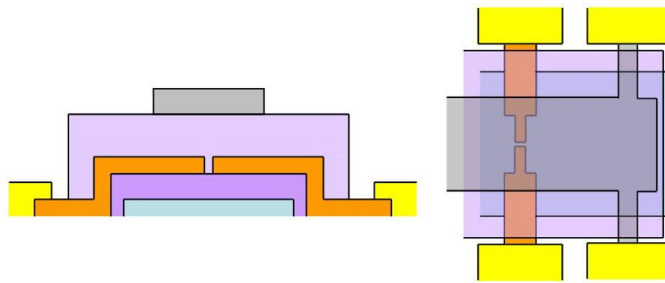


Figure 5.2: Schematic diagrams of cross-sectional and plan views of polyimide insulation layers (purples) around the SGs (orange). These prevent electrical contact with both the mesa (blue) and the top gate (grey). The yellow sections represent the gate contact arms for both split- and top-gates (connections to the top-gate have been omitted for clarity in the cross-sectional view).

A greater challenge was the insulation of the SGs from the channel. In order to achieve good control over the width and profile of the 1D channel, it is important that the lateral boundary of the depletion region around each gate is well resolved. The shape of this depleted region becomes increasingly poorly-defined as it extends into the semiconductor surface. As a result it was critical that the vertical distance between the SGs and the 2DEG was kept to a minimum. It was therefore essential that the final cured thickness of the polyimide layer beneath the SGs was as low as possible.

5.3.2 Thin Polyimide Films I

The thickness of the insulating layer could be varied by using a solvent thinner to dilute the polyimide. To investigate the available range of thicknesses, variously diluted solutions were applied to test-chips, which were then processed as described in section 2.2.4. Following curing, insulator thicknesses were measured using the Dektak profiler [Fig. 5.3]. Polyimide films covering the range of thicknesses from $50\text{-}450\text{nm}$ can be readily achieved using this process. However, this does not guarantee that the thinnest layers will be good insulators. The process described on page 30 was optimised for a $\sim 100\%$ yield of $\geq 300\text{nm}$ -thick layers of polyimide. For polyimide thicknesses approaching the $\sim 50\text{nm}$ ideally required for this work, the number of devices with leaking gates increased substantially. Polyimide thickness was now of the same order of magnitude as variations in film thickness across a chip due to the nature of the ‘spin-on’ process. These very thin

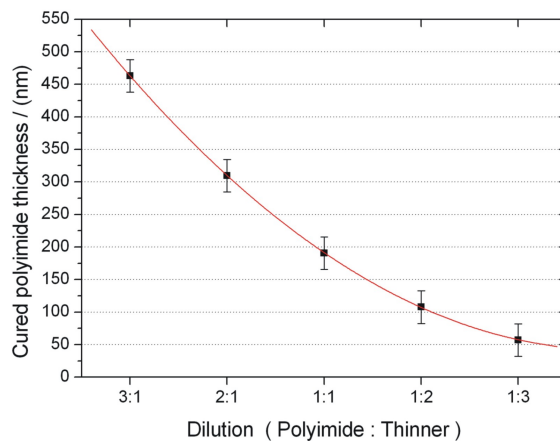


Figure 5.3: Variation of cured film thickness with polyimide dilution. The red-curve shows a second order polynomial fit to the data.

films also exacerbated problems with short solution-lifetime and water absorption which were already something of an issue with thick polyimide layers. The combination of these effects meant that the realistic limits of the polyimide process had been reached.

5.3.3 Silicon Nitride Insulation

Silicon nitride (Si_3N_4), was trialled as an alternative to polyimide. Plasma-enhanced chemical vapour deposition was used which provides much closer control over film thickness and uniformity compared with the polyimide spin-on process [157]. Trial chips from previously characterised InGaAs HEMT samples were processed into devices with standard large-area gates insulated with Si_3N_4 . After the mesa etch the entire chip was covered in Si_3N_4 . A photolithographic process involving hydrofluoric acid was used to open up windows in the Si_3N_4 , through which the ohmic contacts were formed. The remainder of the gates processing was then carried out directly onto the Si_3N_4 .

These chips exhibited excellent electrical isolation of the gate from the channel, even with insulator thickness as low as 50nm. However, the electrical behaviour of these devices was significantly worse than identical chips insulated with thick polyimide. Samples which had previously shown very strong SdH oscillations (see page 15) now gave a very noisy response to the same experiments. In addition, gate operation with Si_3N_4 was highly hysteretic. This approach was therefore discontinued.

5.3.4 InGaAs Cap Removal

A second alternative to polyimide involved removal of the InGaAs cap and placement of the SG on the semi-insulating $\text{In}_x\text{Al}_{1-x}\text{As}$ layer underneath. This has a higher Schottky barrier, experimentally determined to be between 1.2 and 0.75eV over the composition

range $0.43 \leq x \leq 0.62$ [158].

After Ohmic contact processing, a window above the mesa was opened in a layer of resist. A buffered solution of adipic acid ($\text{pH}5.5$) : H_2O_2 (30%), mixed in the ratio 24:1, has been shown to preferentially etch InGaAs at $\sim 50\text{nm}/\text{minute}$ with a reported selectivity of 250 compared to InAlAs [159]. After agitation in this solution to remove the InGaAs cap, the chip was rinsed in deionised water and dried with N_2 . NiCr was then evaporated to form the top-gate directly onto the InAlAs surface exposed by the etched recession. Microscope photographs clearly show the region where the dark-grey InGaAs cap has been etched away to reveal the blue-grey-coloured InAlAs underneath [Fig. 5.4]. However,

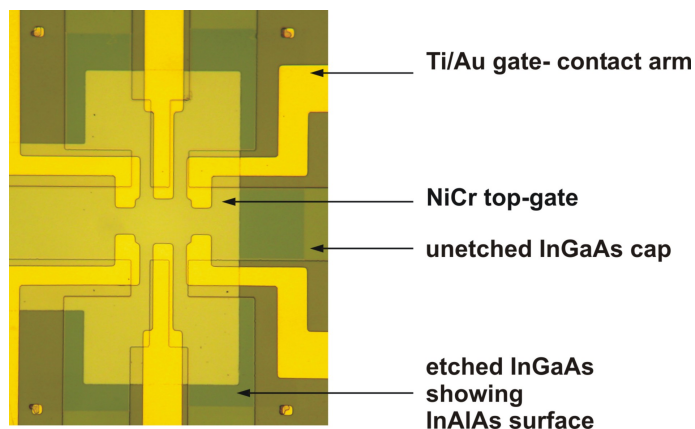


Figure 5.4: Optical microscope image, at $\times 50$ magnification, showing the recessed-gate etch region at one end of the central mesa (here shown running left to right).

leakage currents $> 10\text{nA}$ were still formed at low gate bias between the gate and channel. This seemed to indicate incomplete removal of the InGaAs. To confirm the etch rate, an ungated, lattice-matched InGaAs/InAlAs HEMT device (see Fig. 1.7) was processed and bonded into a chip carrier. The room temperature 2DEG resistance of this device was measured and then the entire chip and package was agitated in the adipic acid etch solution for five minute intervals before being rinsed and dried. The channel resistance was measured between each successive etch [Fig. 5.5]. The channel resistance remains fairly constant until close to 80 minutes of etching have elapsed. It is proposed that this corresponds to the time at which the doped layer of n -InAlAs begins to be etched away, removing carriers from the 2DEG and hence increasing its resistance. For this sample the n -InAlAs lies under a 3nm InGaAs cap and 16nm of undoped InAlAs. The 3nm InGaAs cap will be removed quickly. However, etching 16nm of InAlAs in ~ 80 minutes gives an etch-rate of $2 \text{ \AA}/\text{minute}$, which is exactly the rate predicted in the literature.

Therefore, subsequent chips were over-etched for up to 30 minutes, to ensure complete removal of the InGaAs cap. For samples with an expected cap thickness of 10nm, the depth of the final recessed region was measured at 13nm using AFM. This confirmed that

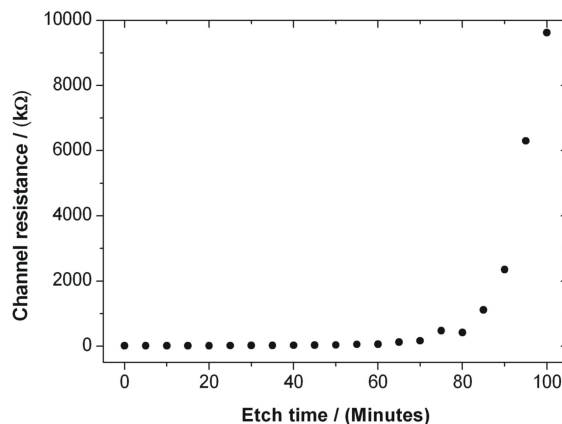


Figure 5.5: Experiment to confirm etch-rate of adipic acid solution showing variation of 2DEG resistance in a lattice-matched InGaAs/InAlAs HEMT, with etch time.

the entire cap layer had indeed been removed. However, gates formed on these chips still formed leakage currents $> 100\text{nA}$. It was proposed that although Φ_B for $\text{In}_x\text{Al}_{1-x}\text{As}$ is larger than the equivalent barrier on InGaAs, it is still small enough for appreciable electron-tunnelling to occur. This is especially likely to be the case as $x \rightarrow 1$, since $\Phi_B = 0$ for InAs [160]. This approach to forming electrostatic gates was also therefore abandoned.

5.3.5 Thin Polyimide Films II

Although device yields using thin polyimide were poor, there were still chips which demonstrated reasonable gate behaviour. Given the drawbacks to the alternatives described above, the polyimide process was reassessed in order to optimise the yield.

Polyimide Solution Age

Stock polyimide is stored at -20°C . However, the various dilutions described on page 106 were made periodically from the main bottle and then stored at -5°C for several months. Evidence emerged that insulator quality was inversely proportional to solution age. Small bubbles form over time in these solutions and result in the creation of microscopic holes in the cured polyimide. As a result, freshly-mixed dilutions were used wherever possible and a policy of replacing these weekly was instituted.

Polyimide Curing

The second issue concerned the furnace used to cure the polyimide. Poor process control was resulting over-baking of the polyimide. Optimisation of the PID settings and the high-temperature limit led to temperature control to within $\pm 10^\circ\text{C}$. An investigation to

optimise the curing temperature found that using 300 °C or 350 °C gave no improvement in process yield, but led to increased hysteresis in gate operation. This bistability arises from charging and discharging of interface states at the junction between the insulator and semiconductor. For more on this topic see Refs. [22, 89]). The cure temperature was therefore returned to 250 °C.

Humidity Control

Section 2.2.4 describes some of the precautions used to limit the exposure of hydrophilic polyimide to water. However, even with relative humidity (RH) below 60%, it was found that for films thinner than ~300nm, the propensity for film leakage was proportional to RH. The cabinet housing the polyimide spinner was thus adapted to be filled with dry N₂ gas, locally reducing RH to <30%. Although the polyimide is still exposed to atmospheric humidity during subsequent processing, an improvement in films processed in this way was certainly obtained.

5.4 Split-Gate Fabrication

Following the implementation of the improvements described in the preceding section, the following process was adopted to define SGs onto a device. The steps outlined in sections 2.2 to 2.2.3 were used to create a Hall-bar with Ohmic contacts. With RH around the spinner reduced to ~30%, a 1:3 dilution of polyimide:thinner was spun-on at 8000rpm for 60s. Subsequent polyimide processing was identical to that described in section 2.2.4. Cured polyimide thicknesses of ~50nm were achieved in this way (see Fig. 5.3).

Polymethyl methacrylate (PMMA) was used as the e-beam resist chemical. This was deposited onto the chip in a two-layer process. Neat 495K A5 PMMA was spun onto the chip at 7000rpm for 60s and then baked for 1 hour in a dry 150 °C oven. Next, a solution of 950K A4 PMMA, diluted 1:1 with methyl-isobutyl ketone (MiBK), was spun onto the chip at 5000rpm for 60s, followed by a second 1 hour bake.

The e-beam tool was subsequently used to write the SG design into the PMMA as described in section 5.2.1. Exposed areas of the PMMA were removed in 4–6 seconds using a developer consisting of IPA:MiBK:MEK at 15:5:1. After rinsing in IPA, the chip was dried with N₂. The different chemistry of the two PMMA layers means that they react slightly differently to the e-beam. The result was that a larger region of the underlying PMMA was removed during developing than the top layer. This created a natural undercut profile which facilitated lift-off after gate-metal evaporation. 10nm Ti and 20nm Au were evaporated onto the chip. Immersion in acetone for several hours was required to lift-off the unwanted metal and ensure good definition of the tiny features of the SGs. Standard photolithography of the gate contact arms was then performed.

A thick insulation layer of 3:1 polyimide:thinner was fabricated. The PMMA procedure described above was repeated and the e-beam was used to define the top-gate pattern. After developing, 7nm NiCr gate-metal was evaporated. Each device, containing four SGs, was packaged into a standard 20-pin chip holder. However, care was taken to ensure that electrostatic discharge during bonding was prevented, since this could lead to destruction of the SGs.

Even with this optimised fabrication process, the overall yield of working devices was still < 5%. As a result, future work will include the installation of a new, purpose-designed oxide deposition unit for insulators. It is hoped that this will combine the benefits of the polyimide process with greater control over film quality and thickness. This will improve drastically the fabrication yield for these devices.

5.5 1D Transport Measurements

5.5.1 1D Transport in GaAs/AlGaAs

To validate the above process, SGs were fabricated onto a GaAs/AlGaAs HEMT sample as described in section 1.5. Also grown on the Veeco MBE chamber, previous measurements had confirmed electron mobility and density for this 2DEG to be $\mu = 4.89 \times 10^6 \text{ cm}^2/\text{Vs}$ and $n_s = 3.13 \times 10^{11} \text{ cm}^{-2}$ respectively, measured in the light at 1.5K. The completed chip containing the four SGs was cooled in the dark to $\sim 1.5\text{K}$ in a ${}^4\text{He}$ bath cryostat. Constant-voltage conductance measurements were then carried out (see page 39). Using a symmetric negative gate-bias (V_g) a 1D channel in the 2DEG was created midway between the SGs. As expected for this material system, gate leakage was low at $\ll 1\text{nA}$. Conductance was measured in the dark as the magnitude of V_g was steadily increased, until eventually the channel became pinched-off. Fig. 5.6a) shows the conductance data measured for two different SGs on this chip. These gates have dimensions of type 2 (red) and type 3 (black) as defined in the table on page 104. The curved region just below 0V is known as ‘definition’. This arises from the onset of depletion and the 2DEG width begins to shrink. The kink in the traces observed close to -0.2V indicates that the 1D channel has begun to form between the SGs. Although quantised plateaux are resolved on both traces, the confinement from Gate 3 is stronger than that from Gate 2. This might be expected since Gate 3 is 100nm longer than Gate 2 and the split in the gates is 100nm smaller.

The chip was then illuminated using a red LED and the conductance measurement was repeated for Gate 3 only [Fig. 5.6b)]. Illumination clearly increased the number of electrons in the system, since both the channel conductance at 0V, and the $|V_g|$ required to pinch-off the channel, have increased; the latter by a factor of three. The top-gate and polyimide were hence shown to be transparent at this wavelength. It may just be possible to distinguish a ‘double-hump’ on the definition section of Fig. 5.6b). This is indicative of

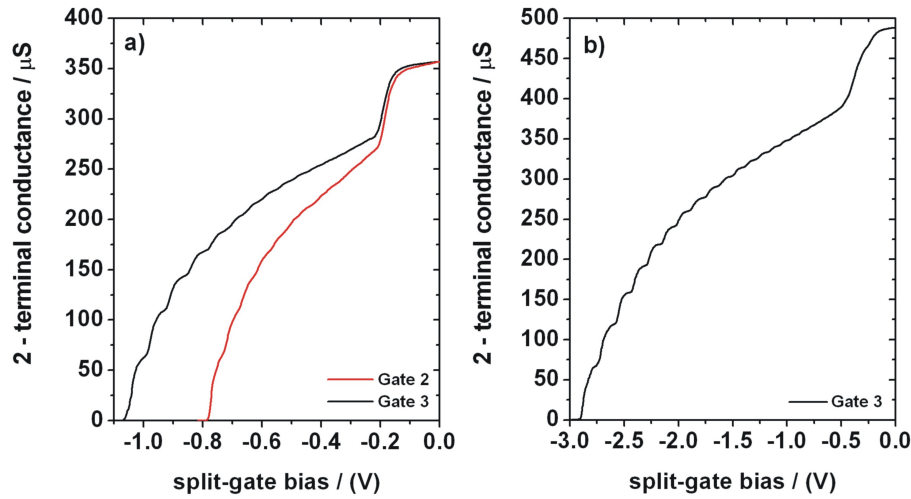


Figure 5.6: The dependence of 1D channel conductance on V_g **a)** before and **b)** after device illumination, for a GaAs/AlGaAs 2DEG at 1.5K.

electron population of the 2DEG second subband.

Fig. 5.7 presents the same data as Fig. 5.6a) but looking only at the region close to pinch-off. The data have been normalised to the conductance quantum, $2e^2/h$. A series resistance of $2.7\text{k}\Omega$ has been included in these calculations, the majority of which comes from the Ohmic contacts and measurement circuit. It is clear that the plateaux predicted by Eqn. (1.49) do indeed take integer values on this scale. The same analysis of the data in Fig. 5.6b) was then performed [Fig. 5.8]. The increase in electron population via illumination on the device has markedly increased the number of plateaux, with as many as 17 now resolved.

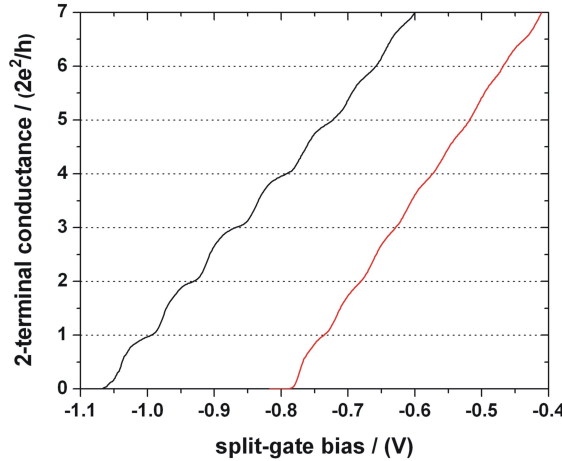


Figure 5.7: 1D conductance plateaux measured in the dark for Gates 2 and 3, in a GaAs/AlGaAs 2DEG at 1.5K.

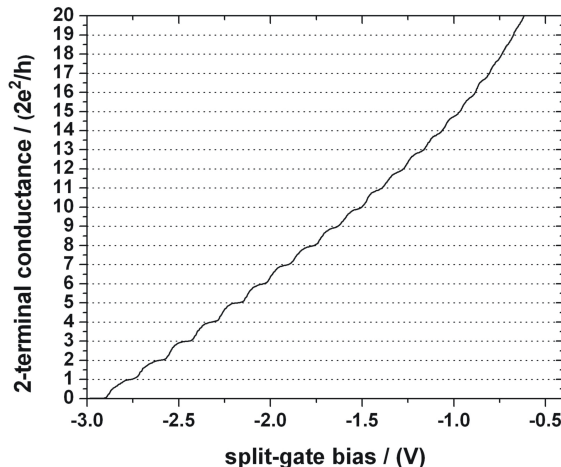


Figure 5.8: 1D conductance plateaux measured after illumination for Gate 3, in a GaAs/AlGaAs 2DEG at 1.5K.

Finally, operation of the top-gate was verified: electron density was shown to increase under positive bias, while the channel could be fully depleted of carriers and pinched-off under negative bias. The conclusion from this experiment was that the fabrication process described in section 5.4 was now validated and was capable of yielding operational SG devices.

5.5.2 1D Transport in $\text{In}_{0.75}\text{Ga}_{0.25}\text{As}$

The next challenge was to obtain working 1D devices for 2DEGs in InGaAs. Hall-bars were processed from one of the optimised undoped $\text{In}_{0.75}\text{Ga}_{0.25}\text{As}$ HEMT samples grown at 410°C (see section 4.4). Following the procedure outlined in section 5.4, SGs were then fabricated. After immersion in liquid ${}^4\text{He}$ the leakage currents for each chip were measured at 4.2K with a source measure unit (SMU). Due to the limitations of the $\sim 50\text{nm}$ thin polyimide films discussed in section 5.3, the majority of devices developed leakage currents at very small negative V_g . However, one particular chip, with SGs of types 5–8, showed slightly more interesting leakage characteristics [Fig. 5.9].

Where a leakage current is formed, a continuous rise in that current with negative V_g might be expected, as observed for SG 8. However, although the other three gates all leaked, the current quickly reached a plateau. For SGs 5, 6 and 7, the saturation values of the leakage current were measured as 24.5nA, 1.4nA and 49.7nA respectively. Noting the logarithmic scale on the y -axis, these data confirm the lack of control over the polyimide process: the variation in leakage current between the four gates on this single Hall-bar is enormous.

The leakage currents for SGs 5 and 7 were still too large to allow observation of

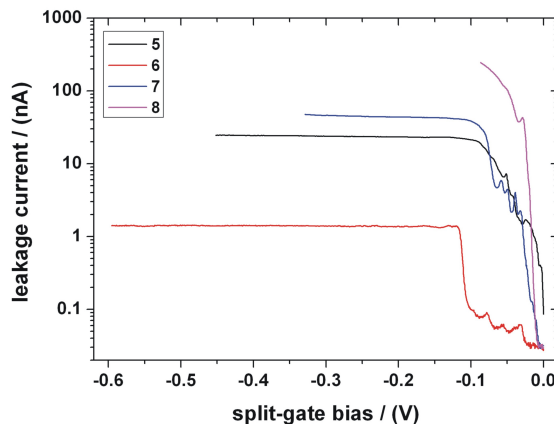


Figure 5.9: Variation of leakage current with V_g , measured at 4.2K for a chip fabricated from sample V277. The legend refers to the four SGs on the device, numbered as per the table on page 104.

quantised behaviour. Whilst a leakage current of 1.4nA is larger than would generally be acceptable, SG 6 was the most promising candidate for a working device. The channel conductance of Gate 6 was measured against V_g [Fig. 5.10 (left)]. The SG showed normal operation inasmuch as the channel could be fully depleted for $V_g \leq -0.6V$. The trace was relatively clean indicating that noise levels due to leakage were not excessive and good reproducibility was demonstrated between successive traces.

This chip was cooled in the dark to 1.5K in a pumped ^4He cryostat. Due to the

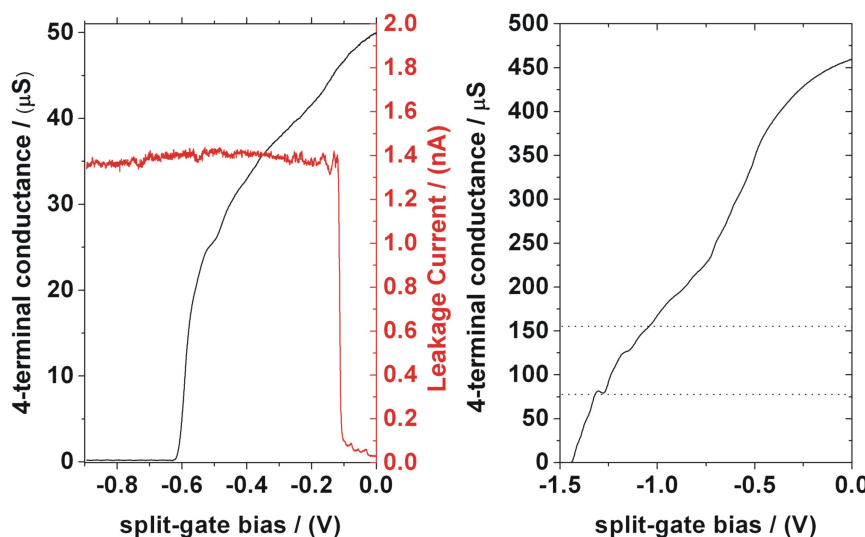


Figure 5.10: The dependence of the conductance on V_g of gate 6, at 4.2K (Left) and 1.5K (Right). The measured leakage current at 4.2K is shown in red. The theoretical positions of the first two conductance plateaux are indicated by dotted lines at 1.5K.

low electron density of the sample, the device was then flood-illuminated until no further increase in the conductance at 0V could be achieved. The 1D conductance was then remeasured [Fig. 5.10 (right)]. The theoretical positions of the first two conductance plateaux are shown at $77.58\mu\text{S}$ and $155.15\mu\text{S}$, respectively.

There is clearly a feature in this trace which coincides with the location of the first plateau. However, the conductance of the next ‘plateau’ is too low. There may be some additional features below the first plateau but these do not appear to correspond to the 0.7 structure discussed in section 1.6.4. This non-ideal behaviour could be explained by the presence of some kind of impurity within the 1D channel affecting the transport.

Differential biasing of the two halves of the SG can be used to vary the lateral position of the quantum wire between the gates. The aim was to find a position for the 1D channel which avoided the impurity suggested above. In addition to lateral biasing, conductance quantisation has been shown to improve in the presence of small, perpendicular magnetic fields. The explanation for this seems to be a reduction in backscattering from the edges of the quantum wire [5]. The plateaux are also widened due to an increase in subband spacing. The combination of these two effects can help to ‘clean-up’ the conductance data.

To this end, a series of conductance measurements using differential SG biasing were carried out in the presence of five different fields: 0.0T, 0.1T, 0.2T, 0.3T and 0.4T. For each field, eight sweeps of V_g were used to progressively vary the lateral position of the channel by $\pm 0.05\text{V}$. Using a typical value of $\sim 2\text{k}\Omega$ to correct for the series resistance of the channel, three traces showed agreement with theory. These were Sweep 3 from the data taken at 0.2T, and Sweeps 3 and 7 from the measurement at 0.4T [Fig. 5.11]. Since

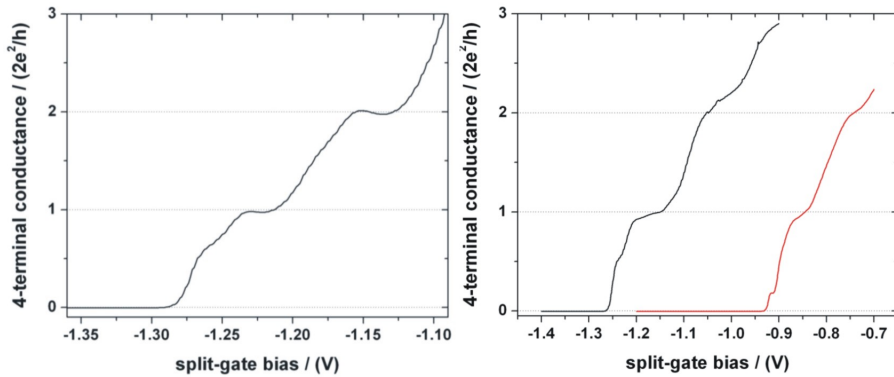


Figure 5.11: Conductance data from Sweep 3 measured at 0.2T (left) and Sweeps 3 and 7 measured at 0.4T (right) at 1.5K.

V_g is not now symmetric, it should be noted that the x -axis corresponds to the half of the SG for which V_g becomes increasingly less negative.

The first two plateaux for each trace are shown with, of the three, Sweep 3 at 0.2T (left) giving arguably the most strongly quantised results and closest agreement with

theory. Features below the first plateau can be discerned on all three traces. It is unclear whether these are spin-polarisation related, or some Coulomb blockade artefact [161].

The differential biasing used for Sweep 3 appeared to provide the optimal position for the 1D channel. During Sweep 3, one half of the gate was varied between -0.4V and -1.8V and the other half varied between 0V and -1.4V. The sweep rate was identical on both halves of the SG at 2V/hr. Unless otherwise stated, these were the conditions used to vary V_g for the remainder of these measurements.

Since the quality of the traces in Fig. 5.11 appeared to improve with field strength, further measurements were performed at still higher fields [Fig. 5.12 (left)]. The first plateau

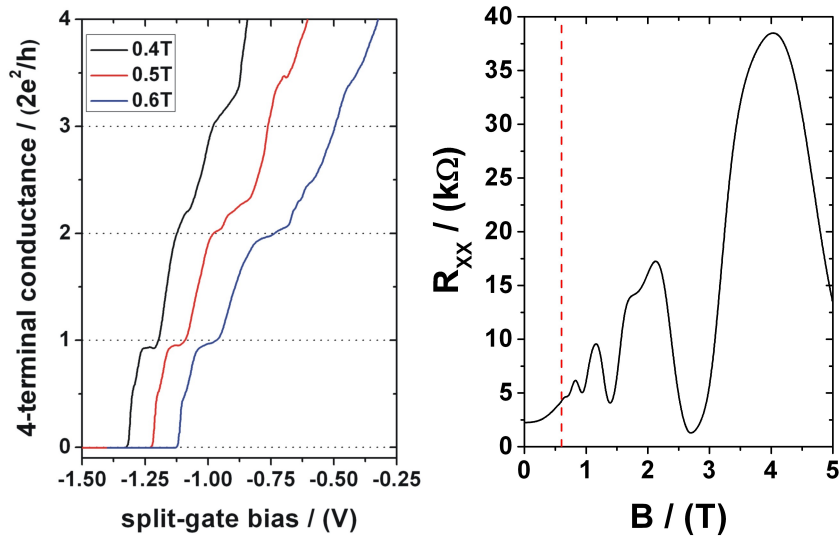


Figure 5.12: **Left:** Conductance data at 1.5K measured in magnetic fields of 0.4T, 0.5T and 0.6T. Traces have been offset by 0.1V for clarity. **Right:** Longitudinal 2DEG resistance with magnetic field up to 5T. The position of the dashed red line indicates $B = 0.6T$.

for each trace is in good agreement with theory. However, as field strength is increased, the position of the second plateau sequentially approaches the expected value of $2(2e^2/h)$, indicating an improvement in transport quality. To assess the overall magnetotransport of the 2DEG in this device, the SGs were grounded and the field dependence of the longitudinal resistance was measured [Fig. 5.12 (right)]. It is clear that the SdH oscillations begin just above 0.6T. This was therefore the highest field used in this work, since the presence of Landau levels would mean that transport was no longer dependent solely on conductance quantisation.

Analysis of the conductance using d.c. bias spectroscopy was then performed at 0.6T. Starting at -0.1mV, a bias, V_{sd} , was applied between the source and drain of the device, the magnitude of which was raised to +5.0mV in 0.05mV increments. V_g on both sides of the SG was swept symmetrically between -0.6V and pinch-off at -1.55V, at each value of V_{sd} [Fig. 5.13].

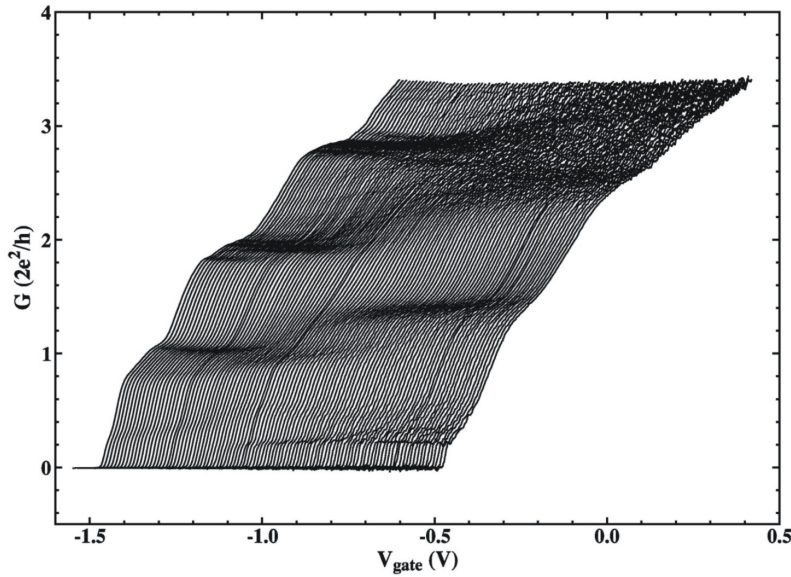


Figure 5.13: D.C. bias spectroscopy at 1.5K of SG 6 in the presence of a perpendicular field at 0.6T. V_{sd} was increased from -0.1mV to +5.0mV in increments of 0.05mV, while V_g was swept symmetrically from -0.6V to -1.55V. Traces are shown here offset by 0.01V for clarity.

The first three integer plateaux are well resolved in this measurement, as well as a plateau at $1.5(2e^2/h)$. This half-integer plateau is not due to spin-splitting but rather to the effect of applying a finite source-drain bias. Assuming that the integer plateau observed at $V_{sd} = 0V$ are the result of electrons moving in either direction, an increase in V_{sd} means that electron transport through the SG will be suppressed in one direction. This reduces the conductance by half. For the plateau at $1.5(2e^2/h)$, E_f has been raised sufficiently by V_{sd} that electrons moving in both directions from the first level are both now below E_f and so contribute to conduction. However, only half of those from the second level contribute giving rise to the observed conductance value.

For the highest values of V_{sd} used here, noise becomes an issue, particularly as V_g tends toward zero. Nevertheless it is possible to resolve the third half-integer plateau at $2.5(2e^2/h)$. The 0.7 structure is also present in this measurement, the position of which is raised with increasing V_{sd} , until it stabilises at $0.85(2e^2/h)$. This behaviour has been observed previously in GaAs/AlGaAs devices [50, 162]. At around the same source-drain bias, the 0.25 structure, introduced on page 24, also develops.

This d.c. bias spectroscopy experiment was repeated, using instead the Sweep 3 bias conditions described above to vary V_g asymmetrically. A source-drain bias range of $-0.1mV \leq V_{sd} \leq +4.0mV$ was used here, with 0.05mV increments between each sweep of V_g [Fig. 5.14].

A comparison of this data with Fig. 5.13 reveals several differences. While there is

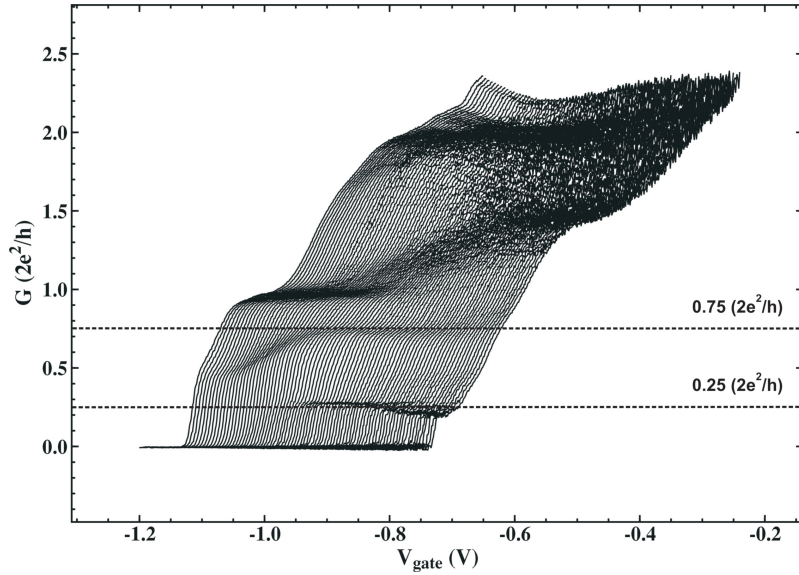


Figure 5.14: D.C. bias spectroscopy at 1.5K of SG 6 in the presence of a 0.6T perpendicular field. V_{sd} was increased from -0.1mV to +4.0mV in increments of 0.05mV. V_g was varied asymmetrically using Sweep 3 bias conditions. Traces are shown here offset by 0.005V for clarity.

no plateau at $3(2e^2/h)$, several other features may be distinguished in addition to the clear first and second integer plateaux. What appears to be the suggestion of a plateau at $0.5(2e^2/h)$ was shown later to be some kind of broadened Coulomb blockade feature [161]. As V_{sd} is increased a plateau develops at $0.75(2e^2/h)$ while the feature at $0.25(2e^2/h)$ is again observed at the same bias. The data presented in Fig. 5.13 shows what are believed to be the first measurements of these plateaux at $0.75(2e^2/h)$ and $0.25(2e^2/h)$ in $\text{In}_{0.75}\text{Ga}_{0.25}\text{As}$. In addition to their clarity and flatness, what is particularly striking about them is the accuracy with which they lie on the prefactor values of 0.75 and 0.25. Features of this kind are consistent with the ‘*spin-gap model*’ which has been proposed to explain these phenomena in other materials [48, 162, 163]. Good correlation between these results and the predicted values lend added credence to this model.

As before, the sweeps at high values of V_{sd} are noise-limited but the half-integer plateau at $1.5(2e^2/h)$ is again resolved. The data in Fig. 5.14 bears a certain resemblance to several figures presented in Ref. [164]. These show the equivalent conductance structure for quantum wires etched into GaAs/AlGaAs devices, measured using this d.c. bias technique. However, in that work magnetic fields of $\sim 12\text{T}$ were required to resolve the non-integer plateaux at $0.25(2e^2/h)$ and $0.75(2e^2/h)$. This is consistent with the higher g -factor of $\text{In}_{0.75}\text{Ga}_{0.25}\text{As}$ compared with GaAs. These results demonstrate that high-quality $\text{In}_{0.75}\text{Ga}_{0.25}\text{As}$ can also be used to study electron-electron interactions.

The dependence of the longitudinal (R_L) resistance of the 2DEG on perpendicular

magnetic field was then remeasured at various values of V_g to assess how the SdH oscillations were affected by the width of the 1D channel. Five different widths of the 1D channel were investigated, with the magnetic field swept each time between 0T and 5T. In addition to Sweep 1 measured at $V_g = 0V$ and Sweep 5 at $V_g = -1.0V$, three intermediate measurement positions were selected, with Sweeps 2, 3 and 4 at $V_g = -0.25V, -0.50V$ and $-0.75V$ respectively. These are marked on Fig. 5.15, with Sweeps 3 and 4 chosen to coincide with the first two integer plateaux.

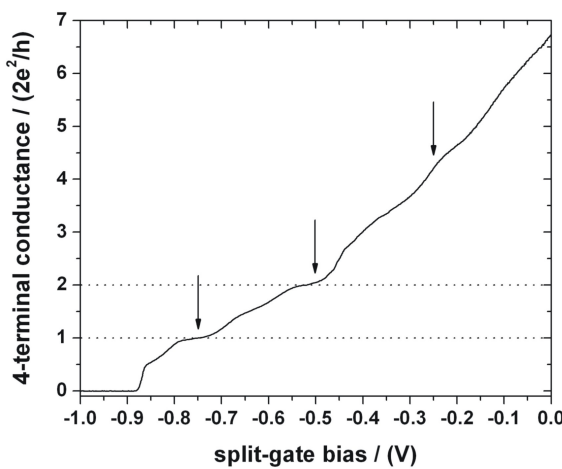


Figure 5.15: SG biases of $V_g = -0.25V, -0.50V$ and $-0.75V$ chosen for investigations into the dependence of channel resistance on magnetic field strength (measurement positions at $V_g = 0V$ and $V_g = -1.0V$ are not shown). The first two spin-split plateaux are also discernable here.

For Sweep 1, where $V_g = 0V$, similar SdH oscillations to those shown in Fig. 5.12 (right) were measured [Fig. 5.16]. Hall data was also measured for this sweep (red) which shows good quantisation, with the expected, spin-resolved plateaux at $\nu_{2D} = 1, 2, 3, \dots, 6$. For Sweep 5 (purple), with $V_g = -1V$ and the channel pinched-off, the resistance was high and showed no evidence of oscillatory behaviour. However, for the three intermediate V_g positions, the situation was more complex, as predicted by Eqns. (1.55) and (1.56). The zero-field resistance for each trace is shown in the inset to Fig. 5.16. With the y -axes normalised to h/e^2 , R_{xx} is equivalent to $1/\nu$. The spin-resolved filling factor is reduced from $\nu = 8$ in Sweep 2, to $\nu = 4$ in Sweep 3, to $\nu = 2$ in Sweep 4. By raising $|V_g|$ it is thus possible to observe directly the depopulation of edge states in the 1D channel. As the magnetic field is increased, sweeps 2 and 3 show SdH oscillations but when E_f is between Landau levels, R_L is non-zero due to edge state reflection at the 1D channel, as discussed in section 1.6.3.

Below $\sim 2T$, Sweep 4 also follows the SdH oscillations of the previous measurements. At higher fields however, behaviour begins to diverge from that measured in the previous

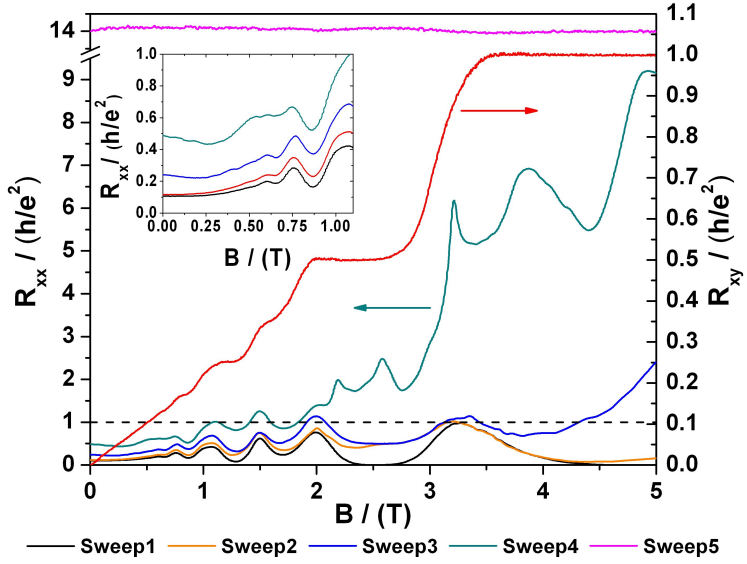


Figure 5.16: Dependence of longitudinal resistance at 1.5K on magnetic field strength, at five SG voltages. The Hall resistance for Sweep 1 (red) corresponds to the right y -axis. The dashed black line at $R_{xx} = 1$ (left y -axis) shows the resistance above which the last edge state in the 1D channel is depopulated. The inset shows an expanded view of the low-field part of the main graph.

sweeps. The transport appears to approximate some series combination of the 2DEG SdH oscillations and quantised resistance of the 1D channel at $h/\nu e^2$. This type of behaviour has been observed previously for GaAs/AlGaAs devices [5]. However, the well-resolved plateaux measured just above channel pinch-off in that study are not seen here. Instead, the ‘plateaux’ are superimposed with irregular oscillatory features.

For resistances above $1/\nu = 1$, indicated by the dashed line, the last edge state in the 1D channel has been depopulated and transport through the wire is via tunnelling alone. In this device, separation between the Ohmic contacts and the SG is of the order of $4 - 6 \mu\text{m}$. It is therefore possible that scattering between edge states over this length scale in the 2DEG may have communicated some artefact of the SdH oscillatory response. This then tunnels between the edge states adjacent to the 1D channel. However, the appearance of resonance-like structures, over and above those expected from the SdH oscillations, are more difficult to explain. Repeating these measurements using the diagonal voltage-probe geometry described on page 23 will simplify the data by removing any dependence on the 2DEG filling factor from the experiment. It is hope that this will help confirm the origin of these structures.

5.6 Summary

In this chapter the use of electrostatic SGs to form 1D channels in a 2DEG was described. SG design and e-beam lithography were discussed. A new process to fabricate SG devices was developed and the particular challenges posed by the need for gate insulation were covered. Two alternative approaches to polyimide were trialled and finally discarded: the use of silicon nitride insulation and the use of adipic acid to form a recessed gate. Polyimide insulation was finally adopted as the best available option. The process was shown to be at the very limit of its capability, with poor reproducibility and low device yields. Nevertheless, the process was successfully validated and working devices were fabricated.

The last section of the chapter describes low-temperature measurements performed on these quantum wires in $\text{In}_{0.75}\text{Ga}_{0.25}\text{As}$. Optimised biasing and perpendicular magnetic field conditions were found which enabled good, reproducible measurements of 1D conductance. Integer quantised conductance plateaux were measured which showed agreement with theory. Using a d.c. bias technique, the development of various additional structures in the conductance data were also observed. These included the formation of plateaux at half-integer values of $2e^2/h$, the 0.7 structure and features at $0.75(2e^2/h)$ and $0.25(2e^2/h)$, which were seen at high V_{sd} and are consistent with a spin-gap model.

It is believed that this is the first measurement of these features at $0.75(2e^2/h)$ and $0.25(2e^2/h)$ in $\text{In}_{0.75}\text{Ga}_{0.25}\text{As}$ and demonstrates that this material may prove to be a useful tool for studying electron-electron interaction effects such as these.

An interesting magnetoresistance response was measured in the quantum wire with V_g fixed so that conductance was located at the first plateaux. Some series superposition of the SdH oscillations with the quantised resistance of the channel is seen, although the situation is complicated by the fact that above $\sim 2T$, conductance through the wire is via electron tunnelling alone. Further work is essential in order to fully understand these properties.

In future it is hoped that a more reliable insulation process will improve the fabrication yield. This will, in turn, enable an in-depth study of both $\text{In}_{0.75}\text{Ga}_{0.25}\text{As}$ quantum wires such as these, and $\text{In}_x\text{Ga}_{1-x}\text{As}$ for $x < 0.75$, for example to probe the 0.7 structure and its analogues. The higher Landé g -factor of these materials compared with GaAs means that they show spin-polarisation at much lower magnetic fields. As a result this work may assist with the construction of a comprehensive explanation of these 1D conductance features.

Chapter 6

Zero-Dimensional Electron Systems: Self-Assembled Quantum Dots

6.1 Introduction

Self-assembled quantum dots (SAQDs) were introduced in section 1.6.5. InAs SAQDs grown in the GaAs/AlGaAs material system have been widely investigated [165–167]. The incorporation of such SAQDs into a resonant tunnelling diode (RTD) heterostructure has been shown to enable the detection of single photons at wavelengths below 800nm [168]. The ability to detect individual light quanta is an essential component of some quantum key distribution (QKD) systems for secure cryptography and quantum computers [169, 170]. The potential advantages of a RTD-based device over the commonly-used avalanche photodiode (APD) single-photon detector are higher efficiency with lower dark-count rates.

As discussed previously, $\text{In}_{0.532}\text{Ga}_{0.468}\text{As}$ and $\text{In}_{0.524}\text{Al}_{0.476}\text{As}$, hereafter referred to in this chapter as InGaAs and InAlAs, are lattice matched to InP at 300K. The band gap energies of 0.76eV for InGaAs and 1.46eV for InAlAs, correspond to a wavelength range from $1.3\mu\text{m}$ to $1.6\mu\text{m}$ [171]. This region of the electromagnetic spectrum is of particular interest since it coincides with the absorption minima of standard silica-based optical fibres at $\sim 1.3\mu\text{m}$ and $\sim 1.55\mu\text{m}$, respectively. The motivation behind the work presented in this chapter was to build a novel, long-wavelength, single photon detector (SPD), based on a RTD [168], with potential applicability to fibre-based QKD.

Section 6.2 introduces the mechanism of SAQD formation. Studies on numerous aspects of the growth of InAs SAQDs on InAlAs and InGaAs have been published previously [172–174]. However, to-date there has been no single comprehensive analysis of the de-

pendence of both the structural and optical SAQD properties on MBE growth conditions. Section 6.3 seeks to provide, for the first time, such a study. The effects of InAs deposition thickness, temperature, growth interruptions, InAs growth rate and buffer material on SAQD properties are investigated. In section 6.4, initial work to optimise a RTD device and to subsequently place InAs SAQDs within this heterostructure are discussed. Finally, in section 6.5, a working SPD of this type is demonstrated for the first time, operating at $1.3\mu\text{m}$. The device characteristics are comparable to those reported for the short-wavelength detector in Ref. [168], which has a dark-count rate of $4 \times 10^{-6}\text{ns}^{-1}$ and an internal efficiency of $\sim 5\%$.

As a consequence of the work described in this chapter, several papers have been published. In particular, there are significant overlaps between Ref. [175] and section 6.3; Ref. [176] and section 6.4; Ref. [177] and section 6.5.

6.2 Theory of SAQD Formation

A thermodynamic explanation of surface segregation states “...that the component with the lower heat of vaporisation should be enriched in the surface to minimise the surface free energy” [82]. For the formation of 3D islands of InGaAs on GaAs, a mechanism has been proposed which is based on the surface segregation of In since this is the largest atom in the system [178]. As InGaAs is deposited, an In-rich layer is formed at the surface of the 2D film. When the In mole fraction in this layer reaches $x = 0.85$, its strain is such that the Stranski-Krastanov (SK) transition occurs and growth proceeds via 3D islanding.

InAs SAQDs form readily on GaAs [Fig. 6.1]. For this system, intermixing between InAs and the underlying GaAs means that this critical In concentration is not achieved immediately. Deposition of one monolayer (ML) of InAs results in the formation of a 2D $\text{In}_x\text{Ga}_{1-x}\text{As}$ layer, where $x \sim 0.82$, after which chains of ‘floating’ InAs form on the surface. The strain required for the SK transition is reached soon afterwards, by which time 0.5-0.6ML of highly mobile InAs chains exist on the surface. These are then available

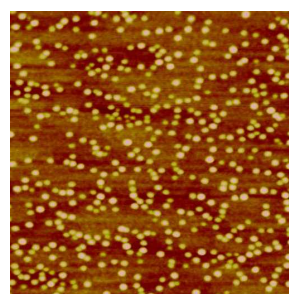


Figure 6.1: $1 \times 1\mu\text{m}^2$ AFM image of $\sim 2.23\text{ML}$ InAs SAQDs on GaAs (sample grown by Dr. M.E. Ikpi, at the Cavendish Laboratory, University of Cambridge).

for incorporation into well-defined, quasi-circular SAQDs. Steps at the edges of monolayer terraces are known to be favourable SAQD nucleation sites [179, 180]. The dimensions of each SAQD dictate its individual subband spacing. The finite distribution in feature size across an array of SAQDs means that the band gap energy of the system will have a finite width. Average dot size and density can be tuned by adjusting the deposition thickness and growth conditions.

An extension of these ideas is required to describe the growth of InAs SAQDs on InAlAs. Vertical In segregation is known to be pronounced in InAlAs [181]. This means that prior to InAs growth, the In composition of the InAlAs buffer surface will be higher than in the bulk. This will inhibit intermixing, thus enhancing the In concentration of the 2D alloy layer. However, at 3.2%, the mismatch between InAs and InAlAs is significantly smaller than for the InAs/GaAs system. This means that the critical thickness required for the SK transition will be larger.

6.3 InAs Quantum Dots on InAlAs and InGaAs

Using RHEED analysis during the deposition of InAs on InAlAs, the change from 2D to 3D morphology was monitored enabling a critical thickness of $2.5 \pm 0.5\text{ML}$ to be measured. This correlates well with previously measured values [182, 183]. The relatively high growth rates used here contribute to this error, although the high temperature-dependency of the In sticking coefficient is also a factor [108]. Depending on Group V overpressure, growth rate is drastically reduced above $\sim 500^\circ\text{C}$ due to desorption and as a result the apparent deposition thickness before the SK transition takes place is increased.

Calibration of the InAs growth rate was discussed in section 3.4 and control of the In mole fraction within bulk InAlAs layers was shown to be within $\pm 0.5\%$ using XRD. This meant that all layers were thus fully strained. A set of samples were grown to test the effect of MBE growth conditions on the structural and optical properties of InAs SAQDs on InAlAs. They were grown on semi-insulating (SI) InP (0 0 1) substrates with the heterostructure summarised in Fig. 6.2. Nominally identical growth conditions were

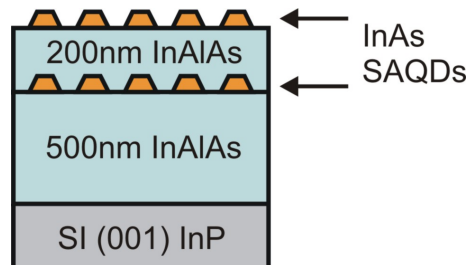


Figure 6.2: Schematic diagram of the InAs SAQD calibration heterostructure. The positions of the InAs dot layers are represented by the truncated orange pyramids.

maintained for both the buried SAQDs and those grown on the free surface. Optical properties of the buried SAQDs were probed by photoluminescence (PL) measurements, while the structure of the surface dots could be imaged directly, using atomic force microscopy (AFM).

The V/III BEP ratio was maintained at ~ 30 . Unless otherwise specified, the growth temperature as measured by optical pyrometry was 460°C and the InAs deposition rate for the SAQDs was nominally 0.1ML/s, which corresponds to an In flux five times lower than that used for the bulk InAlAs layers. These growth rates were determined through a combination of RHEED and XRD measurements, as described in section 3.4. Since there was only one In cell, ten minute growth interruptions under As_4 were introduced before and after each SAQD layer, during which time the In flux could be adjusted. Following deposition and the growth interruption associated with the surface dots, the sample was cooled under As_4 to 450°C , in < 5 minutes.

6.3.1 Effect of Deposition Thickness

The first experimental series investigated the effect of InAs deposition thickness on SAQD structural and optical properties. Samples were grown with 1.5ML, 2.0ML, 3.0ML, 4.0ML, 5.0ML and 6.0ML of InAs. The InAs layer in the 1.5ML sample is below the critical thickness. AFM analysis of the InAs wetting layer revealed a 2D morphology, with root mean square (RMS) roughness of $1.52 \pm 0.03\text{\AA}$ over a $2.5 \times 2.5\mu\text{m}^2$ area. The surface structure of the other five samples was then assessed using AFM [Fig. 6.3]. The sample

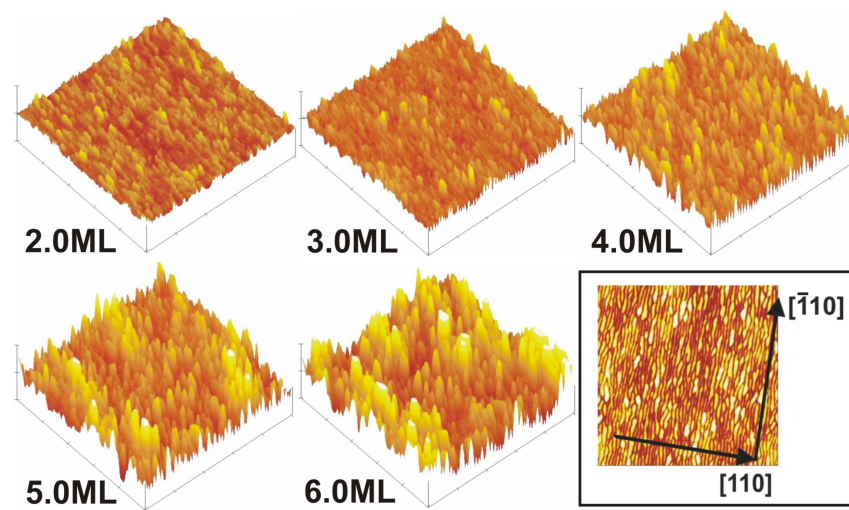


Figure 6.3: $1\mu\text{m}^2$ AFM images showing the deposition thickness dependence of the surface morphology of InAs on InAlAs. To enable ease of comparison, the scale on the z -axis is 5nm for each image. The bordered image is a plan-view of the 4.0ML sample, clearly showing the anisotropy of the InAs features.

with 2.0ML InAs also appears to be relatively flat, although the RMS roughness is almost three-times higher, at $4.37 \pm 0.09\text{ \AA}$. SAQDs are then resolved on each of the other samples where the InAs deposition thickness is $\geq 3\text{ML}$. Comparing the inset image of the 4.0ML sample with Fig. 6.1 shows that, in contrast with the discrete circular dots formed by InAs on GaAs, these features are highly anisotropic. These ‘dash-like’ InAs SAQDs extend along the $[1\bar{1}0]$ crystal axis, in agreement with previous studies of this material system [184]. ‘Dot-like’ InAs features have been reported on InP where very low V/III ratios were used [185]. However, to prevent the InAlAs from being Group III-rich, the V/III ratio required in this chamber is at least ~ 25 .

Analysis of the inset AFM image yielded an average feature periodicity of $19.4 \pm 2\text{nm}$ parallel to $[110]$ and $79.6 \pm 12\text{nm}$ parallel to $[\bar{1}10]$; a length-to-width ratio of ~ 4 . On a (001) oriented surface, step-edges in the $[110]$ direction are anion-terminated. This makes them more reactive with respect to In than the perpendicular cation-terminated step-edges. InAs growth therefore proceeds more quickly parallel to $[\bar{1}10]$ [186]. In addition, it has been proposed that strain effects are responsible for limiting growth in the $[110]$ direction [187].

All SAQD counting and dimensional analysis of the AFM data in this dissertation was carried out using the *SPM Image Magic* program written by A. Kryzhanovsky [188]. For the images in Fig. 6.3, SAQD heights and radii were measured and the feature density calculated [Fig. 6.4]. InAs SAQD size increases linearly with deposition thickness over

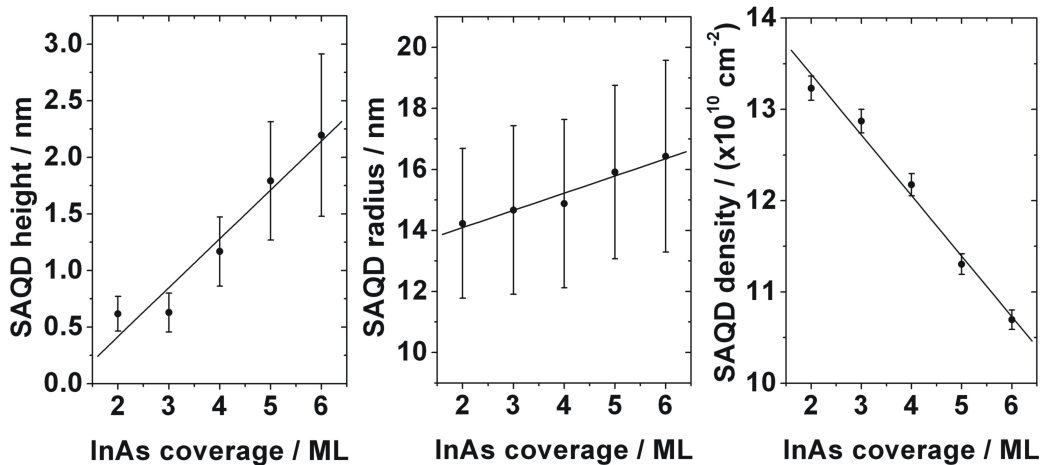


Figure 6.4: The effect of deposition thickness on the size and density of InAs SAQDs on InAlAs.

the range studied, while the density conversely falls. This indicates that small dots which form initially, coalesce into larger features as InAs coverage is increased. It should be noted that the bars on these plots show the variance in feature size across the sampled area, rather than measurement error. These measurements are complicated by the fact

that the software was primarily designed for analysis of the circular InAs SAQDs formed on GaAs. This can therefore compromise the reliable identification of the dash-like InAs SAQDs on InAlAs.

PL emission spectra of the buried SAQDs were then measured [Fig. 6.5]. Gaussian

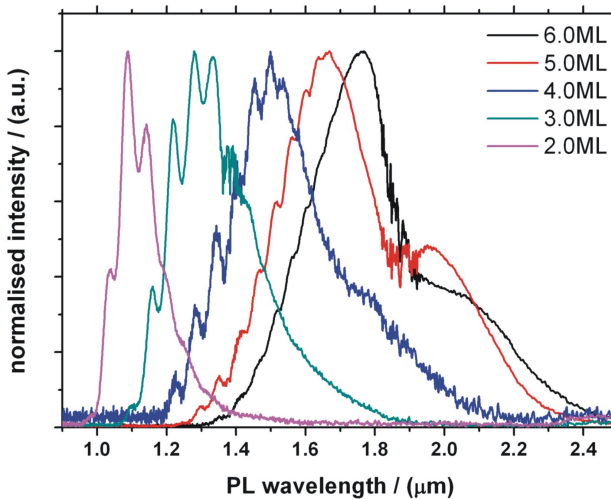


Figure 6.5: The effect of deposition thickness on PL from InAs SAQDs. The samples were cooled to 4.2K in a continuous-flow ${}^4\text{He}$ cryostat and excited using a 488nm Ar^+ pump laser. The absorption features just below $1.4\mu\text{m}$ are due to the presence of water vapour in the beam path.

distributions were fitted to the spectra and a peak emission wavelength determined for each. These peak wavelengths undergo a red-shift as the InAs deposition thickness increases. As expected, the subband energy spacing is reduced in larger SAQDs. The width of each spectral peak is directly related to the range in SAQD size across the area probed by the pump laser. The full width at half maximum (FWHM) of each spectrum also increases with InAs coverage, from $100 \pm 12\text{nm}$ at 2.0ML to $190 \pm 5\text{nm}$ at 6.0ML. This confirms the trends in Fig. 6.4, particularly in SAQD height, of increasing size variance with InAs thickness. Fig. 6.6 shows that the emission wavelength can be tuned linearly, at $170\text{nm}/\text{ML}$, between $1.09 \pm 0.04\mu\text{m}$ and $1.76 \pm 0.07\mu\text{m}$.

Structure can be resolved on each of the spectra in Fig. 6.5. These oscillatory-like features become less pronounced but increase in number for samples with greater InAs thicknesses. The temperature dependence of the PL spectrum was investigated to ascertain whether this structure derived from the sample itself or was merely some artefact of the measurement technique [Fig. 6.7 (Left)]. The quality factors of these resonant features are reduced due to thermal broadening as the measurement temperature is raised. This confirms that these features do indeed originate from the sample. The peaks superimposed on these spectra experience a red-shift as the measurement temperature is increased. The

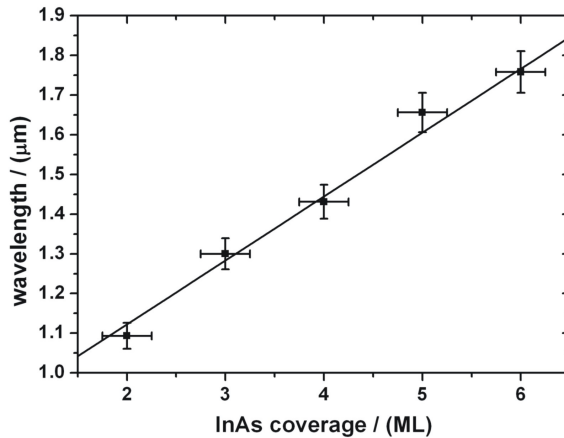


Figure 6.6: The effect of deposition thickness on the peak PL wavelengths from Fig. 6.5, at 4.2K.

position of the peak close to $1.3\mu\text{m}$ shows an excellent fit to a second-order dependence with measurement temperature [Fig. 6.7 (Right)]. Similar structure has been previously observed on PL spectra from InAs SAQDs such as these which was shown to be due to monolayer fluctuations in the InAs thickness [189–191]. Given the extremely non-uniform InAs morphology which is apparent on these samples, this explains the spectral features seen here.

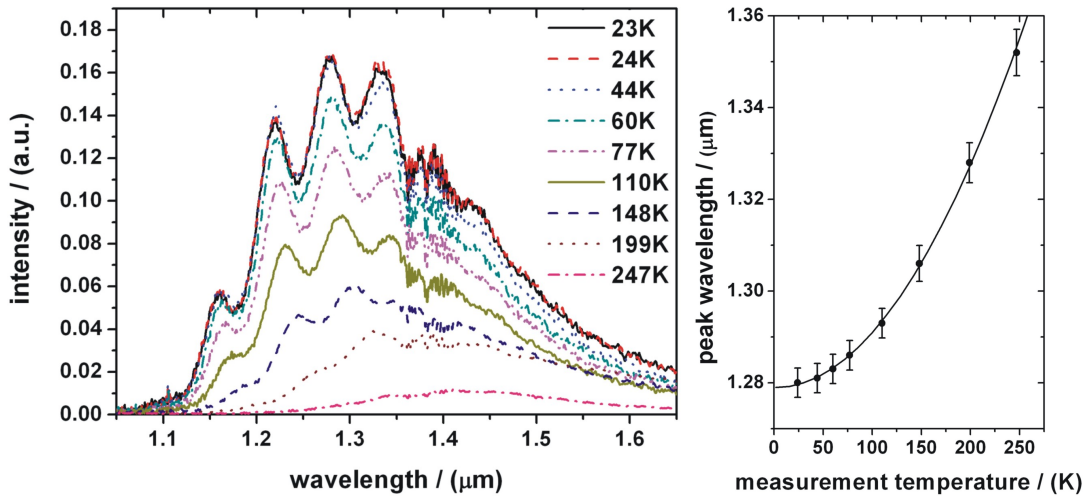


Figure 6.7: **Left:** The effect of the analysis temperature on the PL spectrum measured for a sample with 4.0ML InAs deposition thickness, at 4.2K. **Right:** The temperature dependence of the position of the peak just below $1.3\mu\text{m}$ at 23K.

6.3.2 Uniformity of SAQD Formation

AFM images were taken at 5mm intervals across the diameter of a 2" sample. Variation in average dot radius, height and density was plotted against position, enabling an assessment of SAQD uniformity [Fig. 6.8]. Dot height and radius are essentially constant, with mean

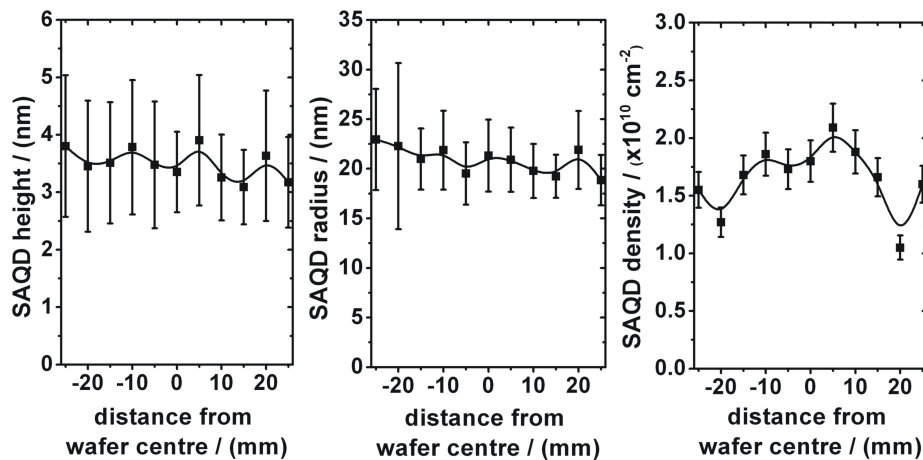


Figure 6.8: Variation of SAQD size and density with position across a 2" wafer. The bars indicate variance rather than measurement error

values of $3.49 \pm 0.08\text{nm}$ and $20.87 \pm 0.41\text{mm}$ respectively. The density of SAQDs is also relatively flat except for anomalous points at $\pm 20\text{mm}$, where density appears to be rather lower. These overall trends of SAQD uniformity are in keeping with the conclusions from section 3.5.3 which showed that InAs growth rate was constant to within $\pm 1\%$ across a 2" wafer.

6.3.3 Effect of Growth Temperature

Using RHEED, the InAs growth rate was calibrated at 460°C as measured by pyrometer. Three samples, with nominally 7.5ML InAs coverage, were grown at 440°C , 460°C and 480°C , as measured by optical pyrometry [Fig. 6.9].

As the substrate temperature is increased, the InAs features appear to become smaller and more uniform in size. These qualitative observations are borne out by analysis of these images [Fig. 6.10].

Each variable shows a linear dependence on growth temperature over the range studied. While SAQD density increases, height and radius are reduced. This can be explained by the fact that the In-sticking coefficient reduces significantly with increasing temperature. For a constant In flux and growth time, the final thickness of the epilayer will be highly dependent on substrate temperature. The time taken for the critical thickness to be reached increases with temperature, thus delaying the SK 2D-3D transition [192]. This

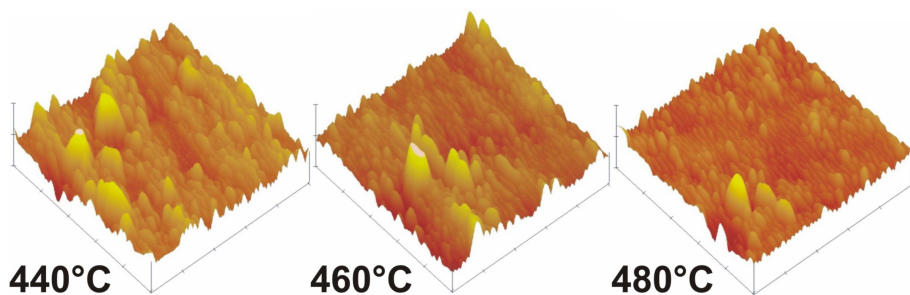


Figure 6.9: $1\mu\text{m}^2$ AFM images showing the temperature dependence of the appearance of InAs SAQDs on InAlAs

means that InAs SAQDs begin to form earliest on the coolest samples and then have longer to grow and coalesce, compared with those grown on hotter substrates. The result is larger, less dense SAQDs. In addition, even a small difference in sticking coefficient with temperature would be exaggerated by the long growth interruption following dot deposition [193].

PL spectra from these samples support these conclusions [Fig. 6.11]. Peak wavelength is blue-shifted by $3.5 \pm 0.6\text{nm}/^\circ\text{C}$ as substrate temperature is raised, due to the reduction in size of the SAQDs [Fig. 6.11 (Left)]. The FWHM of the peaks also contracts with increased growth temperature, indicating improved SAQD size uniformity. For the non-normalised data, a twofold increase in emission intensity is obtained from the sample grown at 480°C , indicating superior crystal quality [Fig. 6.11 (Right)]. The effect of growth temperature on PL wavelength has been studied previously for a similar SAQD system [194]. In that work, InAs SAQDs were grown on InGaAlAs using gas-source (GS)-MBE. Raising growth temperature from 480°C to 500°CA also resulted in increased PL intensity. However,

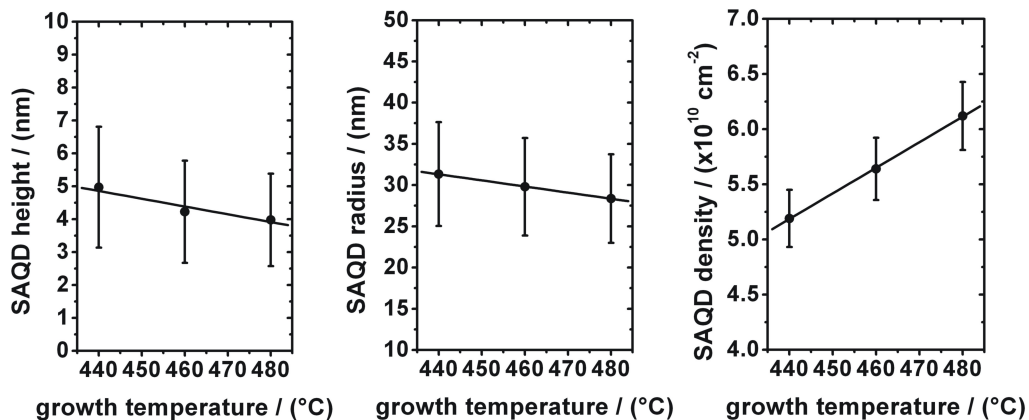


Figure 6.10: Variation of size and density with growth temperature, for InAs SAQDs on InAlAs. The bars indicate variance rather than measurement error

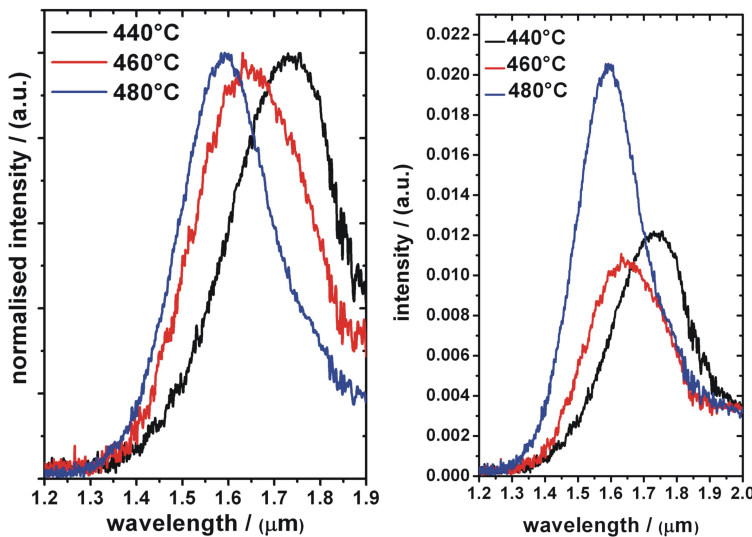


Figure 6.11: **Left:** Variation of normalised PL with growth temperature, for InAs SAQDs on InAlAs. **Right:** The same data presented without intensity normalisation. PL was measured in both cases at 4.2K.

in contrast with the findings presented here, the peak wavelength of their SAQDs were unaffected by growth temperature over this interval. This may be due to a difference in the V/III ratio used for GS-MBE, which will affect the In desorption rate.

6.3.4 Effect of InAs Deposition Rate

SAQD samples containing 4.0ML InAs were grown using InAs deposition rates of 0.2ML/s, 0.3ML/s and 0.5ML/s. PL was measured for each of these samples, revealing that the peak emission wavelength is essentially independent of InAs deposition rate [Fig. 6.12]. Although a small increase of $21 \pm 5\text{nm}$ was observed as the InAs growth rate was raised from 0.2ML/s to 0.5ML/s, this increase in wavelength is within the growth-to-growth reproducibility for these SAQD samples.

6.3.5 Effect of Growth Interruptions

As explained on page 125, growth is interrupted before and after InAs deposition. To investigate the extent to which this affects the properties of the SAQDs, three samples were grown with, respectively, 2×10 minute interruptions, 2×5 minute interruptions, and 2×0 minute interruptions. These pauses were initially introduced to enable the In flux to be altered between bulk and SAQD deposition values. Therefore, in order to be able to grow a sample without interruption, it was necessary to deposit the SAQDs in these samples at $\sim 0.5\text{ML/s}$: the same In flux as for epitaxy of the bulk. However, as shown in the previous section, PL wavelength is essentially unaffected by this change in growth

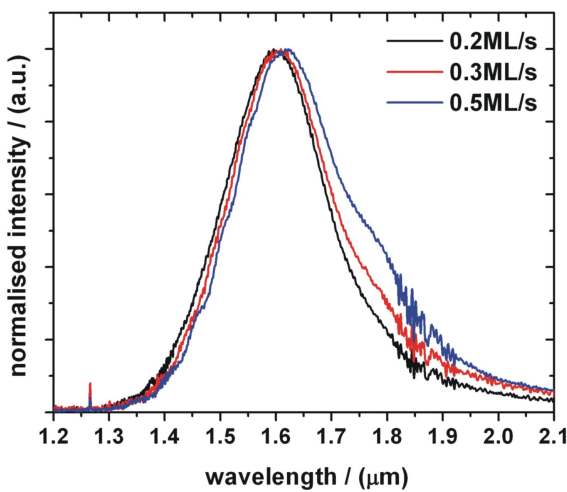


Figure 6.12: Left: Variation of normalised PL with deposition rate for InAs SAQDs on InAlAs. PL measured at 4.2K.

rate.

The AFM image of the sample grown without any interruptions seems to show a relatively uniform distribution of SAQDs of intermediate size [Fig. 6.13]. As the length of the growth interruptions are increased to five and then ten minutes, there seems to be a transition towards the development of larger features. Indium from the initially-formed SAQDs (seen on the sample without growth interruptions) begins to migrate across the surface and to attach to larger dots. Inevitably, this means that some of those initial SAQDs become smaller. The result is the development of a pseudo-bimodal distribution of SAQDs, with a mixture of both smaller and larger features, compared with the size of those initial SAQDs. As discussed on page 127 the *SPM* dot-counting software is not designed for this type of SAQD geometry and so is unable to resolve this bimodality. It indicates a fairly constant dot size and density across the three samples but this might be expected since this is essentially a measurement of the mean across the sampled area.

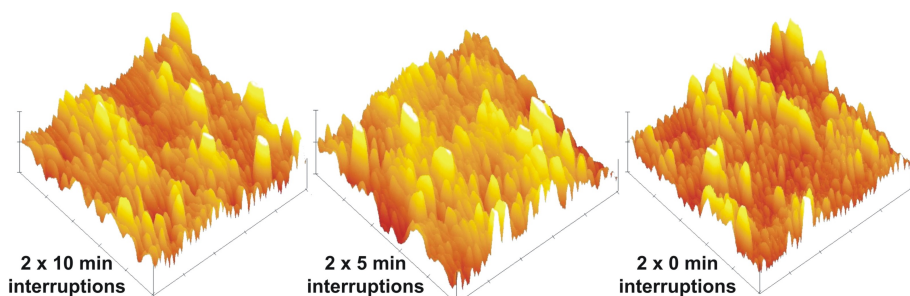


Figure 6.13: 1 μm² AFM images showing the effect of As₄ growth interruptions, before and after InAs deposition, on the appearance of InAs SAQDs on InAlAs.

The PL of these samples however, provides a more concrete confirmation of the above hypothesis [Fig. 6.14].

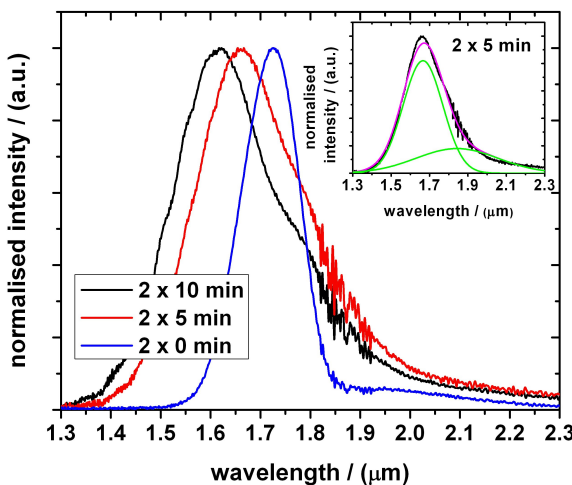


Figure 6.14: Variation of normalised PL at 4.2K with the length of growth interruptions before and after InAs deposition. Inset shows fitting of Gaussian distributions to the spectrum from the 2×5 minute interruption sample.

The first detail which is apparent in the spectrum from the sample grown without interruption is the low FWHM of $100 \pm 10\text{nm}$. In contrast, the peaks from the other two samples are significantly broader: the sample with 2×5 minute interruptions has a FWHM of $180 \pm 20\text{nm}$. The 2×0 minute interruption sample exhibits a peak emission wavelength of $1.725 \pm 0.01\mu\text{m}$. Examination of the other two spectra reveals not only an evolution of the main peak to shorter wavelengths but also the formation of a shoulder on the long-wavelength edge. Using Gaussian fits to deconvolve the data two peaks are revealed, as shown in the inset to Fig. 6.14 for the sample with 2×5 minute interruptions. The main peak moves to shorter wavelengths as the length of the interrupt is increased. This occurs as the size of the SAQDs is decreased due to In migration.

The peak responsible for the small shoulder must then originate from the larger coalesced InAs features. Moving initially to $1.860 \pm 0.05\mu\text{m}$ as these objects start to form in the 2×5 minute sample, this peak is then blue shifted to $1.725 \pm 0.03\mu\text{m}$ for the 2×10 minute sample. This perhaps indicates some secondary In redistribution and equilibration between the large and small SAQD features and is reflected by a small reduction in the FWHM to $160 \pm 20\text{nm}$.

6.3.6 Growth of InAs SAQDs on InGaAs

InAs SAQD heterostructures were grown as shown in Fig. 6.2, except that the InAlAs layers were replaced with InGaAs. 4.0ML of InAs was deposited at a growth temperature

of 445 °C as measured by optical pyrometry. AFM images reveal that the InAs features

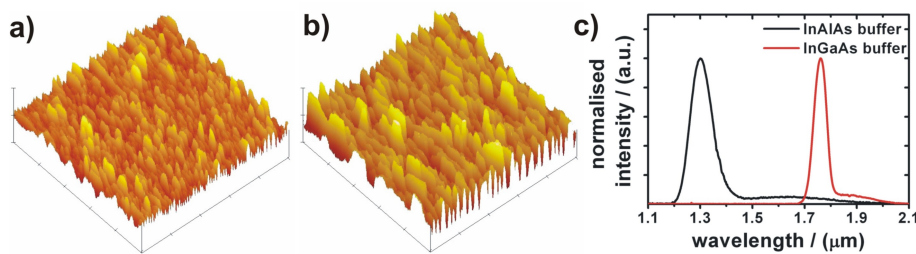


Figure 6.15: $1\mu\text{m}^2$ AFM images showing variation in the appearance of InAs SAQDs with buffer type. **Left:** InAlAs **Centre:** InGaAs. **Right:** 4.2K PL spectra from these two samples.

grown on InGaAs are larger, less densely-packed and more uniform in size-distribution than those grown on InAlAs [Fig. 6.15 (Left and Centre)]. PL analysis confirms this [Fig. 6.15 (Right)]. The sample with the InAlAs buffer has a peak emission wavelength $460 \pm 40\text{nm}$ lower than the InGaAs buffer sample. In addition, the FWHM of the InGaAs sample peak is significantly smaller at $43 \pm 4\text{nm}$, compared with $71 \pm 5\text{nm}$ for the InAlAs sample. In the non-normalised spectra, the intensity of the InGaAs sample peak was approximately twice that of the InAlAs sample peak, indicating superior crystalline quality.

These observations can be explained by considering that indium surface segregation has been shown to be significantly lower in InGaAs than in InAlAs [181]. Because of this, In content at the growth front is greater for InAlAs than InGaAs despite the same nominal mole fraction. This $\text{In}_y\text{Al}_{1-y}\text{As}$ layer is therefore more strained than the $\text{In}_x\text{Ga}_{1-x}\text{As}$. Thus, the InGaAs buffer surface will be smoother and more ordered than that of the InAlAs buffer [190]. AFM images show that monolayer terraces on the surface of an InGaAs buffer are large, regular and extend along the $[\bar{1}10]$ crystal axis [Fig. 6.16 (Left)]. In comparison, an InAlAs buffer is shown to have significantly smaller and less-ordered terraces [Fig. 6.16 (Right)]. The huge increase in step-edge density encountered when

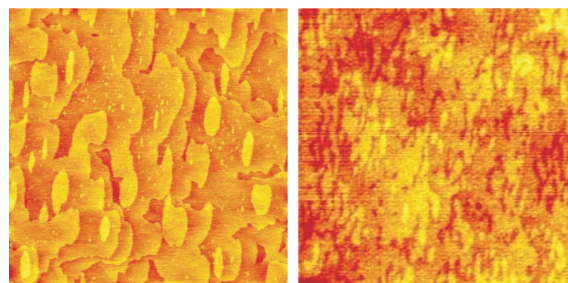


Figure 6.16: $1\mu\text{m}^2$ AFM images showing bulk surface morphology of InGaAs (**Left**) and InAlAs (**Right**). $[\bar{1}10]$ is vertical in both images.

moving from an InGaAs to an InAlAs buffer means that the number of SAQD nucleation sites also increases dramatically [179]. These two contributing factors of surface strain and morphology result in the formation of larger and less dense InAs SAQDs on InGaAs than on InAlAs. This investigation shows that the structural and optical properties of InAs SAQDs can be strongly influenced through choice of buffer material.

6.4 Quantum Dot Resonant Tunnelling Diodes

Single photon detection has been demonstrated in a GaAs/AlGaAs RTD containing InAs SAQDs. A RTD is essentially a single quantum well (QW) bounded on either side by a potential barrier. When a bias is applied across the emitter and collector Ohmic contacts, current can flow limited by electron tunnelling through the double barrier structure [Fig. 6.17 a)] [195]. At some threshold bias (V_T), the Fermi energy (E_F) of the electrons in the emitter become aligned with the first energy level (E_0) of the QW and the tunnelling current through the double barrier begins to rise [Fig. 6.17 b)]. The tunnelling current reaches a maximum when the confined state of the QW coincides with the conduction band edge (E_C) [Fig. 6.17 c)]. Further increase of the applied bias results in misalignment of these energy levels and the tunnelling current falls [Fig. 6.17 d)].

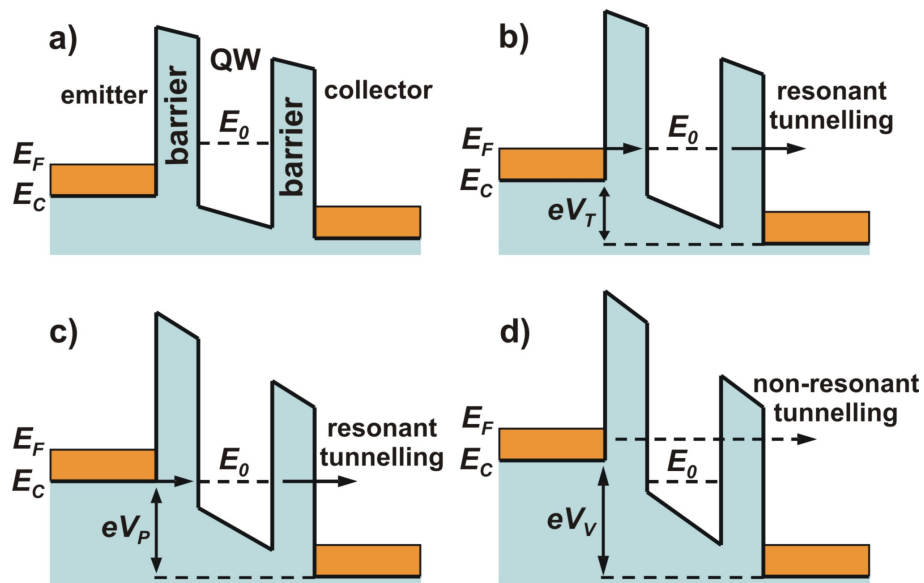


Figure 6.17: Schematic diagram showing the effect of device bias on a ‘flat-band’ approximation to the conduction band profile of an RTD, where $|V_T| < |V_P| < |V_V|$.

A typical I-V response over this bias interval is shown in Fig. 6.18. The peak-to-valley current ratio (PVCR), a commonly quoted figure of merit for RTD devices, is calculated as shown and is ideally as large as possible. A finite valley current (I_V) exists due to

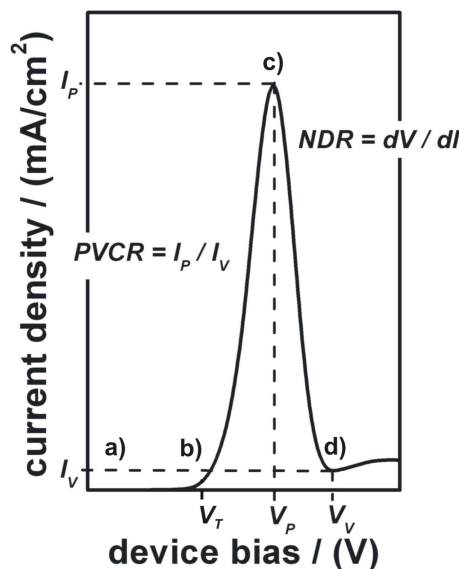


Figure 6.18: A typical resonant peak in the tunnelling current through a RTD, on which the relevant points relating to the four diagrams in Fig. 6.17 are indicated. The PVCR and negative differential resistance (NDR), an indication of device impedance, are also defined.

the presence of non-resonant current paths, including thermionic emission and inelastic scattering processes. Immediately above resonance, the differential resistance is negative.

In order to use a RTD as a single photon detector, a thin layer of InAs SAQDs was deposited just above the top barrier, followed by a thick semi-insulating (SI) absorption layer. Heavily n -doped layers, both at the surface and below the bottom barrier, enable good electrical contact to the device [Fig. 6.19].

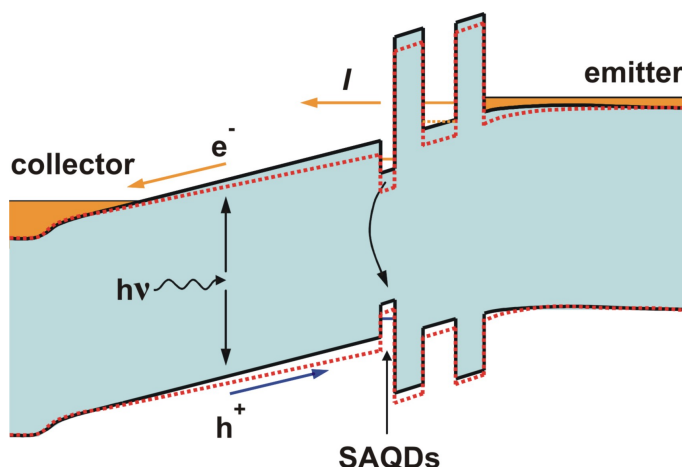


Figure 6.19: Schematic diagram showing the band structure of an RTD containing a layer of SAQDs. Temporary lowering of the SAQD potential following capture of a photohole is represented by the dashed red line (after [168]).

SAQDs confine conduction band electrons. An incoming photon creates an electron-hole pair in the absorption layer and the photoexcited hole is, in turn, captured by a SAQD. This then recombines with the trapped electron and the average charge on the SAQD therefore becomes more positive. Until it is repopulated by another electron thus ‘resetting’ the dot, the overall potential of the SAQD is reduced. The associated change in field brings the QW energy level closer to the electron energy of the emitter, which temporarily moves the resonant position to a lower voltage. In large-area devices, the magnitude of this shift in the position of the resonant peak is controlled directly by the intensity of the device illumination. In time-dependent measurements on small-area devices, discrete steps in the tunnelling current have been observed which correlate directly to single photon capture [168]. Although full theoretical modelling of these devices is beyond the scope of this dissertation, an excellent review of this topic can be found in Ref. [195].

To build on this work and extend it to the InP-based material system, samples based around the heterostructure shown in Fig. 6.20 were grown. An initial series of samples was

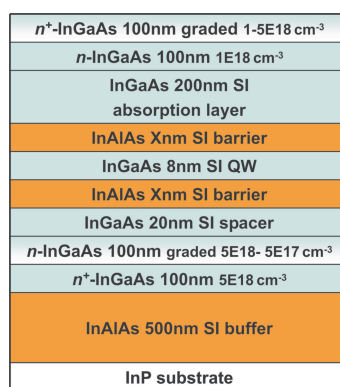


Figure 6.20: Schematic diagram of the basic RTD heterostructure where the InAlAs barrier thickness $X = 5, 7, 10$ or 12nm . Subsequent changes made to this structure are detailed in the text. Where SAQDs were included, these were placed above the top barrier.

grown with the aim of optimising the barrier thickness. A QW width of 8nm was used for each, surrounded by barriers of thickness 12nm , 10nm , 7nm and 5nm and grown without a layer of InAs SAQDs. Similar to the growth conditions for the SAQD calibration samples described previously, the V/III BEP ratio was ~ 30 and the substrate temperature was 460°C .

Large-area devices were fabricated from these samples following the wet-etch processing steps described in Ref. [196]. RTDs with active region areas of $10 \times 10\mu\text{m}^2$, $14 \times 14\mu\text{m}^2$, $20 \times 20\mu\text{m}^2$, $30 \times 30\mu\text{m}^2$, $40 \times 40\mu\text{m}^2$ and $50 \times 50\mu\text{m}^2$ were fabricated from each sample. The d.c. I-V characteristics of these devices were measured using the method described in section 2.3.4 [Fig. 6.21]. The quality factor of the resonant peak under forward bias

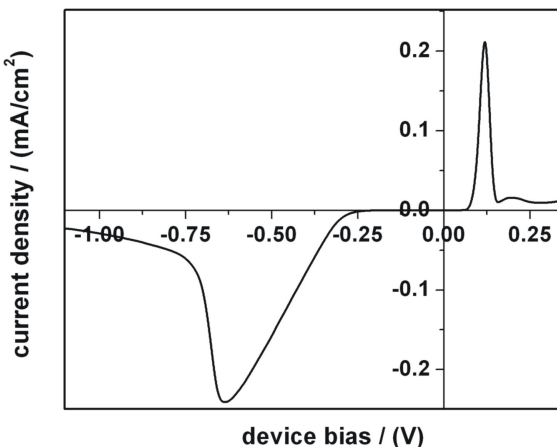


Figure 6.21: Typical I-V characteristics for an InGaAs/InAlAs RTD structure at 4.2K. The data shown is for a device with a $50 \times 50\mu\text{m}^2$ active region, with 12nm InAlAs barriers and an 8nm InGaAs QW.

is significantly higher than that under reverse bias. This is due to the asymmetry of the device. With the device emitter grounded, the conduction band is moved downwards under forward bias and upwards under reverse bias. Under forward bias the majority of the voltage is dropped across the double barrier. When under reverse bias, the voltage is dropped across the undoped InGaAs absorption layer, in series with the double barrier. This extra resistance means that the current rises comparatively slowly. Therefore, this wider peak, appears on the negative side of the I-V trace. Were the collector to be grounded instead, as shown in Fig. 6.19 for example, the voltage dependence would be reversed. For the positive peak in [Fig. 6.21], the PVCR was 22.7 and the average NDR was $-5.32\text{k}\Omega\text{cm}^2$. For the negative peak, the PVCR and average NDR values were 13.3 and $-2.57\text{k}\Omega\text{cm}^2$ respectively.

Note that the *y*-axis scale is current density, the measured current per unit area. Devices with active regions of different size can be directly compared by representing the current in this way. For the six large-area devices from each sample, the I-V curves were shown to be identical when thus normalised. This shows that the current density scales linearly with active area which is a useful check on material and device quality.

The average peak current densities were calculated from the I-V curves of each large-area device, for each sample. This analysis was carried out for both positive and negative bias peaks.[Fig. 6.22] By varying the barrier thickness between 5nm and 12nm, a huge dynamic range is demonstrated for these devices. Peak current density can be accurately tuned over seven orders of magnitude. In agreement with previous work, peak current density falls exponentially with increasing barrier thickness [197, 198]. These RTD devices can hence be designed with any desired carrier density. The average PVCR values were

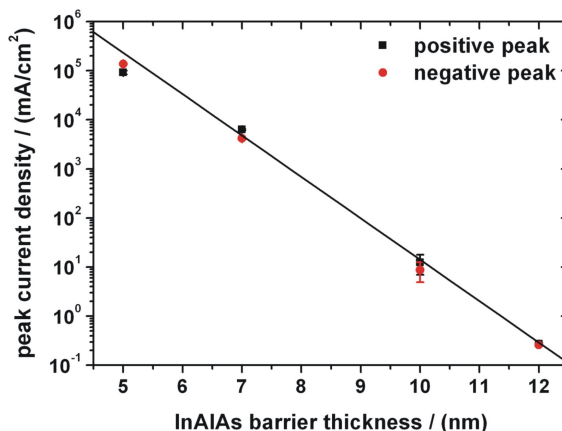


Figure 6.22: Dependence of peak current density on InAlAs barrier thickness for the four RTD structures.

also calculated and the results are summarised as follows.

barrier/well/barrier (nm / nm / nm)	PVCR (positive bias peak)	PVCR (negative bias peak)
12/8/12	22.7 ± 0.1 (12.5 ± 0.1)	13.3 ± 0.3 (9.3 ± 0.2)
10/8/10	24.0 ± 0.1 (16.9 ± 0.1)	13.7 ± 0.7 (10.2 ± 0.3)
7/8/7	9.7 ± 0.0 (7.0 ± 0.0)	3.8 ± 0.0 (3.1 ± 0.0)
5/8/5	20.5 ± 0.1 (12.2 ± 0.1)	12.1 ± 1.0 (9.6 ± 0.2)

The values in black are for measurements at 4.2K while the red bracketed values indicate the results at 77K. With the exception of the device with 7nm barriers, the PVCR values for these devices are relatively consistent and are independent of barrier thickness. Since RTD-type devices are typically used in electrical equipment designed to operate at room temperature, the majority of PCVR figures quoted in literature are measured at 300K. However, the room temperature I-V curves for these devices were extremely thermally broadened and accurate calculation of PVCR was difficult [Fig. 6.23].

Nevertheless, where published data measured at 77K does exist, PCVR values of between 10 and 20 are quite respectable [199, 200]. This confirms that the basic RTD device, which will form the basis of the SPD, exhibits good operational characteristics. It is interesting to note that although warming a device from 4.2K to 77K reduces the PVCR of the positive bias peak, the negative bias peak is almost unaffected. In the final structure, the InAs SAQDs will be placed above the top InAlAs barrier. As a result, it is changes to the position of this negative bias peak which will indicate single photon detection and it is encouraging that this resonant feature is robust with regard to device heating.

A high differential conductance (dI/dV) leads to a single photon detection signal with a large amplitude. However, a large dI/dV is often also associated with a large current density, which reduces the time after a detection event before a SAQD becomes repopulated. This reset time must be within the time-resolution of the measurement electronics

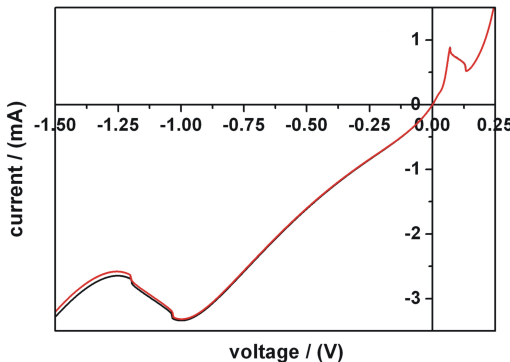


Figure 6.23: Room temperature I-V characteristics for a $50 \times 50 \mu\text{m}^2$ RTD with 12nm InAlAs barriers. Approximate PVCR values of 1.29 and 1.71 were determined.

or the strength of detection signal will be reduced. Hence, to reach a suitable compromise between dI/dV and reset time, 5nm barriers were chosen. SAQD-RTD samples were then grown, each with a 7.5MLs of InAs. The SAQDs were deposited without growth interrupts, at 0.5ML/s; the same flux as for bulk growth.

These RTDs were measured using an a.c. technique which had the advantage over d.c. measurements that the time taken was significantly shorter. Initial measurements on these devices showed that random telegraph signal (RTS) noise was particularly high. As a result, future devices had an undoped InGaAs spacer layer inserted between the top InAlAs barrier and the InAs in a bid to decrease electron tunnelling in and out of the SAQDs. Spacers with widths of 0nm, 2nm, 4nm and 8nm, were investigated. In common with the final device design in the GaAs/AlGaAs RTD [168], a 4nm spacer was selected to provide an optimal balance between tunnelling characteristics and reduced noise.

In order to assess the sensitivity of these devices to low-level light they were cooled to 4.2K. The I-V measurements were repeated both in the dark, and under illumination with a red LED. Light intensity was varied by changing the LED current [Fig. 6.24]. In this

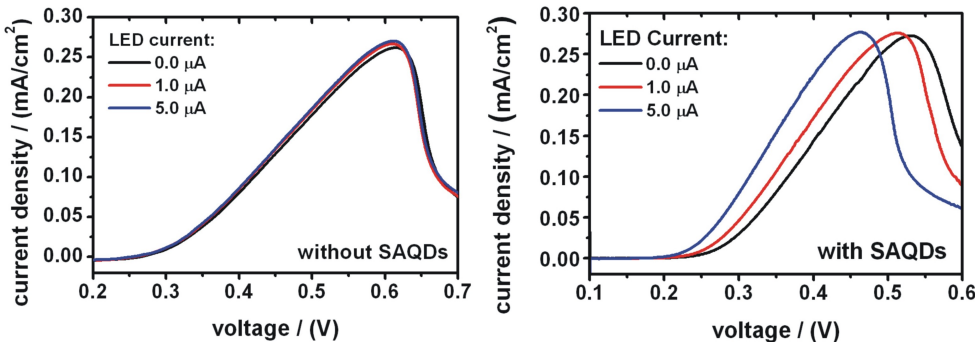


Figure 6.24: Light sensitivity of 10nm barrier large-area RTDs without (Left) and with (Right) an imbedded layer of InAs SAQDs.

measurement the collector was grounded and so the broad detection peak now appears under forward bias. For the RTD without a layer of SAQDs, increasing illumination intensity had negligible effect on the resonant position. Conversely, RTDs containing the InAs dots showed a definite lowering of the peak voltage as the illumination intensity was increased. This is the expected behaviour for these dot-containing devices (see page 137).

Small-area devices were fabricated by Dr. H.W. Li using the process described in Refs. [168, 177] to create a ‘cross-wire’ active region of $\sim 1 - 2\mu\text{m}^2$ [Fig. 6.25]. Small-area devices are required to facilitate the resolution of any quantised steps in the tunnelling current. Unlike the large-area devices, the Ohmic-contacts on these cross wire devices are situated some distance from the optically active region which greatly improves coupling efficiency.

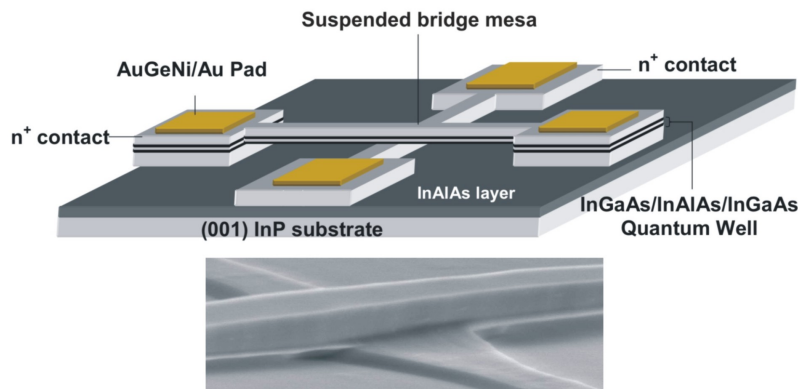


Figure 6.25: **Top:** Schematic diagram of a small-area cross-wire RTD. **Bottom:** Scanning electron microscope image of the active region of such a device (images courtesy of Dr. Li).

However, even though the SAQD RTDs exhibited good functionality and light sensitivity, single-photon detection could not be demonstrated. In order to investigate the reason for this, a series of devices were grown to study the effect of changing both QW width and the absorption layer thickness, as well as the size of the InAs SAQDs. Although each of these changes affected the large-area characteristics as expected, it was still not possible to achieve single-photon detection. The proposed reason for this came down to the nature of the SAQDs themselves. The extended dash-like structure of the InAs features means that carrier confinement is weak [201]. As a result, the reset time for the dots was too short to enable the counting electronics to resolve steps due to single-photon capture in the tunnelling current. A fundamental change to the SAQD RTD design was required if a working SPD was to be realised.

6.5 Single Photon Detection at $1.3\mu\text{m}$

It was shown in section 6.3.6 that the choice of buffer material plays an important rôle in determining the structural properties of the SAQDs. As a result, an adjustment was made to the RTD heterostructure shown in Fig. 6.20 such that the InAlAs barriers were replaced with AlAs. The reasons for this were twofold. Firstly, the bandgap of AlAs is 2.15eV at 300K, [6] which means that QW confinement will be enhanced. Secondly and perhaps more importantly, the mismatch between InAs and AlAs is $\sim 6.6\%$, which makes the strain of the system much closer to the situation for InAs SAQDs on GaAs. It was hoped that this might result in the formation of discrete SAQDs, instead of the dash-like structure of the InAs features on InAlAs.

This higher strain does however introduce a new consideration into the device design. The critical thickness of AlAs on InGaAs is expected to be $< 10\text{nm}$ which places a cap on maximum barrier thickness. Indeed, an early calibration sample grown with 7nm AlAs barriers exhibited a heavily cross-hatched surface, indicating that the critical thickness had been exceeded. A look at Fig. 6.22 shows that this puts a finite lower-limit on the minimum carrier density available. The device design used for the remainder of this work had 5ML (1.42nm) AlAs barriers.

A switch was also made to using As_2 instead of As_4 during growth of these structures. It has been shown that dimeric As can lead to significantly smoother surfaces due to a reduction in arsenic clustering [202]. To assess the structure of InAs SAQDs deposited on AlAs under As_2 , a series of calibration samples were grown. Growth conditions were chosen to replicate those during epitaxy of the full RTD structure. The InAs thicknesses in these samples were 2.0ML, 2.5ML, 3.0ML and 4.0ML [Fig. 6.26]. After 2.0ML of InAs has been deposited, the layer is still below the critical thickness for the SK transition. Terraces can be distinguished and the epilayer is 2D with a RMS roughness of $2.02 \pm 0.03\text{\AA}$. Large dots have begun to form on the sample with 2.5ML InAs. As the deposition thickness is increased, the density of the SAQDs rises extremely quickly [Fig. 6.27]. It is interesting to note however, that although the radii of the dots are reduced as more InAs is deposited, the SAQD height increases. This means that these SAQDs develop from having a ‘pyramid-like’ profile, to adopting a more conical shape as InAs thickness is increased. Feature profile can thus be tuned by selecting an appropriate deposition thickness. The discrete nature of these dots made them ideal candidates for placement into the RTD structure.

SAQD RTD samples were grown as summarised in Fig. 6.28, with InAs SAQDs deposited directly onto the top InAs barrier. Note that the absorption layer and top *n*-doped layers are thinner than in the earlier design to improve coupling of light into the device and improve the capture efficiency of photoholes. I-V measurements were carried out at 4.2K. The peak current density of the detection peak was found to be close to 13kA/cm^2 , with a PVCR of 12.

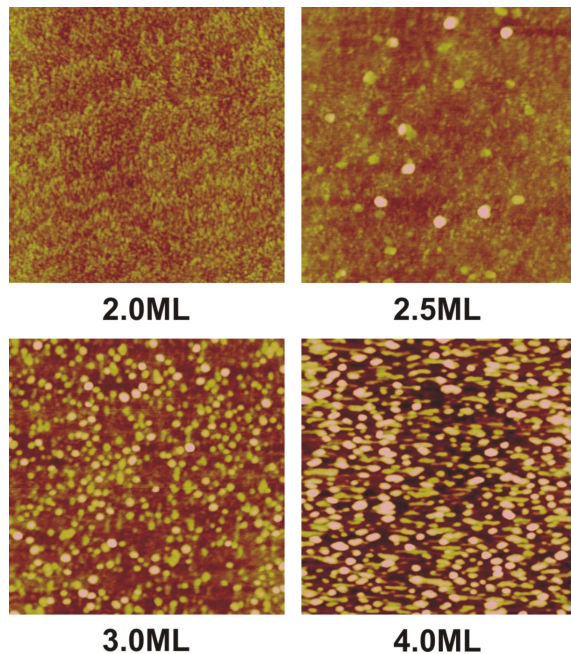


Figure 6.26: $1\mu\text{m}^2$ AFM images showing the evolution of InAs SAQD formation on AlAs with increasing deposition thickness. The z -axis scale is 3nm in each case.

The device was cooled to 4.5K in a continuous-flow ${}^4\text{He}$ cryostat. A lens was used to focus a 1310nm laser, driven at 500kHz, onto the active area of the detector. The device was held at a finite bias between V_T and V_P and then illuminated with the laser pulses. The laser was calibrated such that the average photon flux could be accurately controlled, taking values between 0.0025 and 10 photons per pulse. However, the intensity actually

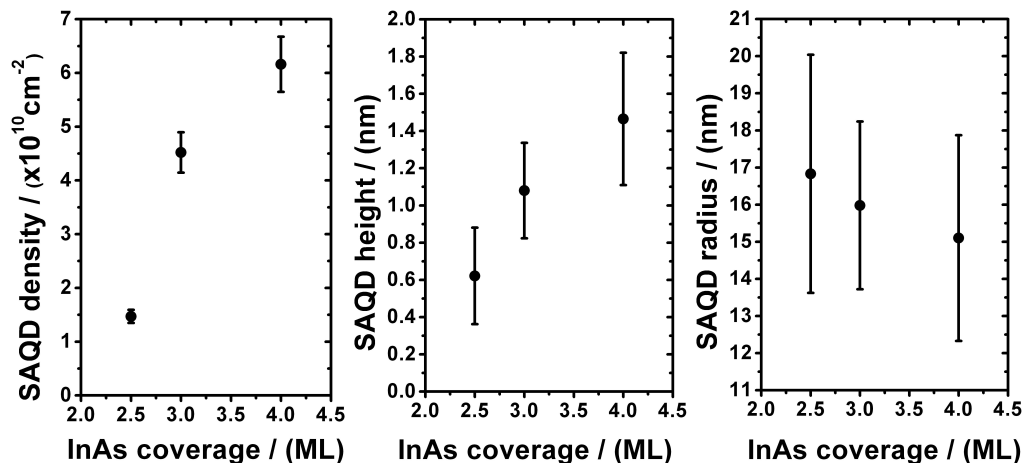


Figure 6.27: The effect of deposition thickness on the density and size of InAs SAQDs on AlAs.

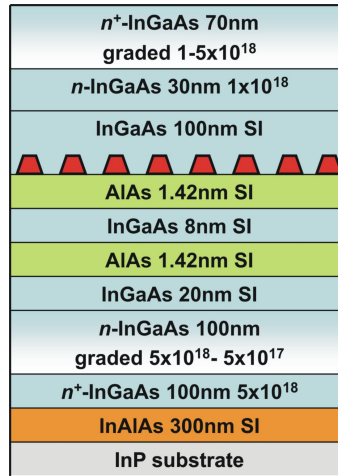


Figure 6.28: Schematic diagram showing the final device heterostructure for the RTD with AlAs barriers. The InAs SAQDs are represented by the red trapezoids.

coupling into the device could be as low as half these calibrated values. Further details of the measurement can be found in Refs. [168, 177, 203]. During illumination, time-dependent measurements resolved discrete ‘spikes’ in the tunnelling current, a definitive indication of single photon detection [Fig. 6.29 (Left)]. Between laser pulses, current spikes with opposite polarity were observed as the SAQDs reset. The dark counts were measured 1.0 μ s after each laser pulse [Fig. 6.29 (Right)].

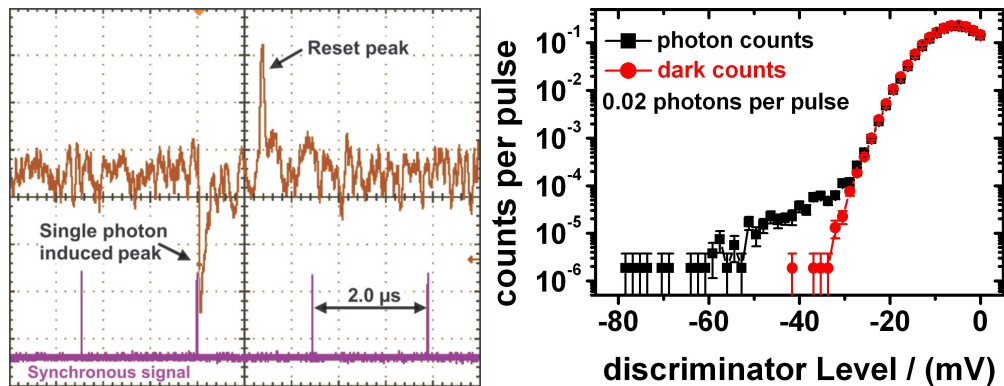


Figure 6.29: **Left:** Typical single photon detection and SAQD reset current signals. **Right:** Dependence of photon detection and dark count rates on discriminator level. In this measurement, the laser flux was 0.02 photons per pulse.

The photon detection counts form a ‘wing’ which extends over the Gaussian dark count background noise. For discriminator levels below approximately -30 mV, the photon induced counts can clearly be resolved above the noise background. Using a discriminator level of -28 mV, the device efficiency was investigated by assessing the dependence of the

detection rate on the incident photon flux. Having removed the dark count background,

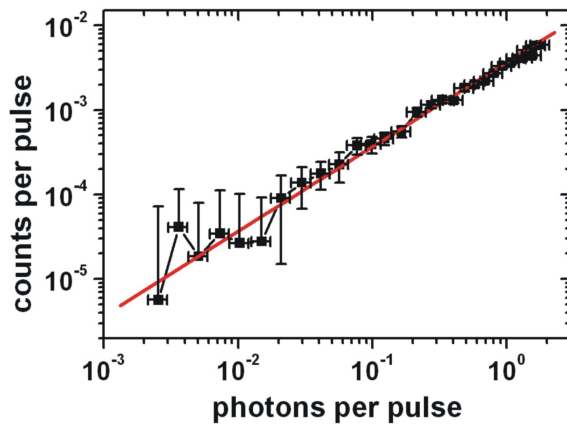


Figure 6.30: Dependence of photon detection counts on the photon flux, at a discriminator level of -28 mV. A linear fit to these data is shown.

Fig. 6.30 shows that the photon induced count rate is linear over three orders of magnitude, with laser flux. This serves to confirm that this device operates as a SPD. The internal efficiency was found to be $\sim 6.3\%$, while the detection efficiency was calculated to be $0.35 \pm 0.07\%$ with a dark count rate of $1.58 \times 10^{-6} \text{ ns}^{-1}$. The dark count rate can be reduced by increasing the magnitude of the discriminator level, although this reduces detection efficiency. With the discriminator level set to -34mV, the dark count rate is reduced to $7.4 \times 10^{-9} \text{ ns}^{-1}$, with an efficiency of $0.23 \pm 0.04\%$.

Although internal efficiency is comparable, these values are somewhat lower than those realised in the analogous GaAs/AlGaAs SAQD RTD [168]. However, coupling loss has not been taken into account and the use of antireflection coatings could reduce these losses significantly, resulting in comparable overall detection efficiency. It is estimated that $\sim 5.6\%$ of incident photons create electron-hole pairs in the absorption region. Detection efficiency could therefore also be increased by thickening this layer. It may also be desirable to reduce the peak current density since this would bring down the dark count rate. Although increasing the AlAs barrier thickness would achieve this, there is a finite limit to this, which is dictated by material strain as discussed previously. An alternative approach would be to increase the QW width. A previous study into GaAs/AlGaAs SAQD RTDs found that light sensitivity was highly dependent on the size and density of the InAs dots [204]. The latest results (not included here), indicate that the best performance was achieved where InAs SAQD density was low ($< 10^{10} \text{ cm}^{-3}$). By depositing the SAQDs at lower InAs growth rates in future devices, far greater control over dot size and density will be possible.

6.6 Summary

A comprehensive study of the growth of InAs SAQDs on InAlAs has been presented. AFM and PL were used to assess both the structural and optical properties of the SAQDs. Both morphology, and peak emission wavelength were shown to scale with deposition thickness. The PL wavelength could be accurately tuned over a range of nearly 700nm, at a rate of 170nm/ML.

Good dot uniformity was demonstrated across a 2" sample. An increase in growth temperature between 440 °C and 480 °C reduced SAQD size and correspondingly blue-shifted the PL wavelength by 3.5nm/ °C. This was shown to be linked to the temperature dependence of the In-sticking coefficient. As expected, material quality was shown to improve as the growth temperature was raised. Although SAQD properties were unaffected by changing InAs deposition rate, a bimodal size distribution was shown to develop as growth interruptions were introduced before and after InAs deposition. The PL emission was observed to move to shorter wavelengths as the length of the growth interruption was increased. Deposition of InAs on lattice-matched InGaAs produced larger, lower-density features, with a correspondingly longer PL wavelength of 1.750μm. This was explained by relative In-segregation, intermixing, strain and roughness arguments and indicated that careful choice of buffer material is critical to the way in which QDs are formed.

The operation of double barrier RTDs was described, together with the concept of creating a SPD through the integration of a layer of SAQDs. A series of RTD devices were grown, the I-V characteristics of which were measured at 4.2K. Respectable PVCR values were demonstrated and the peak current density of these devices was shown to scale exponentially over seven orders of magnitude with barrier thickness. Large area RTDs containing SAQDs were sensitive to LED illumination. However, even after an extended process of device optimisation, the detection of single photons could not be achieved. It is believed that the large, dash-like nature of the InAs features led to very short reset times for the SAQDs and so steps in the tunnelling current could not be resolved by the counting electronics.

InAs was shown to form discrete circular SAQDs when deposited on AlAs, with a critical thickness for the SK transition of between 2.0ML and 2.5ML. Although dot height was shown to increase linearly with increased deposition thickness, SAQD radius was found to decrease, indicating a change in feature profile. By replacing the InAlAs barriers in the RTD with 5ML of AlAs, these discrete dots could be placed into the heterostructure, with the intention of increasing the SAQD reset time.

For the first time, these devices were shown to behave as SPDs at 1310nm, under illumination by laser pulses. A detection efficiency of $0.35 \pm 0.07\%$, was achieved, with a dark count rate of $1.58 \times 10^{-6} \text{ ns}^{-1}$. By lowering the discriminator level, the dark count rate was reduced to $7.4 \times 10^{-9} \text{ ns}^{-1}$, but with the efficiency lowered to $0.23 \pm 0.04\%$. Future

work will involve a full optimisation of the device structure in order to improve efficiency and reduce dark count rates. It is hoped that eventually this novel SPD will lead to advances in QKD and other systems that require low-noise, single photon detection.

Chapter 7

Conclusions and Further Work

7.1 Introduction

The main focus of this dissertation has been the growth by MBE of high-quality InGaAs and InAlAs. However, during the course of this work, numerous other topics of III-V semiconductor research have also been addressed. These have ranged from the commissioning of a new MBE chamber to the optimisation of material growth; and from device fabrication, to characterisation and measurement. The conclusions reached which are expected to be of greatest importance to further work are presented here. This research has given rise to some interesting results. Where appropriate, directions in which these findings can be extended and developed in future are proposed.

7.2 Molecular Beam Epitaxy and Device Fabrication

The aim of this body of work was to commission a new MBE chamber in readiness for device growth. The Veeco MOD Gen. II machine has been demonstrated to be capable of growing high-quality III-V material. Using optical pyrometry, XRD and RHEED to accurately measure GaAs, AlAs and InAs growth rates, reliable calibrations were constructed for each cell. Similarly, the uniformity of growth rate and material composition was measured across 2" and 3" wafers and shown to $\leq 1.5\%$ for all variables measured.

Perhaps for the first time, a Ga SUMO cell has been shown to be capable of high-quality growth when located in a downward-looking port at -12° . No degradation in performance is observed compared with an identical cell mounted conventionally in an upward-looking port.

Given a Schottky barrier of less than 0.196eV [21] for the InGaAs compositions studied here, the major challenge encountered in device fabrication centred on the problem of gate insulation. For standard top-gates, $\sim 300\text{nm}$ of polyimide was shown to prevent gate leakage for voltage levels $< -15\text{V}$. However, the split gates used in chapter 5 to study

1D transport required polyimide thicknesses closer to 50nm. Reliably achieving good insulation with such thin polyimide layers was shown to be realistically unfeasible with this process. A new method for insulating gates with silicon oxides will be introduced in the near future. It is hoped that this process will improve device yields by allowing better control over layer thickness while still providing good insulation characteristics. A working insulation process could be readily incorporated into the novel split-gate fabrication process that has been validated in this research.

7.3 Two-Dimensional Electron Systems

The growth of high-quality $\text{In}_x\text{Ga}_{1-x}\text{As}$ ($x \geq 0.53$) was explored, with a view to this material forming the basis for various novel applications; for example devices with tunable g -factor. To assess and optimise material quality, heterostructures based around $\text{In}_x\text{Ga}_{1-x}\text{As}$ QWs with $0.53 \leq x \leq 0.75$, were grown on (001) InP in order to study 2D electrical transport. Peak electron mobilities of $\mu \geq 1.0 \times 10^5 \text{ cm}^2/\text{Vs}$ were obtained for all compositions over this range. These values are comparable to the highest reported for similar heterostructures. These materials were shown to exhibit transport anisotropy, with currents flowing parallel to [110] having higher electron mobility. This was a direct result of reduced interface-roughness scattering along this crystal axis, due to the surface morphology.

Samples based around $\text{In}_{0.53}\text{Ga}_{0.47}\text{As}$ were shown to be relatively insensitive to growth temperature over the range 410 °C to 480 °C, whereas an optimal growth temperature of 410 °C was found for $\text{In}_{0.75}\text{Ga}_{0.25}\text{As}$ -based heterostructures. Increased indium mole fraction reduced alloy-disorder scattering while, through the growth of undoped heterostructures, the detrimental effect of remote-ionised-dopant-impurity scattering could be removed completely.

Undoped $\text{In}_{0.75}\text{Ga}_{0.25}\text{As}$ QWs were grown with electron mobilities equalling the highest values published to-date [140], with $\mu \geq 2.0 \times 10^5 \text{ cm}^2/\text{Vs}$. The crucial detail however, was that through the use of a significantly thinner InAlAs buffer, the overall sheet electron density in these devices was more than halved. These high- μ , low- n_s devices are expected to enable the study of various phenomena at comparatively low magnetic fields. Further work will involve studying the effect of arsenic overpressure on material quality for both As_4 and As_2 . In addition, a second indium cell will permit a study of the effect on device performance of the growth interruption prior the growth of the active layers.

Beating in the SdH oscillations, accompanied by double peaks in the FFT spectra, were shown to be evidence of Rashba SOC effects in $\text{In}_{0.53}\text{Ga}_{0.47}\text{As}$ QWs. The magnitude of the spin-splitting could be varied between zero at low and high n_s and some finite amount at intermediate values. This response was different to previously measured systems

where a single symmetric point was found [131, 133]. Further work, both theoretical and experimental, will be required to obtain a full understanding of the observed behaviour. In future, doped $\text{In}_x\text{Ga}_{1-x}\text{As}$ heterostructures, with $x > 0.53$ will be grown in order to investigate whether similar SOC effects are seen in these materials. δ -doping may be required to prevent parallel conduction in these materials. It is hoped that materials such as these could lead to devices in which spin-degeneracy could be switched rapidly on and off.

The effective g -factor of the $\text{In}_{0.75}\text{Ga}_{0.25}\text{As}$ QWs was measured to be $g^* = -9.2$ at $\nu = 4$, while the bare g -factor for $\text{In}_{0.53}\text{Ga}_{0.47}\text{As}$ is known to be close to -5 [125]. For any required g -factor in this range, the ability to grow a suitable composition of high- μ InGaAs material has been demonstrated. Other projects within this group have focussed on the growth of very low g -factor III-V materials [151]. By growing $\text{In}_x\text{Ga}_{1-x}\text{As}$ channels with $x < 0.53$ it might be possible to extend their work into InGaAs. The high g -factor materials studied in this dissertation will be combined with that low g -factor material into double-QW or inverted structures. Using front and back gates to vary the confinement position of the electron wavefunction, it will be possible to directly modulate g^* . This will lay the foundation for the design of future spintronic devices.

7.4 One-Dimensional Electron Systems

Transport measurements in $\text{In}_{0.75}\text{Ga}_{0.25}\text{As}$ quantum wires were carried out at 1.5K. Reproducible quantised conductance plateaux were measured and a d.c. bias technique resulted in the observation of various additional conductance structures. In particular these included the formation of plateaux at $0.75(2e^2/h)$ and $0.25(2e^2/h)$ which were observed at high V_{sd} . These well-resolved features are consistent with a spin-gap model [48]. This is thought to be the first measurement of these features in $\text{In}_{0.75}\text{Ga}_{0.25}\text{As}$ which demonstrates that the high-quality material grown here represents a useful way of probing electron-electron interactions. Continuing study of this and similar systems will contribute to the effort to fully understand these phenomena.

Further investigation is required into some interesting resonant features observed in the longitudinal resistance of the 1D channel biased at the first conductance plateau. By removing any dependence on the 2DEG filling factor from the experiment it is hoped that these structures can be understood.

To this end, it is hoped that a new, more reliable process for insulating split-gates will improve the fabrication yield, as mentioned above. A more comprehensive study of InGaAs quantum wires for which $0.53 < x < 0.75$ will then be possible. High g -factors mean that these materials may also show some interesting spin-polarisation effects and it may be possible to observe Rashba SOC in 1D transport [205, 206].

7.5 Zero-Dimensional Electron Systems

This final section had two major aims. The first was to complete a comprehensive study of the growth of InAs SAQDs on InAlAs and InGaAs surfaces lattice-matched to InP. The structural and optical properties of these dash-like SAQDs were investigated as a function of deposition thickness, growth temperature, InAs growth rate and length of anneal time. Buffer material was shown to be critical to SAQD formation. PL emission wavelength from these SAQDs could be tuned linearly with deposition thickness from $1.09 \pm 0.04\mu\text{m}$ to $1.76 \pm 0.07\mu\text{m}$, at a rate of 170nm/ML. Future work on the growth of such systems is likely to be extended to look at the growth of alternative SAQDs on InGaAs and InAlAs, for example GaSb [89]. It would also be most interesting to study the effect on electron transport of placing of InAs or GaSb SAQDs close to the high-quality InGaAs 2DEGs described in chapter 4.

The second aim of this section was to incorporate the InAs SAQDs into an RTD heterostructure, in order to achieve single photon detection at optical fibre wavelengths. Without SAQDs, RTD device structures were grown on InP substrates which showed good electrical characteristics at 4.2K. Choice of InGaAs barrier thickness allowed the peak current density to be tuned over seven orders of magnitude. After the addition of InAs SAQDs, these RTDs demonstrated light sensitivity.

To achieve single photon detection, the InGaAs barriers were replaced with thin, strained layers of AlAs. InAs was shown to form discrete circular SAQDs on AlAs which led to improved electron transport characteristics. These novel devices demonstrated single photon detection at 1300nm. A maximum detection efficiency of $0.35 \pm 0.07\%$ was measured with a dark count rate of $1.58 \times 10^{-6}\text{ns}^{-1}$.

Further work to develop these detectors will also follow two routes. The first will be to optimise the growth of InAs SAQDs on AlAs. The addition of a second indium cell to the MBE chamber will offer a low deposition rate source for SAQD growth. This will provide accurate, submonolayer control over InAs thickness, while negating the need for growth interrupts. The second direction will involve engineering the heterostructure to provide higher detection efficiency and reduced dark count rates. Based on this work, it is hoped that improved single photon detectors will be realised for use in fibre-based, single photon systems.

Bibliography

- [1] C. Kittel. *Introduction to Solid State Physics*. John Wiley & Sons, Inc., New York, 2005.
- [2] J.R. Hook and H.E. Hall. *Solid State Physics*. John Wiley & Sons Inc., New York, 1994.
- [3] B.K. Tanner. *Introduction to the Physics of Electrons in Solids*. Cambridge University Press, Cambridge, 1996.
- [4] J.S. Blakemore. *Solid State Physics*. W. B. Saunders Co., Philadelphia, 1974.
- [5] B.J. van Wees, L.P. Kouwenhoven, E.M.M. Willems, C.J.P.M. Harmans, J.E. Mooij, H. van Houten, C.W.J. Beenakker, J.G. Williamson, and C.T. Foxon. Quantum Ballistic and Adiabatic Electron-Transport Studied with Quantum Point Contacts. *Phys. Rev. B*, 43:12431–12453, 1991.
- [6] Landolt-Börnstein. *New Series III/17a, Physics of Group IV Elements and III-V Compounds*. Springer-Verlag Berlin-Heidelberg, 1982.
- [7] G.B. Stringfellow. Calculation of Ternary-III-V and Quaternary-III-V Phase-Diagrams. *J. Cryst. Growth*, 27:21–34, 1974.
- [8] B.K. Bhattacharya, editor. *Properties of Lattice-Matched and Strained Indium Gallium Arsenide*. INSPEC, 1993.
- [9] H. Reiss and J.O. McCaldin, editors. *Progress in Solid State Chemistry - Vol. 7*. Pergamon Press, Oxford, 1972.
- [10] S.M. Sze. *Physics of Semiconductor Devices*. John Wiley & Sons Inc., New York, 1981.
- [11] D.C. Look. *Electrical Charaterisation of GaAs Materials and Devices*. John Wiley & Sons Inc., New York, 1989.
- [12] C.M. Wolfe, G.E. Stillman, and W.T. Lindley. Electron Mobility in High-Purity GaAs. *J. Appl. Phys.*, 41:3088–3091, 1970.
- [13] D.L. Rode and S. Knight. Electron Transport in GaAs. *Phys. Rev. B*, 3:2534, 1971.
- [14] H. Ehrenreich. Band Structure and Properties of Some 3-5 Compounds. *J. Appl. Phys.*, 32:2155–2166, 1961.
- [15] J. Bardeen and W. Shockley. *Phys. Rev.*, 80:72, 1950.
- [16] H.J.G. Meijer and D. Polder. Note on Polar Scattering of Conduction Electrons in Regular Crystals. *Physica*, 19:255–264, 1953.
- [17] A. Gold. Electronic Transport-Properties of a Two-Dimensional Electron-Gas in a Silicon Quantum-Well Structure at Low-Temperature. *Phys. Rev. B*, 35(2):723–733, 1987.
- [18] G. Snider. 1D Poisson/Schrödinger. This program can be downloaded from <http://www.nd.edu/~gsnider/>.
- [19] C.K. Peng, A. Ketterson, H. Morkoc, and P.M. Solomon. Determination of the Conduction-Band Discontinuity Between $\text{In}_{0.53}\text{Ga}_{0.47}\text{As}/\text{In}_{0.52}\text{Al}_{0.48}\text{As}$ Using n^+ -InGaAs/InAlAs/ n^- -InGaAs Capacitors. *J. Appl. Phys.*, 60:1709–1712, 1986.
- [20] J.J. Harris, C.T. Foxon, D.E. Lacklison, and K.W.J. Barnham. Scattering Mechanisms in (Al,Ga) As/GaAs 2DEG Structures. *Superlattices and Microstructures*, 2:563–568, 1986.
- [21] K. Kajiyama, Mizushima.Y, and S. Sakata. Schottky-Barrier Height Of n - $\text{In}_x\text{Ga}_{1-x}\text{As}$ Diodes. *Appl.*

- Phys. Lett.*, 23(8):458–459, 1973.
- [22] H. Hasegawa. Fermi Level Pinning and Schottky Barrier Height Control at Metal-Semiconductor Interfaces of InP and Related Materials. *Jap. J. Appl. Phys. Pt. 1*, 38:1098–1102, 1999.
- [23] R.H. Harrell. *Induced Electron Gases in Undoped GaAs/AlGaAs heterostructures*. PhD thesis, University of Cambridge, 1998.
- [24] I. Vurgaftman, J. R. Meyer, and L. R. Ram-Mohan. Band parameters for III-V compound semiconductors and their alloys. *J. Appl. Phys.*, 89(11):5815–5875, 2001.
- [25] A. Gold. Scattering Time and Single-Particle Relaxation-Time in a Disordered Two-Dimensional Electron-Gas. *Phys. Rev. B*, 38(15):10798–10811, 1988.
- [26] J.P. Eisenstein, K.B. Cooper, L.N. Pfeiffer, and K.W. West. Insulating and Fractional Quantum Hall States in the First Excited Landau Level. *Phys. Rev. Lett.*, 88:076801 1–4, 2002.
- [27] T. Kitada, T. Aoki, I. Watanabe, S. Shimomura, and S. Hiyamizu. Optimized channel thickness for high electron mobility in pseudomorphic $\text{In}_{0.74}\text{Ga}_{0.26}\text{As}/\text{In}_{0.52}\text{Al}_{0.48}\text{As}$ quantum-well HEMT structures with (411)A super-flat interfaces grown by MBE. *J. Cryst. Growth*, 227:289–293, 2001.
- [28] M. Yoshita, H. Akiyama, L.N. Pfeiffer, and K.W. West. Quantum Wells with Atomically Smooth Interfaces. *Appl. Phys. Lett.*, 81:49–51, 2002.
- [29] V. Drouot, M. Gendry, C. Santinelli, P. Viktorovitch, G. Hollinger, S. Elleuch, and J. L. Pelouard. High-Electron-Mobility In Pseudomorphic Modulation-Doped $\text{In}_{0.75}\text{Ga}_{0.25}\text{As}/\text{InAlAs}$ Heterostructures Achieved With Growth Interruptions. *J. Appl. Phys.*, 77(4):1810–1812, 1995.
- [30] S. Gozu, K. Tsuboki, M. Hayashi, C. L. Hong, and S. Yamada. Very High Electron Mobilities at Low Temperatures in $\text{In}_x\text{Ga}_{1-x}\text{As}/\text{In}_y\text{Al}_{1-y}\text{As}$ HEMTs Grown Lattice-Mismatched on GaAs Substrates. *J. Cryst. Growth*, 202:749–752, 1999.
- [31] H. X. Li, J. Wu, Z. G. Wang, J. B. Liang, B. Xu, C. Jiang, Q. Gong, F. Q. Liu, and W. Zhou. Growth and Characterization of InGaAs/InAlAs/InP High-Electron-Mobility Transistor Structures Towards High Channel Conductivity. *J. Cryst. Growth*, 186(3):309–314, 1998.
- [32] H. L. Stormer, A. C. Gossard, and W. Wiegmann. The Onset Of Intersubband Scattering In A Two-Dimensional Electron-System. *Journal Of Vacuum Science & Technology*, 21(2):507–508, 1982.
- [33] F. Capotondi, G. Biasiol, D. Ercolani, and L. Sorba. Scattering mechanisms in undoped $\text{In}_{0.75}\text{Ga}_{0.25}\text{As}/\text{In}_{0.75}\text{Al}_{0.25}\text{As}$ two-dimensional electron gases. *J. Cryst. Growth*, 278(1-4):538–543, 2005.
- [34] K. von Klitzing, G. Dorda, and M. Pepper. New Method for High-Accuracy Determination of the Fine-Structure Constant Based on Quantised Hall Resistance. *Phys. Rev. Lett.*, 45:494–497, 1980.
- [35] M Büttiker. Absence of Backscattering in the Quantum Hall Effect in Multiprobe Conductors. *Phys. Rev. B*, 38:9375–9389, 1988.
- [36] R. Landauer. Electrical Resistance of Disordered One-Dimensional Lattices. *Phil. Mag.*, 21:863, 1970.
- [37] M Büttiker. 4-Terminal Phase-Coherent Conductance. *Phys. Rev. Lett.*, 57:1761–1764, 1986.
- [40] K.F. Berggren, T.J. Thornton, D.J. Newson, and M. Pepper. Magnetic Depopulation of 1D Subbands in a Narrow 2D Electron-Gas in a GaAs/AlGaAs Heterojunction. *Phys. Rev. Lett.*, 57:1769–1772, 1986.
- [38] T.J. Thornton, M. Pepper, H. Ahmed, D. Andrews, and G.J. Davies. One-Dimensional Conduction in the 2D Electron-Gas of a GaAs-AlGaAs Heterojunction. *Phys. Rev. Lett.*, 56:1198–1201, 1986.
- [39] H.Z. Zheng, H.P. Wei, D.C. Tsui, and G. Weimann. Gate-Controlled Transport in Narrow GaAs/ $\text{Al}_x\text{Ga}_{1-x}\text{As}$ Heterostructures. *Phys. Rev. B*, 34:5635–5638, 1986.
- [41] D.A. Wharam, T.J. Thornton, R. Newbury, M. Pepper, H. Ahmed, J.E.F. Frost, D.G. Hasko, D.C. Peacock, D.A. Ritchie, and G.A.C. Jones. One-Dimensional Transport and the Quantization of the Ballistic Resistance. *J. Phys. C*, 21:L209–214, 1988.

- [42] B.J. van Wees, H. van Houten, C.W.J. Beenakker, J.G. Williamson, L.P. Kouwenhoven, D. van der Marel, and C.T. Foxon. Quantized Conductance of Point Contacts in a Two-Dimensional Electron-Gas. *Phys. Rev. Lett.*, 60:848–850, 1988.
- [43] D.L. Maslov, C. Barnes, and G. Kirczenow. Ballistic Transport in a Disordered Environment: Why is Conductance Quantization Observable? *Phys. Rev. Lett.*, 70:1984–1987, 1993.
- [44] D.L. Maslov, C. Barnes, and G. Kirczenow. Ballistic Conductor Connected to Disordered Reservoirs: Suppression of the Mesoscopic Conductance Fluctuations. *Phys. Rev. B*, 48:2543–2552, 1993.
- [45] K.J. Thomas, J.T. Nicholls, M.Y. Simmons, M. Pepper, D.R. Mace, and D.A. Ritchie. Possible Spin Polarisation in a One-Dimensional Electron Gas. *Phys. Rev. Lett.*, 77:135–138, 1996.
- [46] A.C. Graham, K.J. Thomas, M. Pepper, M.Y. Simmons, and D.A. Ritchie. 0.7 Structure in Quantum Wires Observed at Crossings of Spin-Polarised 1D Subbands. *Physica E*, 22:264–267, 2004.
- [47] A.A. Starikov, I.I. Yakimenko, and K.F. Berggren. Scenario for the 0.7-Conductance Anomaly in Quantum Point Contacts. *Phys. Rev. B*, 67:235319 1–8, 2003.
- [48] A.C. Graham, D.L. Sawkey, M. Pepper, M.Y. Simmons, and D.A. Ritchie. Energy-Level Pinning and the 0.7 Spin State in One Dimension: GaAs Quantum Wires Studied Using Finite-Bias Spectroscopy. *Phys. Rev. B*, 75:035331 1–6, 2007.
- [49] A. Graham. *Many-Body Interactions in Quantum Wires*. PhD thesis, University of Cambridge, 2003.
- [50] K.S. Pyshkin, C.J.B. Ford, R.H. Harrell, M. Pepper, E.H. Linfield, and D.A. Ritchie. Spin Splitting of One-Dimensional Subbands in High Quality Quantum Wires at Zero Magnetic Field. *Phys. Rev. B*, 62:15842–15850, 2000.
- [51] A.C. Graham, M. Pepper, M. Y. Simmons, and D. A. Ritchie. New Interaction Effects in Quantum Point Contacts at High Magnetic Fields. *Physica E*, 34:588–591, 2006.
- [52] S.M. Cronenwett, H.J. Lynch, D. Goldhaber-Gordon, L.P. Kouwenhoven, C.M. Marcus, K. Hirose, N.S. Wingreen, and V. Umansky. Low-Temperature Fate of the 0.7 Structure in a Point Contact: A Kondo-Like Correlated State in an Open System. *Phys. Rev. Lett.*, 88:226805 1–4, 2002.
- [53] R. de Picciotto, L.N. Pfeiffer, K.W. Baldwin, and K.W. West. Temperature-Dependent 0.7 Structure in the Conductance of Cleaved-Edge-Overgrowth One-Dimensional Wires. *Phys. Rev. B*, 72:033319 1–4, 2005.
- [54] D.W. Langer, A. Ezis, and A.K. Rai. Structure and Lateral Diffusion of Ohmic Contacts in Al-GaAs/GaAs High Electron-Mobility Transistors and GaAs Devices. *J. Vac. Sci. Tech. B*, 5:1030–1032, 1987.
- [55] E. Relling and A.P. Botha. Solid State Diffusion in GaAs/AuGe/Ni and GaAs/Ni/AuGe/Ni Ohmic Contacts. *Appl. Surf. Sci.*, 35:380–387, 1988.
- [56] W.L. Bragg. The Analysis of Crystals by the X-Ray Spectrometer. *Proceedings of the Royal Society*, A89:248–277, 1914.
- [57] L Vegard. *Z. Physik.*, 5:17, 1921.
- [58] S Gehrsitz, H Sigg, N Herres, K Bachem, K Kohler, and FK Reinhart. Compositional Dependence of the Elastic Constants and the Lattice Parameter of $\text{Al}_x\text{Ga}_{1-x}\text{As}$. *Phys. Rev. B*, 60:11601 – 11610, 1999.
- [59] M.S. Goorsky, T.F. Kuech, M.A. Tischler, and R.M. Potemski. Determination of Epitaxial $\text{Al}_x\text{Ga}_{1-x}\text{As}$ Composition from X-Ray Diffraction Measurements. *Appl. Phys. Lett.*, 59:2269–2271, 1991.
- [60] D.K. Bowen and B.K. Tanner. *High Resolution X-ray Diffractometry and Topography*. Taylor & Francis Ltd, London, 1998.
- [61] S. Dhar, W.P. Hong, P.K. Bhattacharya, Y. Nashimoto, and F.Y. Juang. A Detailed Investigation of the D-X Center and other Trap Levels in GaAs- $\text{Al}_x\text{Ga}_{1-x}\text{As}$ Modulation-Doped Heterostructures Grown by Molecular Beam Epitaxy. *IEEE Trans. on Elect. Dev.*, 33:698–706, 1986.

- [62] T. N. Theis and S. L. Wright. Origin Of Residual Persistent Photoconductivity In Selectively Doped GaAs/Al_xGa_{1-x}As Heterojunctions. *Appl. Phys. Lett.*, 48(20):1374–1376, 1986.
- [63] E. Skuras, C. R. Stanley, A. R. Long, E. A. Johnson, A. MacKinnon, H. Yaguchi, M. van der Burgt, and J. Singleton. Shubnikov-de Haas effect and persistent photoconductivity in In_{0.52}Al_{0.48}As. *J. Appl. Phys.*, 86(11):6593–6595, 1999.
- [64] P. Atkinson. *Growth and Characterisation of Low-Dimensional Semiconductor Structures*. PhD thesis, University of Cambridge, 2002.
- [65] C. Jiang, D.C. Tsui, and G Weimann. Threshold Transport of High-Mobility Two-Dimensional Electron-Gas in GaAs/AlGaAs Heterostructures. *Appl. Phys. Lett.*, 53:1533–1535, 1988.
- [66] J.R. Arthur. Interaction of Ga and As₂ Molecular Beams With GaAs Surfaces. *J. Appl. Phys.*, 39:4032–4034, 1968.
- [67] A. Y. Cho. Film Deposition By Molecular-Beam Techniques. *J. Vac. Sci. Tech.*, 8(5):S31, 1971.
- [68] A. Y. Cho. Growth Of Periodic Structures By Molecular-Beam Method. *Appl. Phys. Lett.*, 19(11):467, 1971.
- [69] P.K. Gallagher and S.N.G. Chu. Kinetics of the Dissociation of InP under Vacuum. *J. Phys. Chem.*, 86:3246–3250, 1982.
- [70] A.J. SpringThorpe, S.J. Ingrey, B. Emmerstorfer, P. Mandeville, and W.T. Moore. Measurement of GaAs Surface Oxide Desorption Temperatures. *Appl. Phys. Lett.*, 50:77–79, 1987.
- [71] C. Lenox, H. Nie, G. Kinsey, C. Hansing, J. C. Campbell, A. L. Holmes, and B. G. Streetman. Substrate preparation and interface grading in InGaAs InAlAs photodiodes grown on InP by molecular-beam epitaxy. *J. Vac. Sci. Technol. B*, 17(3):1175–1179, 1999.
- [72] M. R. Bruni, N. Gambacorti, S. Kaciulis, G. Mattogno, M. G. Simeone, L. G. Quagliano, N. Tomassini, and B. Jusserand. Role Of The Substrate Deoxidation Process In The Growth Of Strained InAs/InP Heterostructures. *J. Cryst. Growth*, 150(1-4):123–127, 1995.
- [73] G. Leveque and M. Nouaoura. Temperature Measurements by Optical Pyrometry During the Epitaxial Growth of Semiconductors. *Eur. Phys. J.-Appl. Phys.*, 4(2):227–233, 1998.
- [74] I. Farrer, J.J. Harris, R. Thomson, D. Barlett, C.A. Taylor, and D.A. Ritchie. Substrate Temperature Measurement Using a Commercial Band-Edge Detection System. *J. Cryst. Growth*, 301:88–92, 2007.
- [75] E Bauer. *Z. Kristallogr.*, 110:372, 1958.
- [76] H.E. Beere. *Selective Area Growth of III-V Semiconductor Compounds Using Ga⁺ FIB Deposition During MBE Growth*. PhD thesis, University of Cambridge, 1999.
- [77] F. C. Frank and J. H. van der Merwe. One-Dimensional Dislocations. I. Static Theory. *Proc. R. Soc. A*, 198:205–216, 1949.
- [78] I.N. Stranski and Von L. Krastanov. *Akad. Wiss. Lit. Mainz Math.-Natur. Kl. IIb*, 146:797, 1939.
- [79] M Volmer and A Weber. *Z. Phys. Chem.*, 119:277, 1926.
- [80] C. T. Foxon and B. A. Joyce. Interaction Kinetics Of As₄ And Ga On [100] GaAs Surfaces Using a Modulated Molecular-Beam Technique. *Surf. Sci.*, 50(2):434–450, 1975.
- [81] C. T. Foxon. MBE Growth Of GaAs and III-V-Alloys. *J. Vac. Sci. Tech. B*, 1(2):293–297, 1983.
- [82] C. T. Foxon and B. A. Joyce. Surface Processes Controlling Growth Of Ga_xIn_{1-x}As And Ga_xIn_{1-x}P Alloy-Films By MBE. *J. Cryst. Growth*, 44(1):75–83, 1978.
- [83] R.A. Stradling and P.C. Klipstein. *Growth and Characterisation of Semiconductors*. Adam Hilger, Bristol, 1991.
- [84] W.T. Taferner, K. Mahalingam, D.L. Dorsey, and K.G. Eyink. In Situ Monitoring of GaAs Growth at High Temperature by Spectroscopic Ellipsometry and Desorption Mass Spectroscopy. *J. Cryst. Growth*, 201/202:128–131, 1999.
- [85] T.M. Brennan, J.Y. Tsao, and B.E. Hammons. Reactive Sticking of As₄ During Molecular Beam Homoepitaxy of GaAs, AlAs and InAs. *J. Vac. Sci. Tech. A*, 10:33–45, 1992.

- [86] T. Fujii, T. Inata, K. Ishii, and S. Hiyamizu. Heavily Si-Doped InGaAs Lattice-Matched to InP Grown by MBE. *Electron. Lett.*, 22:191–192, 1986.
- [87] R.C. Newman. The Upper Limits of Useful *n*- and *p*-type doping in GaAs and AlAs. *Mat. Sci. and Eng. B*, 66:39–45, 1999.
- [88] J. Matthews and A. Blakeslee. Defects in Epitaxial Multilayers. I. Misfit Dislocations. *J. Cryst. Growth*, 27:118–125, 1974.
- [89] I. Farrer. *Growth and Applications of Self-Assembled Quantum Dots*. PhD thesis, University of Cambridge, 2001.
- [90] C. T. Foxon. Three decades of molecular beam epitaxy. *J. Cryst. Growth*, 251(1-4):1–8, 2003.
- [91] PF Fewster. X-Ray Analysis of Thin Films and Multilayers. *Rep. Prog. Phys.*, 59:1339 – 1407, 1996.
- [92] A. J. Springthorpe and A. Majeed. Epitaxial-Growth Rate Measurements During Molecular-Beam Epitaxy. *J. Vac. Sci. Technol. B*, 8(2):266–270, 1990.
- [93] L. Goldstein, F. Glas, J. Y. Marzin, M. N. Charasse, and G. Leroux. Growth By Molecular-Beam Epitaxy And Characterization Of InAs/GaAs Strained Layer Superlattices. *Appl. Phys. Lett.*, 47(10):1099–1101, 1985.
- [94] D. Leonard, K. Pond, and P. M. Petroff. Critical Layer Thickness For Self-Assembled InAs Islands On GaAs. *Phys. Rev. B*, 50(16):11687–11692, 1994.
- [95] M. Hovinen, A. Salokatve, and H. Asonen. Properties of Strained $\text{In}_{0.2}\text{Ga}_{0.8}\text{As}/\text{GaAs}$ Superlattices with Various Barrier Thicknesses. *J. Appl. Phys.*, 69:3378–3380, 1991.
- [96] R. M. Sieg, R. N. Sacks, and S. A. Ringel. Application of pyrometric interferometry to the in situ monitoring of $\text{In}_{0.52}\text{Al}_{0.48}\text{As}$, $\text{In}_{0.53}\text{Ga}_{0.47}\text{As}$, and quaternary alloy growth on InP substrates. *J. Cryst. Growth*, 175:256–261, 1997.
- [97] A.Y. Cho. Morphology of Epitaxial Growth of GaAs by a Molecular Beam Method - Observation of Surface Structures. *J. Appl. Phys.*, 41:2780 – 2786, 1970.
- [98] P. K. Larsen, J. H. Neave, J. F. Vanderveen, P. J. Dobson, and B. A. Joyce. GaAs(001)-C (4x4) - A Chemisorbed Structure. *Phys. Rev. B*, 27(8):4966–4977, 1983.
- [99] X. Wallart. A combined RHEED and photoemission comparison of the GaP and InP(001) (2x4) surface reconstructions. *Surf. Sci.*, 506(3):203–212, 2002.
- [100] P.J. Dobson, N.G. Norton, J.H. Neave, and B.A. Joyce. Temporal Intensity Variations in RHEED Patterns During Film Growth of GaAs by MBE. *Vacuum*, 33:593–596, 1983.
- [101] G. W. Turner, B. A. Nechay, and S. J. Egash. Frequency-Domain Analysis Of Time-Dependent Reflection High-Energy Electron-Diffraction Intensity Data. *J. Vac. Sci. Technol. B*, 8(2):283–287, 1990.
- [102] T. E. Harvey, K. A. Bertness, R. K. Hickernell, C. M. Wang, and J. D. Splett. Accuracy of AlGaAs growth rates and composition determination using RHEED oscillations. *J. Cryst. Growth*, 251(1-4):73–79, 2003.
- [103] R. F. Kopf, J. M. Kuo, and M. Ohring. Growth-Rate And Composition Calibration Of III/V Materials On GaAs And InP Using Reflection High-Energy Electron-Diffraction Oscillations. *J. Vac. Sci. Technol. B*, 9(4):1920–1923, 1991.
- [104] P.J. van Hall, H. Kokten, M.R. Leys, and M. Bosch. Monte-Carlo Simulation of MBE Growth of GaAs Analysis of RHEED. *Surf. Rev. and Lett.*, 4:869–872, 1997.
- [105] H. Akiyama, M. Yoshita, L.N. Pfeiffer, and K.W. West. One-Dimensional Excitonic States and Lasing in Highly Uniform Quantum Wires formed by Cleaved-Edge Overgrowth with Growth-Interrupt Annealing. *J. Phys. - Cond. Matt.*, 16:S3549–566, 2004.
- [106] J.M. Van Hove, C.S. Lent, P.R. Pukite, and P.I. Cohen. Damped Oscillations in Reflectance High-Energy Electron-Diffraction. *J. Vac. Sci. Tech. B*, 1:741–746, 1983.
- [107] C. Ungermanns, M. V. D. Ahe, R. Carius, A. Forster, M. Hollfelder, H. Hardtdegen, M. Matt,

- K. Nicoll, R. Schmidt, B. Setzer, and H. Luth. Optimization of III/V binary growth with RHEED in MOMBIE. *Fresenius J. Anal. Chem.*, 358(1-2):101–104, 1997.
- [108] C. Heyn and W. Hansen. Desorption of InAs quantum dots. *J. Cryst. Growth*, 251(1-4):218–222, 2003.
- [109] R. Fernandez, A. Harwit, and D. Kinell. Accurate Measurements Of Transients And Intentional Rates Of Change In Molecular-Beam Epitaxy Growth-Rate Calibrations. *J. Vac. Sci. Technol. B*, 12(2):1023–1025, 1994.
- [110] L. Pfeiffer and K.W. West. The Role of MBE in Recent Quantum Hall Effect Physics Discoveries. *Physica E*, 20:57 – 64, 2003.
- [111] D.C. Tsui, H.L. Stormer, and A.C. Gossard. Two-Dimensional Magnetotransport in the Extreme Quantum Limit. *Phys. Rev. Lett.*, 48:1559–1562, 1982.
- [112] T. Kita, Y. Sato, S. Gozu, and S. Yamada. Large Spontaneous Spin-Splitting and Enhanced Effective g-Factor in Two-Dimensional Electron Gases at $\text{In}_{0.75}\text{Ga}_{0.25}\text{As}/\text{In}_{0.75}\text{Al}_{0.25}\text{As}$ Metamorphic Heterojunctions. *Physica B*, 298:65–69, 2001.
- [113] Y. Sato, T. Kita, S. Gozu, and S. Yamada. Large Spontaneous Spin-Splitting in Gate-Controlled Two-Dimensional Electron Gases at Normal $\text{In}_{0.75}\text{Ga}_{0.25}\text{As}/\text{In}_{0.75}\text{Al}_{0.25}\text{As}$ Heterojunctions. *J. Appl. Phys.*, 89:8017–8021, 2001.
- [114] Y. A. Bychkov and E. I. Rashba. Oscillatory Effects And The Magnetic-Susceptibility Of Carriers In Inversion-Layers. *J. Phys. C*, 17(33):6039–6045, 1984.
- [115] S. Datta and B. Das. Electronic Analog of the Electro-optic Modulator. *Appl. Phys Lett.*, 56:665–667, 1990.
- [116] M.J. Gilbert and J.P. Bird. Application of Split-Gate Structures as Tunable Spin Filters. *Appl. Phys. Lett.*, 77:1050–1052, 2000.
- [117] H.W. Jiang and E. Yablonovitch. Gate-Controlled Electron Spin Resonance in $\text{GaAs}/\text{Al}_x\text{Ga}_{1-x}\text{As}$ Heterostructures. *Phys. Rev. B*, 64:041307 1–4, 2001.
- [118] J. Nitta, Y. Lin, T. Akazaki, and T. Koga. Gate-Controlled Electron g Factor in an InAs-Inserted-Channel $\text{In}_{0.53}\text{Ga}_{0.47}\text{As}/\text{In}_{0.52}\text{Al}_{0.48}\text{As}$ Heterostructure. *Appl. Phys. Lett.*, 83:4565–4567, 2003.
- [119] E.P. de Poortere and M. Shayegan. A Hybrid $\text{Al}_{0.10}\text{Ga}_{0.90}\text{As}/\text{AlAs}$ Bilayer System with Tunable g -Factor. *Appl. Phys. Lett.*, 84:3837–3839, 2004.
- [120] M.D. Godfrey, A. Husmann, H.E. Beere, D.A. Ritchie, S.N. Holmes, and M. Pepper. Gating Schemes for Controlling the Electron Wavefunction Between GaAs and $\text{In}_{0.05}\text{Ga}_{0.95}\text{As}$ Quasi-One-Dimensional Channels. *J. Phys. - Cond. Matt.*, 18:L123–128, 2006.
- [121] P.J. Simmonds, H.E. Beere, S.N. Holmes, and D.A. Ritchie. Growth-Temperature Optimisation for Low Carrier-Density $\text{In}_{0.75}\text{Ga}_{0.25}\text{As}$ -Based HEMTs on InP. Submitted for publication in *J. Appl. Phys.* July 2007.
- [122] R.J. Nicholas, M.A. Brummel, J.C. Portal, K.Y. Cheng, A.Y. Cho, and T.P. Pearsall. An Experimental Determination of Enhanced Electron g -Factors in GaInAs-AlInAs Heterojunctions. *Solid State Comm.*, 45:911–914, 1983.
- [123] G.R. Johnson, A. Kana-ah, B.C. Cavenett, M.S. Skolnick, and S.J. Bass. Magnetic Resonance of 2D Electrons in a Single Quantum Well of InP/GaInAs. *Semicond. Sci. Technol.*, 2:182–184, 1987.
- [124] Y. Lin, J. Nitta, T. Koga, and T. Akazaki. Electron g Factor in a Gated InGaAs Channel with Double InAs-Inserted Wells. *Physica E*, 21:656–660, 2004.
- [125] H. Kosaka, A. A. Kiselev, F. A. Baron, K. W. Kim, and E. Yablonovitch. Electron g factor engineering in III-V semiconductors for quantum communications. *Electron. Lett.*, 37(7):464–465, 2001.
- [126] X. Wallart, J. Lastennet, D. Vignaud, and F. Mollot. Performances and Limitations of InAs/InAlAs Metamorphic Heterostructures on InP for High Mobility Devices. *Appl. Phys. Lett.*, 87:043504 (1–3), 2005.

- [127] D.D. Awschalom, D. Loss, and N. Samarth. *Semiconductor Spintronics and Quantum Computation*. Springer-Verlag, 2002.
- [128] G Dresselhaus. Spin-Orbit Coupling Effects in Zinc Blende Structures. *Phys. Rev.*, 100:580, 1955.
- [129] J.P. Lu, J.B. Yau, S.P. Shukla, M. Shayegan, L. Wissinger, U. Rössler, and R. Winkler. Tunable Spin-Splitting and Spin-Resolved Ballistic Transport in GaAs/AlGaAs Two-Dimensional Holes. *Phys. Rev. Lett.*, 81:1282–1285, 1998.
- [130] J.P. Eisenstein, H.L. Störmer, V. Narayanamurti, A.C. Gossard, and W. Wiegmann. Effect of Inversion Symmetry on the Band Structure of Semiconductor Heterostructures. *Phys. Rev. Lett.*, 53:2579–2582, 1984.
- [131] W. Zawadzki and P. Pfeffer. Spin Splitting of Subband Energies due to Inversion Asymmetry in Semiconductor Heterostructures. *Semicond. Sci. Technol.*, 19:R1–17, 2004.
- [132] J. Nitta, T. Akazaki, H. Takayanagi, and T. Enoki. Gate Control of Spin-Orbit Interaction in an Inverted $\text{In}_{0.53}\text{Ga}_{0.47}\text{As}/\text{In}_{0.52}\text{Al}_{0.48}\text{As}$ Heterostructure. *Phys. Rev. Lett.*, 78:1335–1338, 1997.
- [133] R. Winkler, S.J. Papadakis, E.P. De Poortere, and M. Shayegan. Anomalous Magneto-Oscillations in Two-Dimensional Systems. *Phys. Rev. lett.*, 84:713–716, 2000.
- [134] T. H. Sander, S. N. Holmes, J. J. Harris, D. K. Maude, and J. C. Portal. Determination of the Phase of Magneto-Intersubband Scattering Oscillations in Heterojunctions and Quantum Wells. *Phys. Rev. B*, 58(20):13856–13862, 1998.
- [135] S.H. Simon and B.I. Halperin. Explanation for the Resistivity Law in Quantum Hall Systems. *Phys. Rev. Lett.*, 73:3278–3281, 1994.
- [136] R. Winkler. *Spin-Orbit Coupling Effects in Two-Dimensional Electron and Hole Systems*. Springer, 2003.
- [137] S. Mendach, C. M. Hu, C. Heyn, S. Schnull, H. P. Oepen, R. Anton, and W. Hansen. Strain relaxation in high-mobility InAs inserted-channel heterostructures with metamorphic buffer. *Physica E*, 13(2-4):1204–1207, 2002.
- [138] B. A. Piot, D. K. Maude, M. Henini, Z. R. Wasilewski, K. J. Friedland, R. Hey, K. H. Ploog, A. I. Toropov, R. Airey, and G. Hill. Quantum Hall ferromagnet at high filling factors: A magnetic-field-induced Stoner transition. *Phys. Rev. B*, 72(24):11, 2005.
- [139] S. Koch, R.J. Haug, K. von Klitzing, and M. Razeghi. Suppression of the Landau-Level Coincidence - A Phase-Transition in Tilted Magnetic Fields. *Phys. Rev. B*, 47:4048–4051, 1993.
- [140] F. Capotondi, G. Biasiol, I. Vobornik, L. Sorba, F. Giazotto, A. Cavallini, and B. Fraboni. Two-dimensional electron gas formation in undoped $\text{In}_{0.75}\text{Ga}_{0.25}\text{As}/\text{In}_{0.75}\text{Al}_{0.25}\text{As}$ quantum wells. *J. Vac. Sci. Technol. B*, 22(2):702–706, 2004.
- [141] J.K. Luo, H. Thomas, S.A. Clark, and R.H. Williams. The Effect of Growth Temperature on the Electrical Properties of AlInAs/InP Grown by Molecular Beam Epitaxy and Metal-Organic Chemical-Vapor Deposition. *J. Appl. Phys.*, 74:6726–6733, 1993.
- [142] S. M. Wang, C. Karlsson, N. Rorsman, M. Bergh, E. Olsson, T. G. Andersson, and H. Zirath. Molecular beam epitaxy growth and characterization of $\text{In}_x\text{Ga}_{1-x}\text{As}$ ($0.57 \leq x \leq 1$) on GaAs using InAlAs graded buffer. *J. Cryst. Growth*, 175:1016–1021, 1997.
- [143] F.F. Fang and P.J. Stiles. Effects of a Tilted Magnetic Field on a Two-Dimensional Electron Gas. *Phys. Rev.*, 178:823–828, 1968.
- [144] T. Ando and Y. Uemura. Theory of Oscillatory g Factor in an MOS Inversion Layer under Strong Magnetic Fields. *J. Phys. Soc. Jap.*, 37:1044–1052, 1974.
- [145] A. Usher, R. J. Nicholas, J. J. Harris, and C. T. Foxon. Observation Of Magnetic Excitons And Spin-Waves In Activation Studies Of A 2-Dimensional Electron-Gas. *Phys. Rev. B*, 41(2):1129–1134, 1990.
- [146] M.D. Godfrey. *Transport properties of GaAs/InGaAs Double Quantum Wells and Graded InGaAs*

- Heterostructures.* PhD thesis, University of Cambridge, 2006.
- [147] F. Tremblay. *Quantum Interference and Localization in GaAs.* PhD thesis, University of Cambridge, 1989.
 - [148] Q.Y. Ye, B.I. Shklovskii, A. Zrenner, F. Koch, and K. Ploog. Hopping Transport in Delta-Doping Layers in GaAs. *Phys. Rev. B*, 41:8477–8484, 1990.
 - [149] A.V. Buyanov, A.C. Ferreira, E. Soderstrom, I.A. Buyanova, P.O. Holtz, B. Sernelius, B. Monemar, M. Sundaram, K. Campman, J.L. Merz, and A.C. Gossard. Thermally Activated Intersubband and Hopping Transport in Center-Doped p-Type $\text{GaAs}/\text{Al}_x\text{Ga}_{1-x}\text{As}$ Quantum Wells. *Phys. Rev. B*, 53:1357–1361, 1996.
 - [150] S.P. Shukla, M. Shayegan, S.R. Parihar, S.A. Lyon, N.R. Cooper, and A.A. Kiselev. Large Skyrmions in an $\text{Al}_{0.13}\text{Ga}_{0.87}\text{As}$ Quantum Well. *Phys. Rev. B*, 61:4469–4472, 2000.
 - [151] V.H. Russell, S.N. Holmes, P. Atkinson, D.K. Maude, F. Sfigakis, D.A. Ritchie, and M. Pepper. Suppression of Spin-Splitting in $\text{Al}_{0.33}\text{Ga}_{0.67}\text{As}/\text{Al}_y\text{Ga}_{1-y}\text{As}$ Heterostructures with y varying from 0.10 to 0.15. *Semicond. Sci. Technol.*, 22:722–727, 2007.
 - [152] S. Gozu, C.L. Hong, and S. Yamada. Low Temperature High Electron Mobility in $\text{In}_{0.75}\text{Ga}_{0.25}\text{As}/\text{In}_{0.75}\text{Al}_{0.25}\text{As}$ Modulation-Doped Heterostructures Grown on GaAs Substrate. *Jap. J. Appl. Phys.*, 37:L1501–1503, 1998.
 - [153] W. Desrat, F. Giazotto, V. Pellegrini, F. Beltram, F. Capotondi, G. Biasiol, L. Sorba, and D. K. Maude. Magnetotransport in high-g-factor low-density two-dimensional electron systems confined in $\text{In}_{0.75}\text{Ga}_{0.25}\text{As}/\text{In}_{0.75}\text{Al}_{0.25}\text{As}$ quantum wells. *Phys. Rev. B*, 69(24):245324(1–5), 2004.
 - [154] W. Desrat, F. Giazotto, V. Pellegrini, M. Governale, F. Beltram, F. Capotondi, G. Biasiol, and L. Sorba. Anticrossings of Spin-Split Landau Levels in an InAs Two-Dimensional Electron Gas with Spin-Orbit Coupling. *Phys. Rev. B*, 71:153314 (1–4), 2005.
 - [155] T. Lundberg. Quantum Ballistic Transport in Semiconductor Nanostructures; Effect of Smooth Features in Confining Potentials. *Comp. Mater. Sci.*, 3:78–94, 1994.
 - [156] A.N. Broers, A.C.F. Hoole, and J.M. Ryan. Electron Beam Lithography - Resolution Limits. *Micro. Eng.*, 32:131–142, 1996.
 - [157] R.B. Beck, M. Giedz, A. Wojtkiewicz, A. Kudla, and A. Jakubowski. PECVD Formation of Ultrathin Silicon Nitride Layers for CMOS Technology. *Vacuum*, 70:323–329, 2003.
 - [158] P. Chu, C.L. Lin, and H.H. Wieder. Schottky Barrier Height of $\text{In}_x\text{Al}_{1-x}\text{As}$ Epitaxial and Strained Layers. *Appl. Phys. Lett.*, 53:2423–2425, 1988.
 - [159] K. Higuchi, H. Uchiyama, T. Shiota, M. Kudo, and T. Mishima. Selective wet-etching of InGaAs on InAlAs Using Adipic Acid and its Application to InAlAs/InGaAs HEMTs. *Semicond. Sci. Tech.*, 12:475–480, 1997.
 - [160] R. E. Allen, T. J. Humphreys, J. D. Dow, and O. F. Sankey. Theory Of Surface-Defect States And Schottky-Barrier Heights - Application To InAs. *J. Vac. Sci. Technol. B*, 2(3):449–452, 1984.
 - [161] D.V. Averin and K.K. Likharev. Coulomb Blockade of Single-Electron Tunnelling and Coherent Oscillations in Small Tunnel-Junctions. *J. Low Temp. Phys.*, 62:345–373, 1986.
 - [162] A. Kristensen, H. Bruus, A.E. Hansen, J.B. Jensen, P.E. Lindelof, C.J. Marckmann, J. Nygard, C.B. Sorensen, F. Beuscher, A. Forchel, and M. Michel. Bias and Temperature Dependence of the 0.7 Conductance Anomaly in Quantum Point Contacts. *Phys. Rev. B*, 62:10950–10957, 2000.
 - [163] D.J. Reilly. Phenomenological Model for the 0.7 Conductance Feature in Quantum Wires. *Phys. Rev. B*, 72:033309 (1–4), 2005.
 - [164] F. Sfigakis. *Electron Transport in Etched GaAs/AlGaAs Quantum Wires.* PhD thesis, University of Cambridge, 2005.
 - [165] F. Adler, M. Geiger, A. Bauknecht, F. Scholz, H. Schweizer, M.H. Pilkuhn, B. Ohnesorge, and A. Forchel. Optical Transitions and Carrier Relaxation in Self Assembled InAs/GaAs Quantum

- Dots. *J. Appl. Phys.*, 80:4019–4026, 1996.
- [166] K. Jacobi. Atomic Structure of InAs Quantum Dots on GaAs. *Prog. Surf. Sci.*, 71:185–215, 2003.
- [167] P. Atkinson, M.B. Ward, S.P. Bremner, D. Anderson, T. Farrow, G.A.C. Jones, A.J. Shields, and D.A. Ritchie. Site-Control of InAs Quantum Dots using Ex-Situ Electron-Beam Lithographic Patterning of GaAs Substrates. *Jap. J. Appl. Phys. Pt1*, 45:2519–2521, 2006.
- [168] J. C. Blakesley, P. See, A. J. Shields, B. E. Kardynal, P. Atkinson, I. Farrer, and D. A. Ritchie. Efficient Single Photon Detection By Quantum Dot Resonant Tunneling Diodes. *Phys. Rev. Lett.*, 94(6):4, 2005.
- [169] N. Namekata, Y. Makino, and S. Inoue. Single-Photon Detector for Long-Distance Fiber-Optic Quantum Key Distribution. *Opt. Lett.*, 27(11):954–956, 2002.
- [170] E. Knill, R. Laflamme, and G.J. Milburn. A Scheme for Efficient Quantum Computation with Linear Optics. *Nature*, 409:46–52, 2001.
- [171] S. F. Yoon, P. H. Zhang, H. Q. Zheng, K. Radhakrishnan, and S. Swaminathan. Substrate Temperature Effects on the Growth of $\text{In}_{1-x-y}\text{Ga}_x\text{Al}_y\text{As}$ on InP Substrates by Molecular Beam Epitaxy. *J. Cryst. Growth*, 186(3):315–321, 1998.
- [172] J. Brault, M. Gendry, O. Marty, M. Pitaval, J. Olivares, G. Grenet, and G. Hollinger. Staggered vertical self-organization of stacked InAs/InAlAs quantum wires on InP(001). *Appl. Surf. Sci.*, 162:584–589, 2000.
- [173] S. Frechengues, V. Drouot, B. Lambert, D. Lemoine, S. Loualiche, A. LeCorre, and H. Lharidon. Direct correlation of structural and optical properties of InAs self-assembled dots deposited on InP(100). *Appl. Phys. Lett.*, 71(19):2818–2820, 1997.
- [174] B. H. Koo, Y. G. Park, H. Makino, J. H. Chang, T. Hanada, D. Shindo, and T. Yao. Molecular beam epitaxy growth and characterization of self-assembled InAs quantum dots on (100) InAlAs/InP substrates. *Appl. Surf. Sci.*, 190(1-4):226–230, 2002.
- [175] P.J. Simmonds, H.E. Beere, H.W. Li, P. See, A.J. Shields, and D.A. Ritchie. Growth by Molecular Beam Epitaxy of Self-Assembled InAs Quantum Dots on InAlAs and InGaAs Lattice-Matched to InP. *J. Vac. Sci. Tech. B*, 25:1044–1048, 2007.
- [176] H.W. Li, P. Simmonds, H.E. Beere, B.E. Kardynal, P. See, D.A. Ritchie, and A.J. Shields. Optimisation of Quantum Dot Resonant Tunnelling Diodes for Fibre Wavelength Detection. *Phys. Status Solidi C*, 3:4035–4038, 2006.
- [177] H.W. Li, B.E. Kardynal, P. See, A.J. Shields, P.J. Simmonds, H.E. Beere, and D.A. Ritchie. Quantum Dot Resonant Tunnelling Diode for Telecom Wavelength Single Photon Detection. *Appl. Phys. Lett.*, 91:073516 1–3, 2007.
- [178] T. Walther, A. G. Cullis, D. J. Norris, and M. Hopkinson. Nature of the Stranski-Krastanow transition during epitaxy of InGaAs on GaAs. *Phys. Rev. Lett.*, 86(11):2381–2384, 2001.
- [179] F. Patella, S. Nufris, F. Arciprete, M. Fanfoni, E. Placidi, A. Sgarlata, and A. Balzarotti. Tracing the two- to three-dimensional transition in the InAs/GaAs(001) heteroepitaxial growth. *Phys. Rev. B*, 67(20):5, 2003.
- [180] A. G. Cullis, D. J. Norris, T. Walther, M. A. Migliorato, and M. Hopkinson. Stranski-Krastanow transition and epitaxial island growth. *Phys. Rev. B*, 66(8):4, 2002.
- [181] G. Grenet, E. Bergignat, M. Gendry, M. Lapeyrade, and G. Hollinger. In situ XPS investigation of indium surface segregation for $\text{Ga}_{1-x}\text{In}_x\text{As}$ and $\text{Al}_{1-x}\text{In}_x\text{As}$ alloys grown by MBE on InP(001). *Surf. Sci.*, 352:734–739, 1996.
- [182] B. H. Koo, T. Hanada, H. Makino, J. H. Chang, and T. Yao. RHEED investigation of the formation process of InAs quantum dots on (100) InAlAs/InP for application to photonic devices in the 1.55 μm range. *J. Cryst. Growth*, 229(1):142–146, 2001.
- [183] H. Li, Z. Wang, J. Liang, B. Xu, J. Wu, Q. Gong, C. Jiang, F. Liu, and W. Zhou. InAs quantum

- dots in InAlAs matrix on (001)InP substrates grown by molecular beam epitaxy. *J. Cryst. Growth*, 187(3-4):564–568, 1998.
- [184] D. Fuster, L. Gonzalez, Y. Gonzalez, J. Martinez-Pastor, T. Ben, A. Ponce, and S. Molina. Emission wavelength engineering of InAs/InP(001) quantum wires. *Eur. Phys. J. B*, 40(4):433–437, 2004.
- [185] H. J. Parry, M. J. Ashwin, J. H. Neave, and T. S. Jones. Growth of InAs/InP(001) nanostructures: The transition from quantum wires to quantum dots. *J. Cryst. Growth*, 278(1-4):131–135, 2005.
- [186] R. H. Wang, A. Stintz, P. M. Varangis, T. C. Newell, H. Li, K. J. Malloy, and L. F. Lester. Room-temperature operation of InAs quantum-dash lasers on InP (001). *IEEE Photonics Technol. Lett.*, 13(8):767–769, 2001.
- [187] V. Bressler-Hill, A. Lorke, S. Varma, P.M. Petroff, K. Pond, and W.H. Weinberg. Initial Stages of InAs Epitaxy on Vicinal GaAs(001)-(2x4). *Phys. Rev. B*, 50:8479–8487, 1994.
- [188] A Kryzhanovsky. SPM Image Magic. Author contact information: alex@agvb.ioffe.rssi.ru.
- [189] A. Weber, O. Gauthier-Lafaye, F.H. Julien, Brault J., M. Gendry, Y. Dsieres, and T. Benyattou. Strong Normal-Incidence Infrared Absorption in Self-Organized InAs/InAlAs Quantum Dots Grown on InP(001). *Appl. Phys. Lett.*, 74:413–415, 1999.
- [190] J. Brault, M. Gendry, G. Grenet, G. Hollinger, Y. Desieres, and T. Benyattou. Role of Buffer Surface Morphology and Alloying Effects on the Properties of InAs Nanostructures Grown on InP(001). *Appl. Phys. Lett.*, 73(20):2932–2934, 1998.
- [191] S. Raymond, S. Studenikin, S.J. Cheng, M. Pioro-Ladriere, M. Ciorga, P.J. Poole, and M.D. Robertson. Families of Islands in InAs/InP Self-Assembled Quantum Dots: A Census Obtained from Magneto-Photoluminescence. *Semicond. Sci. Technol.*, 18:385–389, 2003.
- [192] F. Patella, F. Arciprete, M. Fanfoni, A. Balzarotti, and E. Placidi. Apparent critical thickness versus temperature for InAs quantum dot growth on GaAs(001). *Appl. Phys. Lett.*, 88(16):3, 2006.
- [193] S. Kiravittaya, Y. Nakamura, and O.G. Schmidt. Photoluminescence Linewidth Narrowing of InAs/GaAs Self-Assembled Quantum Dots. *Physica E*, 13:224–228, 2002.
- [194] R. Schwertberger, D. Gold, J. P. Reithmaier, and A. Forchel. Epitaxial growth of $1.55\text{ }\mu\text{m}$ emitting InAs quantum dashes on InP-based heterostructures by GS-MBE for long-wavelength laser applications. *J. Cryst. Growth*, 251(1-4):248–252, 2003.
- [195] H. Mizuta and T. Tanoue. *The Physics and Applications of Resonant Tunnelling Diodes*. Cambridge University Press, 1995.
- [196] U.S.P. See. In situ *Focused Ion Beam Patterned Resonant Tunnelling Diodes*. PhD thesis, University of Cambridge, 1999.
- [197] T.S. Moise, Y.C. Kao, A.J. Katz, T.P.E Broekaert, and F.G. Celii. Experimental Sensitivity Analysis of Pseudomorphic InGaAs/AlAs Resonant Tunnelling Diodes. *J. Appl. Phys.*, 78:6305–6317, 1995.
- [198] Y. Miyamoto, H. Tobita, K. Oshima, and K. Furuya. Barrier Thickness Dependence of Peak Current Density in GaInAs/AlAs/InP Resonant Tunneling Diodes by MOVPE. *Solid State Electron.*, 43:1395–1398, 1999.
- [199] T. Inata, S. Muto, Y. Nakata, T. Fujii, H. Ohnishi, and S. Hiyamizu. Excellent Negative Differential Resistance of InAlAs-InGaAs Resonant Tunneling Barrier Structures Grown By MBE. *Jap. J. Appl. Phys. Pt. 2*, 25:L983–985, 1986.
- [200] I. Mehdi and G. Haddad. Lattice Matched and Pseudomorphic $\text{In}_{0.53}\text{Ga}_{0.47}\text{As}/\text{In}_x\text{Al}_{1-x}\text{As}$ Resonant Tunneling Diodes With High Current Peak-To-Valley Ratio For Millimeter-Wave Power Generation. *J. Appl. Phys.*, 67:2643–2646, 1990.
- [201] F. Fossard, A. Helman, G. Fishman, F.H. Julien, J. Brault, M. Gendry, E. Peronne, A. Alexandrou, S.E. Schacham, G. Bahir, and E. Finkman. Spectroscopy of the Electronic States in InAs Quantum Dots Grown on $\text{In}_x\text{Al}_{1-x}\text{As}/\text{InP}(001)$. *Phys. Rev. B*, 69:155333 1–6, 2004.
- [202] Y. C. Pao and J. S. Harris. Molecular-Beam Epitaxial-Growth And Structural Design Of

- In_{0.52}Al_{0.48}As/In_{0.53}Ga_{0.47}As/InP HEMTs. *J. Cryst. Growth*, 111(1-4):489–494, 1991.
- [203] B.E. Kardynal, A.J. Shields, N.S. Beattie, I. Farrer, K. Cooper, and D.A. Ritchie. Low-Noise Photon Counting with a Radio-Frequency Quantum-Dot Field-Effect Transistor. *Appl. Phys. Lett.*, 84:419–421, 2004.
- [204] S.S. Hees, B.E. Kardynal, P. See, A.J. Shields, I. Farrer, and D.A. Ritchie. Effect of InAs Dots on Noise of Quantum Dot Resonant Tunneling Single-Photon Detectors. *Appl. Phys. Lett.*, 89:153510 1–3, 2006.
- [205] M. Governale and U. Zülicke. Rashba Spin Splitting in Quantum Wires. *Solid State Comm.*, 131:581–589, 2004.
- [206] T. Schapers, J. Knobbe, and V. A. Guzenko. Effect of Rashba spin-orbit coupling on magnetotransport in InGaAs/InP quantum wire structures. *Phys. Rev. B*, 69(23):235323(1–5), 2004.